



UNIVERSITAT DE
BARCELONA

Solution Processed Chalcogenide Nanomaterials for Thermoelectric Application

Zhang Yu



Aquesta tesi doctoral està subjecta a la llicència **Reconeixement- NoComercial – SenseObraDerivada 4.0. Espanya de Creative Commons.**

Esta tesis doctoral está sujeta a la licencia **Reconocimiento - NoComercial – SinObraDerivada 4.0. España de Creative Commons.**

This doctoral thesis is licensed under the **Creative Commons Attribution-NonCommercial-NoDerivs 4.0. Spain License.**

Tesi doctoral

Solution Processed Chalcogenide
Nanomaterials for Thermoelectric
Application

Autor:

Yu Zhang

Directors:

Prof. Andreu Cabot i Prof. Doris Cadavid



UNIVERSITAT DE
BARCELONA

Solution Processed Chalcogenide Nanomaterials for Thermoelectric Application

Memòria presentada per optar al grau de doctor per la
Universitat de Barcelona

Programa de doctorat en Nanociències

Autor:

Yu Zhang

Directors:

Prof. Andreu Cabot i Prof. Doris Cadavid

Tutor:

Prof. Alejandro Perez-Rodriguez

Lloc on s'ha dut a terme la tesi

Institut de Recerca en Energia de Catalunya (IREC)



UNIVERSITAT DE
BARCELONA

Contents

Acknowledgement.....	7
List of publications.....	9
Authors' contributions	10
Preface.....	13
Summary of results.....	14
Resumen de Resultados	17
Chapter 1	20
1.1 Thermoelectricity	20
1.2 Optimization of TE efficiency.....	22
1.3 TE nanomaterial synthetic approaches	26
1.4 Molecular inks	27
1.5 Colloidal synthesis of nanomaterials.....	29
1.4.1 Size control	30
1.4.2 Shape control.....	30
1.4.3 Phase and composition control	31
1.4.4 Nanocrystal purification and surface modification	33
1.6 Objectives	33
1.7 Reference.....	35
Chapter 2 Tin Diselenide Molecular Precursor for Solution-Processable TE Materials	42
2.1 Abstract	42
2.2 Introduction.....	42
2.3 Experimental Section.....	44
2.4 Result and Discussion	47
2.5 Conclusions.....	60
2.6 References	60
Chapter 3 Tin Selenide Molecular Ink for the Solution-Processing of TE Materials and Devices	64
3.1 Abstract	64
3.2 Introduction.....	65
3.3 Experimental Section.....	66
3.4 Result and discussion	69
3.5 Conclusions.....	83
3.6 Reference	83

Chapter 4 Bismuth telluride-copper telluride nanocomposites from heterostructured building blocks.....	87
4.1 Abstract	87
4.2 Introduction.....	88
4.3 Experimental section	90
4.4 Results and discussion.....	92
4.5 Conclusions.....	107
4.6 References	108
Chapter 5 Influence of copper telluride nanodomains on the transport properties of n-type bismuth telluride	112
5.1 Abstract	112
5.2 Introduction.....	113
5.3 Experimental section	115
5.4 Result and discussion	118
5.5 Conclusions.....	129
5.6 References	129
Result and Discussions	133
Conclusions.....	136
Future work	138
CURRICULUM VITAE	139
.....	140
Annex.....	143

Acknowledgement

The four years PhD journey would be one of the best memories in my life. When I try to remember someone or something, those pictures immediately come to my mind like it just happened yesterday.

My deep gratitude goes first to professor Andreu Cabot. As a great supervisor, he has taught me, both consciously and unconsciously, how to perform a good scientific research. He is a great advisor who always offer helps whenever we need, who likes to make jokes to defuse awkward situations, who trusts us and respects our own choice... With his kind guidance, we all feel very comfortable to be part of the team. Thank you for your understanding, wisdom, patience and encouragement during the four years.

The team members of the FN group have contributed immensely to my personal and lab time at Barcelona. I would like to thank their pleasant accompany and generous help. They are: Dr. Zhishan Luo, Dr. Evgenii Liashenko, Ms Xiaoting Yu, Dr. Junfeng Liu, Dr. Taisiia Berestok, Kai Pan, Dr. Junshan Li, Yong Zuo, Congcong Xing, Ruifeng Du, Chaoqi Zhang, Mengyao Li, Alberto Ramón Ferrer, Sergi V. S, Dawei Yang, Xiang Wang, Ke xiao, Guillem Montaña, Dr. Michaela Meyns, Dr. Maria Soria, Dr. Marcos Costa, Dr. Pablo Guardia, Maria Garcia and Marcos Sanles, thank you for all your caring, sharing, helping and discussing in the past four years, I feel very lucky to be one of the group.

I would like to specifically thank the help from the TE mini group, they are: Dr. Doris Cadavid Rodriguez, Dr. Silvia Ortega, Dr. Yu Liu and Dr. Lim Khak Ho, thanks for your physically and mentally accompany year by year, I will never forget the delightful moments we had in the lab.

My appreciation also extends to Prof. Jordi Arbiol, Maria Chiara, Pengyi Tang, Ting Zhang and Xu Han for helping me with HRTEM testing. Thank you for your time for helping me to get nice images and data!

I would also like to thank Prof. Jordi Llorca for helping with the XPS measurement. Thank you for your great patience to arrange the meetings every

time for discussing and sending us results with detailed XPS data analysis.

My sincere thanks also goes to Dr. Maria Ibáñez, thank you for hosting me as an exchange PhD student in the Institute of Science and Technology Austria. It's a pleasure to work with great people from the group, they are: Seungho Lee, Mariano Calcabrini, Dr. Dogukan Apaydin and Helen Tan.

I am grateful that my four years PhD studies was financially supported by the Chinese Scholarship Council, and a big thanks to EIT InnoEnergy for providing funding supporting to allow me to attend various courses abroad as well as providing living expenses during international mobility.

And the last but not the least, I would like to acknowledge the support from my lovely families. Your encouragement always makes me confidently move forward!

List of publications

My PhD research work have been disseminated in three manuscripts, which have already been published or accepted in first quartile peer-reviewed journals. A full copy of each of the publications can be found in the Annex part. The following is the list of publications included in this thesis:

1. **Y. Zhang**, Y. Liu, K.H. Lim, C. Xing, M. Li, T. Zhang, P. Tang, J. Arbiol, J. Llorca, M. Ka, M. Ibáñez, G. Pablo, P. Mirko, D. Cadavid, A. Cabot. *Tin Diselenide Molecular Precursor for Solution-Processable Thermoelectric Materials*. *Angewandte Chemie*, 2018, 130 (52), 17309-17314.
2. **Y. Zhang**, Y. Liu, C. Xing, T. Zhang, M. Li, M. Pacios, X. Yu, J. Arbiol, J. Llorca, D. Cadavid, M. Ibáñez, A. Cabot. *Tin Selenide Molecular Precursor for the Solution-Processing of Thermoelectric Materials and Devices*. *ACS Applied Materials & Interfaces*, 2020, 12, 24, 27104–27111.
3. **Y. Zhang**, Y. Liu, M. Calcabrini, C. Xing, X. Han, J. Arbiol, D. Cadavid, M. Ibáñez, A. Cabot. *Bismuth telluride-copper telluride nanocomposites from heterostructured building blocks*. *Journal of Materials Chemistry C*, 2020, DOI: 10.1039/D0TC02182B.

Authors' contributions

The work presented in this thesis was performed in Catalonia Institute for Energy Research (IREC). The PhD student, **Yu Zhang**, has primary contribution in all experimental work, data processing and manuscript writing for each of the publications included in this thesis. The contribution of co-authors corresponding to each paper are specifically mentioned in the paragraphs below. The impact factor in 2018 of the journals where the manuscripts were published is provided. All of the publications belong to the 1st quartile according to the Science Citation Index. None of these papers has been previously presented in any other PhD thesis.

In all the publications, Andreu Cabot and Doris Cadavid conceived and guided the projects, participated in the experiment design and manuscript writing.

Chapter 2:

Y. Zhang, Y. Liu, K.H. Lim, C. Xing, M. Li, T. Zhang, P. Tang, J. Arbiol, J. Llorca, M. Ka, M. Ibáñez, G. Pablo, P. Mirko, D. Cadavid, A. Cabot. *Tin Diselenide Molecular Precursor for Solution-Processable Thermoelectric Materials*. *Angewandte Chemie*, 2018, 130 (52), 17309-17314.

Impact factor 2019: **12.959**

In this work, Y. Zhang designed the experiments, performed X-ray diffraction analyses (XRD), scanning electron microscopy (SEM), X-ray spectrometer (EDX), transmission electron microscopy (TEM), TE characterization and wrote the first draft of the manuscript. Y. Liu and K.H. Lim participated in experiment design and material synthesis, C. Xing, M. Ka, M. Ibáñez and M. Li participated in data analysis. T. Zhang and J. Arbiol participated in High Resolution TEM (HRTEM) characterization, P. Mirko, G. Pablo and J. Llorca participated in X-ray photoelectron spectroscopy (XPS) measurement.

Chapter 3:

Y. Zhang, Y. Liu, C. Xing, T. Zhang, M. Li, M. Pacios, X. Yu, J. Arbiol, J.

Llorca, D. Cadavid, M. Ibáñez, A. Cabot. *Tin Selenide Molecular Precursor for the Solution-Processing of Thermoelectric Materials and Devices*. *ACS Applied Materials & Interfaces*, 2020, 12, 24, 27104–27111.

Impact factor 2019: **8.758**

In this work, Y. Zhang designed the experiments, prepared the molecular precursor, performed XRD, SEM-EDX, TEM, TGA, UV, FTIR TE characterization and wrote the first draft of the manuscript. Y. Liu participated in experiment design and material synthesis, C. Xing, X. Yu, M. Ibáñez and M. Li participated in data analysis. M. Pacios conducted AFM characterization. T. Zhang and J. Arbiol participated in HRTEM characterization, J. Llorca participated in XPS measurement.

Chapter 4:

Y. Zhang, Y. Liu, M. Calcabrini, C. Xing, X. Han, J. Arbiol, D. Cadavid, M. Ibáñez, A. Cabot. *Bismuth telluride-copper telluride nanocomposites from heterostructured building blocks*. *Journal of Materials Chemistry C*, 2020. (accepted, DOI: 10.1039/D0TC02182B)

Impact factor 2019: **7.059**

In this work, Y. Zhang designed the experiments, performed UV, XRD, SEM-EDX, TEM, TE characterization and wrote the first draft of the manuscript. Y. Liu participated in experiment design and material synthesis, C. Xing and M. Ibáñez participated in data analysis. M. Calcabrini conducted thermal conductivity calculation. X. Han and J. Arbiol participated in HRTEM characterization.

Chapter 5:

Y. Zhang, Y. Liu, C. Xing, M. Li, K. Xiao, S. Lee, X. Han, J. Arbiol, D. Cadavid, M. Ibáñez, A. Cabot. *Influence of copper telluride nanodomains on the transport properties of n-type bismuth telluride*, (submitted).

In this work, Y. Zhang designed the experiments, synthesized nanomaterials,

performed XRD, SEM, TEM, TE characterization and wrote the first draft of the manuscript. Y. Liu participated in experiment design and material synthesis, C. Xing, M. Li, K. Xiao and M. Ibáñez participated in data analysis. S. Lee, X. Han and J. Arbiol participated in HRTEM characterization.

Prof. Andreu Cabot

and Prof. Doris Cadavid

certify the information provided above is true.

Barcelona, 7th of September 2020

Preface

The five chapters incorporated in this PhD thesis cover the work performed by the PhD candidate Yu Zhang at the Institut de Recerca en Energia de Catalunya (IREC) in Sant Adrià de Besòs, Barcelona, in the period 2016-2020, supported by China Scholarship Council (No. 201606370026). The thesis focuses on the bottom-up engineering of high-performance Thermoelectric (TE) nanomaterial with fine tuned properties.

In the first chapter, a fundamental introduction to the basic concepts of the involved fields, their state of the art, the remaining challenges and the thesis objectives are presented. Experimental work is incorporated in chapters two to five. Within the general frame of optimizing TE materials through bottom-up engineering, the work presented in this thesis aims at solving main challenges in this field: 1) To decrease the cost of TE materials and modules by means of developing an using cost-effective and scalable molecular inks for the printing of TE modules. 2) to control the charge carrier concentration in the matrix by means of a modulation doping; 3) to increase the nanocomposites (NCs) Seebeck coefficient by the selective scattering of low energy charge carriers; 4) to decrease the thermal conductivity by phonon scattering. In chapter two and chapter three, I detail a solution-based molecular ink method to synthesize SnSe_x NPLs with controlled amounts of dopant and their use to produce crystallographically textured nanomaterials. In chapter four and chapter five, I detail strategies to engineer optimized TE NCs, in this case based on $\text{Bi}_2\text{Te}_3\text{-Cu}_{2-x}\text{Te}$, with improved TE performance. I analyze their TE performance and explain it by several mechanisms, including energy filtering, modulation doping, and phonon scattering.

Summary of results

The bottom-up engineering of nanomaterials using solution-processing strategies is of particular interest for reducing cost and optimizing the performance of TE materials and devices. Solution processing offers a promising path towards low-cost mass production of TE devices as it avoids high capital investment, energy intensive processes, operating and maintenance costs. Additionally, nanomaterials can contribute in improving TE properties in several ways: a) Small amounts of nanoparticles (NPs) inserted inside a crystalline matrix could provide higher charger carrier concentration without significantly damaging the carrier mobility. b) Nanodomains introduce numerous grain boundaries which effectively scatter long- and mid-wavelength phonons to reduce thermal conductivities. c) Nanostructured materials could give rise to larger Seebeck coefficients by modifying the density of states as well as provide energy dependent carrier scattering.

Conventional strategies to produce nanomaterials and particularly NCs lack of precise control over structural and chemical parameters, which limit the proper optimization of TE properties. This thesis focuses on the development of scalable methods for the production of TE nanomaterials with optimized performance. In these directions, the general goal of this thesis is to develop cost-effective TE devices with improved TE conversion efficiency and low production cost. Some particular goals have been targeted: a) Exploring earth abundant, low-cost, and less toxic materials with superior thermoelectric performance to realize the large-scale commercial applications; b) Developing low-cost and scalable methodologies to produce cost effective TE materials and modules; c) Improving TE performance by applying nanostructure-based materials; d) Optimizing TE efficiency by means of a modulation doping and energy filtering mechanisms.

The thesis is divided into 5 chapters. Chapter 1 introduces solution-based approaches for producing functional nanomaterials and the general state of the art in the field of thermoelectricity. Chapter 2 and chapter 3 present a fast and simple molecular ink-based method to produce low cost and crystallographically

textured SnSe₂ and SnSe nanomaterials. Molecular ink printing techniques could offer a scalable approach to fabricate TE devices on flexible substrates. In these chapters, I proved that cost-effective p-type SnSe NPLs could be produced by a molecular ink-based strategy that allowed introducing controlled amounts of Te to achieve unprecedentedly high TE figure of merit. On the other hand, n-type SnSe₂ nanomaterials were also intentionally produced from the same strategy to complement an all Sn-Se based device. Both of the bulk nanomaterials displayed significant crystallographic texture after hot pressing, resulting in highly anisotropic charge and heat transport properties. Additionally, the possible mechanism was explored to control the shape of SnSe from square NPL to dendritic nanostructure, as well as explained a screw dislocation-driven mechanism to obtain flower-like SnSe₂ particles. Different approaches were applied to optimize their TE performance: SnSe₂ NPLs were blended with metal NPs to produce a metal-semiconductor NC. The electrical conductivities of the blends were significantly improved with respect to bare SnSe₂ bulk nanomaterial and a three-fold increase in the TE figure of merit was obtained, reaching unprecedented values up to $ZT = 0.65$ for SnSe₂ material. For SnSe nanomaterials, I demonstrate that the introduction of small amounts of tellurium in the precursor ink allowed reducing the band gap, increasing both charge carrier concentration and mobility, especially cross plane, with a minimal decrease of the Seebeck coefficient. This strategy translated into record out of plane ZT values at 800 K, $ZT=1.05$. The results in Chapter 2 were published in *Angewandte Chemie* in 2018, and the results of Chapter 3 were published in *ACS Applied Materials & Interfaces* in 2020.

In spite of achieving controllable engineering on SnSe_x single crystal phase, properly designed NCs allow improving TE performance by several mechanism, including phonon scattering, modulation doping and energy filtering, we subsequently focus on producing nanomaterials with more complicated phase and structure.

Chapter 4 and chapter 5 describe two different strategies to produce Bi₂Te₃-Cu₂-

x Te NCs based on the consolidation of nanostructured building blocks. I first detail a two-step solution-based process to produce the $\text{Bi}_2\text{Te}_3\text{-Cu}_{2-x}\text{Te}$ heteronanostructures, based on the growth of Cu_{2-x}Te nanocrystals on the surface of Bi_2Te_3 nanowires. The transport properties of the NCs are investigated as a function of the amount of Cu introduced, which reveal that the presence of Cu decreases the material thermal conductivity through promotion of phonon scattering, modulates the charge carrier concentration through electron spillover, and increases the Seebeck coefficient through filtering of charge carriers at energy barriers. These effects result in an improvement of over 50% of the TE figure of merit of Bi_2Te_3 . As comparison, I produced $\text{Bi}_2\text{Te}_3\text{-Cu}_{2-x}\text{Te}$ NCs by directly mixing proper ratio of individual Bi_2Te_3 nanowires with Cu_{2-x}Te nanocubes and consolidating the resulting NP mixture by hot-press. A significant difference of transport properties was detected when compared with NCs fabricated by hot-pressing heterostructured $\text{Bi}_2\text{Te}_3\text{-Cu}_{2-x}\text{Te}$ nanowires. On the contrary to the composite obtained from hetero-nanostructures, the presence of Cu_{2-x}Te nanodomains did not lead to a significant reduction of the lattice thermal conductivity of the reference Bi_2Te_3 , which is already very low here, but it resulted in a nearly threefold increase of its power factor. Additionally, the presence of Cu_{2-x}Te resulted in a strong increase of the Seebeck coefficient. This increase is related to the energy filtering of charge carriers at energy barriers within Bi_2Te_3 domains created by the accumulation of electrons in the regions nearby $\text{Cu}_{2-x}\text{Te}/\text{Bi}_2\text{Te}_3$ junctions. Overall, a significant improvement of figure of merit, up to a 250%, was obtained with the suitable combination of Cu_{2-x}Te NPs and Bi_2Te_3 nanowires. The results in Chapter 4 has been accepted in *Journal of Materials Chemistry C* in 2020. The results of Chapter5 have been submitted for publication in 2020.

Finally, the main conclusions of this thesis and some perspectives for future work are presented.

Resumen de Resultados

La ingeniería de nanomateriales a partir del procesado en solución es de particular interés para optimizar el rendimiento de los materiales y dispositivos termoeléctricos. Estos materiales pueden contribuir a reducir el coste de los materiales y dispositivos y a su vez a mejorar las propiedades termoeléctricas de varias maneras: a) Una pequeña cantidad de nanopartículas insertadas dentro de una matriz cristalina podría proporcionar mayor concentración de portadores de carga sin dañar significativamente la movilidad de los portadores. b) Los nanodominios crean numerosas fronteras de grano que dispersarían en gran medida los fonones de longitud de onda larga y media para reducir la conductividad térmica. c) Los materiales nanoestructurados podrían dar lugar a coeficientes Seebeck más grandes al modificar la densidad de estados, así como proporcionar una dispersión de portadores en función de su energía.

Dado que las estrategias convencionales de producción de nanopartículas no ofrecen un control preciso sobre los parámetros estructurales y químicos. Esta tesis está se centra en el diseño y el ensamblaje racional de nanomateriales termoeléctricos de alto rendimiento a través de procesado en solución con los siguientes objetivos: a) Sintetizar nanomateriales adecuados a través del control preciso del tamaño, la forma, la ingeniería de composición y la química de la superficie. b) Desarrollar estrategias adecuadas para fabricar nanocompuestos seleccionando materiales matriz y dopajes con el rendimiento deseado, y consolidar su combinación en materiales nanoestructurados. c) Establecer primeros pasos para producir dispositivos termoeléctricos rentables mediante tintas y procesos de impresión.

La tesis se divide en 5 capítulos. El Capítulo 1 aborda la introducción fundamental del enfoque sintético para producir nanomateriales funcionales. Los capítulos 2 y 3 presentan un método rápido y simple basado en soluciones para producir nanomateriales SnSe_2 y SnSe con textura cristalográfica. Dado que los calcogenuros de estaño son materiales especialmente interesantes para la conversión de energía termoeléctrica, se sintetizaron nanoplacas SnSe de tipo p

controlables por forma mediante una estrategia basada en tinta molecular para lograr una figura de mérito termoeléctrica sin precedentes por dopaje con Te. Por otro lado, los nanomateriales SnSe₂ de tipo n también se produjeron para complementar un dispositivo basado en Sn-Se. Ambos nanomateriales mostraron una textura cristalográfica significativa después del prensado en caliente, lo que dio como resultado unas propiedades de transporte de carga calor altamente anisotrópicas. Además, exploramos el posible mecanismo para controlar la forma de SnSe desde la nanoplaca cuadrada hasta la nanoestructura dendrítica, y explicamos un mecanismo impulsado por la dislocación de tornillo para obtener capas de SnSe₂ estructuradas con flores. Se aplicaron diferentes enfoques para optimizar su rendimiento termoeléctrico: las nanoplacas SnSe₂ se mezclan con nanopartículas metálicas para fabricar un nanocompuesto semiconductor-metal, donde las conductividades eléctricas de las mezclas se mejoran significativamente con respecto al SnSe₂ y un aumento de tres veces en el Se obtuvo la mayor figura de mérito TE, alcanzando valores sin precedentes de hasta $ZT = 0.65$ para el material SnSe₂. Para los nanomateriales SnSe, demostramos que la introducción de pequeñas cantidades de telurio en la tinta precursora permite reducir el bandgap, aumentar tanto la concentración como la movilidad del portador de carga, especialmente el plano transversal, con una disminución mínima del coeficiente Seebeck, que se traduce en mayor valores de ZT a 800 K. Los resultados del Capítulo 2 se publicaron en *Angewandte Chemie* en 2018, y los resultados del Capítulo 3 se publicaron en *ACS Applied Materials & Interfaces* en 2020.

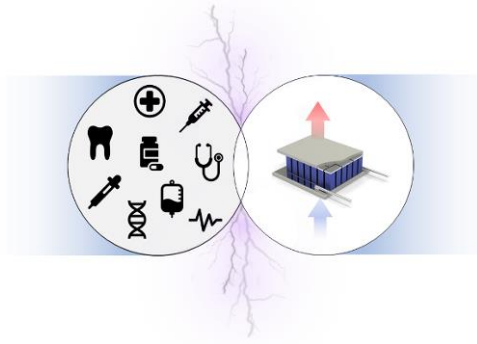
Los capítulos 4 y 5 describen dos estrategias diferentes para producir nanocompuestos Bi₂Te₃-Cu_{2-x}Te basados en la consolidación de nanoestructuras. Primero detallamos un proceso basado en dos pasos para producir las heteronanoestructuras Bi₂Te₃-Cu_{2-x}Te, basadas en el crecimiento de nanocristales Cu_{2-x}Te en la superficie de los nanocables Bi₂Te₃. Las propiedades de transporte de los nanocompuestos se investigan en función de la cantidad de Cu introducido. La presencia de Cu disminuye la conductividad térmica del material a través de la promoción de la dispersión de fonones, modula la

concentración del portador de carga a través del derrame de electrones y aumenta el coeficiente Seebeck a través del filtrado de portadores de carga en barreras energéticas. Estos efectos resultan en una mejora de más del 50% de la figura de mérito termoeléctrica de Bi_2Te_3 . Como comparación, producimos nanocompuestos $\text{Bi}_2\text{Te}_3\text{-Cu}_{2-x}\text{Te}$ mezclando directamente la proporción adecuada de nanohilos de Bi_2Te_3 con nanocubos de Cu_{2-x}Te y prensando en caliente la mezcla de nanopartículas resultante. Se detectó una diferencia significativa de las propiedades de transporte en comparación con el nanocompuesto fabricado por nanoestructuras $\text{Bi}_2\text{Te}_3\text{-Cu}_{2-x}\text{Te}$. Al contrario de la hetero-nanoestructura, la presencia de nanodominios Cu_{2-x}Te no conduce a una reducción significativa de la conductividad térmica del Bi_2Te_3 de referencia, que ya es muy baja aquí, pero resulta en un aumento de casi tres veces de su factor de potencia termoeléctrica. Además, la presencia de Cu_{2-x}Te da como resultado un fuerte aumento del coeficiente de Seebeck. Este aumento está relacionado con el filtrado de los portadores de carga en función de su energía en las barreras de energía dentro de los dominios Bi_2Te_3 creados por la acumulación de electrones en las regiones cercanas a las uniones $\text{Cu}_{2-x}\text{Te} / \text{Bi}_2\text{Te}_3$. En general, se obtiene una mejora significativa de la figura de mérito, hasta un 250%, con la adecuada incorporación de nanopartículas de Cu_{2-x}Te con nanohilos Bi_2Te_3 . Los resultados del Capítulo 4 han sido aceptados en Journal of Materials Chemistry C en 2020. Los resultados del Capítulo 5 y el Capítulo 6 se han enviado a diferentes revistas en 2020.

Finalmente, en el último capítulo se presentan las principales conclusiones de esta tesis y algunas perspectivas para trabajos futuros.

Chapter 1

General Introduction



1.1 Thermoelectricity

Thermoelectricity provides direct conversion of thermal energy into electrical energy through the Seebeck effect. Statistical data show that most of the energy liberated by burning fossil fuels or by nuclear fission among other processes is lost in the form of waste heat (Figure 1). TE technology have attracted growing attention of investors and governments in recent years.¹⁻⁸ In addition, the earth receives large quantity of heat from the sun every day, which further promote the development of environmental-friendly TE technology for energy conversion.

TE technology can be also applied to precisely control temperature, either by heating or cooling. A heat flow is generated when an electrical current is applied through semiconductor materials, which is called Peltier effect. Solid state TE cooling generators have been widely applied in medical, consumer, military, industrial and scientific areas. Uses range from simple portable food refrigerators to sophisticated temperature control systems in missiles.⁹⁻¹²

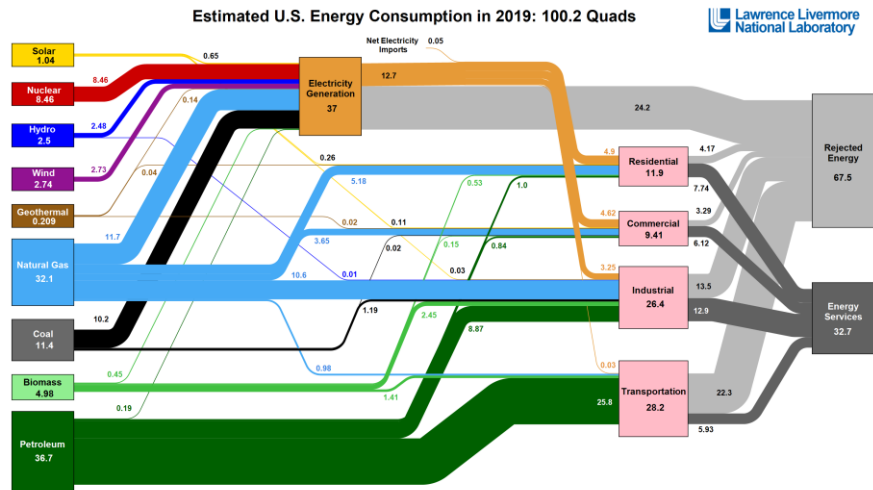


Figure 1. Energy statistics: estimated U.S energy consumption in 2019.¹³

TE devices typically consist of tens to hundreds of p-type and n-type semiconductor blocks that are connected together electrically in series to produce the desired electrical voltage, as shown in Figure 2. The blocks are sandwiched between two parallel ceramic substrates to provide structural rigidity, a dielectric space to avoid electrical short circuits and a flat surface for mounting. TE devices are manufactured by many companies and products are applied in numerous areas.¹⁴⁻¹⁷

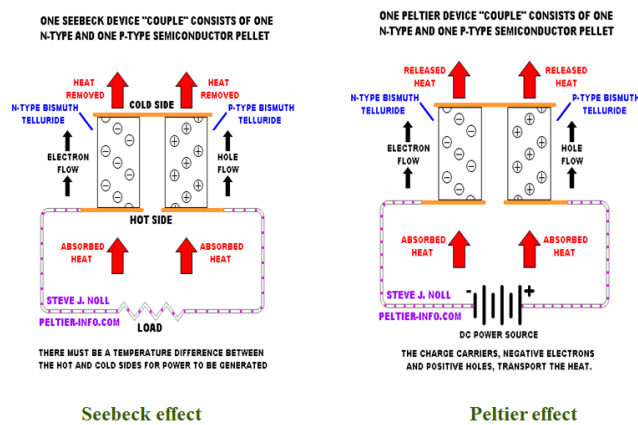


Figure 2. Working principle of a TE device.¹⁸

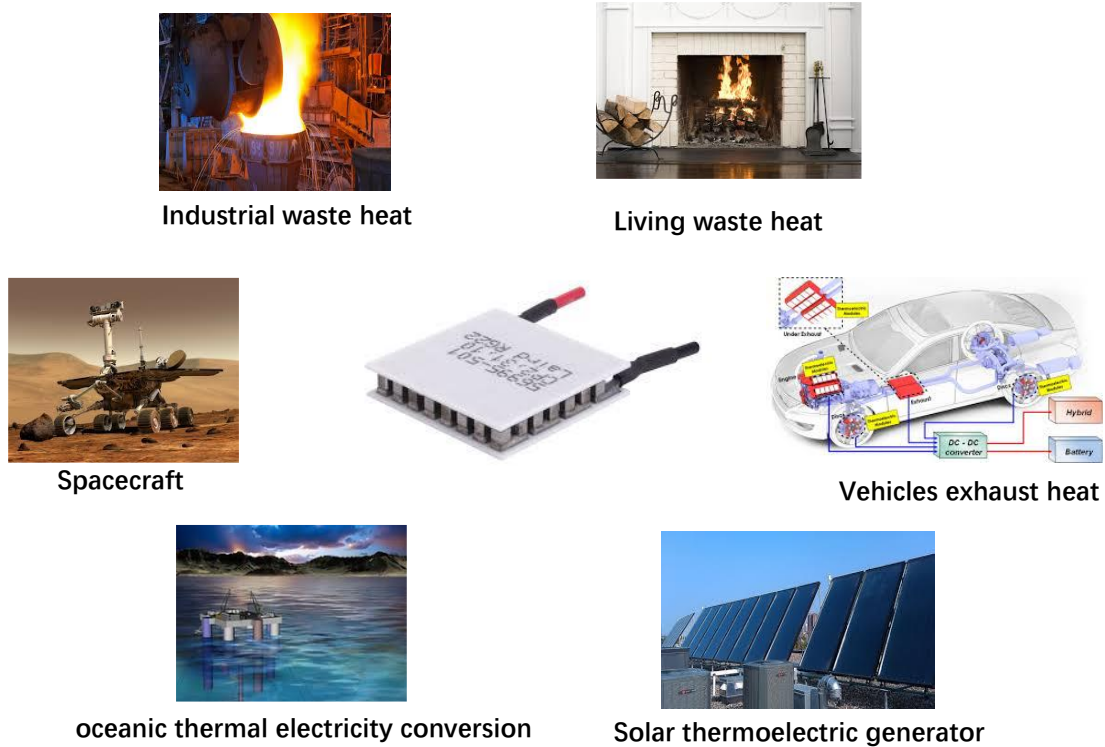


Figure 4. Widespread TE generator applications.

TE systems have lots of advantages over competing temperature control and thermal energy harvesting technologies including no moving parts, small size, feasible shape, high reliability, adaptability in a wide temperature range and no pollutants. However, the high cost and low efficiency of TE devices are their main drawback. Recently lots of effort has been invested to optimize the material parameters to maximize its TE figure of merit with $ZT > 2.5$ (e.g. SnSe). Combined with cost-effective printing technologies, solution phase printing of nanomaterials is becoming increasingly promising for the production of scalable flexible TE devices.¹⁹⁻²¹

1.2 Optimization of TE efficiency

In spite of countless of promising applications of TE devices, this technology has been commercially realized in few markets for temperature control and is yet to be effectively commercialized for electricity generation. The main bottom neck that constrains TE to potential market is a critical combination of relatively high price associated to the used semiconductor materials and a poor efficiency

compared with its competing technologies.²²⁻²⁵

The maximum coefficient of performance (COP) and the energy conversion efficiency (η) depend on the temperature difference between the hot side (T_h) and cold side (T_c), and a material figure of merit (Z):

$$COP = \frac{T_c \sqrt{1+ZTa} - \frac{T_h}{T_c}}{\Delta T \sqrt{1+ZTa} + 1} \quad (1)$$

$$\eta = \frac{\Delta T \sqrt{1+ZTa} - 1}{T_h \sqrt{1+ZTa} - \frac{T_h}{T_c}} \quad (2)$$

where $\Delta T = T_h - T_c$ refers to temperature difference, $T_a = \Delta T / 2$ refers to average temperature.²⁶⁻²⁸ The dimensionless TE figure of merit (ZT) could be expressed in following equation:

$$ZT = \frac{\sigma S^2}{\kappa} T \quad (3)$$

Where T is the absolute temperature, σ is electrical conductivity, S is the Seebeck coefficient and κ is the thermal conductivity. A good TE material would display high σ , large S and low κ . However, these three parameters are tightly interrelated and highly dependent on each other.^{27, 29-31}

To optimize ZT , a first key strategy is adjusting charge carrier concentration as it strongly affects not only σ but also S and the electronic thermal conductivity (κ_e) in the following way:

$$\sigma = ne\mu \quad (4)$$

$$S = \frac{8\kappa_B^2 \pi^2}{3eh^2} m^* T \left(\frac{\pi}{3n}\right)^{2/3} \quad (5)$$

$$\kappa_e = L\sigma T \quad (6)$$

Where n is the charge carrier concentration, e is the elementary charge, μ is the carrier mobility, K_B is the Boltzmann constant, h is the Planck constant, m^* is the effective mass, and L is the Lorenz number.³²

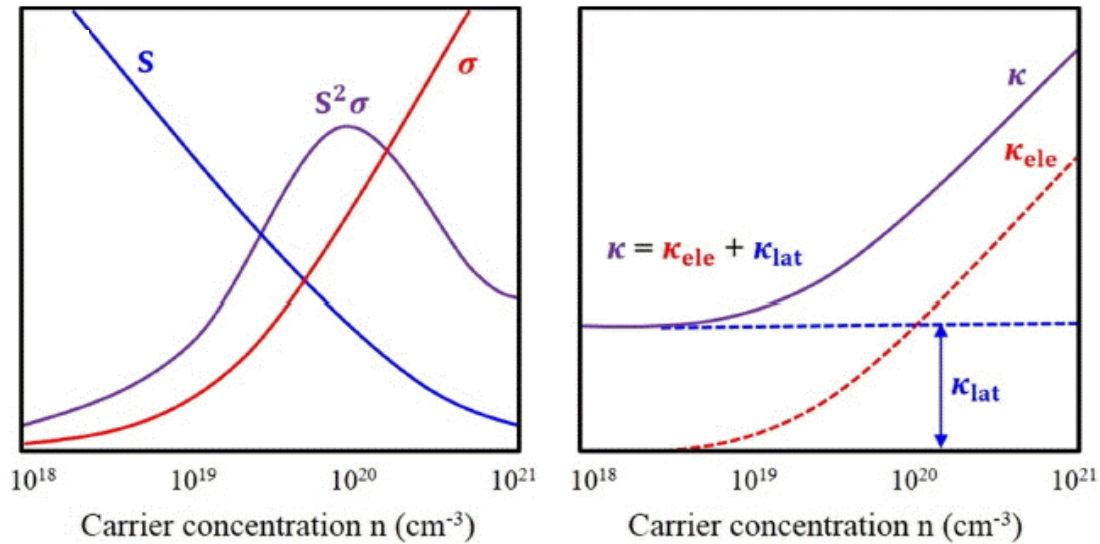


Figure 4. Dependence of electrical conductivity, Seebeck coefficient and thermal conductivity on carrier concentration.³²

The carrier concentration could be adjusted by doping material with extrinsic impurities, using off-stoichiometric chemical compositions or through alteration of intrinsic defects. Usually a good TE material requires large charge carrier concentrations, around 10^{19} cm^{-3} . To achieve this high carrier concentrations, it is necessary to introduce large quantities of defects or impurities, which negatively impacts the carrier mobility. Such disadvantage could be overcome by concentrating impurities in nanoinclusions. This strategy is known as modulation doping. The introduced nanoinclusions would be able to donate (spill) carriers to the matrix. Removing the impurities from the matrix significantly improves the electrons mean free path compared with conventional doping strategies. Such modulation doping approach has been proved effective to increase TE performance in many types of materials.³³⁻³⁴

On the other hand, heat transport is contributed from two parts: charge carriers and phonons, which could be expressed as $\kappa = \kappa_e + \kappa_L$, where κ_e is determined by electrical conductivity as I mentioned above. The lattice thermal conductivity (κ_L) is depending on the phonon transport through the material. There are two main strategies to minimize heat transport: identify semiconductor materials with intrinsically low κ_L and introduce effective phonon scattering center to

enhance phonon scattering at all scales.^{30, 35} Since point defects are typically capable of scatter high frequency phonons, an effective approach to scatter medium and low frequency phonons is to introduce large amounts of grain boundaries. In this direction, the appliance of nanomaterials has been verified effective to reduce κ_L even below the alloy limit. Attributed to efficient phonon scattering at interfaces of two-phase materials, excellent TE performance has been achieved through using NCs.³⁶ It is also necessary to properly design the composite to minimize the effect of interfaces on the majority carrier's mobility, to conserve a high σ .³⁷⁻³⁸

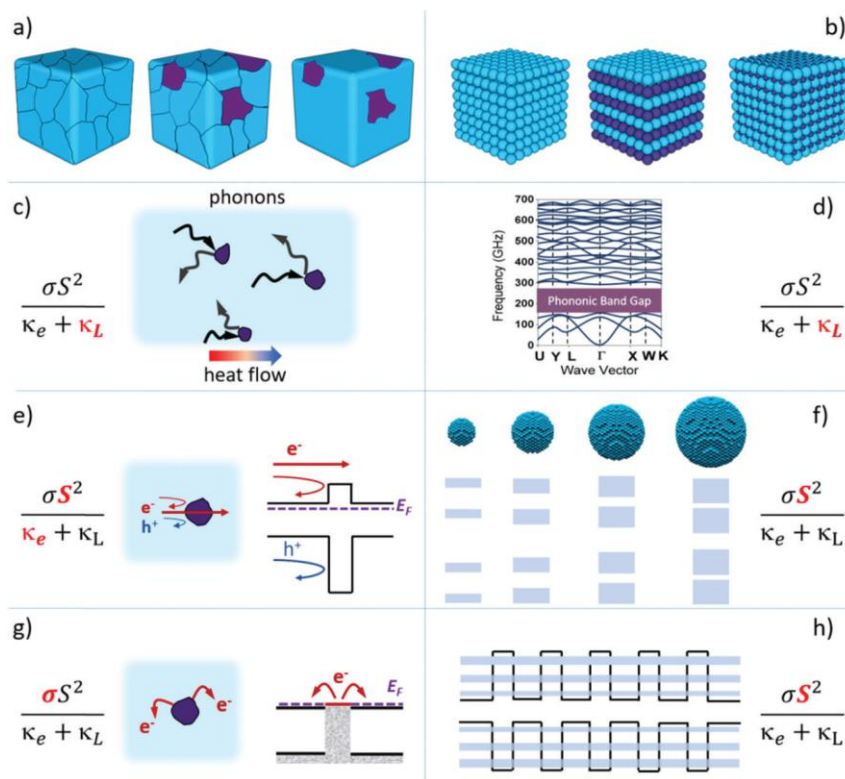


Figure 5. Schematic illustration of different types of disorganized (a) and organized nanomaterials (b) and schemes of the effect of nanocrystals on the TE figure of merit: (c) phonon scattering; (d) phononic band gap; (e) charge carrier type- and energy-dependent filtering; (f) DOS modification by quantum confinement in quantum dots; (g) modulation doping; (h) DOS modification within quantum dot superlattices.²⁷

Apart from minimizing κ_L and optimizing carrier concentration, there are some other important methodologies to produce high performance TE materials which focus on increasing S . In general, two strategies have been considered effectively to enhance S : 1) to maximize the asymmetry of density of states (DOS) with respect to the Fermi level; and 2) to introduce mechanisms for the selective scattering of charge carriers depending on their energy and charge sign (Figure 5e).

In conclusion, nanomaterials play a critical role in achieving high TE performance by enhancing electrical conductivity through modulation doping, optimizing Seebeck coefficient through engineering of DOS at Fermi level or by a mechanism to filter minority and low energy carriers, and diminishing thermal conductivity by creating plenty of interfaces to enhance phonon scattering.

1.3 TE nanomaterial synthetic approaches

Numerous methodologies have been applied to produce TE nanomaterials. Thin film vacuum-based deposition method is a mature technology which could precisely adjust composition at nanoscale through atom by atom growth. This technology has produced TE thin film with high ZT values.³⁹⁻⁴¹ However, from an economic point of view, this technology is characterized with high operational cost, as well as low production rates and low yields. Moreover, vacuum-based thin film technologies are not able to fabricate the relatively thick TE bulk modules required by most commercial applications. To overcome this limitation, it is necessary to develop technologies which could produce bulk TE NCs with improved capability over composition engineering. However, traditional approaches such as ball-milling and phase segregation to produce bulk TE NC lack of precise control over the size and shape of nanomaterials. In addition, these methodologies are highly energy intensive and time consuming, which reduce their economic rewarding.

Solution processing technologies produce nanocrystalline materials directly from atomic or molecular precursors in a controlled manner, as in vacuum-based

thin film technologies, what allows an accurate control of size, shape and composition within nanoscale. Additionally, it could be operated at low processing temperature and has associated much higher production yield and throughput, which in total greatly reduce the processing cost and make it potentially suitable for the TE market. At the same time, solution processing methods allow a post surface engineering that give rise to an additional strategy to manipulate transport properties of TE material.

1.4 Molecular inks

Molecular inks are excellent precursors for obtaining crystals/layer with uniform phase and composition. At the same time, molecular inks provide potential to easily introduce dopants with finely controlled stoichiometry. One strategy to obtain the inks is to dissolve solid inorganic precursors in a proper solvent. An ideal system should have the capability to dissolve a wide range of materials quickly and allow to recover phase pure crystals at low temperature. Unfortunately, bulk inorganic chalcogenides are nearly insoluble or have limited solubility in most traditional solvents.

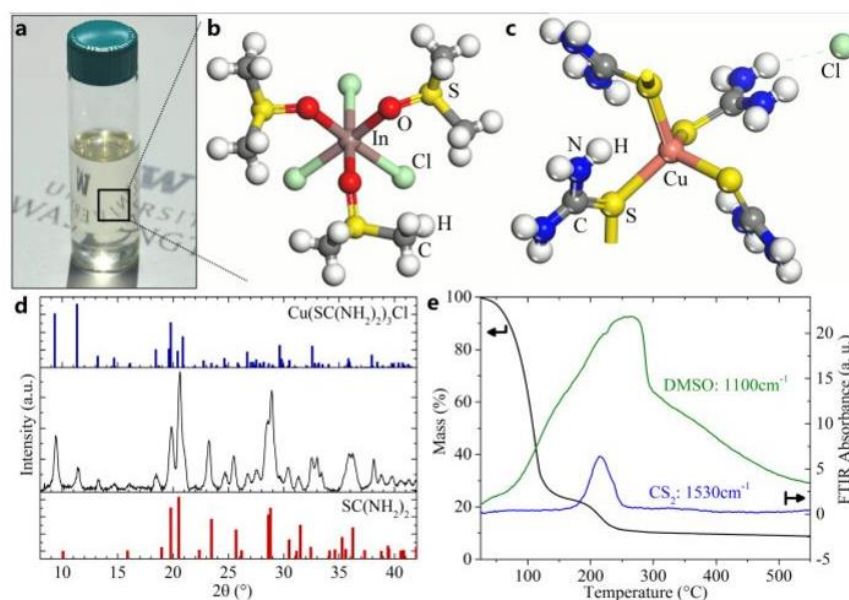


Figure 6. A dimethyl sulfoxide-based molecular ink route to produce low-bandgap $\text{CuIn}(\text{S,Se})_2$ for solar cells application.⁸²

To improve solvent solubility, Afzali's group first reported the use of hydrazine as a solvent to dissolve SnSe_2 and SnS_2 in presence of excess chalcogen (S or Se), by the mechanism of dimensional reduction.⁸³ Hydrazine firstly reduce the elemental chalcogen to yield chalcogenide anions, which could subsequently assist to dissolve bulk SnSe_2 and SnS_2 to produce soluble chalcogenide species. This molecular ink can be deposited on thin film by spin coating and thermally annealed to phase pure $\text{SnS}_{2-x}\text{Se}_x$ crystalline at low temperature. Afterwards, researchers have applied the similar way to dissolve a series of bulk metal chalcogenides (e.g., In_2Se_3 , GeSe , GeSe_2 , Cu_2Se , Sb_2Se_3 , Sb_2S_3 , Sb_2Te_3 , Bi_2S_3 , and HgSe) in hydrazine to prepare variety of useful ternary or quaternary molecular inks.⁸⁴⁻⁹⁵ The hydrazine based molecular inks has the advantage to allows to recover chalcogenides in a carbon-free environment, thus to avoid carbonaceous impurities. In addition, the volatile nature of hydrazine also facilitates low temperature thin film crystallization with high quality. Unfortunately, hydrazine is extremely corrosive, toxic and explosive, making it impractical to perform large scale production of this method for commercial applications. Nevertheless, this method provides an example to inspire researchers to explore a simple dissolution and recovery technique, with comparable solvation power and less toxicity.

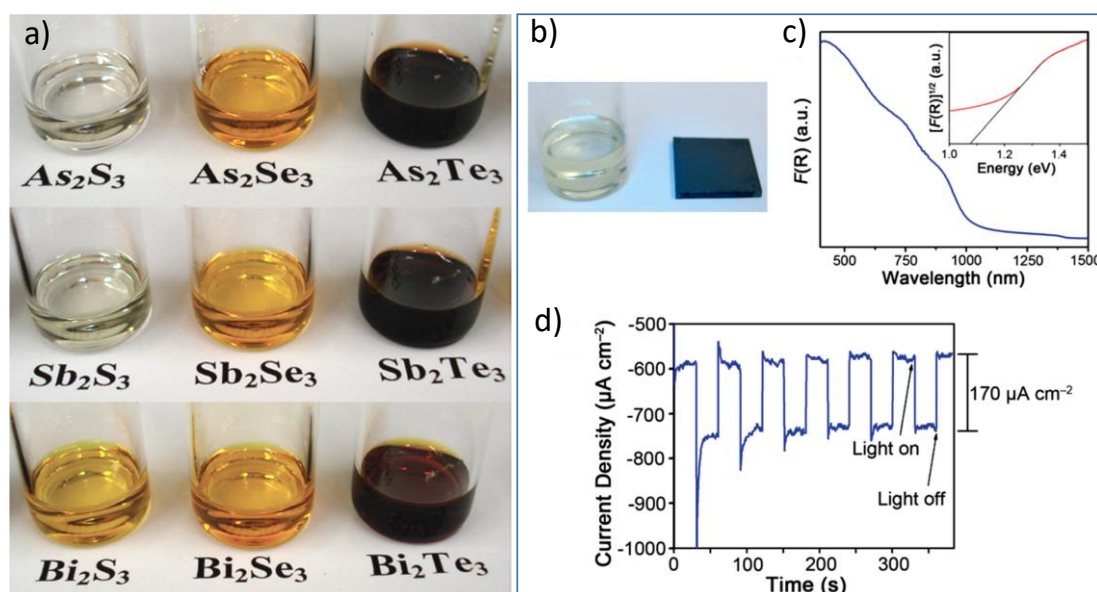


Figure 7. (a) A series of metal chalcogenides inks prepared from corresponding

bulk precursors. (b) SnS molecular ink (left) and a SnS thin film recovered from the SnS ink on a glass substrate (right); (c) UV-vis-NIR absorbance and corresponding Tauc plot measured for the recovered SnS; (c) transient photocurrent response of SnS thin film produced by spin coating.

To this end, Brutchey's and coworkers recently reported the remarkably solvation ability of an amine-dithiol system. A binary mixture of ethylenediamine and ethanedithiol shows outstanding capability to dissolve bulk gray selenium, tellurium, metal chalcogenides at ambient temperature within few hours, as displayed in Figure 7.⁹⁶⁻⁹⁸ Authors further revealed these as-prepared semiconductor molecular inks could be used to yield high quality and uniform crystalline thin film by directly spin coating inks onto silicon/glass substrates. The amine-dithiol solvents showing the ability to dissolve ten bulk oxide materials at room temperature with considerable high solubility of the inks (i.e., ZnO, Ag₂O, CdO, SnO, Sb₂O₃, and PbO).⁹⁹ Phase-pure sulfides (i.e., ZnS, Ag₂S, CdS, SnS, Sb₂S₃, and PbS) could be lately recovered by annealing the inks to elevated temperature (300-375 °C) under nitrogen atmosphere, where the sulfur was originated in the thiol from the solvent system. Moreover, there have been reports on the possibility of using the amine-dithiol method to synthesize more complex materials such as CuSbS₂, Cu(InGa)S₂, and Cu₂ZnSnS₄, to apply in the field of photovoltaic devices, electrocatalysts, TE materials and so on.¹⁰⁰⁻¹⁰³

With a strong understanding of the state of the art, the binary thiol/amine solvent mixture gives a versatile solution-based method to produce high quality binary/ternary/quandary chalcogenides, to yield technologically relevant semiconductor materials that may not yet achievable by other solution-processed methods over a range of applications.

1.5 Colloidal synthesis of nanomaterials

Compared with other solution processed synthetic route, colloidal synthesis has numerous advantages as associated with the growth of suspended NPs without

aggregation during the whole synthetic process. It allows the large scale production of huge amounts of NPs with extreme precise controlling of size, shape and surface properties.⁴²⁻⁴⁵ Since colloidal synthesis offers highest standard of control of NPs' parameters during the exact the same conditions, it becomes a suitable approach to produce nanoscale building blocks required for TE applications.

In colloidal synthesis, NPs (binary/ternary/quaternary compounds) could be produced through reaction or decomposition of molecular or atomic monomers which take place in solvent heated to required temperature.⁴⁶⁻⁴⁷ To obtain high quality nanocrystals, it is of great importance to select proper types of chemical precursors, solvent, reductant/oxidant, and the critical reacting temperature, to achieve high yield and purity. A standard synthetic facility to produce colloidal nanocrystals at lab scale is to use a Schlenk line which allows to efficiently remove low boiling point organic impurities and perform experiment under inert atmosphere.

1.4.1 Size control

The size of nanocrystal could be effectively controlled by regulating the amount of surfactant and its binding strength, what influence the surface coverage and the behavior of monomers addition.⁴⁸⁻⁵² Higher number/concentration of binding surfactant usually give rise to smaller nanocrystals. Another way to realize size controlling is to adjust nucleation and the growth behavior by rationally select precursors and corresponding reaction conditions.⁵³ In a hot-injection reaction, higher concentration of injected monomers results in larger amount of nuclei seeds, thus translate into smaller size of nanocrystals.⁵³⁻⁵⁵ In addition, a fast-increasing rate of temperature during heating up procedure would also lead to small size NPs.

1.4.2 Shape control

The shape of nanocrystal is a determined by minimizing surface energy during crystal growth.⁵⁶⁻⁶³ In this regard, the nanocrystal shape is depending on the free energy of each facet of crystal and its intrinsic crystal structure, which could be

controlled by proper choosing surfactants. The surfactants selectively bind in each facet to block the reagents transport to specific sites and to alter free energy of a particular facet. Furthermore, post-synthesis procedures and selective etching are also workable in regulating NP shape.⁶⁴⁻⁶⁷

Although the relationship of TE performance and characteristic of interfaces is still not yet clearly learned, regulating the shape and crystal domain size in a desired range allows to achieve quantum confinement effects thus to rationally modify the electronic band structure. Bottom up colloidal synthesis provides an easy strategy to do adjustment of size and shape in a controllable way, and further to logically engineer TE properties.

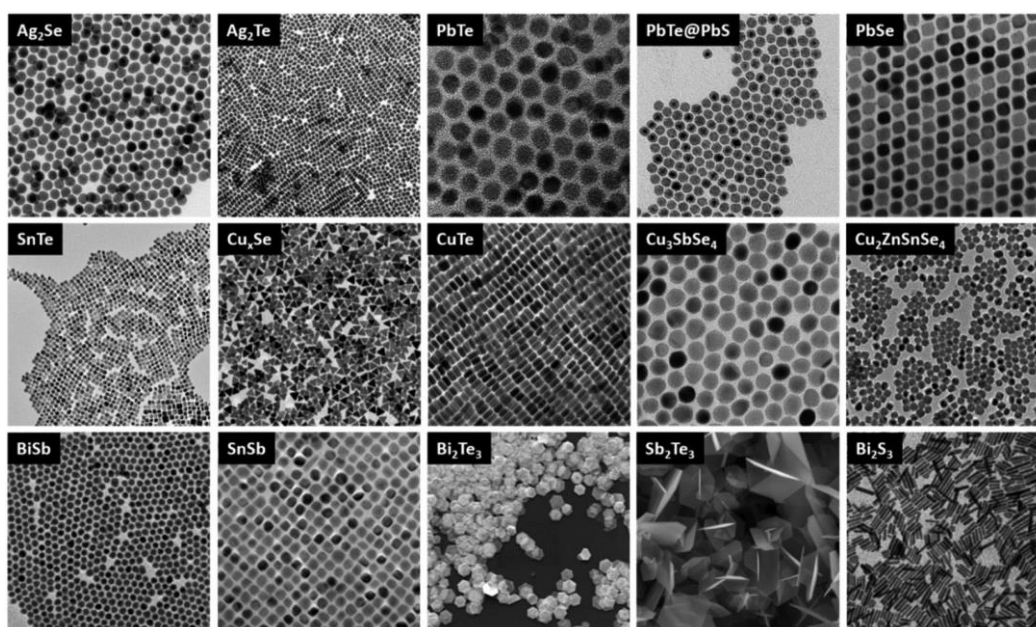


Figure 9. Electron microscopy micrographs of a selection of solution-processed NPs with sizes in the range from 5 nm to around 100 nm produced by within our group.²⁷

1.4.3 Phase and composition control

The colloidal synthetic method provides an accurate approach to do phase and composition engineering, what could be reached by selecting proper kind and concentration of precursors, using proper solvent, surfactant and appropriate react temperatures.⁶⁸⁻⁷¹ In addition, a complex nanocrystal phase could also be modified by adding various elements through a proper multi-step treatment to

attain desired compositions. In this way, colloidal synthesized NPs naturally enable a post-synthetic adjustment to get complex phase and composition, through replacing, adding or/and removing atoms as displayed in Figure 10.^{27, 72-75} This facilitates precise phase and composition engineering to acquire multinary compounds which is of particular importance to optimize TE performance.

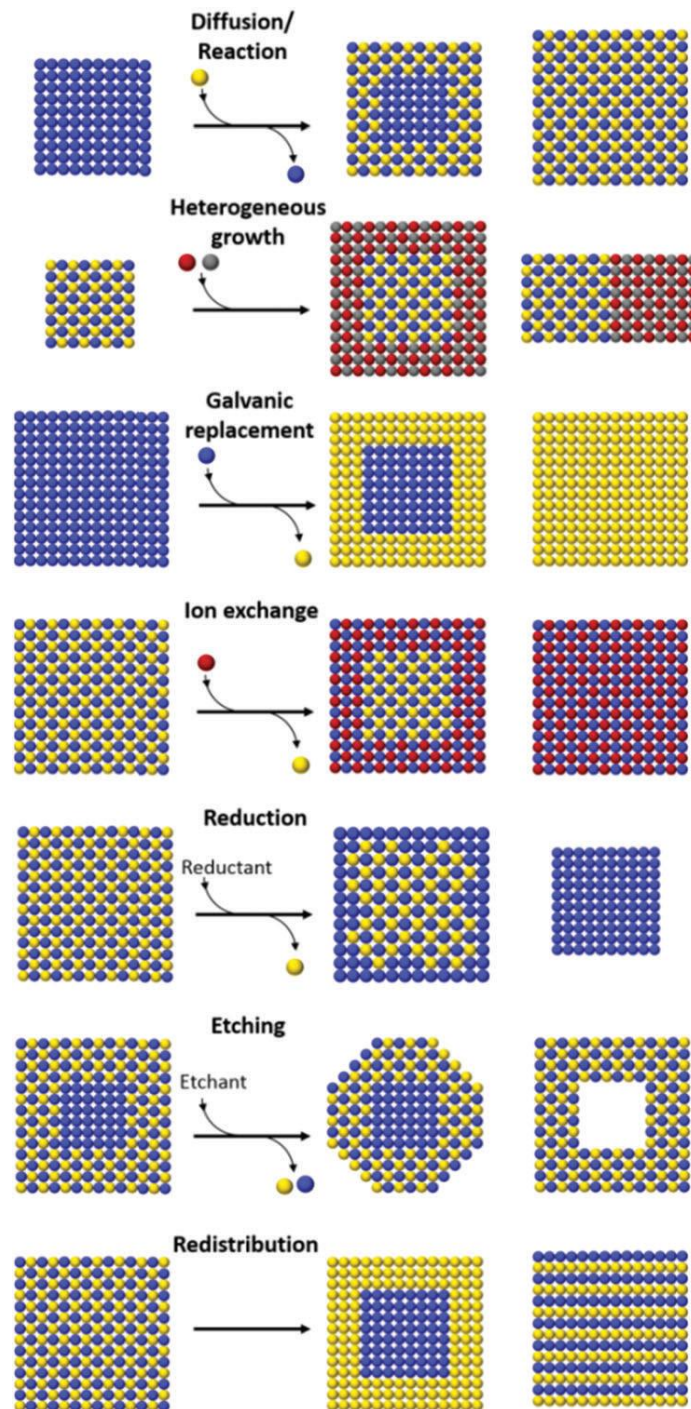


Figure 10. Scheme of possible post-synthetic compositional adjustments, including atomic addition, substitution, removal and redistribution.²⁷

1.4.4 Nanocrystal purification and surface modification

Compared with solvent-free methodologies, the use of liquid solvent in colloidal synthesis usually require further purification steps to separate nanocrystals from solvents, remove non-reacted precursors and set apart side products. This could be realized by centrifuging, filtration, magnetic separation or electrophoresis according to chemical stability and specific properties of nanocrystals.⁷⁶⁻⁸⁰ Subsequent procedure aims to remove surface ligand which typically bind with NPs through covalent bond.⁸¹ One of the simplest strategies to remove surface organic ligands is to apply an annealing process at relative high temperature under inert gas atmosphere. Annealing would contribute in nanocrystals with enhance transport properties, but on the other side the high temperature may also somehow sintering the nanomaterials and leave a layer of carbon residue on the surface which could has an effect on TE performance. An alternative strategy to minimize this consequence is to replace original surface ligands with short and/or weak coordinating molecules such as chloride, hydroxide and cyanide group.⁸¹

1.6 Objectives

This thesis aims at developing fundamental knowledge and know-how beyond the state of the art in the field of charge and heat transport in nanomaterials and by applying emerging technologies such as the solution processing of high-performance nanomaterials. Furthermore, the thesis aims at developing key enabling technologies, such as nanotechnology and ink-based additive manufacturing technologies. To accomplish the overall goals, it will be necessary to get over several main challenges encountered when aiming at the production of TE nanomaterials using solution-processing. This includes the optimization of the carrier concentration, the size, shape and surface control of the nanocrystals, the consolidation of the NPs into NCs by hot pressing, without losing control over parameters and possibly the production of textured

nanomaterials. To overcome these challenges, the following objectives have been defined in this thesis:

- a) To develop chalcogenides molecular ink to yield high quality and uniform crystalline thin film.
- b) To develop solution synthesis routes to produce high quality (narrow size, shape and composition distributions) NPs of three different families of relevant functional materials (Bi-Te, Sn and Cu chalcogenides).
- c) To develop well-engineered electronic doping strategies to control the charge carrier concentration of bottom-up assembled nanomaterials.
- d) To develop assembly and consolidation strategies that allow controlling with nanometer-scale precision the composition, density of interphases, crystal domain size and distribution of phases in dense macroscopic NCs.
- e) To thoroughly characterize the structural, chemical and functional properties of the TE NCs.
- f) To correlate the functional properties of the TE NCs with the structural and chemical parameters.
- g) To establish steps toward fabricating TE devices based on molecular inks by means of printing technologies to reduce cost.
- h) To gain fundamental understanding on the mechanisms of charge and heat transport in NCs by modelling the correlation of the functional properties of the TE NCs with the structural and chemical parameters.

1.7 Reference

1. Yang, J.; Stabler, F. R., Automotive applications of TE materials. *Journal of electronic materials* **2009**, *38* (7).
2. Twaha, S.; Zhu, J.; Yan, Y.; Li, B., A comprehensive review of TE technology: Materials, applications, modelling and performance improvement. *Renewable and sustainable energy reviews* **2016**, *65*, 698-726.
3. Mori, M.; Yamagami, T.; Oda, N.; Hattori, M.; Sorazawa, M.; Haraguchi, T. *Current possibilities of TE technology relative to fuel economy*; 0148-7191; SAE Technical Paper: 2009.
4. Jiang, W.; Yuan, D.; Xu, S.; Hu, H.; Xiao, J.; Sha, A.; Huang, Y., Energy harvesting from asphalt pavement using TE technology. *Applied Energy* **2017**, *205*, 941-950.
5. Allen, D.; Hauge, R.; Kajor, M.; Namazian, M. In *Small TE generators*, Twenty-First International Conference on TEs, 2002. Proceedings ICT'02., IEEE: 2002; pp 424-426.
6. Yang, J., Development of TE technology for automotive waste heat recovery. *FY2008 DOE Vehicle Technologies Annual Merit Review* **2008**.
7. Fleuriel, J.-P., TE power generation materials: Technology and application opportunities. *Jom* **2009**, *61* (4), 79-85.
8. Ismail, B. I.; Ahmed, W. H., TE power generation using waste-heat energy as an alternative green technology. *Recent Patents on Electrical & Electronic Engineering (Formerly Recent Patents on Electrical Engineering)* **2009**, *2* (1), 27-39.
9. Ghoshal, U., TE devices. Google Patents: 2005.
10. Xi, H.; Luo, L.; Fraisse, G., Development and applications of solar-based TE technologies. *Renewable and Sustainable Energy Reviews* **2007**, *11* (5), 923-936.
11. Petsagkourakis, I.; Tybrandt, K.; Crispin, X.; Ohkubo, I.; Satoh, N.; Mori, T., TE materials and applications for energy harvesting power generation. *Science and technology of advanced materials* **2018**, *19* (1), 836-862.
12. Zebarjadi, M.; Esfarjani, K.; Dresselhaus, M.; Ren, Z.; Chen, G., Perspectives on TEs: from fundamentals to device applications. *Energy & Environmental Science* **2012**, *5* (1), 5147-5162.
13. <https://flowcharts.llnl.gov/>.
14. Chein, R.; Huang, G., TE cooler application in electronic cooling. *Applied Thermal Engineering* **2004**, *24* (14-15), 2207-2217.
15. LeBlanc, S., TE generators: Linking material properties and systems engineering for waste heat recovery applications. *Sustainable Materials and Technologies* **2014**, *1*, 26-35.
16. He, W.; Zhang, G.; Zhang, X.; Ji, J.; Li, G.; Zhao, X., Recent development and application of TE generator and cooler. *Applied Energy* **2015**, *143*, 1-25.
17. Zhao, D.; Tan, G., A review of TE cooling: materials, modeling and applications. *Applied Thermal Engineering* **2014**, *66* (1-2), 15-24.

18. Shafiei, N.; Harun, M. H.; Annuar, K.; Halim, M.; Aras, M.; Azahar, A., Development of Portable Air Conditioning System Using Peltier and Seebeck Effect. *Journal of Telecommunication, Electronic and Computer Engineering (JTEC)* **2016**, *8* (7), 97-100.
19. Zhou, W.; Fan, Q.; Zhang, Q.; Cai, L.; Li, K.; Gu, X.; Yang, F.; Zhang, N.; Wang, Y.; Liu, H., High-performance and compact-designed flexible TE modules enabled by a reticulate carbon nanotube architecture. *Nature communications* **2017**, *8* (1), 1-9.
20. Suarez, F.; Nozariasbmarz, A.; Vashaee, D.; Öztürk, M. C., Designing TE generators for self-powered wearable electronics. *Energy & Environmental Science* **2016**, *9* (6), 2099-2113.
21. Yang, L.; Chen, Z. G.; Dargusch, M. S.; Zou, J., High performance TE materials: progress and their applications. *Advanced Energy Materials* **2018**, *8* (6), 1701797.
22. Kim, G.-H.; Shao, L.; Zhang, K.; Pipe, K. P., Engineered doping of organic semiconductors for enhanced TE efficiency. *Nature materials* **2013**, *12* (8), 719-723.
23. Nakpathomkun, N.; Xu, H. Q.; Linke, H., TE efficiency at maximum power in low-dimensional systems. *Physical Review B* **2010**, *82* (23), 235428.
24. Pei, Y.; LaLonde, A. D.; Heinz, N. A.; Shi, X.; Iwanaga, S.; Wang, H.; Chen, L.; Snyder, G. J., Stabilizing the optimal carrier concentration for high TE efficiency. *Advanced materials* **2011**, *23* (47), 5674-5678.
25. Fei, R.; Faghaninia, A.; Soklaski, R.; Yan, J.-A.; Lo, C.; Yang, L., Enhanced TE efficiency via orthogonal electrical and thermal conductances in phosphorene. *Nano letters* **2014**, *14* (11), 6393-6399.
26. Champier, D., TE generators: A review of applications. *Energy Conversion and Management* **2017**, *140*, 167-181.
27. Ortega, S.; Ibáñez, M.; Liu, Y.; Zhang, Y.; Kovalenko, M. V.; Cadavid, D.; Cabot, A., Bottom-up engineering of TE nanomaterials and devices from solution-processed NP building blocks. *Chemical Society Reviews* **2017**, *46* (12), 3510-3528.
28. Rowe, D. M., *TEs handbook: macro to nano*. CRC press: 2018.
29. Li, J.-F.; Liu, W.-S.; Zhao, L.-D.; Zhou, M., High-performance nanostructured TE materials. *NPG Asia Materials* **2010**, *2* (4), 152-158.
30. Snyder, G. J.; Toberer, E. S., Complex TE materials. In *Materials for sustainable energy: a collection of peer-reviewed research and review articles from Nature Publishing Group*, World Scientific: 2011; pp 101-110.
31. Mahan, G., Introduction to TEs. *APL Materials* **2016**, *4* (10), 104806.
32. Jonson, M.; Mahan, G., Mott's formula for the thermopower and the Wiedemann-Franz law. *Physical Review B* **1980**, *21* (10), 4223.
33. Ibáñez, M.; Luo, Z.; Genc, A.; Piveteau, L.; Ortega, S.; Cadavid, D.; Dobrozhan, O.; Liu, Y.; Nachttegaal, M.; Zebarjadi, M., High-performance TE nanocomposites from nanocrystal building blocks. *Nature communications* **2016**, *7* (1), 1-7.
34. Zebarjadi, M.; Joshi, G.; Zhu, G.; Yu, B.; Minnich, A.; Lan, Y.; Wang, X.; Dresselhaus, M.; Ren, Z.; Chen, G., Power factor enhancement by modulation doping

in bulk nanocomposites. *Nano letters* **2011**, *11* (6), 2225-2230.

35. Zeier, W. G.; Zevalkink, A.; Gibbs, Z. M.; Hautier, G.; Kanatzidis, M. G.; Snyder, G. J., Thinking like a chemist: intuition in TE materials. *Angewandte Chemie International Edition* **2016**, *55* (24), 6826-6841.
36. Zebarjadi, M.; Liao, B.; Esfarjani, K.; Dresselhaus, M.; Chen, G., Enhancing the TE power factor by using invisible dopants. *Advanced Materials* **2013**, *25* (11), 1577-1582.
37. Soni, A.; Shen, Y.; Yin, M.; Zhao, Y.; Yu, L.; Hu, X.; Dong, Z.; Khor, K. A.; Dresselhaus, M. S.; Xiong, Q., Interface driven energy filtering of TE power in spark plasma sintered Bi₂Te₂₋₇Se_{0.3} nanoplatelet composites. *Nano letters* **2012**, *12* (8), 4305-4310.
38. Bahk, J.-H.; Bian, Z.; Shakouri, A., Electron energy filtering by a nonplanar potential to enhance the TE power factor in bulk materials. *Physical Review B* **2013**, *87* (7), 075204.
39. Talapin, D. V.; Lee, J.-S.; Kovalenko, M. V.; Shevchenko, E. V., Prospects of colloidal nanocrystals for electronic and optoelectronic applications. *Chemical reviews* **2010**, *110* (1), 389-458.
40. Thornburg, D.; Wayman, C., TE Power of Vacuum-Evaporated Au–Ni Thin-Film Thermocouples. *Journal of Applied Physics* **1969**, *40* (7), 3007-3013.
41. Damodara, V. D.; Bhat, K. S., Temperature variation of TE power of vacuum deposited PbSe thin films and its thickness dependence. *Journal of Materials Science: Materials in Electronics* **1990**, *1* (4), 169-174.
42. Murray, C. B.; Sun, S.; Gaschler, W.; Doyle, H.; Betley, T. A.; Kagan, C. R., Colloidal synthesis of nanocrystals and nanocrystal superlattices. *IBM Journal of Research and Development* **2001**, *45* (1), 47-56.
43. Yin, Y.; Alivisatos, A. P., Colloidal nanocrystal synthesis and the organic–inorganic interface. *Nature* **2005**, *437* (7059), 664-670.
44. Parak, W. J.; Gerion, D.; Pellegrino, T.; Zanchet, D.; Micheel, C.; Williams, S. C.; Boudreau, R.; Le Gros, M. A.; Larabell, C. A.; Alivisatos, A. P., Biological applications of colloidal nanocrystals. *Nanotechnology* **2003**, *14* (7), R15.
45. Boles, M. A.; Engel, M.; Talapin, D. V., Self-assembly of colloidal nanocrystals: from intricate structures to functional materials. *Chemical reviews* **2016**, *116* (18), 11220-11289.
46. Punter, V. F.; Krishnan, K. M.; Alivisatos, A. P., Colloidal nanocrystal shape and size control: the case of cobalt. *Science* **2001**, *291* (5511), 2115-2117.
47. Tao, A. R.; Habas, S.; Yang, P., Shape control of colloidal metal nanocrystals. *small* **2008**, *4* (3), 310-325.
48. Shamsi, J.; Dang, Z.; Bianchini, P.; Canale, C.; Di Stasio, F.; Brescia, R.; Prato, M.; Manna, L., Colloidal synthesis of quantum confined single crystal CsPbBr₃ nanosheets with lateral size control up to the micrometer range. *Journal of the American Chemical Society* **2016**, *138* (23), 7240-7243.
49. Ahrenstorf, K.; Albrecht, O.; Heller, H.; Kornowski, A.; Görlitz, D.; Weller, H.,

Colloidal synthesis of $\text{Ni}_x\text{Pt}_{1-x}$ NPs with tuneable composition and size. *small* **2007**, *3* (2), 271-274.

50. Reetz, M. T.; Helbig, W., Size-selective synthesis of nanostructured transition metal clusters. *Journal of the American Chemical Society* **1994**, *116* (16), 7401-7402.

51. Sau, T. K.; Pal, A.; Jana, N.; Wang, Z.; Pal, T., Size controlled synthesis of gold NPs using photochemically prepared seed particles. *Journal of NP Research* **2001**, *3* (4), 257-261.

52. Mott, D.; Galkowski, J.; Wang, L.; Luo, J.; Zhong, C.-J., Synthesis of size-controlled and shaped copper NPs. *Langmuir* **2007**, *23* (10), 5740-5745.

53. Mozaffari, S.; Li, W.; Thompson, C.; Ivanov, S.; Seifert, S.; Lee, B.; Kovarik, L.; Karim, A. M., Colloidal NP size control: experimental and kinetic modeling investigation of the ligand–metal binding role in controlling the nucleation and growth kinetics. *Nanoscale* **2017**, *9* (36), 13772-13785.

54. Vaughn, D. D.; Bondi, J. F.; Schaak, R. E., Colloidal synthesis of air-stable crystalline germanium NPs with tunable sizes and shapes. *Chemistry of Materials* **2010**, *22* (22), 6103-6108.

55. Bock, C.; Paquet, C.; Couillard, M.; Botton, G. A.; MacDougall, B. R., Size-selected synthesis of PtRu nano-catalysts: reaction and size control mechanism. *Journal of the American Chemical Society* **2004**, *126* (25), 8028-8037.

56. Peng, X.; Manna, L.; Yang, W.; Wickham, J.; Scher, E.; Kadavanich, A.; Alivisatos, A. P., Shape control of CdSe nanocrystals. *Nature* **2000**, *404* (6773), 59-61.

57. Manna, L.; Scher, E. C.; Alivisatos, A. P., Shape control of colloidal semiconductor nanocrystals. *Journal of Cluster Science* **2002**, *13* (4), 521-532.

58. Kumar, S.; Nann, T., Shape control of II–VI semiconductor nanomaterials. *Small* **2006**, *2* (3), 316-329.

59. Jun, Y. w.; Choi, J. s.; Cheon, J., Shape control of semiconductor and metal oxide nanocrystals through nonhydrolytic colloidal routes. *Angewandte Chemie International Edition* **2006**, *45* (21), 3414-3439.

60. Peng, X., Mechanisms for the shape-control and shape-evolution of colloidal semiconductor nanocrystals. *Advanced Materials* **2003**, *15* (5), 459-463.

61. Marks, L.; Peng, L., NP shape, thermodynamics and kinetics. *Journal of Physics: Condensed Matter* **2016**, *28* (5), 053001.

62. Ratto, F.; Matteini, P.; Rossi, F.; Pini, R., Size and shape control in the overgrowth of gold nanorods. *Journal of NP Research* **2010**, *12* (6), 2029-2036.

63. Mokari, T.; Zhang, M.; Yang, P., Shape, size, and assembly control of PbTe nanocrystals. *Journal of the American Chemical Society* **2007**, *129* (32), 9864-9865.

64. Bai, Y.; Yang, T.; Gu, Q.; Cheng, G.; Zheng, R., Shape control mechanism of cuprous oxide NPs in aqueous colloidal solutions. *powder technology* **2012**, *227*, 35-42.

65. Grzelczak, M.; Pérez-Juste, J.; Mulvaney, P.; Liz-Marzán, L. M., Shape control in gold NP synthesis. *Chemical Society Reviews* **2008**, *37* (9), 1783-1791.

66. Ahmadi, T. S.; Wang, Z. L.; Green, T. C.; Henglein, A.; El-Sayed, M. A.,

Shape-controlled synthesis of colloidal platinum NPs. *Science* **1996**, 272 (5270), 1924-1925.

67. Wu, Z.; Yang, S.; Wu, W., Shape control of inorganic NPs from solution. *Nanoscale* **2016**, 8 (3), 1237-1259.

68. Kurizki, G.; Shapiro, M.; Brumer, P., Phase-coherent control of photocurrent directionality in semiconductors. *Physical Review B* **1989**, 39 (5), 3435.

69. Fortier, T.; Roos, P.; Jones, D.; Cundiff, S. T.; Bhat, R.; Sipe, J., Carrier-envelope phase-controlled quantum interference of injected photocurrents in semiconductors. *Physical review letters* **2004**, 92 (14), 147403.

70. Dupont, E.; Corkum, P. B.; Liu, H.; Buchanan, M.; Wasilewski, Z., Phase-controlled currents in semiconductors. *Physical review letters* **1995**, 74 (18), 3596.

71. Dynes, J.; Paspalakis, E., Phase control of electron population, absorption, and dispersion properties of a semiconductor quantum well. *Physical Review B* **2006**, 73 (23), 233305.

72. Krupa, A.; Descamps, M.; Willart, J.-F.; Strach, B.; Wyska, E. b.; Jachowicz, R.; Danede, F., High-energy ball milling as green process to vitrify tadalafil and improve bioavailability. *Molecular pharmaceutics* **2016**, 13 (11), 3891-3902.

73. Buck, M. R.; Schaak, R. E., Emerging strategies for the total synthesis of inorganic nanostructures. *Angewandte Chemie International Edition* **2013**, 52 (24), 6154-6178.

74. De Trizio, L.; Manna, L., Forging colloidal nanostructures via cation exchange reactions. *Chemical reviews* **2016**, 116 (18), 10852-10887.

75. Xia, X.; Wang, Y.; Ruditskiy, A.; Xia, Y., 25th Anniversary Article: Galvanic replacement: a simple and versatile route to hollow nanostructures with tunable and well-controlled properties. *Advanced Materials* **2013**, 25 (44), 6313-6333.

76. Kovalenko, M. V.; Manna, L.; Cabot, A.; Hens, Z.; Talapin, D. V.; Kagan, C. R.; Klimov, V. I.; Rogach, A. L.; Reiss, P.; Milliron, D. J., Prospects of nanoscience with nanocrystals. ACS Publications: 2015.

77. Boles, M. A.; Ling, D.; Hyeon, T.; Talapin, D. V., The surface science of nanocrystals. *Nature materials* **2016**, 15 (2), 141-153.

78. Anderson, N. C.; Hendricks, M. P.; Choi, J. J.; Owen, J. S., Ligand exchange and the stoichiometry of metal chalcogenide nanocrystals: spectroscopic observation of facile metal-carboxylate displacement and binding. *Journal of the American Chemical Society* **2013**, 135 (49), 18536-18548.

79. Nag, A.; Zhang, H.; Janke, E.; Talapin, D. V., Inorganic surface ligands for colloidal nanomaterials. *Zeitschrift für Physikalische Chemie* **2015**, 229 (1-2), 85-107.

80. De Roo, J.; De Keukeleere, K.; Hens, Z.; Van Driessche, I., From ligands to binding motifs and beyond; the enhanced versatility of nanocrystal surfaces. *Dalton Transactions* **2016**, 45 (34), 13277-13283.

81. Wang, P.; Xue, Y.; Han, Y.; Lin, L.; Wu, C.; Xu, S.; Jiang, Z.; Xu, J.; Liu, Q.; Cao, X., The STAT3-binding long noncoding RNA lnc-DC controls human dendritic cell differentiation. *Science* **2014**, 344 (6181), 310-313.

82. Uhl, A.; Katahara, J.; Hillhouse, H., Molecular-ink route to 13.0% efficient low-bandgap CuIn (S, Se) 2 and 14.7% efficient Cu (In, Ga)(S, Se) 2 solar cells. *Energy & Environmental Science* **2016**, *9* (1), 130-134.
83. Mitzi, D. B.; Kosbar, L. L.; Murray, C. E.; Copel, M.; Afzali, A., High-mobility ultrathin semiconducting films prepared by spin coating. *Nature* **2004**, *428* (6980), 299-303.
84. Mitzi, D. B., Solution processing of chalcogenide semiconductors via dimensional reduction. *Advanced Materials* **2009**, *21* (31), 3141-3158.
85. Wang, R. Y.; Feser, J. P.; Gu, X.; Yu, K. M.; Segalman, R. A.; Majumdar, A.; Milliron, D. J.; Urban, J. J., Universal and solution-processable precursor to bismuth chalcogenide TEs. *Chemistry of Materials* **2010**, *22* (6), 1943-1945.
86. Feser, J. P.; Chan, E. M.; Majumdar, A.; Segalman, R. A.; Urban, J. J., Ultralow thermal conductivity in polycrystalline CdSe thin films with controlled grain size. *Nano letters* **2013**, *13* (5), 2122-2127.
87. Kovalenko, M. V.; Spokoyny, B.; Lee, J.-S.; Scheele, M.; Weber, A.; Perera, S.; Landry, D.; Talapin, D. V., Semiconductor nanocrystals functionalized with antimony telluride zintl ions for nanostructured TEs. *Journal of the American Chemical Society* **2010**, *132* (19), 6686-6695.
88. Milliron, D. J.; Raoux, S.; Shelby, R. M.; Jordan-Sweet, J., Solution-phase deposition and nanopatterning of GeSbSe phase-change materials. *Nature materials* **2007**, *6* (5), 352-356.
89. Mitzi, D. B.; Raoux, S.; Schrott, A. G.; Copel, M.; Kellock, A.; Jordan-Sweet, J., Solution-based processing of the phase-change material KSb5S8. *Chemistry of materials* **2006**, *18* (26), 6278-6282.
90. Milliron, D. J.; Mitzi, D. B.; Copel, M.; Murray, C. E., Solution-processed metal chalcogenide films for p-type transistors. *Chemistry of materials* **2006**, *18* (3), 587-590.
91. Mitzi, D. B., N4H9Cu7S4: a hydrazinium-based salt with a layered Cu7S4-framework. *Inorganic chemistry* **2007**, *46* (3), 926-931.
92. Mitzi, D. B.; Copel, M.; Murray, C. E., High-mobility p-type transistor based on a spin-coated metal telluride semiconductor. *Advanced Materials* **2006**, *18* (18), 2448-2452.
93. Mitzi, D. B., Synthesis, structure, and thermal properties of soluble hydrazinium germanium (IV) and tin (IV) selenide salts. *Inorganic chemistry* **2005**, *44* (10), 3755-3761.
94. Mitzi, D. B., Polymorphic one-dimensional (N2H4) 2ZnTe: Soluble precursors for the formation of hexagonal or cubic zinc telluride. *Inorganic chemistry* **2005**, *44* (20), 7078-7086.
95. Mitzi, D. B.; Copel, M.; Chey, S. J., Low-voltage transistor employing a high-mobility spin-coated chalcogenide semiconductor. *Advanced Materials* **2005**, *17* (10), 1285-1289.
96. McCarthy, C. L.; Brutchey, R. L., Solution processing of chalcogenide materials using thiol-amine "alkahest" solvent systems. *Chemical Communications*

2017, 53 (36), 4888-4902.

97. Antunez, P. D.; Torelli, D. A.; Yang, F.; Rabuffetti, F. A.; Lewis, N. S.; Brutchey, R. L., Low temperature solution-phase deposition of SnS thin films. *Chemistry of Materials* **2014**, 26 (19), 5444-5446.

98. Webber, D. H.; Brutchey, R. L., Alkahest for V₂VI₃ chalcogenides: dissolution of nine bulk semiconductors in a diamine-dithiol solvent mixture. *Journal of the American Chemical Society* **2013**, 135 (42), 15722-15725.

99. McCarthy, C. L.; Webber, D. H.; Schueller, E. C.; Brutchey, R. L., Solution-Phase Conversion of Bulk Metal Oxides to Metal Chalcogenides Using a Simple Thiol–Amine Solvent Mixture. *Angewandte Chemie* **2015**, 127 (29), 8498-8501.

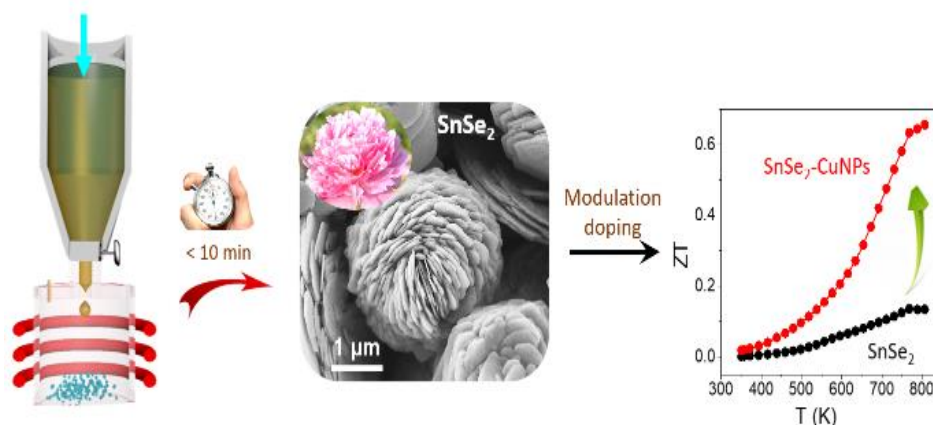
100. Yang, Y.; Kang, X.; Huang, L.; Pan, D., Tuning the band gap of Cu₂ZnSn (S, Se) 4 thin films via lithium alloying. *ACS Applied Materials & Interfaces* **2016**, 8 (8), 5308-5313.

101. Zhao, W.; Pan, D.; Liu, S. F., Kesterite Cu₂Zn(Sn, Ge)(S, Se) 4 thin film with controlled Ge-doping for photovoltaic application. *Nanoscale* **2016**, 8 (19), 10160-10165.

102. Yang, Y.; Kang, X.; Huang, L.; Wei, S.; Pan, D., A general water-based precursor solution approach to deposit earth abundant Cu₂ZnSn (S, Se) 4 thin film solar cells. *Journal of Power Sources* **2016**, 313, 15-20.

103. Tian, Q.; Huang, L.; Zhao, W.; Yang, Y.; Wang, G.; Pan, D., Metal sulfide precursor aqueous solutions for fabrication of Cu₂ZnSn (S, Se) 4 thin film solar cells. *Green Chemistry* **2015**, 17 (2), 1269-1275.

Chapter 2 Tin Diselenide Molecular Precursor for Solution-Processable TE Materials



2.1 Abstract

In the present work, I detail a fast and simple solution-based method to synthesize hexagonal NPLs and their use to produce crystallographically textured SnSe₂ nanomaterials. I also demonstrate that the same strategy can be used to produce orthorhombic SnSe nanostructures and nanomaterials. NPLs are grown through a screw dislocation-driven mechanism with additional detachment of the growing layers, resulting in flower-like structures. SnSe₂ bulk nanomaterials with a significant crystallographic texture and obtained from the hot pressing of the SnSe₂ NPLs display highly anisotropic charge and heat transport properties. The overall TE figures of merit of thus obtained SnSe₂ nanomaterials is limited by their relatively low electrical conductivity. To improve this parameter, SnSe₂ NPLs are blended with metal NPs. The electrical conductivities of the blends are significantly improved with respect to bare SnSe₂ NPLs and a three-fold increase in the TE figure of merit is obtained, reaching unprecedented values up to $ZT = 0.65$ for this material.

2.2 Introduction

The use of molecular precursors to produce inorganic nanomaterials in the form of NPs, thin films, supported nanostructures or self-standing porous or dense nanomaterials is potentially advantageous in terms of reducing fabrication costs and improving performances. In this direction, the amine-dithiol system has been

reported as a versatile solvent to prepare molecular precursors from the dissolution at ambient conditions of metal chalcogenides, pure metals and metal oxides, among others.^[1]

Two dimensional (2D) materials have attracted increasing attention in the past decade. The structure of these materials is formed by atomically thin layers that display strong covalent in plane bonding and weak layer-to-layer bonding. This type of structure results in extraordinary physical, electronic and optical properties, but which are at the same time highly anisotropic. In particular, charge and heat transport properties are especially affected by the strong lattice asymmetry, resulting in much higher thermal and electronic conductivities in plane than cross plane. Owing to these highly anisotropic properties, to produce bulk 2D nanomaterials with a proper crystallographic texture is necessary to optimize their performance in most applications. However, to control the crystallographic texture of materials produced by bottom-up procedures and/or solution-based approaches is not straightforward.

A particularly interesting 2D material family is that of metal chalcogenides, owing to their good chemical stability and semiconducting characteristics. 2D metal chalcogenides are used in numerous applications in the fields of energy conversion and storage,^[2] flexible electronics^[3] and medical diagnosis^[4]. Among them, tin chalcogenides are especially interesting materials for energy conversion.^[5] In particular, p-type SnSe have shown unprecedentedly high TE figure of merits: $ZT = 2.6$ at 923 K.^[6] On the other hand, n-type SnSe₂ could be an ideal compound to complement an all Sn-Se based device, but the measurement of its TE properties and their optimization has been rarely targeted.^[7]

Apart from previously reported synthetic methods to produce tin dichalcogenide nanocrystals,^[8] here I report on a fast solution-based methodology that makes use of molecular precursors to produce SnSe₂ NPLs and SnSe₂ nanomaterials. The synthetic procedure can be easily scaled up, paving the way for commercial application. These NPLs are hot pressed to produce crystallographically textured nanomaterials, whose TE properties are characterized. The final TE performance

of SnSe₂ is further optimized through modulation doping by combining SnSe₂ NPLs with metal NPs.

2.3 Experimental Section

Chemicals: Selenium powder (Se, 200 mesh 99.5%) and oleylamine (OAm, C₁₈H₃₇N, 80-90%) were purchased from Acros Organics. Ethanedithiol (EDT, HSCH₂CH₂SH, ≥98.0%), and tin powder (Sn, ≥99.0%) were purchased from Sigma-Aldrich. Analytical grade ethanol and chloroform were obtained from various sources. All the chemicals were used as received unless specifically noted.

SnSe₂ precursor ink preparation: In a typical synthesis to produce 20 g SnSe₂ NPLs, 9.05 g Sn powder (76 mmol) and 12 g Se powder (152 mmol) were weighted and transferred to a glass bottle. Then 200 mL of OAm and 20 mL of EDT were added. Upon EDT incorporation, the colour of the solution immediately turned from transparent to dark brown. Then, the vial was stirred overnight at 50 °C. The obtained ink was then filtered through a 0.45 μm filter and stored for posterior use. All these processes were carried out inside an argon-filled glove box.

SnSe₂ NPLs: SnSe₂ NPLs were produced from the decomposition under argon atmosphere of the precursor ink at 380 °C. The SnSe₂ precursor ink was continuously injected into a preheated glass flask. The ink immediately decomposed upon arrival to the container. Once decomposed all the ink, the flask was naturally cooled down to room temperature (RT) and the crystalline product was collected using chloroform and precipitated with ethanol. Further purification was performed by additional dispersion of the NPLs in chloroform and precipitating them with ethanol through centrifugation at 5000 rpm for 5 mins.

Metal NPs synthesis: Cu, Sn and Ag NPs with diameter of ~5-12 nm were prepared following published protocols. ^[59-61]

Blends: SnSe₂-based NCs were prepared by blending SnSe₂ with metal NPs in

solution. A typical blending process (1.5 at% of metal) consisted in mixing 3.6 mmol (1 g) of SnSe₂ NPs and 0.16 mmol of metal NPs in 5 mL anhydrous chloroform and sonicating the mixture for 20 min. The blend was next dried under vacuum.

Pellet Preparation: SnSe₂ NPLs and blends of SnSe₂ NPL and metal NP were thermally annealed inside a tube furnace to remove surface organic ligands. The obtained nanopowder was heated to 450 °C at 10 °C/min and subsequently kept at 450 °C for 60 min under argon flow. After cooling to RT, the annealed materials were grounded in a mortar and then loaded into a graphite die inside the glove box. The die was then transferred to a custom-made hot press system within the Ar-filled glove box. The die was heated to 460 °C using an induction coil and held at this temperature for 5 min under 80 MPa pressure. Afterward, the pressure was released and the die was naturally cooled to RT. Finally, compacted cylinders (Ø 10 mm × 10 mm) were produced, which were cut in rectangular bars in two directions: along the press axis (cross plane direction) and normal to this axis (in plane direction).

Structural and chemical characterization: XRD (2θ: 5° - 80°; scanning rate was set at 5°/min) were collected on a Bruker AXS D8 Advance XRD with Ni-filtered Cu-Kα radiation (λ= 0.15406 Å), operating at 40 mA and 40 kV. The morphology and size of initial particles were characterized by TEM (ZEISS LIBRA 120), working at 120 kV and field-emission SEM (Zeiss Auriga) operating at 5.0 kV. HRTEM images and STEM studies were conducted on a FEI Tecnai F20 field emission gun microscope operated at 200 kV with a point-to-point resolution of 0.19 nm, which was equipped HAADF and a Gatan Quantum EELS detector. Elemental analysis was carried out using an Oxford energy dispersive EDX combined with the Zeiss Auriga SEM working at 20.0 kV. XPS was examined on a SPECS system equipped with a Phoibos 150 MCD-9 detector, working at 150 mW with an Al anode XR50 source. XPS measurements were also carried out using a Kratos Axis UltraDLD spectrometer (Kratos Analytical Ltd., UK) XPS spectra were acquired using a monochromatic

Al Ka source operated at 20mA and 15 kV. Survey scan analyses were carried out with an analysis area of 300 x 700 microns and a pass energy of 160 eV. High resolution analyses were carried out on the same analysis area at a pass energy of 10 eV and energy step of 0.1 eV, and the Kratos charge neutralizer system was used on all specimens. Spectra have been charge corrected to the main line of the C 1s spectrum set to 284.8 eV and analysed with CASAXPS software (Casa Software, Ltd., version 2.3.17). Ultraviolet-Visible Spectrophotometry (UV-Vis): Optical absorption spectra were performed on a LAMBDA 950 UV-Vis spectrophotometer from PerkinElmer. Inductively coupled plasma atomic emission spectrometer (ICP-AES, iCAP 6500, Thermo) was used for the elemental analysis, samples were prepared by digestion of nanocrystals in aqua regia overnight followed by dilution in MQ-Water (Milipore). Fourier transform infrared spectroscopy (FTIR, Alpha Bruker) was carried with a platinum attenuated total reflectance single reflection module.

TE Characterization: Seebeck coefficients were measured with a static DC method. Electric resistivity data was measured using a standard four probe method. The Seebeck coefficient and the electric resistivity were measured simultaneously in a LSR-3 LINSEIS system in the temperature range from 323 to 803 K under a helium atmosphere. Bearing in mind of measurement precision and the system accuracy, an error of ca. 5% in the measurement of Seebeck coefficient and electrical conductivity was estimated. A Xenon Flash Apparatus was applied to measure the thermal diffusivities (D) of all samples with accuracies better than 6%. Thermal conductivities were then calculated by the relation $\kappa = C_p D \rho$, where C_p is heat capacity, D is the measured thermal diffusivity and ρ is the mass density of pellet (measured by Archimedes' principle). The Hall carrier concentration (n_H) at room temperature (298 K) were measured with a Physical Property Measurement System (PPMS-9T, 10 % error, Quantum Design Inc., USA) using a magnetic field of 2 T. Values provided correspond to the average of 5 consecutive measurements. Heat capacity, C_p , of SnSe₂ is measured by using DSC, TA Q1000 series, with Sapphire method. Briefly, DSC was first calibrated using standard procedure by using sapphire as

reference and alumina crucible. Then, the samples were heated at heating rate 10 K/min, in N₂ atmosphere, to yield Cp curves as a function of temperature.

2.4 Result and Discussion

Tin diselenide NPs were produced through the thermal decomposition of an ink prepared by the dissolution of elemental Sn and Se powders with a Sn/Se=0.5 molar ratio in an amine-dithiol mixture (Figure 1, see experimental section for details). Upon heating of the ink to 380 °C, the solvent was evaporated and a very rapid crystallization of tin diselenide NPs took place. This simple process could be carried out at virtually any scale and in a continuous manner, using a flow system, to produce very large amounts of material.

This procedure resulted in hexagonal plate-like NPs with average lateral sizes of ca. 500 nm and 70 nm thicknesses, as observed by TEM (Figure 2a). Such NPLs assembled into flower-like clusters with average size of ca. 4 μm (Figure 2b). XRD patterns of the obtained materials (Figure 2c) were consistent with a SnSe₂ crystal structure (P3-m1 space group, JCPDS NO. 01-089-2939). Along the z-axis of this structure, three-atom-thick and covalently bond Se-Sn-Se slabs were piled up together through weak van der Waals interaction (Figure 2d). The relatively strong intensity of the (001) XRD peak pointed at the [001] direction as the normal to the NPL plane. No additional phases were identified by XRD. HRTEM analysis (Figure 2e) confirmed the SnSe₂ trigonal phase (space group = P3-m1) with a=b=3.8110 Å, c=6.1360 Å and the growth of the NPLs with preferentially exposed (001) facets.

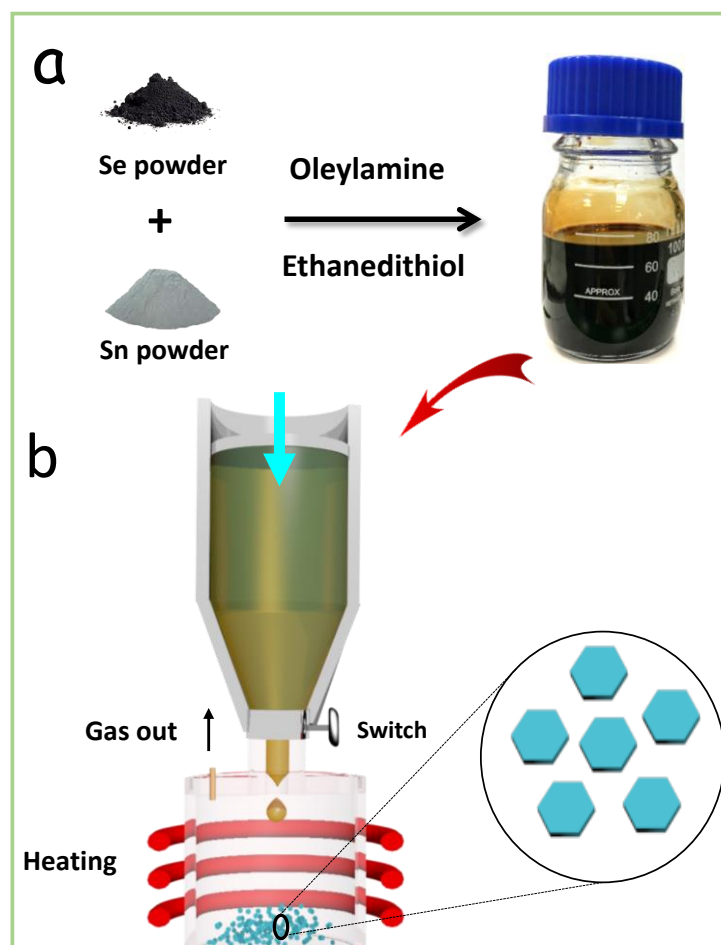


Figure 1. Scheme of (a) the SnSe₂ precursor preparation procedure, and (b) the continuous preparation of SnSe₂ NPLs through the decomposition of the SnSe₂ precursor ink.

EDX analysis showed the SnSe₂ NPLs to be slightly Sn-rich, with a composition Se/Sn=1.9 (Figure 3). XPS analysis showed the surface of SnSe₂ NPLs to be slightly more Sn rich: Se/Sn = 1.7. The Se 3d and Sn 3d regions of the XPS spectra (Figure 8) could be fitted with a unique doublet each one, further proving the phase purity of the sample.^[9] EELS chemical composition maps displayed a homogeneous distribution of both Sn and Se elements in all SnSe₂ NPLs (Figure 2f), although slightly Sn-rich edges could be detected.

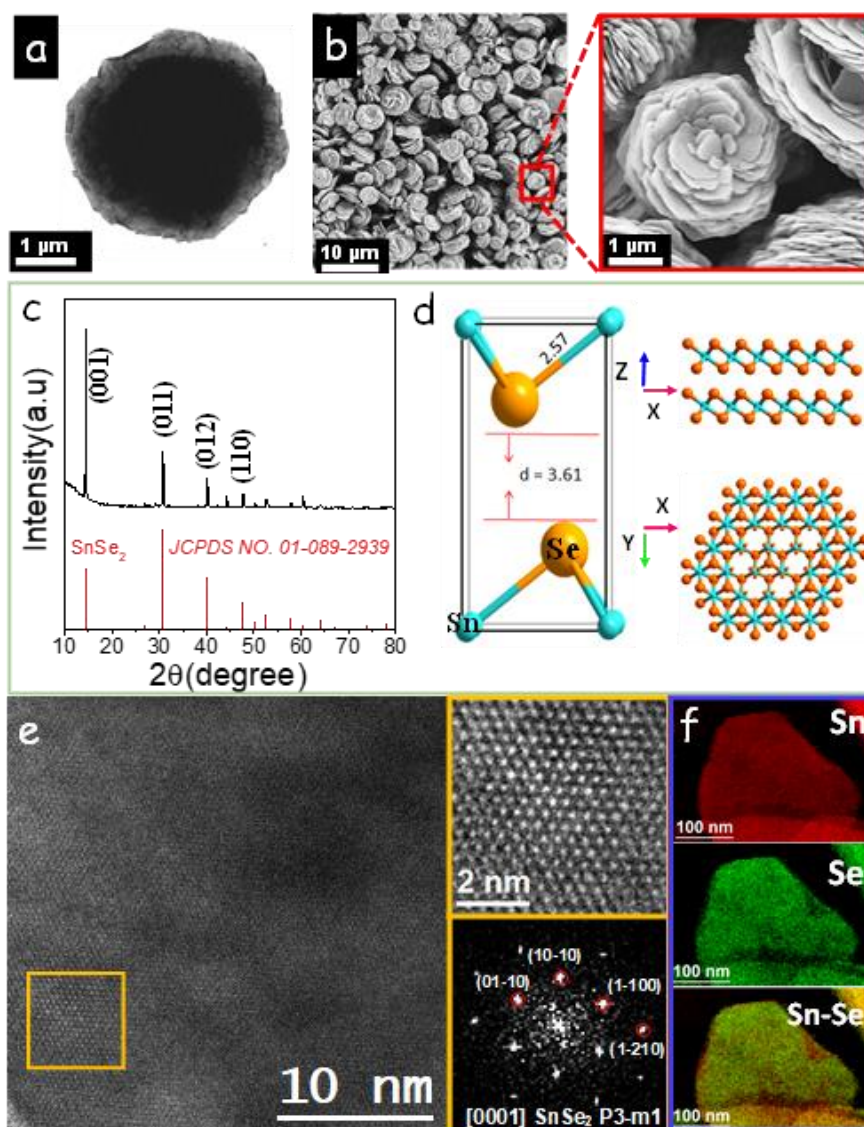


Figure 2. (a) Representative TEM micrograph of a hexagonal SnSe₂ NPL. (b) Representative SEM micrograph of flower-like SnSe₂ nanostructures, including a magnified micrograph of an individual particle. (c) XRD pattern of SnSe₂ NPLs. (d) Atomic model of the SnSe₂ crystal structure (P3m1 space group) along Y and Z axis: Se (orange), Sn (light blue). (e) HRTEM micrograph, with magnified detail of the orange squared region and its corresponding power spectrum. The SnSe₂ lattice fringe distances were measured to be 0.332 nm, 0.327 nm and 0.326 nm, with crystal plane angles of 61.23 and 121.25°, which can be assigned to the trigonal SnSe₂ phase, visualized along its [0001] zone axis. (f) EELS chemical composition maps of SnSe₂ NPLs.

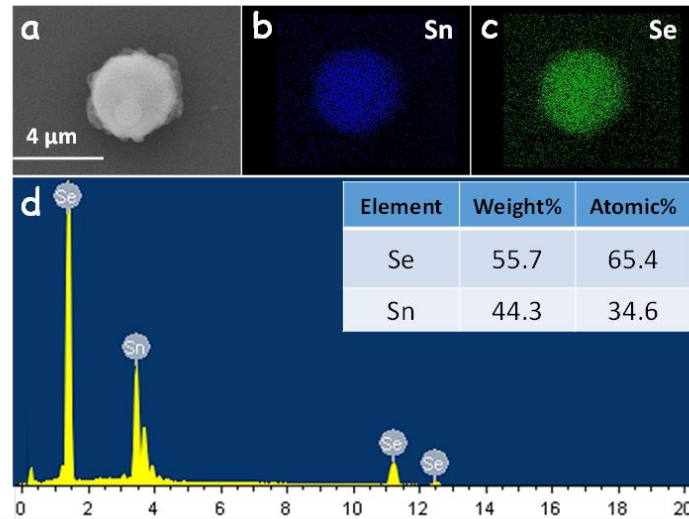


Figure 3. (a-c) SEM-EDX elemental maps of a SnSe₂ NPL. (d) SEM EDX spectrum of SnSe₂ NPLs. Inset shows the obtained composition.

SEM characterization displayed SnSe₂ NPLs to grow through a screw dislocation mechanism.^[10] Figure 4b shows the top view and side view of a SnSe₂ multi-layer nanostructure displaying an helical surface on the top layer with clockwise spiral direction (Figure 4a). Bright field TEM micrographs of some of the NPLs also displayed multiple contours with different contrast also indicating screw dislocation phenomenon. In the screw dislocation growth mechanism self-perpetuating steps along a screw dislocation axis cause the oriental growth.^[11] In contrast with several previous nanostructures obtained by the screw dislocation,^[12] in our materials new SnSe₂ layers grown through the dislocation mechanism detached from previously formed, in our materials several growing centers formed and grown simultaneously in one big plate, resulting in a flower-like structure (Figure 4). It is hypothesize that the layer detachment was resulted from the combination of the stress generated in nanostructures grown from such dislocation-driven mechanism and the weak layer-to-layer bonding in the 2D SnSe₂ crystal structure.

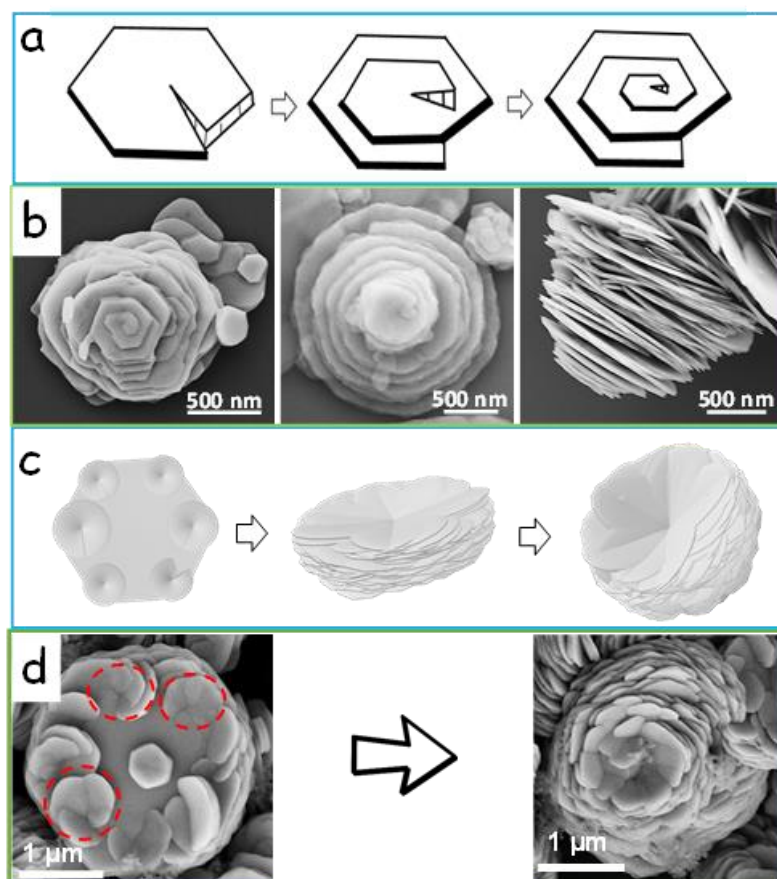


Figure 4. (a) Schematic illustration of the screw dislocation-driven growth mechanism. (b) Representative SEM micrographs of SnSe₂NPL-based structures revealing the screw dislocation growth from top view and side view. (c) Schematic illustration of flower nanostructure formation through multiple growing centers. (d) Representative SEM micrographs of SnSe₂ plate with multiple dislocation cores and flower-like structure.

The temperature and nominal molecular ratio of Sn and Se precursors were key parameters to produce phase pure SnSe₂ NPLs (Figure 5a). Sn/Se molar ratios above 0.5 in the initial ink resulted in the additional formation of a secondary SnSe phase. However, at Sn/Se=1 the ink decomposition at 380 °C did not result in pure orthorhombic SnSe, but a combination of SnSe₂ and SnS₂ due to the reaction of part of the Sn with EDT. Pure-phase SnSe was obtained only at higher ink decomposition temperatures of ca. 500 °C and only when using equal concentrations of the two elements (Figure 5).

SnSe₂ NPLs were purified by multiple precipitation and redispersion steps using chloroform as solvent and ethanol as antisolvent. The purified and dried NPLs were annealed at 450 °C for 60 mins inside a tube furnace under argon flow. The annealed particles still displayed plate-like geometries although with larger lateral dimensions and without displaying the flower-like shape (Figure 4a). It is hypothesized that the multiple layers of the initial NPL-based nanoflowers, combined within a unique plate, resulting in planar but larger nanostructures.

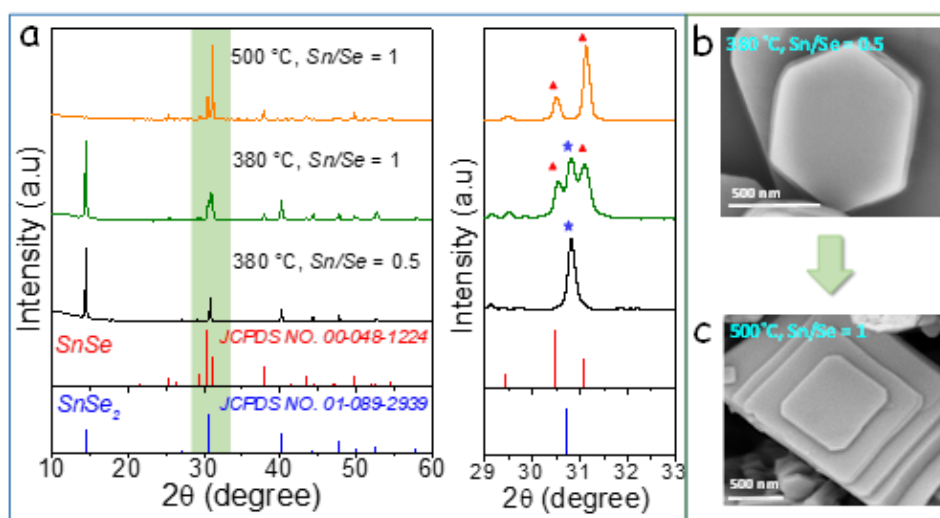


Figure 5. (a) XRD pattern of the material obtained from the decomposition of the precursor ink with different Sn/Se ratios and at different temperatures as specified in each pattern. A magnification of the relevant area around $2\theta = 31^\circ$ is also shown for clarity. (b) SEM micrographs of SnSe₂ NPLs with hexagonal structure and (c) SnSe NPLs with orthorhombic nanostructure obtained in the specified conditions.

Subsequently, the annealed NPLs were loaded into a graphite die and were hot-pressed within an Ar-filled glovebox at 460 °C for 5 min under 80 MPa of uniaxial pressure. This methodology allowed obtaining 10×10 (length \times diameter) mm² cylinders with relative densities of ca. 90% as measured by Archimedes' method.

Such pellets, obtained from the uniaxial press of SnSe₂ NPLs, displayed a clear crystallographic texture, with the SnSe₂ [001] crystallographic direction oriented

along the pressure axis, as observed from XRD characterization (Figure 5d). Top view and cross-section SEM micrographs displayed a clear laminar structure of the pellets (Figure 5b-c), with layers extending tens of microns in the disk plane and having a thickness of ca. 70 nm.

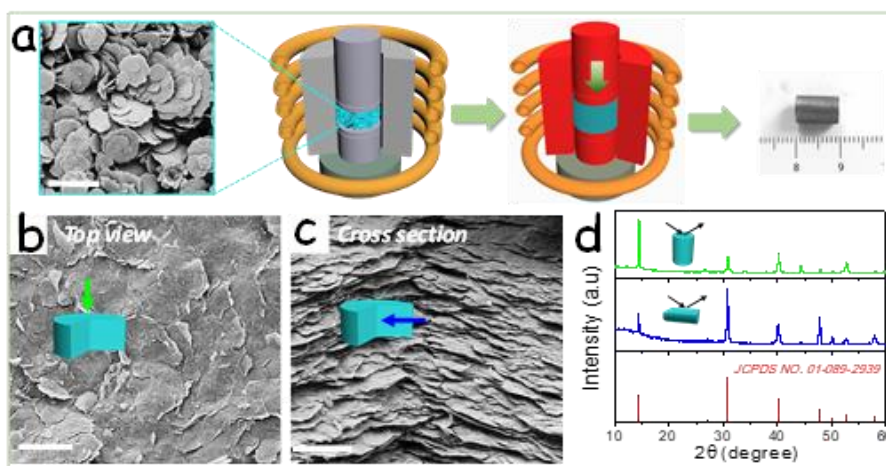


Figure 6. (a) Schematic illustration of the consolidation the annealed nanopowder into a cylindrical pellet. A representative SEM micrograph of the annealed nanopowder and an optical image of the final pellet are included in the scheme. (b) Top-view SEM micrograph of a SnSe₂ pellet. (c) Cross-section SEM micrograph of the same pellet. (d) XRD pattern of the SnSe₂ pellet laid along the cross plane direction (blue) and the in plane direction (green). Scale bar = 10 μm.

Such layered structure anticipated anisotropic transport properties. Thus, the TE properties of the material were measured in two normal directions: cross plane, which corresponds to the pressure axis and the [001] crystallographic direction, and in plane, which mainly corresponds to the ab plane of the SnSe₂ structure.

As expected, the electrical conductivities measured cross plane were lower than those measured in plane: $\sigma_{//}/\sigma_{\perp} = 2.7$ at 750 K. However, SnSe₂ nanomaterials exhibited relatively low electric conductivities in both measured directions (Figure 9a).

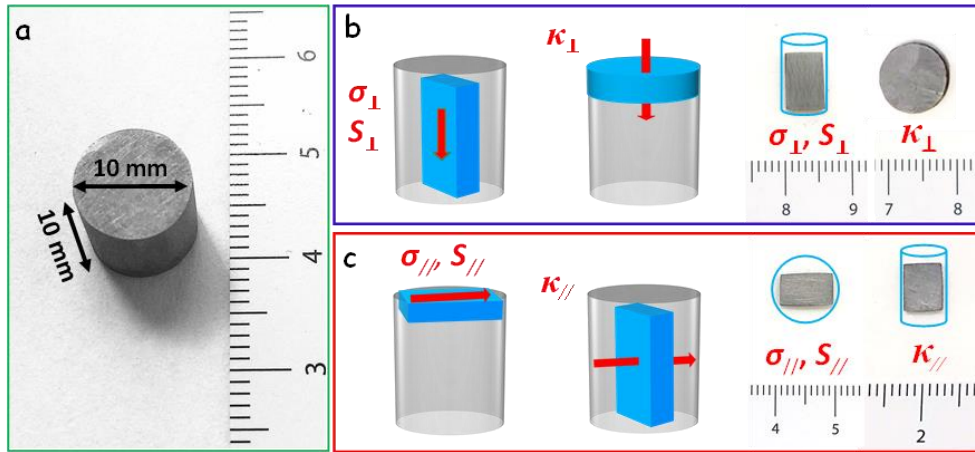


Figure 7. A representative photograph of consolidated cylindrical pellet after hot pressing. Graphic cartoons show corresponding samples obtained from cylindrical pellets and used to measure TE properties along two directions: cross plane (b) and in plane (c) direction.

Negative Seebeck coefficients were obtained in all the temperature range (Figure 9b). The Seebeck coefficients displayed similar values in the two directions: $S_{//}/S_{\perp} = 0.91$ at 750 K. These similar values are explained by the relatively low dependence of this parameter on scattering. Nevertheless, as generally observed in similar crystallographically textured layered nanomaterials, slightly higher values were obtained cross plane, which can be related to a slight preferential scattering of minoritarian and/or low energy carriers, i.e. a filtering mechanism.^[13]

Much lower thermal conductivities were obtained cross plane than in plane: $\kappa_{//}/\kappa_{\perp} = 3.64$ at 750 K (Figure 9d). This anisotropy was associated to the more efficient phonon scattering at the higher density of grain boundaries in the cross plane direction and the anharmonicity of the SnSe₂ crystal structure. In this regard, already in SnSe₂ single crystals highly anisotropic transport properties were generally measured, with electrical conductivity and thermal conductivity ratios up to 6^[14].

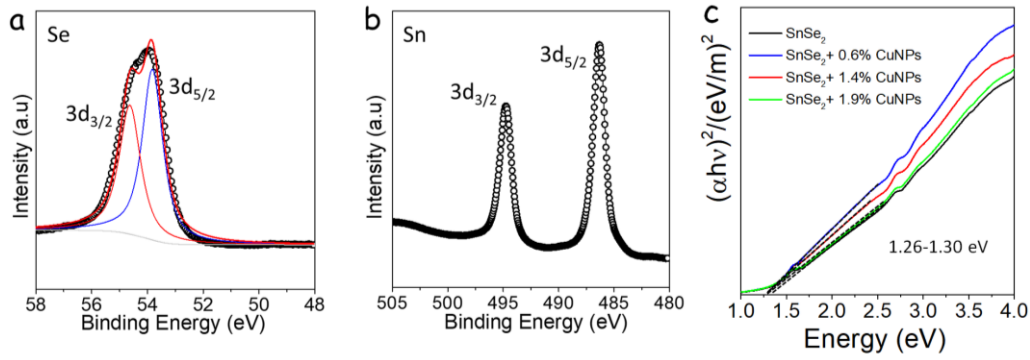


Figure 8. XPS spectrum of SnSe₂ NPLs: (a) Se 3d and (b) Sn 3d. (c) Optical band gap energy of SnSe₂ (black) and x at% SnSe₂-Cu NCs with x=0.6 (blue), 1.4 (red), 1.9 (green), a plot of $(\alpha h\nu)^2$ versus $h\nu$ for determination of band gap.

Overall, higher TE figures of merit were obtained cross plane, with values up to $ZT_{\perp}=0.2$ at 770 K (Figure 9f). These values were comparable to those previously measures for this material obtained by other methods.^[7] Overall, while SnSe₂ nanomaterials displayed relatively high Seebeck coefficients and very low thermal conductivities, their main limitation was a moderate electrical conductivity. This low electrical conductivity was in part related to a moderate charge carrier concentration due to the lack of extrinsic dopants.

Sample	Density (g/cm ³)	Relative density
SnSe ₂	5.41	90.6%
SnSe ₂ -0.6% CuNPs	5.48	91.7%
SnSe ₂ -1.4% CuNPs	5.45	91.2%
SnSe ₂ -1.9% CuNPs	5.53	92.6%

Table1. Density of SnSe₂ and x at% SnSe₂-Cu samples.

To increase electrical conductivity, instead of a conventional doping strategy, I used a modulation doping approach. While ionic doping generally relies on the introduction within a semiconductor matrix of small amounts of substituting impurities with different valence than the replaced element, thus freeing or trapping additional electrons, modulation doping relies on the introduction

within a semiconductor matrix of nanodomains of a different material having an electron energy band structure suitable for injection of majority carriers to the matrix semiconductor.^[15] The modulation doping approach allows separating the ionized donor/acceptor from the charge carrier path, thus strongly reducing charge carrier scattering and improving mobilities. Additionally, in NP-based bottom up assembly approaches, the modulation doping strategy provides a very simple and versatile strategy to optimize electrical properties of semiconductor materials,^[16] since the charge injection nanodomains can be easily introduced in the proper amount during the assembly or consolidation steps.

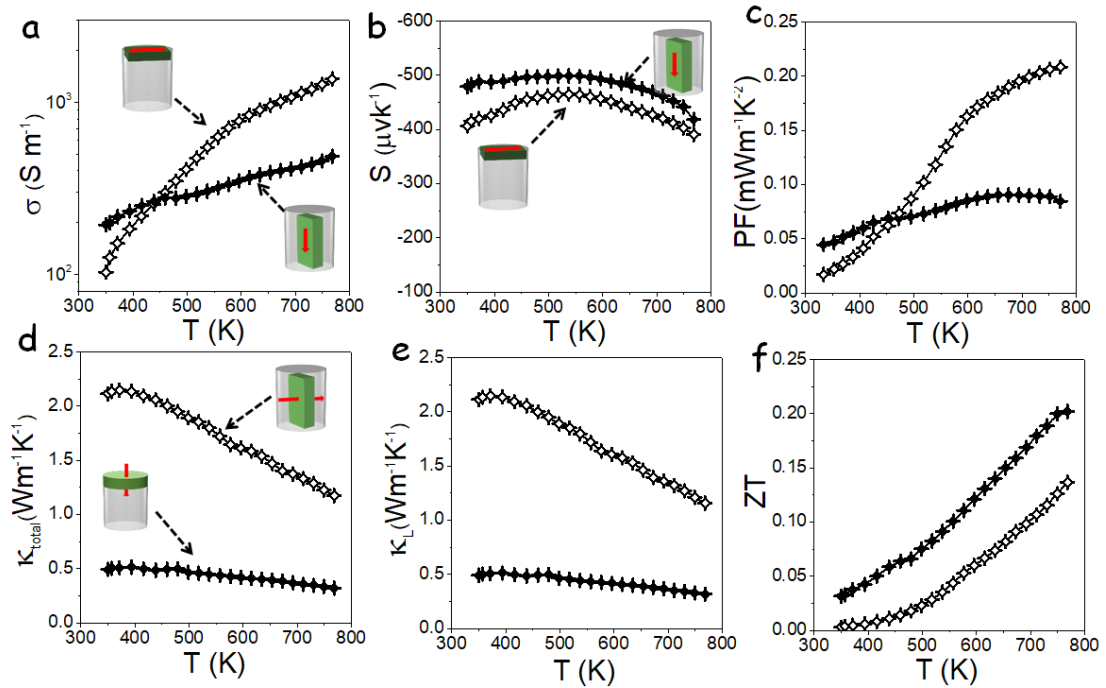


Figure 9. Temperature dependence of (a) electric conductivity, σ ; (b) Seebeck coefficient, S ; (c) power factor or $S^2\sigma$, PF; (d) total thermal conductivity, κ_{total} ; (e) lattice thermal conductivity, κ_L ; and (f) TE figure of merit, ZT of a SnSe_2 pellet measured in the two directions, in-plane (open symbols) and cross-plane (solid symbols).

Being SnSe_2 an n-type semiconductor, I selected a dopant phase with a large charge carrier concentration and a relatively low work function that allowed injection of electrons to the SnSe_2 matrix. Thus, I blended SnSe_2 NPLs with Cu,

Sn and Ag NPs (Figure 14). While Sn had moderate effect on the transport properties of the material, upon incorporation of Cu or Ag NPs a dramatic increase in electric conductivity was measured (Figure 14a). As expected, a parallel decrease of the Seebeck coefficient was also obtained. This Seebeck coefficient decrease was more abrupt with the introduction of Ag NPs than with Cu. Overall, among the different metals tested, the highest power factors were obtained from SnSe₂-Cu NCs (Figure 14c), reaching values three-fold higher than in pure SnSe₂.

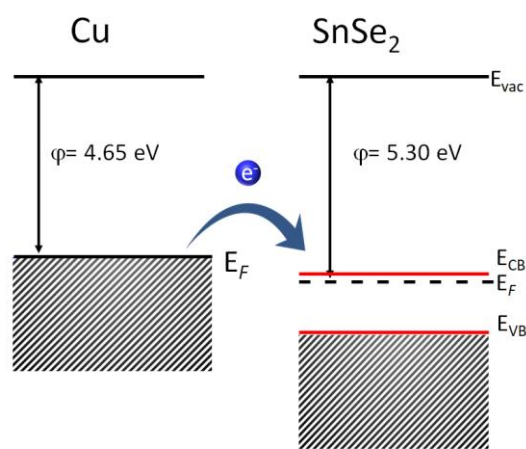


Figure 10. Scheme of energy diagram between the interface of Cu nanodomains and SnSe₂ matrix. E_{vac} is the vacuum level, E_{CB} is the conduction band energy, E_f is the Fermi energy, E_{VB} is the conduction band energy, and e^- is the charge carrier/ electron.

Element	Nominal composition			
	SnSe ₂	SnSe ₂ -0.8% CuNPs	SnSe ₂ -1.5% CuNPs	SnSe ₂ -2.2% CuNPs
Sn (at%)	32.9	33.0	32.8	32.7
Se (at%)	66.1	66.4	65.8	65.4
Cu (at%)	0	0.6	1.4	1.9

Table 2. Composition of SnSe₂ and SnSe₂-CuNPs NC obtained from ICP analysis.

I further studied the effect of the concentration of Cu NPs (Figure 12). I observed

the electrical conductivity to increase with the amount of Cu introduced up to a certain loading. With the introduction of a 1.9 at% of Cu, a decrease in electrical conductivity was observed, which I associated to the formation of significant amounts of Cu_2Se , as observed by XRD characterization. An optimal concentration of 1.4 at% Cu was finally established to maximize TE properties of the material.

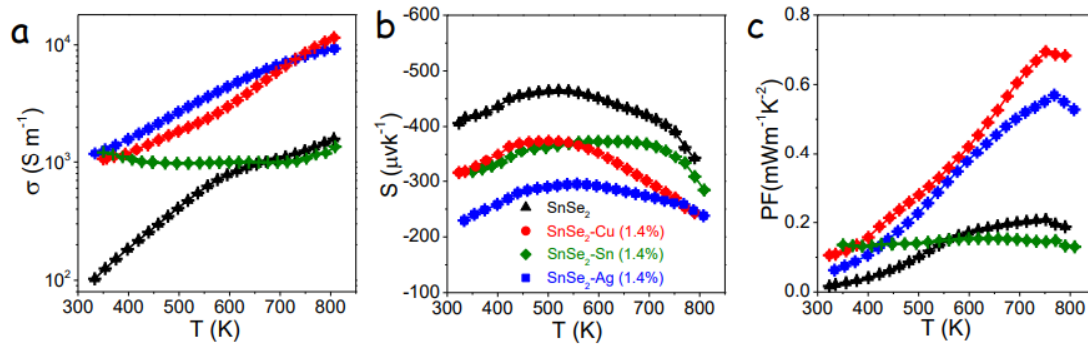


Figure 11. Temperature dependence of the TE properties measured along the in-plane direction from SnSe₂ and SnSe₂-NP NCs: SnSe₂ (black triangle), SnSe₂-Cu (red circle); SnSe₂-Sn (green diamond), SnSe₂-Ag (blue square). (a) electrical conductivity, σ ; (b) Seebeck coefficient, S; and (c) power factor, PF.

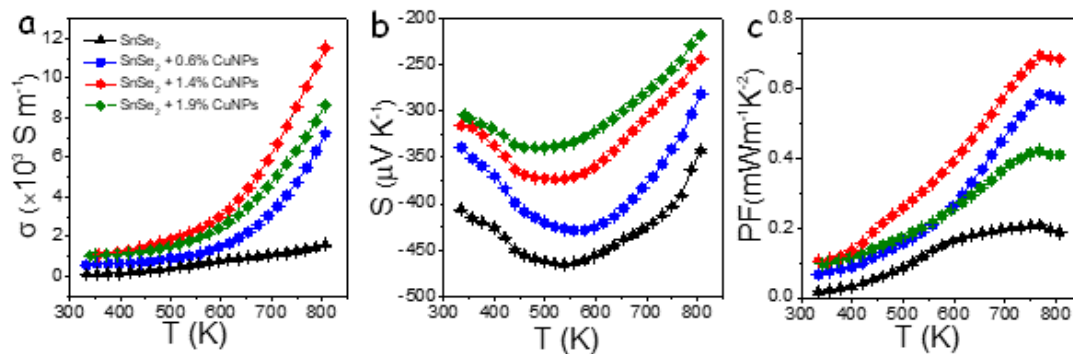


Figure 12. Temperature dependence of (a) electrical conductivity, σ (b) Seebeck coefficient, S; and (c) power factor, PF, measured along in-plane direction from SnSe₂-Cu NCs with different Cu concentrations: 0.0 at. % (black triangle, ▲), 0.6 at.% (blue square, ■), 1.4 at.% CuNPs (red circle, ●), and 1.9 at.% (green diamond, ◆).

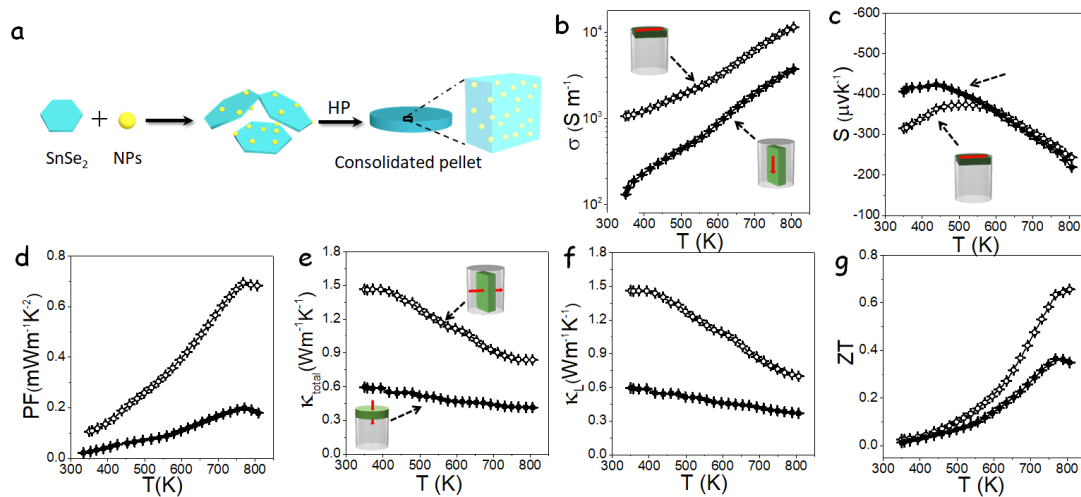


Figure 13. (a) Scheme of the process to produce SnSe₂-NPs NCs. TE characterization of SnSe₂-Cu (1.4 at%) NCs. Temperature dependence of (b) electric conductivity, σ ; (c) Seebeck coefficient, S ; (d) power factor, PF; (e) total thermal conductivity, κ_{total} ; (f) lattice thermal conductivity, κ_L ; and (g) TE figure of merit, ZT. In plane (open symbols); cross-plane (solid symbols).

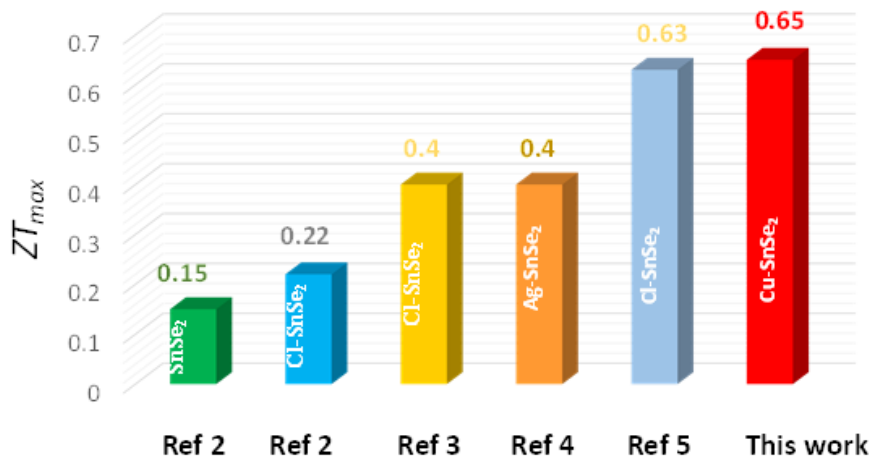


Figure 14. Literature comparison of the TE figures of merit recently reported [46-49] from undoped SnSe₂ and doped SnSe₂.

Figure 13 displays the TE properties measured in the two normal directions of the SnSe₂-Cu NC containing 1.4 at% of Cu. A large increase of electric

conductivity and a moderate decrease of the Seebeck coefficient were observed with the Cu introduction in both directions. This translated into significantly larger power factors in the SnSe₂-Cu NC when compared with pure SnSe₂. The thermal conductivity of SnSe₂-Cu was significantly reduced in plane with respect to SnSe₂, due to the additional scattering at Cu nanoinclusions, but maintained cross plane at the already very low values measured from the SnSe₂ nanomaterial. Overall, a three-fold increase of the TE figure of merit was obtained with the incorporation of Cu, reaching ZT values up to ZT=0.65 at 810 K along the in plane directions.

2.5 Conclusions

In conclusion, I presented a solution-based approach to produce SnSe₂ NPLs and crystallographically textured SnSe₂ bulk nanomaterials and NCs. The precursor solution was prepared by directly dissolving Sn and Se powders in an amine-thiol co-solvent solution. Uniform and pure phase SnSe₂ NPLs could be readily obtained by the crystallization of the ink at 380 °C. The growth of these SnSe₂ NPLs took place through a screw dislocation mechanism and the simultaneous detachment of the newly forming layers from the previously formed ones. The TE properties of thus obtained crystallographically textured SnSe₂ bulk nanomaterials and SnSe₂-Cu NCs were measured in two perpendicular directions, along the press axis (cross-plane) and normal to it (in plane). While bare SnSe₂ nanomaterials displayed notable TE figures of merit, especially cross plane, their relatively low electrical conductivity limited their performance. A modulation doping strategy was used to improve this parameter, to reach TE figures of merit up to ZT = 0.65 at 810 K in in plane SnSe₂-Cu NCs.

2.6 References

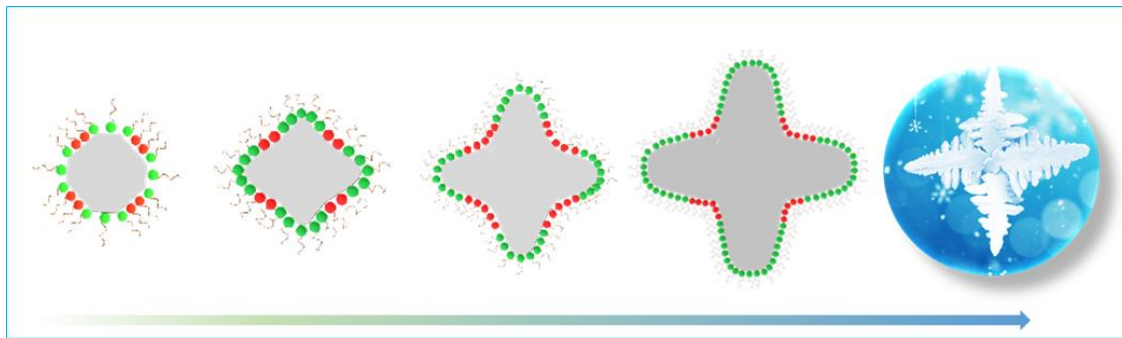
1. D. H. Webber, R. L. Brutchey, *J. Am. Chem. Soc.* **2013**, 135, 15722-15725;
2. P. D. Antunez, D. A. Torelli, F. Yang, F. A. Rabuffetti, N. S. Lewis, R. L. Brutchey, *Chem. Mater.* **2014**, 26, 5444-5446;

3. C. L. McCarthy, D. H. Webber, E. C. Schueller, R. L. Brutchey, *Angew. Chem., Int. Ed.* **2015**, 54, 8378-8381;
4. D. H. Webber, J. J. Buckley, P. D. Antunez, R. L. Brutchey, *Chem. Sci.* **2014**, 5, 2498-2502;
5. R. Zhang, S. Cho, D. G. Lim, X. Hu, E. A. Stach, C. A. Handwerker, R. Agrawal, *Chem. Commun.* **2016**, 52, 5007-5010;
6. Z. Lin, C. Hollar, J. S. Kang, A. Yin, Y. Wang, H. Y. Shiu, Y. Huang, Y. Hu, Y. Zhang, X. Duan, *Adv. Mater.* **2017**, 29, 1606662.
7. D. Voiry, M. Salehi, R. Silva, T. Fujita, M. Chen, T. Asefa, V. B. Shenoy, G. Eda, M. Chhowalla, *Nano Lett.* **2013**, 13, 6222-6227.
8. G. Fiori, F. Bonaccorso, G. Iannaccone, T. Palacios, D. Neumaier, A. Seabaugh, S. K. Banerjee, L. Colombo, *Nat. Nanotech.* **2014**, 9, 768-779;
9. D. Akinwande, N. Petrone, J. Hone, *Nat. Commun.* **2014**, 5, 5678.
10. C. Lu, Y. Liu, Y. Ying, J. Liu, *Langmuir* **2017**, 33, 630-637.
11. A. Banik, U. S. Shenoy, S. Saha, U. V. Waghmare, K. Biswas, *J. Am. Chem. Soc.* **2016**, 138, 13068-13075;
12. A. Banik, K. Biswas, *J. Mater. Chem. A* **2014**, 2, 9620-9625;
13. A. Banik, U. S. Shenoy, S. Anand, U. V. Waghmare, K. Biswas, *Chem. Mater.* **2015**, 27, 581-587;
14. A. Banik, S. Roychowdhury, K. Biswas, *Chem. Commun.* **2018**;
15. A. Banik, B. Vishal, S. Perumal, R. Datta, K. Biswas, *Energy Environ. Sci.* **2016**, 9, 2011-2019; f) S. Chandra, A. Banik, K. Biswas, *ACS Energy Lett.* **2018**, 3, 1153-1158.
16. L.-D. Zhao, S.-H. Lo, Y. Zhang, H. Sun, G. Tan, C. Uher, C. Wolverton, V. P. Dravid, M. G. Kanatzidis, *Nature* **2014**, 508, 373-377.
17. S. Saha, A. Banik, K. Biswas, *Chem.-Eur. J.* **2016**, 22, 15634-15638;
18. P. Xu, T. Fu, J. Xin, Y. Liu, P. Ying, X. Zhao, H. Pan, T. Zhu, *Sci. Bull.* **2017**, 62, 1663-1668;
19. Y. Luo, Y. Zheng, Z. Luo, S. Hao, C. Du, Q. Liang, Z. Li, K. A. Khor, K. Hippalgaonkar, J. Xu, Q. Yan, C. Wolverton, M. G. Kanatzidis, *Adv. Energy Mater.* **2018**, 8, 1702167.
20. L. A. Burton, D. Colombara, R. D. Abellon, F. C. Grozema, L. M. Peter, T. J. Savenije, G. Dennler, A. Walsh, *Chem. Mater.* **2013**, 25, 4908-4916;

21. Y. Lei, S. Song, W. Fan, Y. Xing, H. Zhang, *J. Phys. Chem. C* **2009**, 113, 1280-1285;
22. P. Ramasamy, P. Manivasakan, J. Kim, *CrystEngComm* **2015**, 17, 807-813;
23. K. Liu, H. Liu, J. Wang, L. Feng, *Mater. Lett.* **2009**, 63, 512-514;
24. X. Zhou, L. Gan, W. Tian, Q. Zhang, S. Jin, H. Li, Y. Bando, D. Golberg, T. Zhai, *Adv. Mater.* **2015**, 27, 8035-8041;
25. C. Zhai, N. Du, H. Z. D. Yang, *Chem. Commun.* **2011**, 47, 1270-1272;
26. Y. Du, Z. Yin, X. Rui, Z. Zeng, X.-J. Wu, J. Liu, Y. Zhu, J. Zhu, X. Huang, Q. Yan, *Nanoscale* **2013**, 5, 1456-1459;
27. P. Zheng, Z. Dai, Y. Zhang, K. N. Dinh, Y. Zheng, H. Fan, J. Yang, R. Dangol, B. Li, Y. Zong, *Nanoscale* **2017**, 9, 14820-14825.
28. S. J. Patil, V. C. Lokhande, D.-W. Lee, C. D. Lokhande, *Opt. Mater.* **2016**, 58, 418-425;
29. N. D. Boscher, C. J. Carmalt, R. G. Palgrave, I. P. Parkin, *Thin Solid Films* **2008**, 516, 4750-4757;
30. E. P. Mukhokosi, S. B. Krupanidhi, K. K. Nanda, *Sci. Rep.* **2017**, 7, 15215.
31. W.-K. Burton, N. Cabrera, F. Frank, *Phil. Trans. R. Soc. Lond. A* **1951**, 243, 299-358;
32. F. Wang, X. Wang, *Nanoscale* **2014**, 6, 6398-6414.
33. L. Chen, B. Liu, A. N. Abbas, Y. Ma, X. Fang, Y. Liu, C. Zhou, *ACS nano* **2014**, 8, 11543-11551;
34. F. Meng, S. A. Morin, A. Forticaux, S. Jin, *Acc. Chem. Res.* **2013**, 46, 1616-1626;
35. A. Forticaux, L. Dang, H. Liang, S. Jin, *Nano Lett.* **2015**, 15, 3403-3409;
36. S. A. Morin, M. J. Bierman, J. Tong, S. Jin, *Science* **2010**, 328, 476-480;
37. A. Zhuang, J. J. Li, Y. C. Wang, X. Wen, Y. Lin, B. Xiang, X. Wang, J. Zeng, *Angew. Chem., Int. Ed.* **2014**, 53, 6425-6429.
38. S. A. Morin, A. Forticaux, M. J. Bierman, S. Jin, *Nano Lett.* **2011**, 11, 4449-4455.
39. Y. Liu, Y. Zhang, K. H. Lim, M. Ibáñez, S. Ortega, M. Li, J. David, S. Martí-Sánchez, K. M. Ng, J. Arbiol, *ACS nano* **2018**, 12, 7174-7184 ;
40. Y. Liu, Y. Zhang, S. Ortega, M. Ibáñez, K. H. Lim, A. Grau-Carbonell, S. Martí-Sánchez, K. M. Ng, J. Arbiol, M. V. Kovalenko, *Nano Lett.* **2018**, 18, 2557-2563.
41. B.-Z. Sun, Z. Ma, C. He, K. Wu, *Phys. Chem. Chem. Phys.* **2015**, 17, 29844-29853.

42. M. Zebarjadi, G. Joshi, G. Zhu, B. Yu, A. Minnich, Y. Lan, X. Wang, M. Dresselhaus, Z. Ren, G. Chen, *Nano Lett.* **2011**, 11, 2225-2230;
43. B. Yu, M. Zebarjadi, H. Wang, K. Lukas, H. Wang, D. Wang, C. Opeil, M. Dresselhaus, G. Chen, Z. Ren, *Nano Lett.* **2012**, 12, 2077-2082.
44. M. Ibanez, Z. Luo, A. Genc, L. Piveteau, S. Ortega, D. Cadavid, O. Dobrozhan, Y. Liu, M. Nachtegaal, M. Zebarjadi, J. Arbiol, M. V. Kovalenko, A. Cabot, *Nat. Commun.* **2016**, 7, 10766;
45. S. Ortega, M. Ibanez, Y. Liu, Y. Zhang, M. V. Kovalenko, D. Cadavid, A. Cabot, *Chem. Soc. Rev.* **2017**, 46, 3510-3528;
46. Y. Liu, D. Cadavid, M. Ibáñez, S. Ortega, S. M. Sánchez, O. Dobrozhan, M. V. Kovalenko, J. Arbiol, A. Cabot, *APL Mater.* **2016**, 4, 104813.
47. Saha, S. Banik, A. Biswas, K, *Chem.-Eur. J.* **2016**, 22, 15634-15638.
48. Xu, P. Fu, T. Xin, J. Liu, Y. Ying, P. Zhao, X.; Pan, H.; Zhu, T, *Sci. Bull.* **2017**, 62, 1663- 1668.
48. Li, F.; Zheng, Z. Li, Y. Wang, W. Li, J.-F. Li, B. Zhong, A. Luo, J. Fan, P, *J. Mater. Sci.* **2017**, 52, 10506-10516.
49. Luo, Y. Zheng, Y. Luo, Z. Hao, S. Du, C. Liang, Q. Li, Z. Khor, K. A. Hippalgaonkar, K.; Xu, J. Yan, Q. Wolverton, C. Kanatzidis, M. G, *Adv. Energy Mater.* **2018**, 8, 1702167.

Chapter 3 Tin Selenide Molecular Ink for the Solution-Processing of TE Materials and Devices



3.1 Abstract

In the present work, I report a solution-based strategy to produce crystallographically textured SnSe bulk nanomaterials and printed layers with optimized TE performance in the direction normal to the substrate. Our strategy is based on the formulation of a molecular ink that can be continuously decomposed to produce a SnSe powder or printed into predefined patterns. The ink formulation and decomposition conditions are optimized to produce pure phase 2D SnSe NPLs. The printed layer and the bulk material obtained after hot press displays a clear preferential orientation of the crystallographic domains, resulting in ultralow thermal conductivity of $0.55 \text{ Wm}^{-1}\text{K}^{-1}$ in the direction normal to the substrate. Such textured nanomaterials present highly anisotropic properties, with best TE performance in plane, *i.e.* in the directions parallel to the substrate, which coincide with the crystallographic *bc* plane of SnSe. This is an unfortunate characteristic because TE devices are designed to create/harvest temperature gradients in the direction normal to the substrate. I further demonstrate that this limitation can be overcome with the introduction of small amounts of tellurium in the precursor ink. The presence of tellurium allows reducing the band gap, increase both charge carrier concentration and mobility, especially cross plane, with a minimal decrease of the Seebeck coefficient. These

effects translate into record out of plane ZT values at 800 K.

3.2 Introduction

Solid state TE devices offer a direct and solid state means of conversion between thermal and electrical energy, which makes them extremely appealing for a wide range of applications.¹⁻⁸ However, the relatively low energy conversion efficiency and high manufacturing cost of current TE devices, which are in most cases designed for cooling applications, makes them cost-efficient only in few niche markets.^{1, 9} Towards improving cost-efficiency of TE devices, it is imperative to: i) implement lower cost fabrication processes; ii) optimize device parameters for each particular application to maximize efficiency and minimize the amount of used material; iii) develop high performance and lower cost TE materials.

TE performance is generally quantified using an adimensional figure of merit, $ZT = \sigma S^2 T / \kappa$.^{3, 7, 10} Among the different families of TE materials proposed,^{2, 4} some two dimensional chalcogenides exhibit the best TE performance.¹¹⁻¹⁷ Bi₂Te₃-based alloys provide the highest ZT values at temperatures around ambient, up to 1.96 at 420 K,¹⁶ and dominate the TE market.¹⁸⁻²¹ On the other hand, SnSe single crystals have recently achieved unprecedented record ZT values in the medium-high temperature range, 2.6 at 923K.^{13, 22} SnSe has a layered crystal structure with weak Van der Waals bonds along the *a* axis and tight covalent bonds along the *bc* plane, which results in highly anisotropic transport properties and an impressively low lattice thermal conductivity. Nonetheless, the high production cost and poor mechanical properties of SnSe single crystals limit their use in real applications. All of these have sparked much interest in producing polycrystalline SnSe with TE performance approaching that of SnSe single crystals. Owing to the anisotropic properties of the material, the optimization of polycrystalline SnSe generally requires producing crystallographic textured samples.²³⁻³⁷ In this direction, while severe plastic deformation techniques are conventionally used to produce textured polycrystalline materials,^{38, 39} spark plasma sintering and hot press approaches,

more commonly used to consolidate TE polycrystalline materials, are also able to produce textured materials when using an open dye to induce extrusion or when incorporating a liquid phase in the process.^{15, 16, 40-44}

Beyond engineering TE materials with improved performance and lower cost, novel strategies to fabricate TE devices that are less labour-intensive and which allow a more rational use of the TE material need to be developed. One potential alternative strategy is ink-jet printing. The main advantages of printing techniques are low cost, potential to produce shape adaptable or flexible devices, control over the thickness of the TE material and high material use efficiency. While printing strategies are currently well developed and used in a large number of applications,⁴⁵⁻⁴⁸ their implementation in new technologies strongly relies on the formulation of proper functional inks.

I report here a thiol-free SnSe molecular ink, which can be used as precursor to produce bulk nanocrystalline SnSe or can be directly printed into SnSe layers. I study the decomposition conditions and demonstrate the possibility to produce pure phase SnSe at moderate temperatures. I further analyse here the processing conditions necessary to obtain crystallographically textured SnSe bulk nanomaterials and layers and characterize their anisotropic TE properties. Finally, the TE performance of the material in the direction normal to the layer substrate is optimized by including small amounts of tellurium within the ink.

3.3 Experimental Section

Chemicals: Tin chloride (SnCl_2 , 98%) and selenium dioxide (SeO_2 , 99.8%) were purchased from Acros Organics. Tri-n-octylphosphine (TOP, $\text{C}_{24}\text{H}_{51}\text{P}$, 97 %), oleic acid (OAc, $\text{C}_{18}\text{H}_{34}\text{O}_2$, 90%) and OAm ($\text{C}_{18}\text{H}_{37}\text{N}$, $\geq 98\%$) were purchased from Sigma-Aldrich. Sodium tellurite (Na_2TeO_3 , 99.5%) was purchased from Fisher. Analytical grade chloroform and ethanol were ordered from various sources. All chemicals were used as received unless specifically noted.

SnSe ink: Within an argon-filled glove box, 5.76 g SnCl_2 (30 mmol) and 3.33 g SeO_2 (30 mmol) were weighted and placed inside a glass bottle. Then 150 mL

OAm and 20 ml TOP were added inside the bottle. The mixture was subsequently sonicated for 20 min until precursors dissolved completely. Small amounts of OAc were included within the ink to produce dendritic SnSe nanostructures.

SnSe_{1-x}Te_x ink: To produce SnSe_{1-x}Te_x (x= 0.01, 0.02, 0.03) precursor inks, 5.76 g SnCl₂ (30 mmol), 3.33g SeO₂ (30 mmol) and 6.65x g Na₂TeO₃ were weighted and placed in a glass bottle, where 150 mL OAm and 20 ml TOP was subsequently added. The mixture was sonicated for 20 min until all precursors dissolved completely.

SnSe ink decomposition: The SnSe precursor ink was continuously injected into a preheated glass flask (420 °C), where it immediately decomposed. The flask was naturally cooled down to room temperature (RT) and the crystalline product was collected by dispersion in chloroform and precipitation with ethanol. Dispersion/precipitation steps were repeated three times using chloroform and ethanol aided by centrifugation at 7200 rpm for 5 min.

Bulk material consolidation: SnSe particles were thermally annealed at 500 °C (heating rate = 10 °C/min) for 60 min inside a tube furnace with argon flow to remove organic residues. After cooling to RT, the annealed material was grounded in a mortar and subsequently loaded into a graphite die. The die was then transferred to a custom-made hot press system inside the glove box, where it was heated to 500 °C by using an induction coil. The die was held at this temperature for 5 min under 80 MPa pressure. Afterward, the pressure was released and the die was naturally cooled down to RT. The obtained cylindrical pellets (Ø8 mm × 12 mm) were cut in rectangular bars in two directions: along the pressure axis (cross-plane direction) and normal to this axis (in-plane direction).

Printed layers: The SnSe molecular ink was printed on a graphite foil using an ink jet nozzle. The graphite foil was then annealed on a hot plate at 420 °C for 5 min within an argon-filled glove box. Afterward, the foil was hot pressed at

500 °C for 3 min under 80 MPa pressure.

Structural and chemical characterization: The particle size and morphology were characterized by TEM (ZEISS LIBRA 120), working at 120 kV and field-emission SEM (Zeiss Auriga) operating at 5.0 kV. HRTEM images and scanning TEM studies were conducted on a FEI Tecnai F20 field emission gun microscope operated at 200 kV with a point-to-point resolution of 0.19 nm, which was equipped with HAADF and Gatan Quantum EELS detectors. Elemental analysis was performed using an Oxford energy dispersive EDX combined with the Zeiss Auriga SEM working at 20.0 kV. XRD (2θ : 5°-80°, scanning rate was set at 5°/min) were carried out on a Bruker AXS D8 Advance XRD with Ni-filtered Cu-K α radiation ($\lambda = 1.5406 \text{ \AA}$), operating at 40 mA and 40 kV. XPS spectroscopy was performed on a SPECS system equipped with a Phoibos 150 MCD-9 detector, working at 150 W with an Al anode XR50 source. FTIR was carried out with a platinum attenuated total reflectance single reflection module. The surface topology was measured by atomic force microscopy (AFM, XE 100 Park System Corp.) Scans were conducted in non-contact mode with a silicon Tap300Al-G cantilever (Budget Sensors, spring constant of $\sim 40 \text{ N/m}$ and resonant frequency of $\sim 300 \text{ kHz}$). AFM images were analysed in the XEI software (Park System Corp). UV-Vis Optical absorption spectra were recorded on a LAMBDA 950 UV-Vis spectrophotometer from PerkinElmer. Inductively coupled plasma atomic emission spectrometer (ICP-AES, iCAP 6500, Thermo) was used for the elemental analysis, samples were prepared by digestion of nanocrystals in aqua regia overnight followed by dilution in MQ-Water (Milipore).

TE characterization: Seebeck coefficients were measured with a static DC method. Electric resistivity data was obtained using a standard four probe method. Electric resistivity and Seebeck coefficients were measured simultaneously in a LSR-3 LINSEIS system in the temperature range from 323 to 807 K under a helium atmosphere. Bearing in mind the measurement precision and system accuracy, an error of ca. 5% in the measurement of Seebeck

coefficient and electrical conductivity was estimated. A Xenon Flash Apparatus was used to measure the D of all samples with accuracies better than 6%. Thermal conductivities were then calculated by the relation $\kappa = C_p D \rho$. Hall charge carrier concentrations (n_H) and mobilities (μ_H) at room temperature (300 K) were measured with Van der Pauw and Hall Bar measurements (ezHEMS 1000, NanoMagnetics) using a magnetic field of 1 T. Values provided correspond to the average of 10 consecutive measurements, from which an error of ca. 10% was estimated.

3.4 Result and discussion

To prepare a SnSe molecular ink, the tin and selenium precursors and the solvent were selected taking into account four main parameters: i) minimize cost; ii) direct the crystal morphology toward obtaining planar structures that facilitate posterior assembly into textured nanomaterials; iii) reach a compromise between solvent volatility, which has implications in toxicity and ink stability, and decomposition temperature, which is a key parameters determining production costs; iv) reduce toxicity, avoiding the use of thiols and hydrazine. Taking into account these points, a SnSe ink was prepared by dissolving SnCl_2 and SeO_2 in a combination of OAm and TOP. OAm played a double role, it reduced Se^{4+} to Se^0 and it coordinated to Sn^{2+} to form a Sn-OAm complex, $\text{Sn}(\text{R-NH})_2$.⁴⁹⁻⁵¹ TOP coordinated with Se^0 to yield TOPSe⁵² (Figure 1).

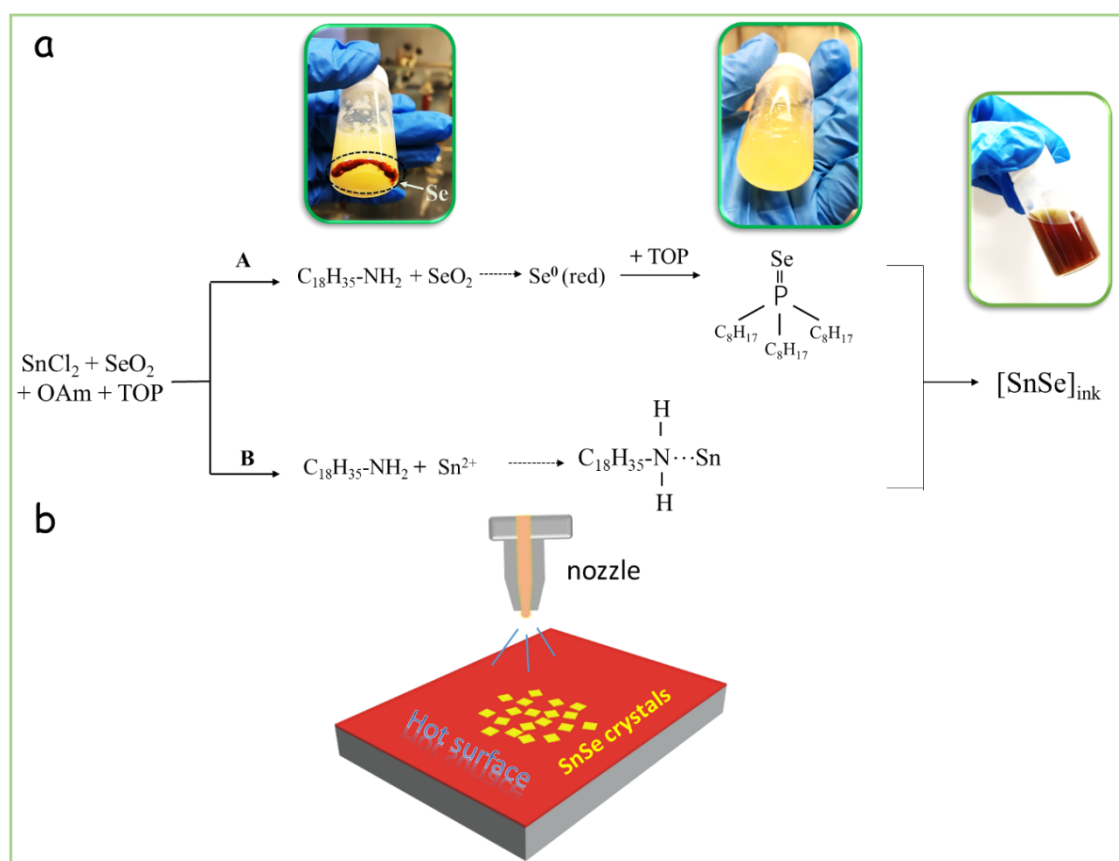


Figure 1. (a) Proposed mechanism for SnSe ink formation. Path A displays SeO_2 is firstly reduced by OAm to form Se (red color in the bottle), which reacts with TOP to form TOPSe. Path B displays OAm combined with Sn^{2+} to form a OAm-Sn complex. The final SnSe ink displays a wine color and contains a mixture of TOPSe and OAm-Sn complex. (b) Subsequently SnSe crystals were produced through decomposition of SnSe ink on a hot surface.

To analyse the product of its decomposition, the ink was dropped onto a substrate heated at $420\text{ }^\circ\text{C}$. Upon reaching the heated substrate, the ink was rapidly decomposed and a black powder was produced. Large amounts of powder could be obtained by continuously injecting/spraying the ink toward a heated receptacle/support (Figure 1). TEM and SEM characterization of the powder obtained from the decomposition of the ink showed the presence of square-like plates with a lateral size of $4\pm 1\text{ }\mu\text{m}$ and a thickness of $90\pm 20\text{ nm}$ (Figure 2 a,b). HRTEM and XRD analyses demonstrated the powder to be highly crystalline and to display a unique crystallographic phase that matched that of orthorhombic SnSe (JCPDS NO. 00-048-1224, Pnma space group, Figure 2 c,e). From the

XRD pattern, the relatively strong intensity of the $2\theta=31.0^\circ$ diffraction peak indexed as (400), indicated a preferential growth in the bc plane, i.e. the plane perpendicular to the [100] crystallographic direction. UV-Vis spectrum showed the SnSe powder to have an indirect band gap at 0.96 eV (Figure 3e). XPS analysis of SnSe displayed two Sn 3d peaks at 494.9 eV (Sn 3d_{3/2}) and 486.4 eV (Sn 3d_{5/2}), which matched well with a Sn²⁺ environment (Figure 2f). Besides, Se 3d_{3/2} and Se 3d_{5/2} peaks located at 54.4 eV and 53.5 eV evidenced the presence of a Se²⁻ oxidation state³⁵. EDX chemical analysis showed the SnSe powder to be slightly Sn rich, with a composition ratio Se/Sn = 0.95. EELS chemical composition maps displayed a homogeneously distribution of both Sn and Se within each particle and from particle to particle (Figure 2d).

To obtain single phase SnSe, the proper adjustment of the nominal element ratio, Sn/Se, and decomposition temperature was fundamental. When increasing the nominal amount of Sn in the ink formulation, a combination of Sn and SnSe phases was obtained upon decomposition at 420 °C (Figures 4). On the other hand, when using a nominal ratio Sn/Se <1, a combination of SnSe and SnSe₂ was produced. Using a nominal Sn/Se=0.5 and decreasing the decomposition temperature to 360 °C, pure-phase SnSe₂ could be produced (Figure 4). Figure 4 shows XRD patterns of the materials obtained at different temperatures using a nominal element ratio Sn/Se=1.

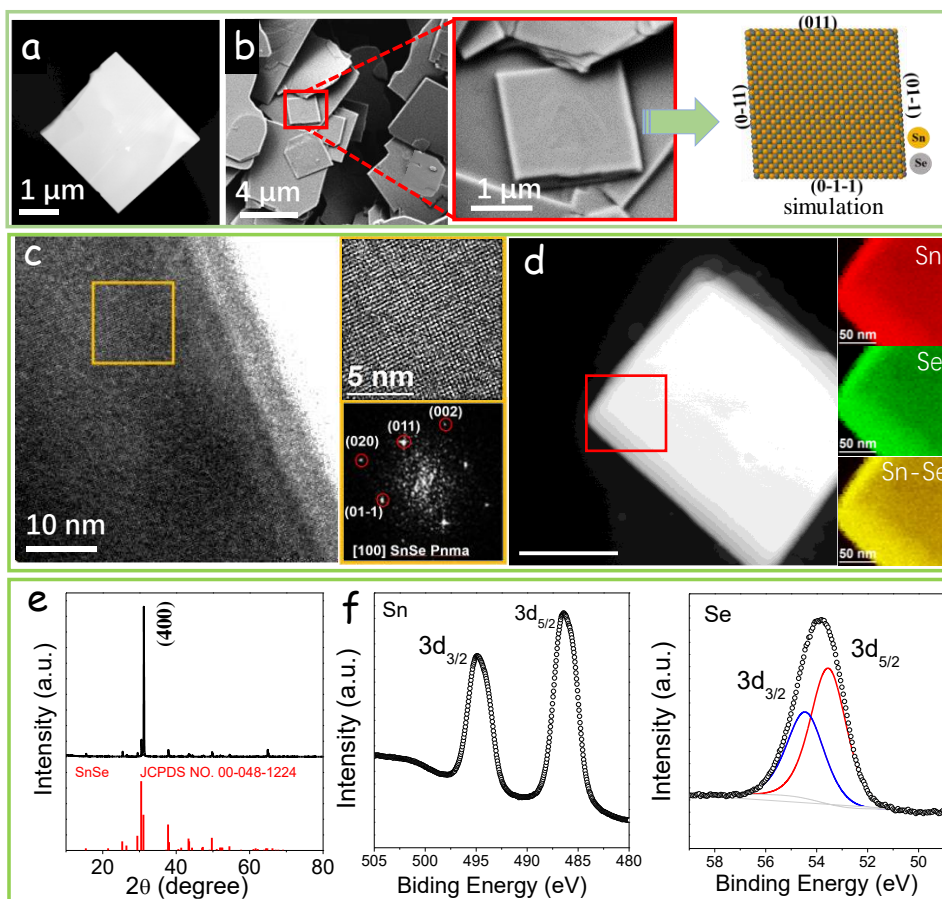


Figure 2. (a) Representative TEM and (b) SEM micrographs of square-like SnSe nanostructures, and a structure model of an individual NPL. (c) HRTEM micrograph of a SnSe NPL, magnified detail of the orange squared region and its corresponding power spectrum. The SnSe lattice fringe distances were measured to be 0.304, 0.207 nm and 0.302 nm, at 43.53, and 87.51 °, which was interpreted as the orthorhombic SnSe phase, visualized along its [100] zone axis. (d) EELS chemical composition maps obtained from the red squared area of the STEM micrograph. Individual Sn M_{4,5}-edges at 485 eV (red) and Se L_{2,3}-edges at 1436 eV (green) as well as its composite. (e) XRD pattern of SnSe. (f) Sn 3d and Se 3d regions of the XPS spectrum of SnSe.

TOP coordinated with Se to yield TOPSe. Without TOP in the precursor solution, SnSe nanostructures could be also obtained, but the ink decomposition required reaction temperatures above 500 °C.⁵³ Additionally, the aspect ratio of the SnSe nanostructures produced in the absence of TOP was strongly reduced (Figure 5). When adding small amounts of TOP to the solution, the ink decomposition

temperature could be reduced down to 420 °C for $V_{TOP}/V_{OAm} > 0.13$, which is associated to the relatively high reactivity of the formed TOPSe.⁵² On the other hand, when replacing OAm by octadecene, SnSe was not formed, probing the important role of OAm in reducing SeO_2 and complexating with Sn^{2+} .

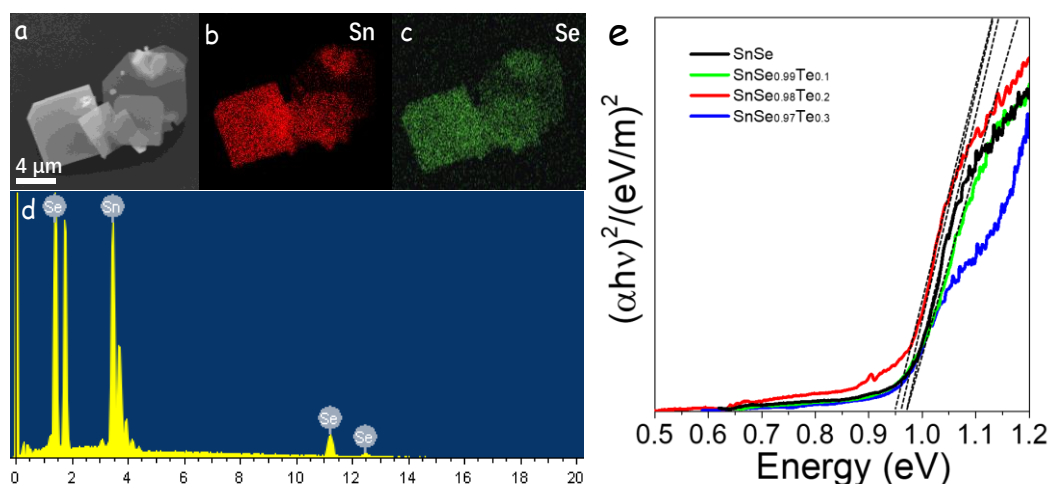


Figure 3. (a-c) SEM micrograph and EDX elemental maps of SnSe plates. (d) SEM-EDX spectrum of SnSe plates. (e) Kubelka-Munk plots and bandgap energy estimation from the UV-vis spectra of SnSe and $SnSe_{1-x}Te_x$ nanomaterials.

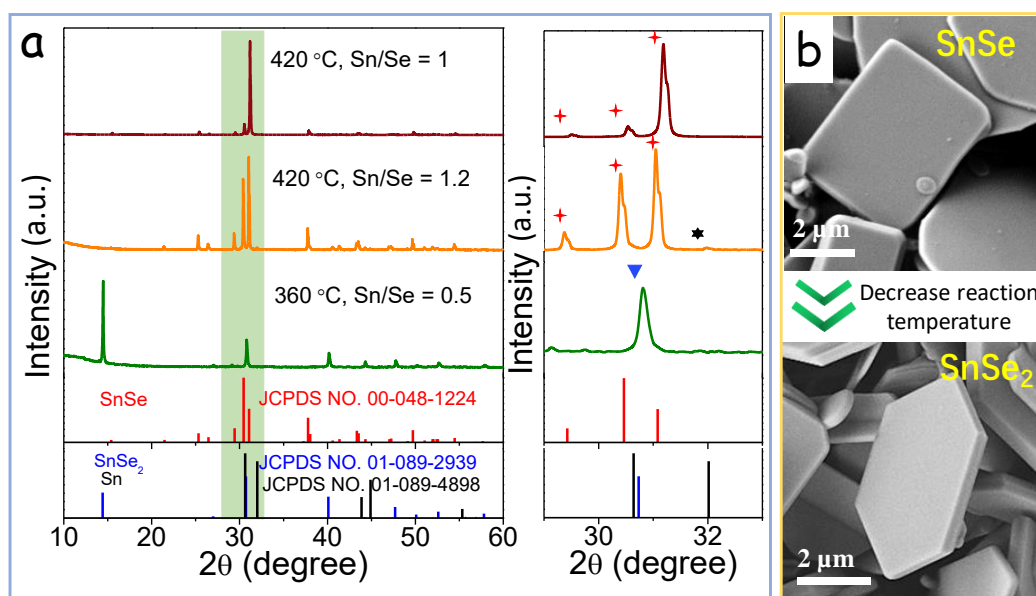


Figure 4. (a) XRD pattern of the powder produced from the decomposition at different temperatures of an ink containing different ratios of Sn/Se. A detail of the XRD pattern around $2\theta=31^\circ$ is displayed for clarity. (b) SEM micrographs of SnSe plates with orthorhombic structure and $SnSe_2$ plates with hexagonal phase

obtained when decomposing an ink containing Sn/Se=1 at 420 °C and an ink containing Sn/Se=0.5 at 360 °C, respectively.

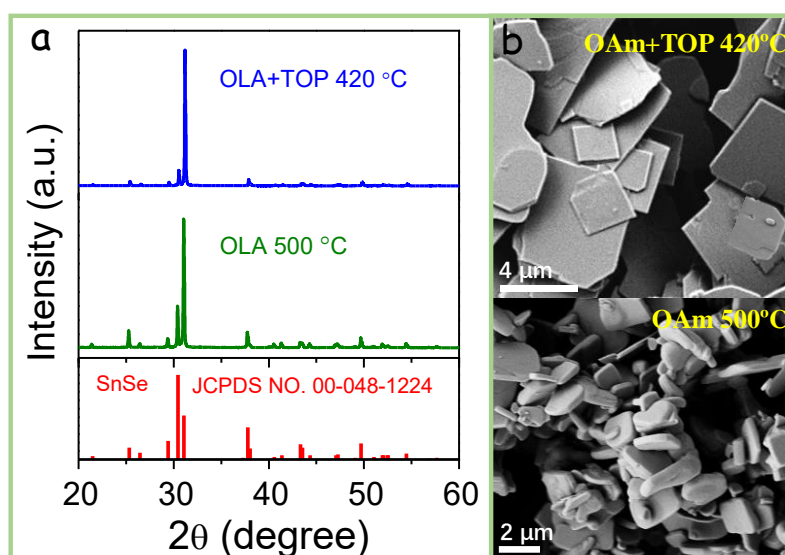


Figure 5. XRD patterns (a) and SEM micrographs (b) of SnSe powders produced from the decomposition at 500 °C of an ink containing OAm and at 420 °C of an ink containing OAm and TOP, $V_{TOP}/V_{OAm}=0.13$.

When adding OAc to the precursor ink, a significant change of the geometry of the produced SnSe particles was observed. Figure 3 shows the evolution of the particle shape with the OAc/OAm ratio. At relatively high OAc concentrations, $OAc/OAm > 0.2$, dendritic structures were produced, which I associate with a selective binding of the carboxylic group in OAc to particular facets during crystal growth.^{54, 55} Through AFM analysis, the thickness of plates and dendritic structures supported on a substrate was measured to be in the range 100-150 nm, which is slightly larger than values obtained from SEM statistics (Figure 6c).

The SnSe powder obtained from the ink decomposition was thermally annealed at 500 °C for 60 min inside a tube furnace with argon flow to remove residual organic ligands. The annealed crystals maintained the original plate geometry and showed no appreciable growth. The annealed powder was subsequently loaded into a graphite die and hot pressed at 500 °C for 5 minutes under a uniaxial pressure of 80 MPa. A cylindrical pellet with a relative density of ca. 95% was finally obtained (Figure 8a).

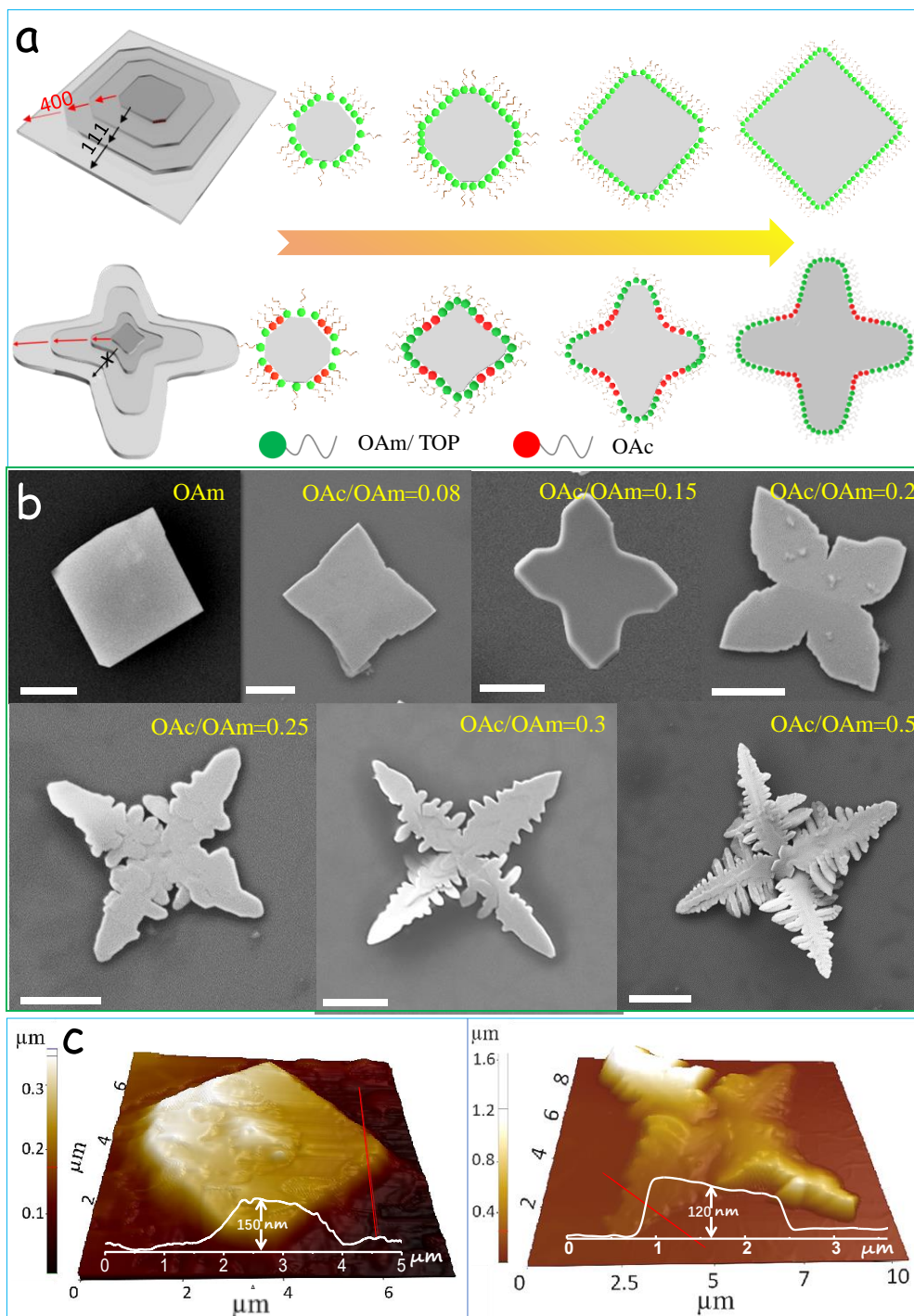


Figure 6. (a) Schematic illustration of the shape evolution for square-like and dendritic crystals. (b) SEM micrographs of the morphology evolution with increasing OAc/OAm ratios. Dendritic nanostructures were obtained when OAc/OAm > 0.2. Scale bars = 2 μm. (c) AFM topography images of a square-like and a dendritic nanostructure and height profiles taken from the displayed red line.

The hot pressed material displayed a clear crystallographic texture, with the SnSe [100] crystal direction oriented along the pressure axis, as shown by XRD analysis of the pellet hold with the diffraction plane coincident and normal to the pressure axis (Figure 8b). This crystallographic orientation is consistent with the [100] being the *softer* crystallographic direction in SnSe. SEM micrographs showed the pellet to have a layered structure, with layers of material assembling normal to the pressure axis, consistent with XRD results (Figure 8c).

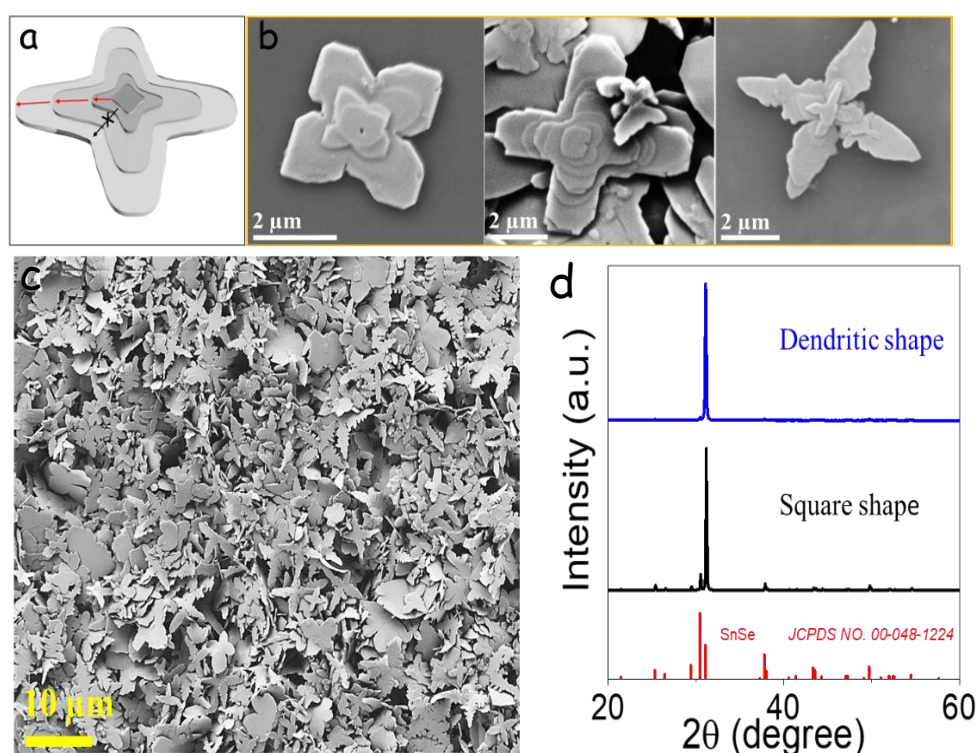


Figure 7. Schematic illustration of the growth (a) and SEM micrographs (b) of dendritic particles. (c) Representative SEM micrographs of dendritic SnSe nanomaterials. (d) PXR patterns of square (black) and dendritic (blue) SnSe NPLs.

To determine the influence of the shape of the SnSe particles on the crystallographic texture of the consolidated material, I hot pressed SnSe particles with 100 nm average size and 50 nm thickness produced by a reported method (Figure 9a).³¹ The hot press of these less asymmetric particles in the same conditions as the SnSe plates resulted in polycrystalline materials with no significant texture (Figure s

9b,c), proving the influence of the initial particle geometry in the texture of the

final polycrystalline material.^{15, 16}

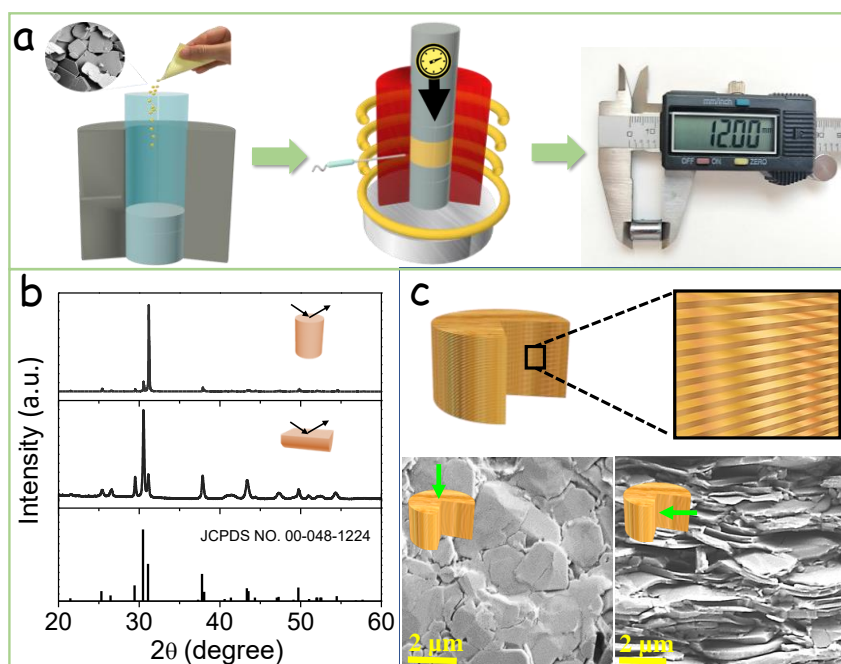


Figure 8. (a) Schematic illustration of the process of consolidation of the SnSe powder into a cylindrical pellet. A SEM micrograph of the annealed SnSe nanopowder and an actual image of consolidated pellet are included in the scheme. (b) XRD pattern of the SnSe pellet laid along the in-plane and cross-plane directions. (c) Representative top view and cross section SEM micrographs of a SnSe pellet.

To demonstrate the potential of the SnSe molecular ink to produce printed SnSe layers/patterns, the ink was printed on a flexible graphite foil using an ink jet nozzle. The graphite foil was then annealed on a hot plate at 420 °C for 5 min and additionally hot pressed at 500 °C for 3 min under 80 MPa pressure. SEM and XRD analyses of the printed layer demonstrated it to contain SnSe plates oriented parallel to the substrate (Figure 10).

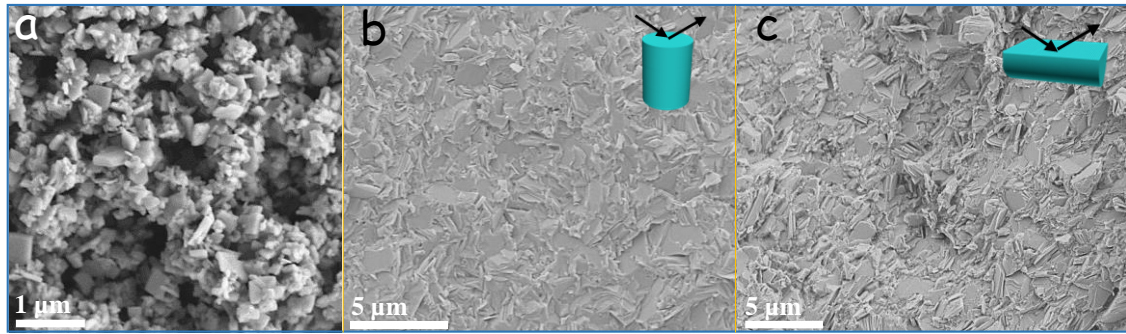


Figure 9. (a) SEM micrograph of SnSe particles produced from the reaction of SnCl₂ and NaHSe in water.^[1] (b-c) Cross section and top-view SEM micrographs of a pellet produced from these SnSe particles.

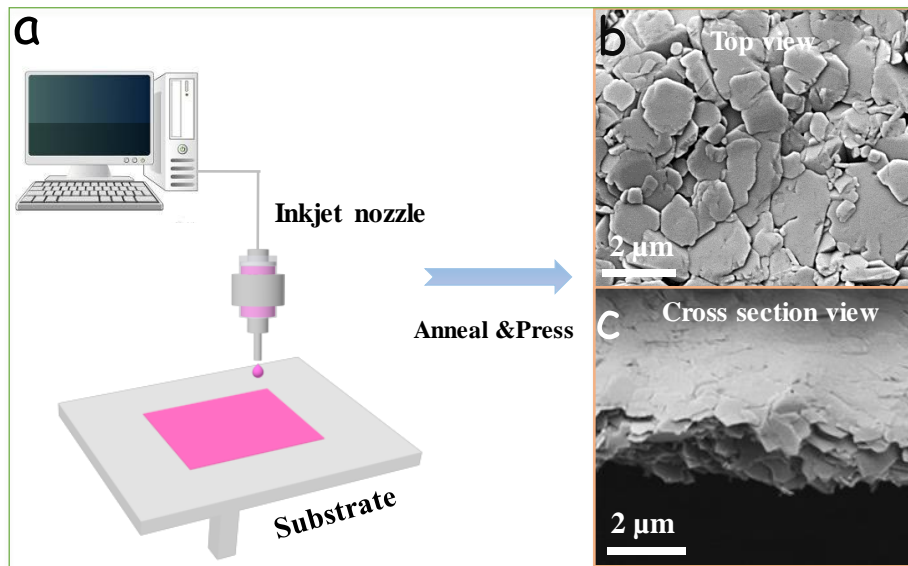


Figure 10. (a) Schematic of the printing of SnSe on a graphite foil. (b) top view and (c) cross section SEM micrographs of the printed SnSe layer.

The TE properties of the polycrystalline SnSe obtained from the ink decomposition were characterized in two directions (Figure 11): cross plane (\parallel), i.e. parallel to the pressure axis, and in plane (\perp), i.e. normal to pressure axis. Electrical conductivities measured in plane (σ_{\perp}), were higher than those measured cross plane (σ_{\parallel}), with $\sigma_{\perp}/\sigma_{\parallel} = 3.30$. This result is consistent with the much higher charge carrier mobilities in the bc crystal plane of SnSe when compared with its a direction.

Positive Seebeck coefficients were measured in all the temperature range,

consistent with the p-type semiconductor character of undoped SnSe. As expected from the minor dependence of this parameter on scattering, similar values of the Seebeck coefficient were measured in both directions, $S_{\perp} \approx S_{//}$. The slightly higher values systematically obtained cross plane could be ascribed to an energy filtering mechanism at grain boundaries, i.e. a preferential scattering of low energy carriers at the plate interfaces, as previously reported for layered materials.^{15, 16}

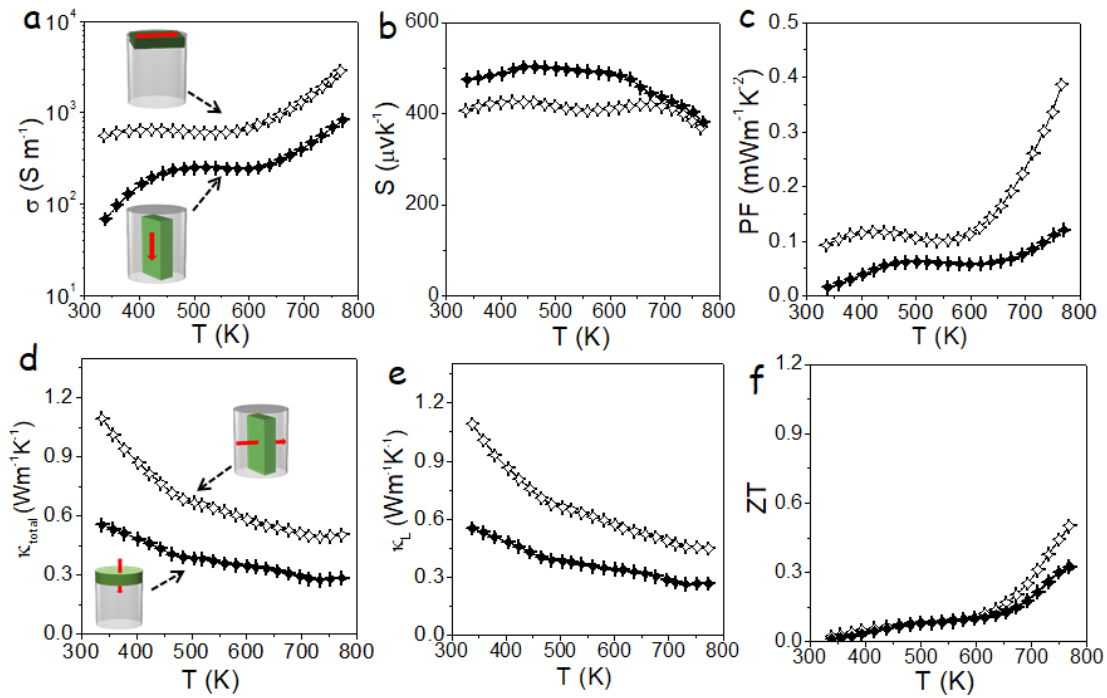


Figure 11. Temperature dependence of (a) electrical conductivity, σ ; (b) Seebeck coefficient, S ; (c) power factor, $S^2\sigma$, PF; (d) total thermal conductivity, κ_{total} ; (e) lattice thermal conductivity, κ_L ; and (f) TE figure of merit, ZT of a SnSe pellet measured in two directions, in-plane (\perp , open symbols) and cross-plane ($//$, solid symbols).

Table 1. Composition of SnSe and SnSe_{1-x}Te_x samples obtained from EDX analysis.

Nominal x x (at%)	0	1	2	3
Element				
Sn	48.96	46.81	45.67	49.75
Se	51.04	52.40	52,68	53.77
Te	0.00	0.79	1.65	2.54

Table 2. Composition of SnSe and SnSe_{1-x}Te_x samples obtained from ICP analysis.

Nominal x x (at%)	0	1	2	3
Element				
Sn	48.96	46.81	45.67	49.75
Se	51.04	52.40	52,68	53.77
Te	0.00	0.79	1.65	2.54

SnSe nanomaterials displayed very low thermal conductivities in both directions, but slightly higher than those obtained from single crystals, most probably due to a certain degree of oxidation.⁵⁶ Significantly lower thermal conductivities were obtained cross plane when compared with in plane, $\kappa_{\perp}/\kappa_{\parallel} = 1.75$ at 750 K, which was again consistent with the preferential orientation of the plates lying normal to the pressure axis.

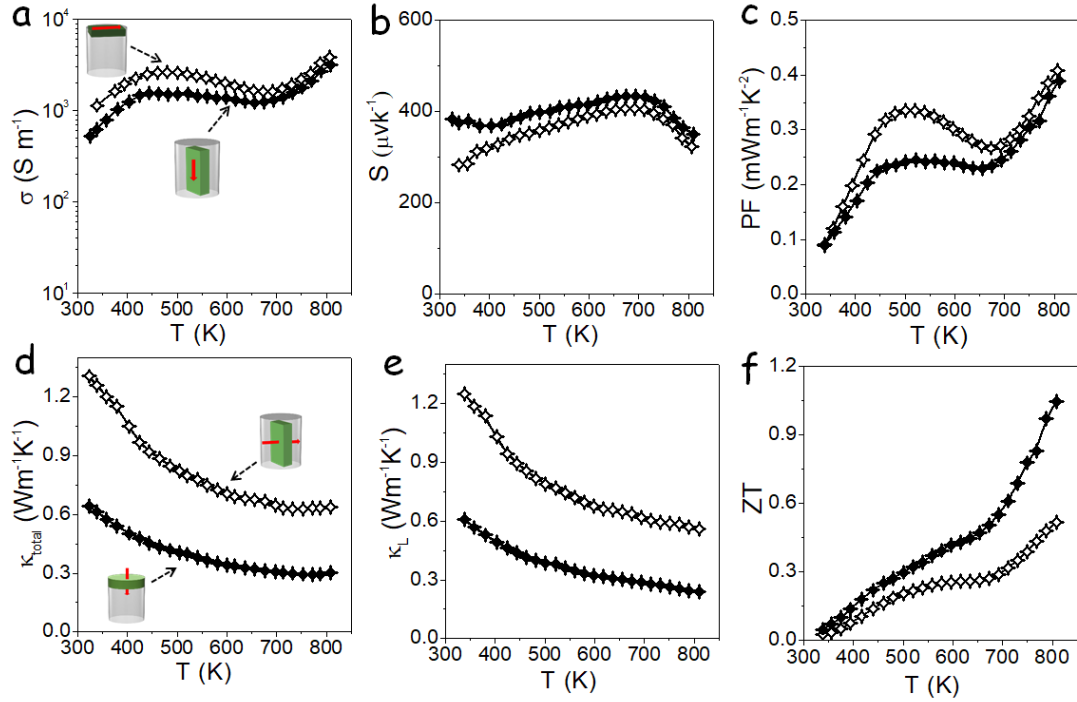


Figure 12. Temperature dependence of (a) electrical conductivity, σ ; (b) Seebeck coefficient, S ; (c) power factor, $S^2\sigma$, PF; (d) total thermal conductivity, κ_{total} ; (e) lattice thermal conductivity, κ_L ; and (f) TE figure of merit, ZT of a $\text{SnSe}_{0.98}\text{Te}_{0.02}$ pellet measured in two directions, in-plane (\perp , open symbols) and cross-plane (\parallel , solid symbols).

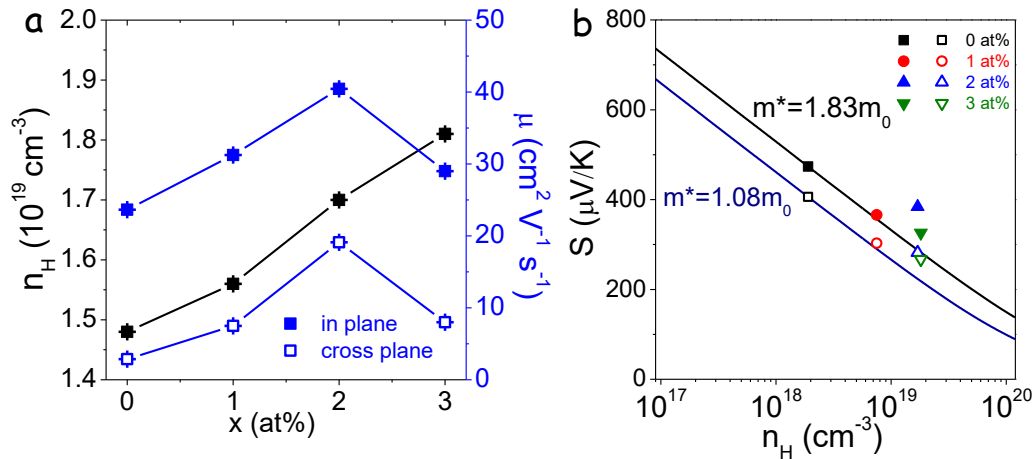


Figure 13. (a) Room temperature carrier carrier concentration and mobility of SnSe and $\text{SnSe}_{1-x}\text{Te}_x$ as a function of Te concentration. (b) Pisarenko plot showing experimental data and theoretical Seebeck coefficients calculated by single parabolic band (SPB) model as a function of carrier concentration and for

different Te concentrations, $\text{SnSe}_{1-x}\text{Te}_x$: 0.0 at% (black), 1 at% (red), 2 at% (blue), and 3 at% (green).

Overall, the highest ZT values, up to $\text{ZT} = 0.5$ at 807 K, were obtained in plane. This result is consistent with measurements on single crystals and previous reports,^{13, 23, 25, 57, 58} but it is unfortunate toward the development of printed SnSe-based modules that target the generation/harvesting of cross plane temperature gradient.

To further promote the TE performance of polycrystalline SnSe layers, small amounts of Te were added to the ink in replacement of equivalent amounts of Se. The polycrystalline material obtained from the decomposition of the Te-containing ink, $\text{SnSe}_{1-x}\text{Te}_x$, was characterized by a slightly reduced band gap (Figure 3), a slightly larger charge carrier concentration, n_H , and most important a significantly increased charge carrier mobility, particularly cross plane (Figure 13). Best TE performance was obtained from the material containing a 2 at% of Te, $\text{SnSe}_{0.98}\text{Te}_{0.2}$ (Figure 12). This material displayed significantly higher electric conductivities than SnSe without a major reduction of the Seebeck coefficient and a minor increase of the total thermal conductivity, associated with the increase of its electronic component. Overall, TE figures of merit up to three-fold larger than those measured for SnSe were obtained. Most important, the highest TE figures of merit were obtained cross plane, reaching $\text{ZT} = 1.03$ at 805 K, which is the highest value reported at this temperature and in this direction for polycrystalline SnSe. This excellent performance was related to the presence of Te facilitating charge transport especially cross plane, which translated into a significant increase of the charge carrier mobility.

3.5 Conclusions

I detailed a fast solution-based approach to produce crystallographic textured SnSe bulk nanomaterials and printed layers. The molecular precursor solution was prepared directly by dissolving ionic Sn and Se species in a thiol-free and nontoxic solvent. Pure phase SnSe powder was obtained by decomposing the molecular precursor at 420 °C. The composition, crystal phase and shape of the produced SnSe nanostructures could be tuned by modifying the nominal elemental ratio, the decomposition temperature and the use of additional surfactants. Crystallographic textured SnSe bulk nanomaterials and layers were obtained after hot-pressing the ink decomposition products. These materials showed moderate TE performances cross plane which was unfortunate for the design a TE devices that generate/harvest temperature gradients in the direction normal to the substrate. The SnSe TE performance was significantly improved, up to a threefold, by introducing small amounts of Te during ink formulation. The presence of this small amount of Te resulted in an important increase of electrical conductivity cross plane associated to an increase of charge carrier concentration and especially mobility with a minor variation of the Seebeck coefficient. The presence of 2 at% of Te in SnSe_{0.98}Te_{0.02} finally translated into record cross plane ZT values at 800 K for polycrystalline SnSe.

3.6 Reference

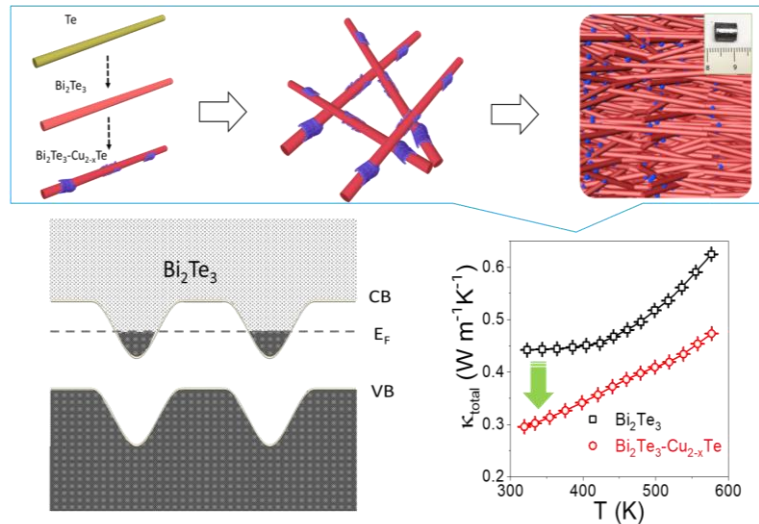
1. Bell, L. E., *Science* **2008**, 321(5895), 1457-1461.
2. Sootsman, J. R.; Chung, D. Y.; Kanatzidis, M. G., *Angew. Chem. Int. Ed.* **2009**, 48(46), 8616-8639.
3. Snyder, G.; Toberer, E., *Nat. Mater.* 2008, 7, 105-114.
4. Minnich, A.; Dresselhaus, M.; Ren, Z.; Chen, G., *Energy Environ. Sci.* **2009**, 2(5), 466-479.
5. Leonov, V.; Torfs, T.; Fiorini, P.; Van Hoof, C., *IEEE Sens. J.* **2007**, 7(5), 650-657.
6. Kraemer, D.; Poudel, B.; Feng, H.-P.; Caylor, J. C.; Yu, B.; Yan, X.; Ma, Y.; Wang, X.; Wang, D.; Muto, A., *Nat. Mater.* **2011**, 10(7), 532.
7. Ortega, S.; Ibáñez, M.; Liu, Y.; Zhang, Y.; Kovalenko, M. V.; Cadavid, D.; Cabot, A., *Chem. Soc. Rev.* **2017**, 46(12), 3510-3528.

8. Ibáñez, M.; Luo, Z.; Genc, A.; Piveteau, L.; Ortega, S.; Cadavid, D.; Dobrozhan, O.; Liu, Y.; Nachtegaal, M.; Zebarjadi, M.; Arbiol, J.; Kovalenko, M. V.; Cabot, A., *Nat. Commun.* **2016**, 7, 10766.
9. Snyder, G. J.; Ursell, T. S., *Phys. Rev. Lett.* **2003**, 91 (14), 148301.
10. Ibáñez, M.; Hasler, R.; Genç, A.; Liu, Y.; Kuster, B.; Schuster, M.; Dobrozhan, O.; Cadavid, D.; Arbiol, J.; Cabot, A., *J. Am. Chem. Soc.* **2019**, 141(20), 8025-8029.
11. Zhou, Y.; Zhao, L. D., *Adv. Mater.* **2017**, 29(45), 1702676.
12. Dresselhaus, M.; Dresselhaus, G.; Sun, X.; Zhang, Z.; Cronin, S.; Koga, T *Phys. Solid State* **1999**, 41(5), 679-682.
13. Zhao, L.-D.; Lo, S.-H.; Zhang, Y.; Sun, H.; Tan, G.; Uher, C.; Wolverton, C.; Dravid, V. P.; Kanatzidis, M. G., *Nature* **2014**, 508 (7496), 373.
14. Rhyee, J. S.; Ahn, K.; Lee, K. H.; Ji, H. S.; Shim, J. H., *Adv. Mater.* **2011**, 23(19), 2191-2194.
15. Liu, Y.; Zhang, Y.; Lim, K. H.; Ibáñez, M.; Ortega, S.; Li, M.; David, J.; Martí-Sánchez, S.; Ng, K. M.; Arbiol, J.; Kovalenko, M. V.; Cadavid, D.; Cabot, *ACS nano* **2018**, 12 (7), 7174-7184.
16. Liu, Y.; Zhang, Y.; Ortega, S.; Ibáñez, M.; Lim, K. H.; Grau-Carbonell, A.; Martí-Sánchez, S.; Ng, K. M.; Arbiol, J.; Kovalenko, M. V.; Cadavid, D.; Cabot, A. *Nano Lett.* **2018**, 18(4), 2557-2563.
17. Dun, C.; Liu, Y.; Al-Qawasmeh, A.; Hewitt, C. A.; Guo, Y.; Xu, J.; Jiang, Q.; Wang, J.; Marcus, G.; Cadavid, D.; Montgomery, D.; Wang, H.; Kovnir, K.; Cabot, A., Carroll, D. L., *2D Materials* **2018**, 5 (4), 045008.
18. Poudel, B.; Hao, Q.; Ma, Y.; Lan, Y.; Minnich, A.; Yu, B.; Yan, X.; Wang, D.; Muto, A.; Vashaee, D., *Science* **2008**, 320 (5876), 634-638.
19. Zhao, X. B.; Ji, X. H.; Zhang, Y. H.; Zhu, T. J.; Tu, J. P.; Zhang, X. B., Bismuth Telluride Nanotubes and the Effects on the *Appl. Phys. Lett.* **2005**, 86(6), 062111.
20. Yamashita, O.; Tomiyoshi, S.; Makita, K., *J. Appl. Phys.* **2003**, 93(1), 368-374.
21. Goldsmid, H. J., *Materials* **2014**, 7(4), 2577-2592.
22. Chang, C.; Wu, M.; He, D.; Pei, Y.; Wu, C.-F.; Wu, X.; Yu, H.; Zhu, F.; Wang, K.; Chen, Y.; Huang, L.; Li, J.-F.; He, J.; Zhao, L.-D., *Science* **2018**, 360(6390), 778-783.
23. Chen, C.-L.; Wang, H.; Chen, Y.-Y.; Day, T.; Snyder, G. J., *J. Mater. Chem. A* **2014**, 2(29), 11171-11176.
24. Sassi, S.; Candolfi, C.; Vaney, J.-B.; Ohorodniichuk, V.; Masschelein, P.; Dauscher, A.; Lenoir, B., *Appl. Phys. Lett.* **2014**, 104(21), 212105.
25. Wei, T.-R.; Tan, G.; Zhang, X.; Wu, C.-F.; Li, J.-F.; Dravid, V. P.; Snyder, G. J.; Kanatzidis, M. G., *J. Am. Chem. Soc.* **2016**, 138(28), 8875-8882.

26. Chere, E. K.; Zhang, Q.; Dahal, K.; Cao, F.; Mao, J.; Ren, Z., *J. Mater. Chem. A* **2016**, 4(5), 1848-1854.
27. Shi, X.; Wu, A.; Liu, W.; Moshwan, R.; Wang, Y.; Chen, Z.-G.; Zou, J., *ACS nano* **2018**, 12 (11), 11417-11425.
28. Chandra, S.; Banik, A.; Biswas, K., *ACS Energy Lett.* **2018**, 3(5), 1153-1158.
29. Wei, W.; Chang, C.; Yang, T.; Liu, J.; Tang, H.; Zhang, J.; Li, Y.; Xu, F.; Zhang, Z.; Li, J.-F., *J. Am. Chem. Soc.* **2017**, 140(1), 499-505.
30. Lee, Y. K.; Ahn, K.; Cha, J.; Zhou, C.; Kim, H. S.; Choi, G.; Chae, S. I.; Park, J.-H.; Cho, S.-P.; Park, S. H., *J. Am. Chem. Soc.* **2017**, 139(31), 10887-10896.
31. Han, G.; Popuri, S. R.; Greer, H. F.; Bos, J. W. G.; Zhou, W.; Knox, A. R.; Montecucco, A.; Siviter, J.; Man, E. A.; Macauley, M.; Paul, D. J.; Li, W. -G.; Paul, M. C.; Gao, M.; Sweet, T.; Freer, R.; Azough, F.; Baig, H.; Sellami, N.; Mallick, T.; K.; Gregory, D. H., *Angew. Chem. Int. Ed.* **2016**, 55(22), 6433-6437.
32. Ge, Z. H.; Qiu, Y.; Chen, Y. X.; Chong, X.; Feng, J.; Liu, Z. K.; He, J., *Adv. Funct. Mater.* **2019**, 1902893.
33. Luo, Y.; Cai, S.; Hua, X.; Chen, H.; Liang, Q.; Du, C.; Zheng, Y.; Shen, J.; Xu, J.; Wolverton, C., *High Adv. Energy Mater.* **2019**, 9(2), 1803072.
34. Shi, X.; Wu, A.; Feng, T.; Zheng, K.; Liu, W.; Sun, Q.; Hong, M.; Pantelides, S. T.; Chen, Z. G.; Zou, J., *Adv. Energy Mater.* **2019**, 9(11), 1803242.
35. Chandra, S.; Biswas, K., *J. Am. Chem. Soc.* **2009**, 141 (15), 6141-6145.
36. Saha, S.; Banik, A.; Biswas, K., *Chem.: Eur. J.* **2016**, 22 (44), 15634-15638.
37. Banik, A.; Roychowdhury, S.; Biswas, K., *Chem. Commun.* **2018**, 54 (50), 6573-6590.
38. Ashida, M.; Hamachiyo, T.; Hasezaki, K.; Matsunoshita, H.; Kai, M.; Horita, Z., *J. Phys. Chem. Solids* **2009**, 70(7), 1089-1092.
39. Rogl, G.; Setman, D.; Schafler, E.; Horky, J.; Kerber, M.; Zehetbauer, M.; Falmbigl, M.; Rogl, P.; Royanian, E.; Bauer, E. *Acta Mater.* **2012**, 60(5), 2146-2157.
40. Angerer, P.; Neubauer, E.; Yu, L.; Khor, K. A., *Int. J. Refract. Met. H.* **2007**, 25(4), 280-285.
41. Jiang, J.; Chen, L.; Bai, S.; Yao, Q.; Wang, Q., *Mater. Sci. Eng. B* **2005**, 117(3), 334-338.
42. Jiang, J.; Chen, L.; Bai, S.; Yao, Q.; Wang, Q., *Scr. Mater.* **2005**, 52(5), 347-351.
43. Li, M.; Liu, Y.; Zhang, Y.; Zuo, Y.; Li, J.; Lim, K. H.; Cadavid, D.; Ng, K. M.; Cabot, A., *Dalton Trans.* **2019**, 48(11), 3641-3647.
44. Zhang, J.; Xu, J.; Tan, X.; Wang, H.; Liu, G.-Q.; Shao, H.; Yu, B.; Yue, S.; Jiang, J. *J. Mater. Chem. C* **2019**, 7(9), 2653-2658.

45. Buckley, J. J.; McCarthy, C. L.; Del Pilar-Albaladejo, J.; Rasul, G.; Brutchey, R. L., *Inorg. Chem.* **2016**, 55(6), 3175-3180.
46. Antunez, P.; Torelli, D.; Yang, F.; Rabuffetti, F.; Lewis, N.; Brutchey, R. L. *Chem. Mater.* **2014**, 26 (19), 5444-5446.
47. Heo, S.; Jo, S.; Kim, H.; Choi, G.; Song, J.; Kang, J.; Jung, J. *Nat. Commun.* **2019**, 10 (1), 1-10.
48. Burton, M. R.; Mehraban, S.; Beynon, D.; McGettrick, J.; Watson, T.; Lavery, N. P.; Carnie, M. J. *Adv. Energy Mater.* **2019**, 9(26), 1900201.
49. Yarema, M.; Caputo, R.; Kovalenko, M. V., *Nanoscale* **2013**, 5 (18), 8398-8410.
50. Kravchyk, K.; Protesescu, L.; Bodnarchuk, M. I.; Krumeich, F.; Yarema, M.; Walter, M.; Guntlin, C.; Kovalenko, M. V., *J. Am. Chem. Soc.* **2013**, 135(11), 4199-4202.
51. Mourdikoudis, S.; Liz-Marzan, L. M., *Chem. Mater.* **2013**, 25 (9), 1465-1476.
52. Evans, C. M.; Evans, M. E.; Krauss, T. D., *J. Am. Chem. Soc.* **2010**, 132(32), 10973-10975.
53. Zhang, Y.; Liu, Y.; Lim, K. H.; Xing, C.; Li, M.; Zhang, T.; Tang, P.; Arbiol, J.; Llorca, J.; Ng, K. M.; Ibáñez, M.; Guardia, P.; Prato, M.; Cadavid, D.; Cabot, A., *Angew. Chem. Int. Ed.* **2018**, 130(52), 17309-17314.
54. Berestok, T.; Guardia, P.; Blanco, J.; Nafria, R.; Torruella, P.; Lopez-Conesa, L.; Estrade, S.; Ibáñez, M.; De Roo, J.; Luo, Z.; Cadavid, D.; Martins, J. C.; Kovalenko, M. V.; Peiró, F.; Cabot, A., *Chem. Mater.* **2017**, 29(10), 4418-4424.
55. Watt, J.; Cheong, S.; Toney, M. F.; Ingham, B.; Cookson, J.; Bishop, P. T.; Tilley, R. D., *ACS nano* **2009**, 4 (1), 396-402.
56. Lee, Y. K.; Luo, Z.; Cho, S. P.; Kanatzidis, M. G.; Chung, I., *Joule* **2019**, 3(3), 719-731.
57. Shi, X.; Zheng, K.; Hong, M.; Liu, W.; Moshwan, R.; Wang, Y.; Qu, X.; Chen, Z.-G.; Zou, J., *Chem. Sci.* **2018**, 9(37), 7376-7389.
58. Ge, Z.-H.; Song, D.; Chong, X.; Zheng, F.; Jin, L.; Qian, X.; Zheng, L.; *J. Am. Chem. Soc.* **2017**, 139(28), 9714-9720.
59. Hung, L.; Tsung, C.; Huang, W.; *Adv. Mater.* **2010**, 22 (17): 1910-1914.
60. Kravchyk, K.; Protesescu, L.; Bodnarchuk, M.; *J. Am. Chem. Soc.* **2013**, 135 (11): 4199-4202.
61. Li, L.; Hu, F.; Xu, D.; *Chem. Comm.* **2012**, 48 (39): 4728-4730.

Chapter 4 Bismuth telluride-copper telluride nanocomposites from heterostructured building blocks



4.1 Abstract

Properly designed NCs allow improving TE performance by several mechanisms, including phonon scattering, modulation doping and energy filtering, while additionally promoting mechanical properties over those of crystalline materials. Here, a strategy to produce Bi₂Te₃-Cu_{2-x}Te NCs based on the consolidation of heterostructured NPs is described and the thermoelectric properties of the obtained materials are investigated. I first detail a two-step solution-based process to produce Bi₂Te₃-Cu_{2-x}Te heteronanostructures, based on the growth of Cu_{2-x}Te nanocrystals on the surface of Bi₂Te₃ nanowires. I characterize the structural and chemical properties of the synthesized nanostructures and of the NCs produced by hot-pressing the particles at moderate temperatures. Besides, the transport properties of the NCs are investigated as a function of the amount of Cu introduced. Overall, the presence of Cu decreases the material thermal conductivity through promoting phonon scattering, modulates the charge carrier concentration through electron spillover, and increases the Seebeck coefficient through filtering of charge carriers at energy barriers. These effects result in an improvement of over 50% of the thermoelectric figure of merit of Bi₂Te₃.

4.2 Introduction

Solid state TE devices, allowing the direct and reversible conversion between heat and electricity, provide numerous advantages over competing technologies for thermal energy harvesting and precise temperature control. Advantages include silent operation, high durability, low weight, no fluids or moving parts and flexible design with great adaptability. Because of their versatility, TE devices can be used in a multitude of applications in the fields of waste heat recovery, refrigeration, energy harvesting for autonomous remote sensing, air conditioning and so on. However, their moderate efficiency and high cost currently limits the spread of this technology in its potential markets.^{1, 2}

The conversion efficiency of TE devices is in large part determined by a material dimensionless figure of merit: $ZT = \sigma S^2 T / \kappa$.³⁻⁵ To produce an efficient TE material one needs to maximize the power factor by optimizing the charge carrier concentration and introducing mechanisms to increase the Seebeck coefficient. Simultaneously, the thermal conductivity needs to be minimized through phonon scattering at different scales. Since all these material parameters are strongly interrelated, to maximize the energy conversion efficiency of TE materials is challenging.⁶⁻⁹

The combination of multiple phases offers additional degrees of freedom to design materials with optimized functional properties.¹⁰ NCs are particularly appealing in the TE field¹¹⁻¹⁴ as they provide not only effective phonon scattering at interphases that dramatically reduce thermal conductivity,¹⁵⁻²¹ but also potential quantum effects and selective charge carrier scattering to increase Seebeck coefficient.²²⁻²⁶ Additionally, properly designed composites allow activating the required large amounts of charge carriers without dramatically decreasing their mobility by means of modulation doping.²⁶⁻³³

The properties of composite materials not only depend on the type and amount of each of the different phases, but also on their distribution, which is extremely difficult to control. Beyond the use of thin film vacuum-based techniques that

are limited in terms of cost, production volume, three dimensional control of the phase distribution and material thickness, the most effective strategy for the large and cost-effective production of nanocomposites with proper phase control is the assembly of heterostructured building blocks.^{10, 34, 35}

Bi_2Te_3 -based alloys provide the highest TE performance at temperatures around ambient and thus most TE commercial devices are produced from highly crystalline ingots of these materials. However, the current performance of Bi_2Te_3 -based alloys is still far from optimum. Besides, owing to their layered structure, these materials are mechanically fragile, which calls for alternative processing strategies able to deliver polycrystalline materials.

When synthesized in an excess of Te, Bi_2Te_3 is generally a degenerated n-type semiconductor because it retains abundant Te_{Bi} antisites due to similar electronegativity and ionic radius of Bi and Te.³⁶ The excessive charge carrier concentration of Bi_2Te_3 deteriorates the Seebeck coefficient and results in low power factors. To adjust this parameter, and at the same time decrease the lattice thermal conductivity, part of the Te within Bi_2Te_3 is generally replaced by Se to produce n-type $\text{Bi}_2\text{Te}_{3-x}\text{Se}_x$.³⁷

To further increase the power factor and decrease thermal conductivity, different elements have been incorporated to Bi_2Te_3 -based alloys.³⁸ Among them, Cu has provided some of the best results.^{30,33-40} The presence of Cu has usually associated an enhanced phonon scattering yielding lower thermal conductivities. Besides, the electronic properties of Bi_2Te_3 are influenced by the presence of Cu in a rather complex way, depending on the Cu amount, location and chemical environment and on the Bi_2Te_3 conductivity type.^{30,39-46} The incorporation of very low amounts of Cu has been reported to reduce the charge carrier concentration presumably due to the reduction of tellurium vacancies.⁴⁶ On the other hand, low concentrations of Cu^+ intercalated at the van der Waals gap between Bi_2Te_3 layers act as a donor.^{43, 45} Besides, Cu^+ ions substituting Bi, $\text{Cu}_{\text{Bi}}^{2-}$, act as acceptors.^{30, 45} The presence of Cu during the material sintering also affects the size of the Bi_2Te_3 crystal domains. Additionally, amounts of Cu above

the solubility limit may result in the segregation of Cu_{2-x}Te , thus removing Te_{Bi} antisites and/or introducing Te vacancies, $\text{V}_{\text{Te}}^{2+}$, both acting as donors.^{30, 45, 46} The Cu presence has been also associated with an enhancement of reproducibility from batch to batch, related to a reduction of the fluctuation of charge concentration owing to the hindered formation of tellurium vacancies.^{30, 46}

Here we report on a strategy to produce $\text{Bi}_2\text{Te}_3\text{-Cu}_{2-x}\text{Te}$ nanocomposites based on the consolidation of $\text{Bi}_2\text{Te}_3\text{-Cu}_{2-x}\text{Te}$ heterostructured nanoparticles. This strategy allows to separate the contribution of Cu ions within the Bi_2Te_3 lattice from that of Cu_{2-x}Te phases. We analyze the TE properties of the produced composites and discuss them in terms of the heterojunctions formed between Cu_{2-x}Te and Bi_2Te_3 nanodomains.

4.3 Experimental section

Chemicals: Bismuth(III) chloride (BiCl_3 , $\geq 98\%$), potassium hydroxide (KOH, $\geq 98\%$), polyvinylpyrrolidone (PVP, $(\text{C}_6\text{H}_9\text{NO})_n$, average molar weight $\sim 55,000$), tellurium dioxide (TeO_2 , $\geq 99\%$), copper(I) chloride (CuCl , $\geq 99.995\%$) and hydrazine monohydrate ($\text{NH}_2\text{NH}_2\cdot\text{H}_2\text{O}$, 64~65%) were purchased from Sigma Aldrich. Ethylene glycol (EG, $\text{HOCH}_2\text{CH}_2\text{OH}$, 99%) was purchased from Fisher. Analytical grade acetone, isopropanol and ethanol were obtained from various sources. All chemicals were used as received without further purification.

Bi_2Te_3 nanowires synthesis: Bi_2Te_3 nanowires were prepared following a previously reported approach based on the reaction of Bi precursor with pre-synthesized Te nanowires.⁴⁷ In a typical synthesis, 5.6 mmol of TeO_2 , 37 mmol of KOH, 1.5 g of PVP, and 56 mL of EG were added into a 250 mL three-neck flask. The mixture was stirred and heated to 140 °C. At this temperature after all the chemicals were dissolved, 0.87 mL of a 64-65% $\text{N}_2\text{H}_4\cdot\text{H}_2\text{O}$ solution was injected into the solution. The reaction mixture was maintained at 140 °C for 1 h to allow all Te to be reduced. Then, the temperature of the solution was raised

to 160 °C. At this point, a hot BiCl₃/EG solution was injected into the flask. This BiCl₃/EG solution was produced by adding 3.6 mmol of BiCl₃ into 15 mL of EG in a glass vial that was heated to 100–120 °C. The BiCl₃/EG solution was allowed to react with the Te nanowires for 1 h at 160 °C. Afterward, the mixture was naturally cooled to room temperature. The product was purified firstly by adding acetone to the solution and centrifuging it. In a second step, ethanol was used to redisperse the particles and acetone ($V_{\text{ethanol}}/V_{\text{acetone}}=1:2$) to precipitate them again. In a third step, deionized water was added to solubilize remaining impurities and NPs were precipitated by slow centrifugation. This procedure was repeated twice. In a last step, particles were once more redispersed with ethanol, precipitated with acetone, and dried under vacuum at room temperature.

Bi₂Te₃–Cu_{2-x}Te heterostructures: Bismuth telluride-copper telluride heterostructures were produced by adding copper precursor to the solution containing Bi₂Te₃ nanowires. Briefly, to produce Bi₂Te₃–Cu_{2-x}Te with a ratio of Bi:Cu =8, after 1h of reaction at 160 °C to form the Bi₂Te₃ nanowires, 0.4 mmol CuCl was added into 5 mL of EG in a glass vial to form a clear solution which was kept at 100~120°C. After 1 h, 1.86 mL of 50-60% N₂H₄·H₂O was first added into the reaction and then the CuCl/EG solution was injected into the reaction, which continued for another 1 h before naturally cooling down to room temperature. Bi:Cu =5 and 10 samples were produced following the above procedure, but using proper amounts of copper precursor. Finally, the obtained material was purified following the same procedure as for Bi₂Te₃ nanowires.

Nanomaterial consolidation: Dried Bi₂Te₃ and Bi₂Te₃-Cu_{2-x}Te particles were annealed at 330 °C for 60 min under Ar flow inside a tube furnace. Annealing at 450 °C was also tested as noted below. The annealed powders, were loaded into a graphite die and compacted into cylinders (Ø 8 mm×10 mm) using a custom-made hot press held at 270 °C and 60 MPa for 5 min. This process was carried out inside an Ar-filled glove box. The relative densities of the compacted pellets were measured by the Archimedes' method. From these cylinders, rectangular bars of about 8 × 6 × 1 mm³ were cut in two normal directions, along the pressing

direction and within the cylinder plane.

Structural and chemical characterization: X-ray diffraction (XRD, 2θ angle: 20° to 80° ; scanning rate: $5^\circ/\text{min}$) analyses were carried out on a Bruker AXS D8 ADVANCE X-ray diffractometer with Cu–K α radiation ($\lambda = 1.5406 \text{ \AA}$). Size and morphology of initial materials were examined by transmission electron microscopy using a ZEISS LIBRA 120, operating at 120 kV, and field-emission SEM on an Auriga Zeiss operated at 5.0 kV. Crystallographic structure and chemical composition were analyzed by HRTEM and EELS, respectively, using a Tecnai F20 field-emission gun microscope at 200 keV with an embedded Gatan QUANTUM image filter. The material composition was analyzed using an Oxford energy EDX attached to a Zeiss Auriga SEM at 20.0 kV.

TE property measurement: Seebeck coefficients were measured using a static DC method. Electrical resistivity data was obtained by a standard four-probe method. Both the Seebeck coefficient and the electrical resistivity were measured simultaneously in a LSR-3 LINSEIS system in the temperature range between room temperature and 573 K, under helium atmosphere. Taking into account the system accuracy and the measurement precision, an error of *ca.* 4 % in the measurement of the electrical conductivity and Seebeck coefficient was estimated. The thermal conductivity was calculated by $\kappa = \lambda C_p \rho$. The constant pressure heat capacity (C_p) was estimated from empirical formulas by the Dulong–Petit limit (3R law), and the density (ρ) values used here were calculated using the Archimedes' method. To avoid cluttering the plots, error bars were not included in the figures. Hall charge carrier concentrations (n_H) and mobilities (μ_H) at room temperature (300 K) were obtained from the Van der Pauw method using a magnetic field of 1 T (ezHEMS, NanoMagnetics). Values provided correspond to the average of 5 measurements, from which an error of *ca.* 10% was estimated.

4.4 Results and discussion

Polycrystalline Bi₂Te₃ nanowires were synthesized in a two-step approach using Te nanowires as reactive template.²² Te nanowires were produced by reducing

TeO₂ in EG at 140 °C. Afterwards, a BiCl₃/EG solution was injected to react with Te (see experimental section). The as-synthesized Bi₂Te₃ kept the Te nanowire geometry, with a relatively narrow distribution of diameters (30 ± 10 nm) and lengths (600 ± 80 nm). XRD characterization showed the samples to be highly crystalline and to present a single phase: Bi₂Te₃ (JCPDS 01-082-0358, Figure 1b). No elemental Te was detected in the final product. HRTEM micrographs confirmed the Bi₂Te₃ nanowires to display the Bi₂Te₃ rhombohedral phase (space group = R3-MH) with a=b= 4.2999 Å and c= 30.5975 Å (Figure 1f). EELS elemental composition maps revealed the nanowires to be uniformly composed of Bi and Te (Figure 1e).

Bi₂Te₃-Cu_{2-x}Te heterostructures with tuned molar ratio (Bi:Cu= 10; 8; 5) were synthesized by injecting a CuCl/EG solution into the flask containing Bi₂Te₃ nanowires at 160 °C (see experimental section). This synthesis protocol was carried out at a sufficient scale to produce 4 g of material per batch. Figure 1b displays the XRD pattern of the material produced with a nominal composition Bi:Cu=8. Only the XRD peaks of the Bi₂Te₃ phase were detected. After Cu incorporation, the particles preserved the nanowire geometry (Figure 1g).

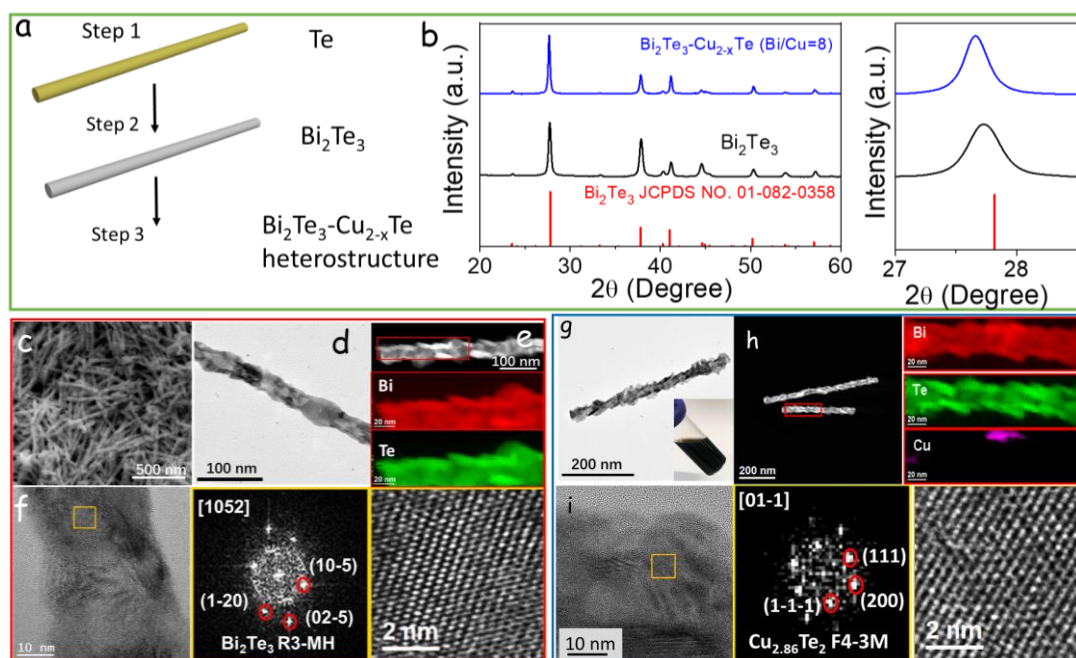


Figure 1. (a) Schematic illustration of the formation of Bi₂Te₃-Cu_{2-x}Te heterostructures. (b) Powder XRD pattern of as-synthesized Bi₂Te₃ and Bi₂Te₃-

Cu_{2-x}Te nanomaterials. (c) SEM micrograph of Bi₂Te₃ nanowires. (d) Representative TEM micrograph of a Bi₂Te₃ nanowire. (e) STEM micrograph and EELS chemical composition maps obtained from the red squared area. Individual Bi N_{6,7}-edge at 157 eV (red), Te M_{4,5}-edge at 572 eV (green). (f) HRTEM micrograph of a Bi₂Te₃ nanowire, detail of the orange squared region and its corresponding power spectrum. Lattice fringe distances were 0.314 nm, 0.177 nm and 0.216 nm, at 56.18° and 90.07° which was interpreted as the rhombohedral Bi₂Te₃ phase, visualized along its [1052] zone axis. (g) Representative TEM micrograph of a Bi₂Te₃-Cu_{2-x}Te heterostructure. The insert shows a vial containing a Bi₂Te₃-Cu_{2-x}Te solution. (h) EELS chemical composition maps obtained from the red squared area in the STEM micrograph. Individual Bi N_{6,7}-edge at 157 eV (red), Te M_{4,5}-edge at 572 eV (green), Cu L_{2,3}-edges at 931 eV (pink). (i) HRTEM micrograph of a Bi₂Te₃-Cu_{2-x}Te heterostructure, detail of the orange squared region and its corresponding power spectrum. Lattice fringe distances were 0.341 nm, 0.305 nm and 0.340 nm, at 51.65° and 106.01° which was interpreted as the cubic Cu_{2.86}Te₂ phase visualized along its [01-1] zone axis.

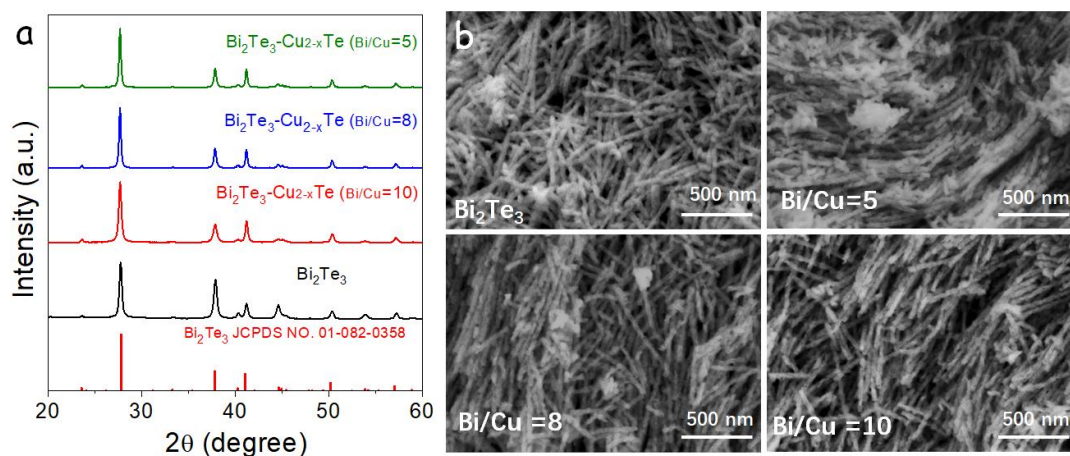


Figure 2. (a) XRD patterns of Bi₂Te₃-Cu_{2-x}Te nanowires. (b) Representative SEM micrographs of Bi₂Te₃-Cu_{2-x}Te nanowires, Bi₂Te₃. Bi₂Te₃-Cu_{2-x}Te (Bi:Cu=5), Bi₂Te₃-Cu_{2-x}Te (Bi:Cu=8) and Bi₂Te₃-Cu_{2-x}Te (Bi:Cu=10), as indicated in each image.

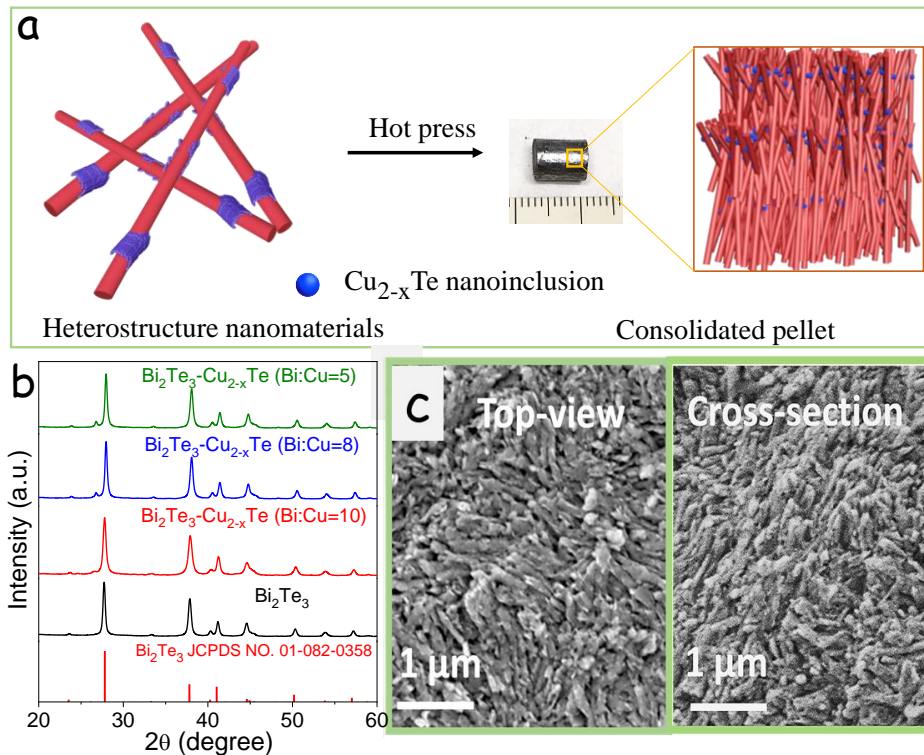


Figure 3. (a) Scheme of the process to produce a $\text{Bi}_2\text{Te}_3\text{-Cu}_x\text{Te}$ pellet from $\text{Bi}_2\text{Te}_3\text{-Cu}_x\text{Te}$ nanowires. (b) XRD patterns of consolidated $\text{Bi}_2\text{Te}_3\text{-Cu}_x\text{Te}$ pellets with different compositions. (c) Top-view and cross-section SEM micrographs of a consolidated $\text{Bi}_2\text{Te}_3\text{-Cu}_{2-x}\text{Te}$ pellet.

HRTEM and power spectrum analysis revealed the presence of small $\text{Cu}_{2.86}\text{Te}_2$ crystallites (space group = $F4\text{-}3\text{M}$; $a=b=c= 6.0320\ \text{\AA}$) on the surface of Bi_2Te_3 nanowires (Figure 1i). EELS analysis also displayed the presence of Cu and Te on such crystallites, further confirming the formation of $\text{Bi}_2\text{Te}_3\text{-Cu}_{2-x}\text{Te}$ heterostructures (Figure 1h).

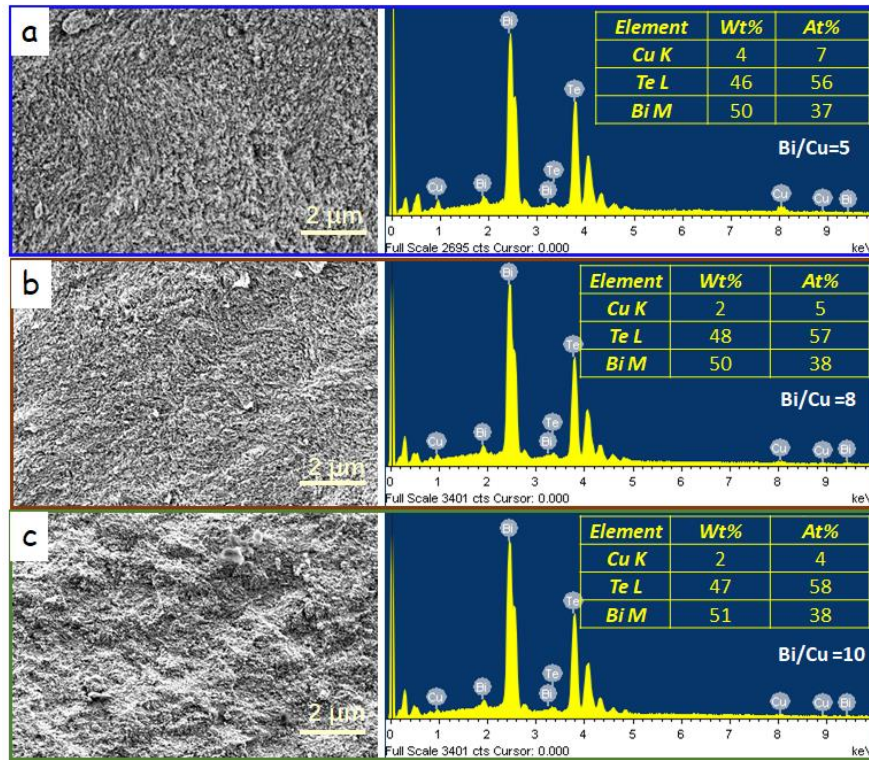


Figure 4. SEM image, EDX pattern and composition of $\text{Bi}_2\text{Te}_3\text{-Cu}_{2-x}\text{Te}$ pellets. (a) $\text{Bi}_2\text{Te}_3\text{-Cu}_{2-x}\text{Te}$ (Bi:Cu=5), (b) $\text{Bi}_2\text{Te}_3\text{-Cu}_{2-x}\text{Te}$ (Bi:Cu=8) and (c) $\text{Bi}_2\text{Te}_3\text{-Cu}_{2-x}\text{Te}$ (Bi:Cu=10), respectively.

$\text{Bi}_2\text{Te}_3\text{-Cu}_{2-x}\text{Te}$ nanowires were purified, dried, annealed and finally used as building blocks to produce cylindrical pellets with 10 mm in thickness and 8 mm in diameter. The consolidated nanomaterials had relative densities around 86-87% (Figure 3a, Table 1).

XRD patterns of $\text{Bi}_2\text{Te}_3\text{-Cu}_{2-x}\text{Te}$ pellets showed the Bi_2Te_3 phase to be predominant, but the small peak at $2\theta = 26.7^\circ$ showed the presence of a small fraction of a Cu_{2-x}Te phase that I tentatively associate with tetragonal $\text{Cu}_{2.8}\text{Te}_2$ (JCPDS 01-085-0606, Figure 3b). The crystallographic transition from a cubic to a tetragonal Cu_{2-x}Te phase during annealing and hot press is consistent with previous reports and with the complex Cu-Te phase diagram.^{48, 49} SEM characterization of the pellets showed them to maintain a filamentous structure denoting a minor sintering of the nanowires (Figure 3c). EDX elemental maps of the pellets displayed a homogeneous distribution of the three elements at a 100 μm scale (Figure 4). Quantitatively, the Cu/Bi/Te atomic ratio of the

Bi:Cu=8 sample was 1/7.9/11.9, and the Te/(Bi+Cu) ratio was 1.34, very close to the nominal value ($3/2.25 = 1.33$). Te/(Bi+Cu) compositions close to the nominal were also obtained for the other samples (Figure 4)..

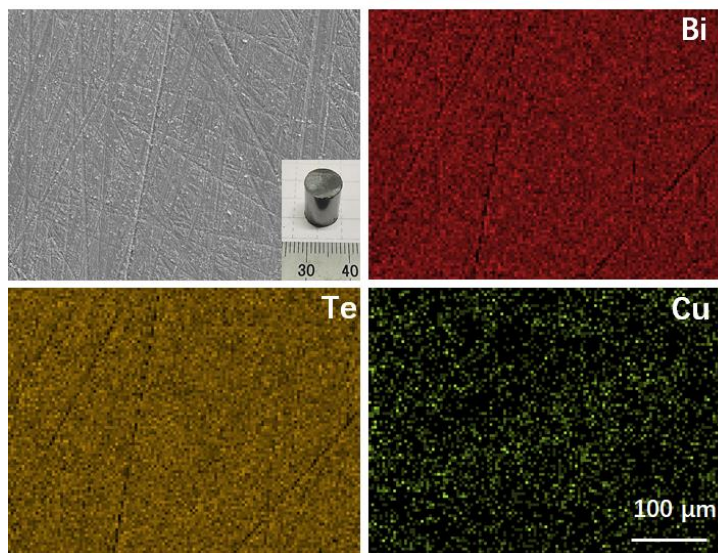


Figure 5. SEM micrograph of a $\text{Bi}_2\text{Te}_3\text{-Cu}_{2-x}\text{Te}$ (Bi:Cu=10) pellet and corresponding EDX elemental maps.

Taking into account the highly anisotropic transport properties of Bi_2Te_3 and the very asymmetric particles used as building blocks to produce the $\text{Bi}_2\text{Te}_3\text{-Cu}_{2-x}\text{Te}$ composites, one could expect the pellet to present anisotropic transport properties. Thus, we measured the TE properties of the composites along two directions: parallel and normal to the pressure axis (Figure 6). Similar results were obtained in both directions, which was ascribed to the lack of crystallographic texture in the produced nanomaterials. Indeed, SEM characterization of the consolidated material showed a random distribution of short-range order domains of quasi-aligned nanowires (Figure 3c). The presence of randomly oriented domains was further confirmed by XRD, which displayed similar relative peak intensities when analysing the samples in two normal directions (Figure 7). Owing to this lack of anisotropy in the material transport properties, in the following we focus our discussion only on results obtained in the direction normal to the pressure axis.

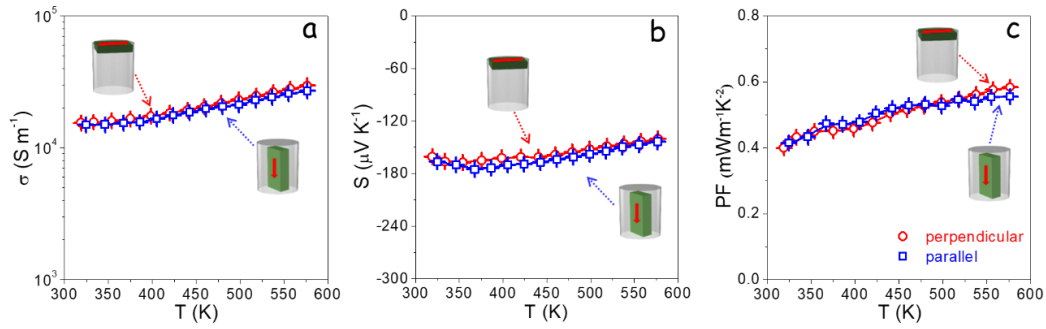


Figure 6. Temperature dependence of TE properties of $\text{Bi}_2\text{Te}_3\text{-Cu}_{2-x}\text{Te}$ (Bi:Cu=8) in two directions, perpendicular (red) and parallel (blue) to the pressure axis, as marked within the graphs: (a) electric conductivity, σ ; (b) Seebeck coefficient, S ; (c) power factor or $S^2\sigma$, PF.

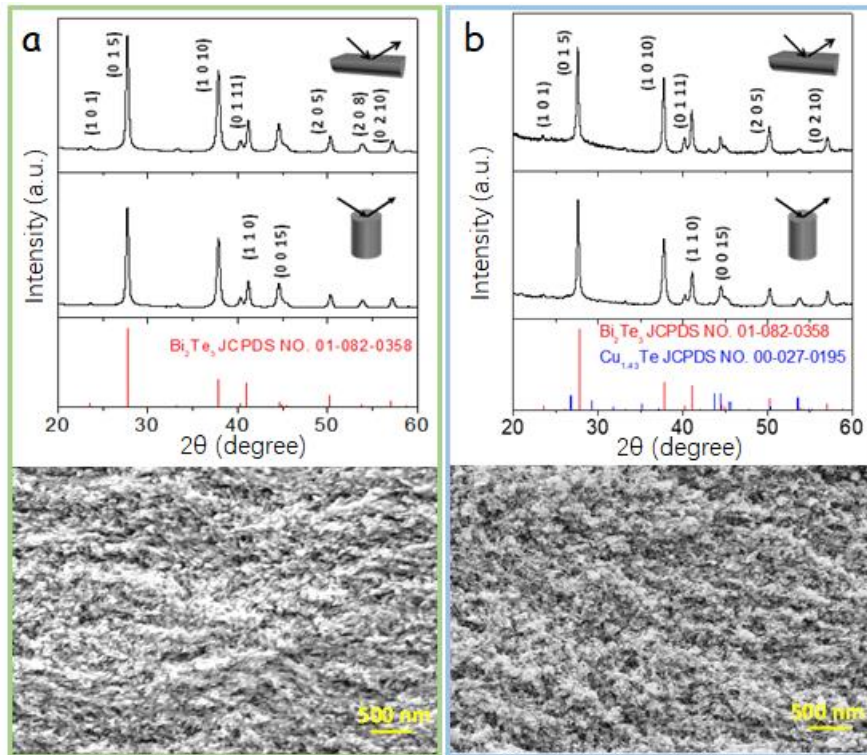


Figure 7. XRD pattern and SEM micrographs of consolidated pellets in two normal directions, perpendicular and parallel to the pressure axis, as marked within the graphs. (a) Bi_2Te_3 and (b) $\text{Bi}_2\text{Te}_3\text{-Cu}_{2-x}\text{Te}$ (Bi:Cu=8).

I initially studied the influence of the annealing temperature on the TE properties of $\text{Bi}_2\text{Te}_3\text{-Cu}_{2-x}\text{Te}$ composites by analysing samples annealed at 330 °C and 450 °C. The materials annealed at higher temperature, 450 °C, displayed lower ZT

values than those annealed at 330 °C. We associated this lower performance with the higher crystallinity of the samples annealed at the higher temperature, which translated into lower S and higher values (Figure 8). Therefore, the following discussion is focused on the properties of materials annealed at 330 °C.

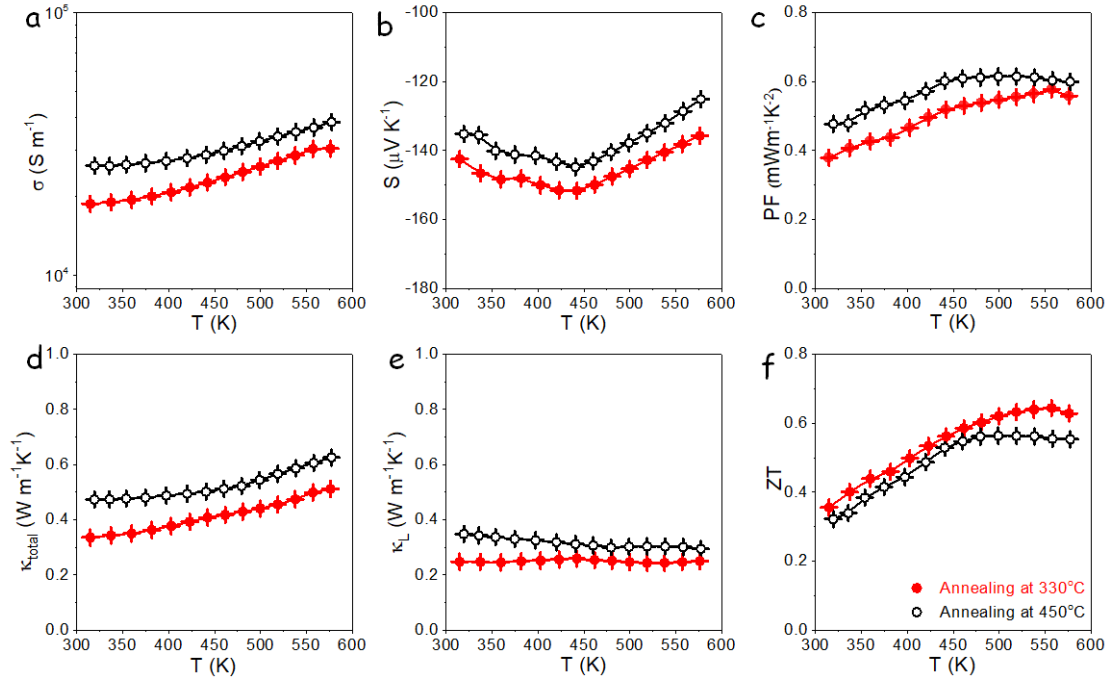


Figure 8. Temperature dependence of TE properties of $\text{Bi}_2\text{Te}_3\text{-Cu}_{2-x}\text{Te}$ (Bi:Cu=8) sample annealed at 330 °C (solid symbols) and 450 °C (open symbols) respectively: (a) electric conductivity, σ ; (b) Seebeck coefficient, S ; (c) power factor or $S^2\sigma$, PF; (d) total thermal conductivity, κ_{total} ; (e) lattice thermal conductivity; (f) TE figure of merit, ZT.

Figure 10 displays the TE properties in the plane normal to the pressure axis of pellets produced from Bi_2Te_3 and $\text{Bi}_2\text{Te}_3\text{-Cu}_{2-x}\text{Te}$ nanowires annealed at 330 °C. Bare Bi_2Te_3 displayed electrical conductivities on the order of 10^4 S m^{-1} . This material presented a relatively high charge carrier concentrations, close to 10^{19} cm^{-3} (Figure 9), which was related with a high density of Te_{Bi} antisite donors.³⁶ Its relatively low electrical conductivity compared with highly crystalline materials is associated to the porosity and large density of grain boundaries, which resulted in a relatively low mobility, $20 \text{ cm}^2 \text{ V}^{-1} \text{ s}^{-1}$.

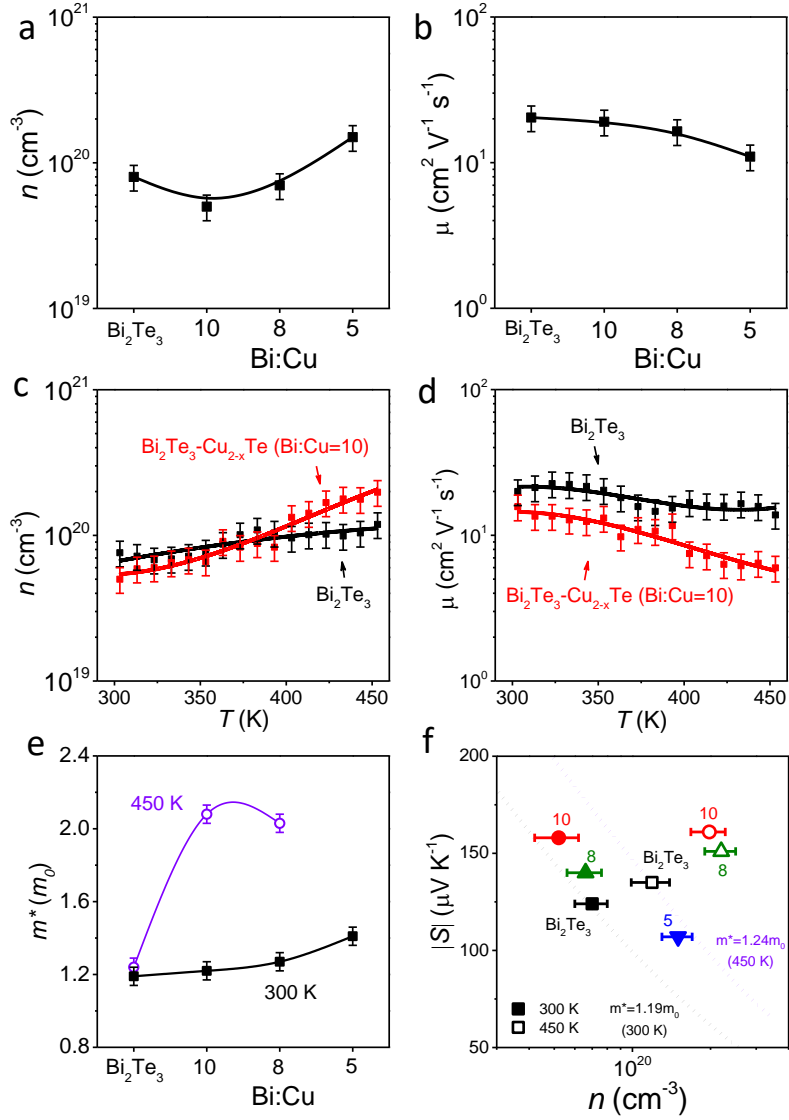


Figure 9. (a) Ambient temperature Hall charge carrier concentration and (b) carrier mobility as the function of the pellet composition. (c) Temperature dependence of the Hall charge carrier concentration and (d) carrier mobility for Bi₂Te₃ and Bi₂Te₃-Cu_{2-x}Te (Bi:Cu = 10). (e) Effective mass calculated using a SPB model at room temperature and 450 K as a function of the pellet composition. (f) $|S|$ vs. n for the different samples at 300 K (solid symbols) and 450 K (open symbols). The composition corresponding to each point (Bi₂Te₃ or the Bi:Cu ratio in Bi₂Te₃-Cu_{2-x}Te) is specified for each point. Solid lines show the theoretical $|S|$ vs. n dependence considering a SPB model obtained using the m^* of bare Bi₂Te₃ at 300 K (black line) and 450 K (purple line).

Table 1. Density of hot pressed Bi₂Te₃ and Bi₂Te₃-Cu_{2-x}Te samples.

Sample	Density (g/cm ³)	Relative Density
Bi ₂ Te ₃	6.63	86.1%
Bi ₂ Te ₃ -Cu _{2-x} Te (Bi:Cu =10)	6.59	86.7%
Bi ₂ Te ₃ -Cu _{2-x} Te (Bi:Cu =8)	6.54	87.2%
Bi ₂ Te ₃ -Cu _{2-x} Te (Bi:Cu =5)	6.44	87.0%

With the introduction of moderate amounts of Cu, a decrease in σ at room temperature was observed, consistent with a lower Hall charge carrier concentration and a slight decrease of mobility. This decrease of the carrier concentration was related to the removal of Te from the Bi₂Te₃ nanowires to form Cu_{2-x}Te domains, reducing the concentration of n-type electroactive Te_{Bi} defects. At higher Cu content, Bi:Cu=5, the electrical conductivity and charge carrier concentration increased with respect to that of bare Bi₂Te₃. We related this increase to a further depletion of Te from Bi₂Te₃, creating donor Te vacancies V_{Te}. Additionally, Cu_{2-x}Te domains could contribute to increase the charge carrier concentration through spillover of electrons to Bi₂Te₃, according to the lower work function of Cu_{2.8}Te₂ (4.7 eV) compared with the Bi₂Te₃ one (5.3 eV).^{50, 51}

This injection of charge carriers compensates for the decrease in mobility with the introduction of large amounts of Cu (Figure 9). The Seebeck coefficient of Bi₂Te₃ nanomaterials and Bi₂Te₃-Cu_{2-x}Te nanocomposites was negative in all the temperature range explored. Compared with Bi₂Te₃, nanocomposites containing relatively small amounts of Cu_{2-x}Te displayed higher Seebeck coefficients, which was consistent with their lower charge carrier concentration. On the other hand, samples containing larger amounts of Cu, Bi:Cu = 5, exhibited lower S values, also consistently with their higher carrier concentration.

For most of the samples, the Seebeck coefficient increased with temperature up to *ca.* 450 K and then decreased at higher temperatures. In contrast to previous works,³⁹ the introduction of Cu barely influenced the temperature of the

maximum Seebeck coefficient, which depends on the concentration of extrinsic carriers and the source of thermally-generated charge carriers that are responsible for the bipolar effect. We associated this experimental evidence with a moderate relative change of the concentration of free electrons with the introduction of Cu.

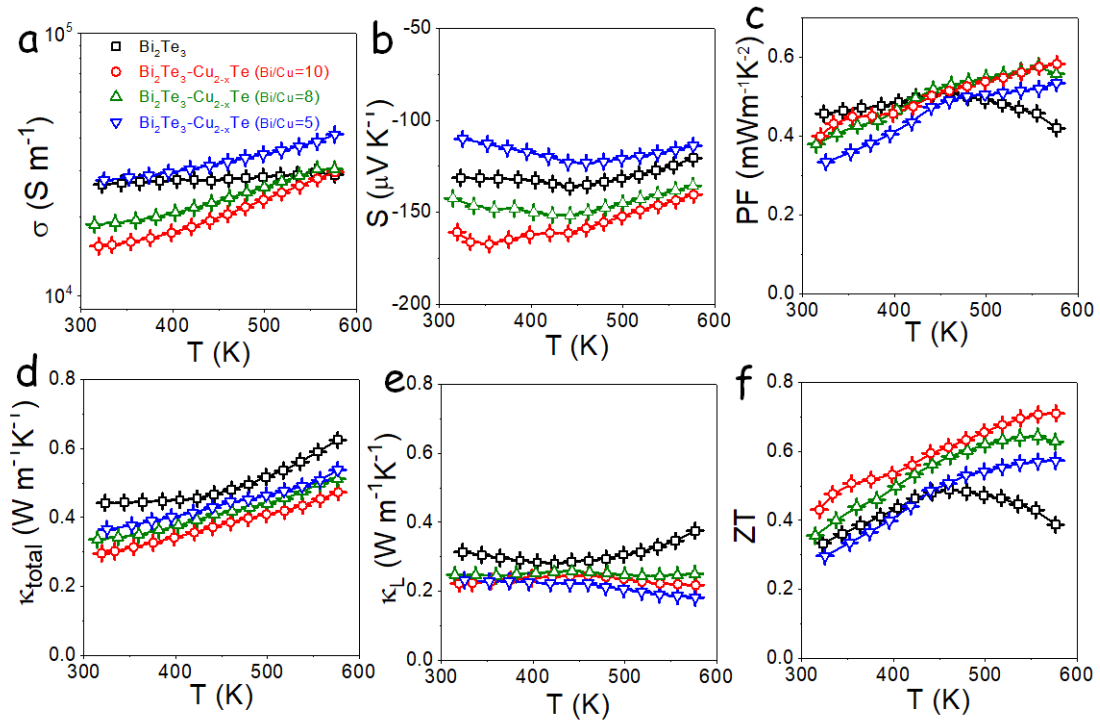


Figure 10. Thermoelectric properties of Bi_2Te_3 and $\text{Bi}_2\text{Te}_3\text{-Cu}_{2-x}\text{Te}$ pellets: (a) electric conductivity, σ ; (b) Seebeck coefficient, S ; (c) power factor or $S^2\sigma$, PF; (d) total thermal conductivity, κ_{total} ; (e) lattice thermal conductivity, κ_{L} ; and (f) TE figure of merit, ZT.

Compared with bare Bi_2Te_3 , all $\text{Bi}_2\text{Te}_3\text{-Cu}_{2-x}\text{Te}$ nanocomposites displayed stronger increase of electrical conductivity with temperature. In the high temperature range tested, the electrical conductivity of all nanocomposites was similar or higher than that of bare Bi_2Te_3 , in spite of the higher density of scattering centres of the former. This stronger dependence of electrical conductivity with temperature was associated with a larger influence of electron energy barriers on the charge transport within nanocomposites.

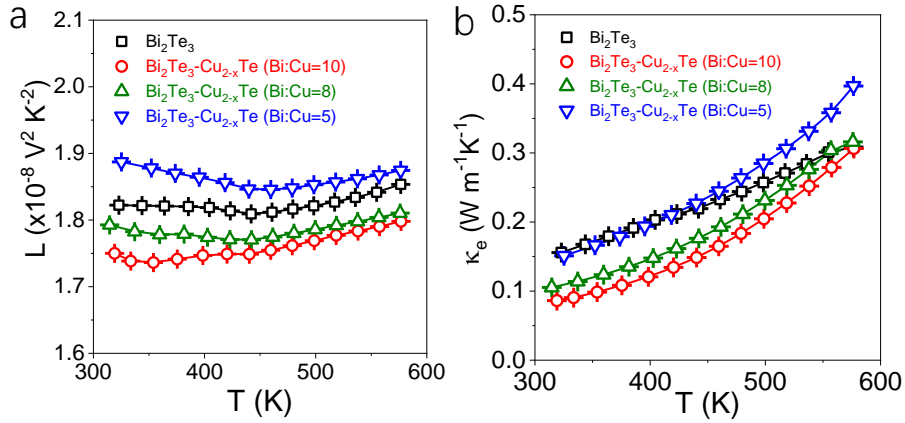


Figure 11. Temperature dependence of (a) Lorentz number (L) and (b) electronic thermal conductivity (κ_e) of Bi_2Te_3 and $\text{Bi}_2\text{Te}_3\text{-Cu}_{2-x}\text{Te}$ pellets.

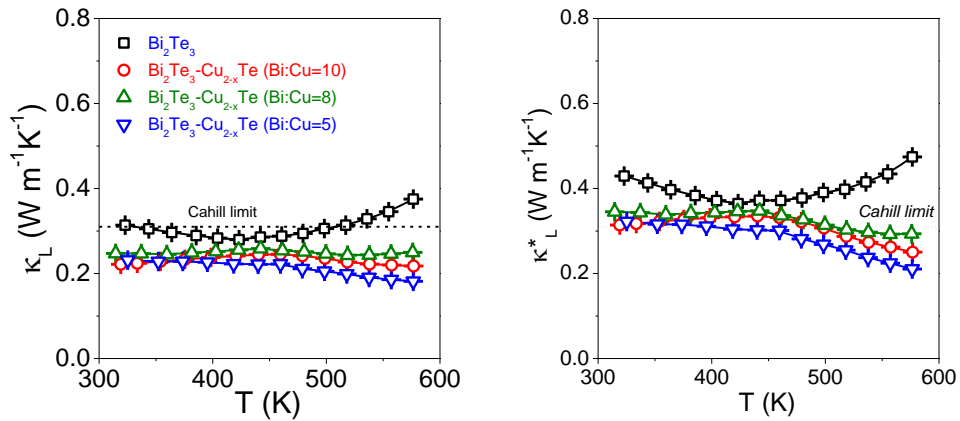


Figure 12. Lattice thermal conductivity before (left) and after (right) porosity correction and including the Cahill limit estimated for pure Bi_2Te_3 at ambient temperature ($0.31 \text{ W m}^{-1} \text{ K}^{-1}$).¹

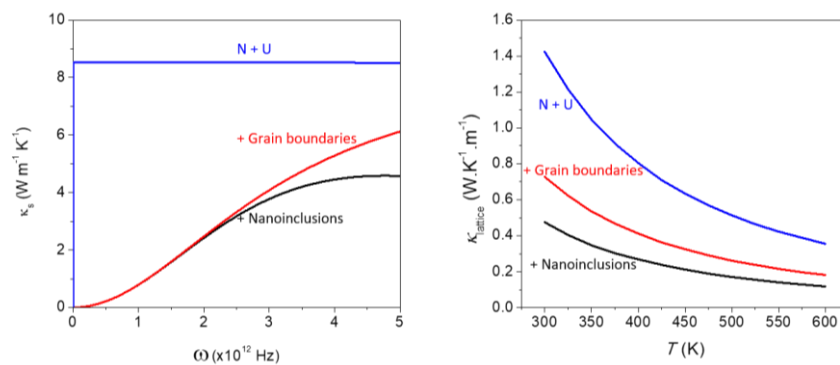


Figure 13. Calculated spectral lattice conductivity at 600 K (a) and thermal

lattice conductivity (b) for a sample of $\text{Bi}_2\text{Te}_3\text{-Cu}_{2-x}\text{Te}$ (Bi:Cu =10). The calculated values are in accordance with our measurements for pristine Bi_2Te_3 (red curves, when nano-inclusions are not considered) and for $\text{Bi}_2\text{Te}_3\text{-Cu}_{2-x}\text{Te}$ (black curves). The higher values of calculated thermal conductivities with respect to the measured ones are an effect of the high porosity of the samples.

Taking into account the higher charge carrier scattering in composites compared with bare Bi_2Te_3 , to explain their high electrical conductivities in the high temperature range, one needs to assume an increase of the concentration of electrons participating in the charge transport. Besides thermal generation in Bi_2Te_3 , which should be similar for all materials, this higher concentration of free carriers need to be provided by spillover from Cu_{2-x}Te domains. This strong enhancement of the electrical conductivity with temperature did not come with the expected decrease of the Seebeck coefficient. Thus, in the high temperature range, the power factors of all nanocomposites were significantly larger than those of bare Bi_2Te_3 (Figure 10c). We hypothesise that these higher power factors are associated with an energy filtering of charge carrier at the energy barriers introduced by the $\text{Bi}_2\text{Te}_3/\text{Cu}_{2-x}\text{Te}$ heterojunctions.

In order to better understand the transport properties dependence with temperature, charge carrier concentrations and mobilities were measured as a function of temperature for samples Bi_2Te_3 and $\text{Bi}_2\text{Te}_3\text{-Cu}_{2-x}\text{Te}$ (Bi:Cu = 10). As shown in Figure 9c, the charge carrier concentration of the Bi_2Te_3 sample monotonously increase with temperature in all the range tested. On the other hand, the $\text{Bi}_2\text{Te}_3\text{-Cu}_{2-x}\text{Te}$ (Bi:Cu = 10) displayed a higher rate of activation of charge carriers, particularly at temperatures above 350 K. We associate this activation with the injection of electrons from Cu_{2-x}Te to Bi_2Te_3 . This different rate of activation of charge carriers resulted in $\text{Bi}_2\text{Te}_3\text{-Cu}_{2-x}\text{Te}$ composites having higher charge carrier concentrations in the high temperature range than bare Bi_2Te_3 . Surprisingly, this large increase of the charge carrier concentration on nanocomposites was not correlated with a similar decrease of the absolute value of the Seebeck coefficient. Besides, the charge carrier mobility monotonously

decreased for both materials with temperature, being the mobility of the composite lower than that of bare $\text{Bi}_2\text{Te}_3\text{-Cu}_{2-x}\text{Te}$ at all temperatures.

When calculating the effective mass of Bi_2Te_3 and $\text{Bi}_2\text{Te}_3\text{-Cu}_{2-x}\text{Te}$ composites using a single parabolic band (SPB) model (Figure 9e), we observe all composites to have slightly higher apparent effective masses at 300 K. This apparent effective mass strongly increases at 450 K, becoming close to a twofold higher than that of Bi_2Te_3 . Figure 9f displays a plot of the absolute value of the Seebeck coefficient as a function of the charge carrier concentration. Lines displaying the theoretical dependence (SPB model) of $|S|$ as a function of n for the calculated effective masses of Bi_2Te_3 at 300 K and 450 K are also plotted as a reference. Notice how at 450 K, the presence of Cu_{2-x}Te results in Seebeck coefficients up to 50 % larger than those predicted for bare Bi_2Te_3 with the same charge carrier concentration.

The large differential electron affinity of Cu_{2-x}Te and Bi_2Te_3 , and the small size of the Cu_{2-x}Te crystal domains inevitably lead to a spillover of electrons from the valence band of Cu_{2-x}Te to the conduction band of Bi_2Te_3 and the consequent pinning of the Cu_{2-x}Te Fermi level within its valence band (Figure 14a). Simultaneously, within the Bi_2Te_3 nanowires, a downward bending of the electron energy bands around the Cu_{2-x}Te domains is expected (Figure 14b,c). Thus, electrons injected from Cu_{2-x}Te accumulate in potential wells within the Bi_2Te_3 nanowire. When increasing temperature, higher amounts of electrons are injected from Cu_{2-x}Te to Bi_2Te_3 , and electrons in the Bi_2Te_3 potential wells have more energy to overcome the barriers and freely move through the Bi_2Te_3 domains. These two phenomena explain the strong increase of the electrical conductivity with temperature in nanocomposites. Besides, electrons travelling through the Bi_2Te_3 crystal domains encounter abundant energy wells able to trap low energy charge carriers. This mechanism of filtering of charge carriers as a function of their energy may be responsible for the significantly higher Seebeck coefficients measured in nanocomposites compared with bare Bi_2Te_3 .

As expected, all $\text{Bi}_2\text{Te}_3\text{-Cu}_{2-x}\text{Te}$ nanocomposites exhibited significantly lower

thermal conductivities than pure Bi_2Te_3 due to enhanced phonon scattering at extensive interphases (Figure 10d,e). The lowest thermal conductivities were obtained from the sample containing the smallest amount of Cu, Bi:Cu = 10, because the electronic contribution to the thermal conductivity increased with the Cu_{2-x}Te content (Figure 11). Figure 13 displays the lattice thermal conductivity obtained with the phonon relaxation time based on the Debye-Callaway model considering the effect of grain boundaries and the presence of Cu_{2-x}Te nanodomains (see SI for details). Compared to the calculations, experimental data showed a slightly lower effect of the incorporation of Cu_{2-x}Te nanodomains on the lattice thermal conductivity, especially at low temperature. This discrepancy could be in part explained by the overestimation of this parameter in nanomaterials when calculated by extracting the electronic contribution, as recently reported by Snyder et al.⁵². This overestimation of the lattice thermal conductivity, especially in the lower temperature range, also hides the bipolar contribution to the thermal conductivity, which is only evident for the Bi_2Te_3 sample in the form of an increase of the calculated lattice thermal conductivity at temperature above 450 K. Notice finally that the low thermal conductivities obtained for Bi_2Te_3 and $\text{Bi}_2\text{Te}_3\text{-Cu}_{2-x}\text{Te}$ are in part related to the relatively high porosity of the produced materials, with densities of around 86-87% (see SI for an estimation of the porosity contribution to the lattice thermal conductivity and a comparison with the Cahill limit, Figure 12)

Figure 10f displays the TE figure of merit obtained from Bi_2Te_3 and $\text{Bi}_2\text{Te}_3\text{-Cu}_{2-x}\text{Te}$ samples. For pure Bi_2Te_3 , a maximum ZT value of 0.48 was achieved at 460 K, which is a notable value for pure Bi_2Te_3 . At higher temperatures, ZT severely decreased due to the bipolar contribution. On the other hand, $\text{Bi}_2\text{Te}_3\text{-Cu}_{2-x}\text{Te}$ composites displayed significantly larger ZT values, up to 0.74 at 576 K for Bi:Cu = 10.

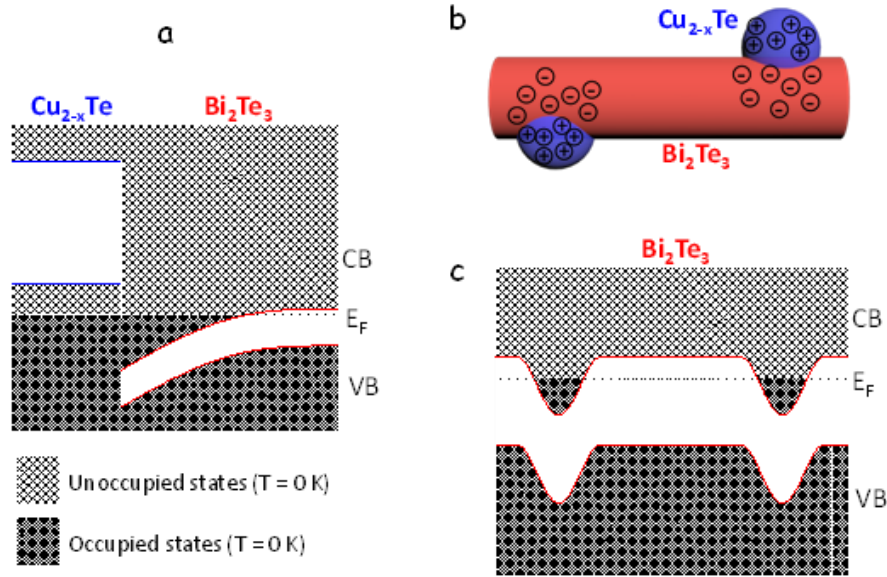


Figure 14. (a) Electron energy band alignment in a heterojunction between a small Cu_{2-x}Te crystal and a larger Bi_2Te_3 domain. (b) Cartoon of the charge distribution within a Bi_2Te_3 nanowire having two Cu_{2-x}Te domains on its surface. (c) Qualitative electron energy band diagram of the same Bi_2Te_3 nanowire having two Cu_{2-x}Te domains on its surface.

4.5 Conclusions

In conclusion, we reported a solution-based protocol to synthesize $\text{Bi}_2\text{Te}_3\text{-Cu}_{2-x}\text{Te}$ heterostructured nanowires that were used to produce $\text{Bi}_2\text{Te}_3\text{-Cu}_{2-x}\text{Te}$ nanocomposites with relative densities close to 90%. We observed the presence of Cu_{2-x}Te to result in an increase of the TE figure of merit of up to a 50%. The higher ZT values measured in $\text{Bi}_2\text{Te}_3\text{-Cu}_{2-x}\text{Te}$ nanocomposites compared with bare Bi_2Te_3 were attributed to a combination of several features: i) the large electrical conductivities measured in the nanocomposites at high temperature, mainly associated to the spillover of charge carrier from Cu_{2-x}Te domains to the Bi_2Te_3 matrix; ii) the enhanced Seebeck coefficients without sacrificing electrical conductivity in the high temperature range associated with the energy-filtering of charge carriers at potential barriers introduced with the formation of the $\text{Bi}_2\text{Te}_3/\text{Cu}_{2-x}\text{Te}$ heterojunctions; and iii) the enhanced phonon scattering at the interphase of two different materials, which notably reduced the thermal

conductivity.

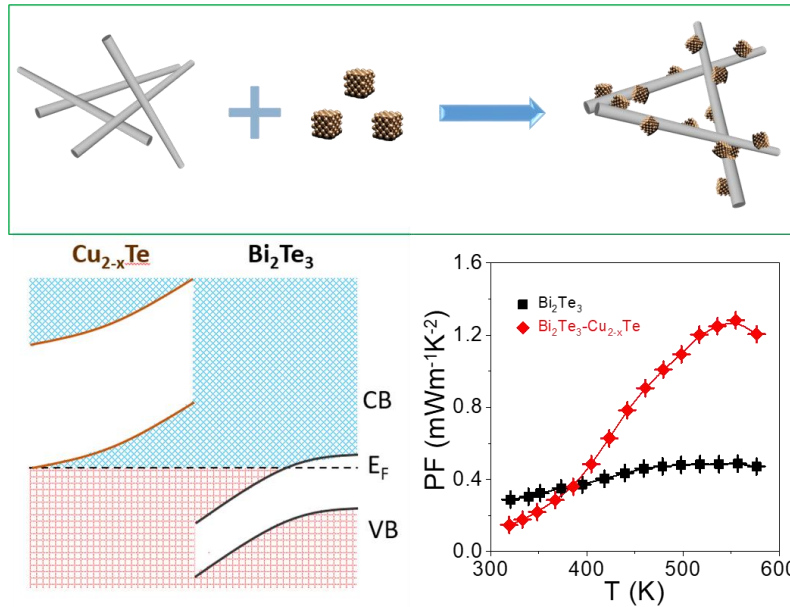
4.6 References

1. Q. H. Zhang, X. Y. Huang, S. Q. Bai, X. Shi, C. Uher and L. D. Chen, *Adv. Eng. Mater* **2016**, 18, 194-213.
2. G. J. Snyder and T. S. Ursell, *Phys. Rev. Lett* **2003**, 91, 148301.
3. T. Humphrey and H. Linke, *Phys. Rev. Lett* **2005**, 94, 096601.
4. S. Ortega, M. Ibáñez, Y. Liu, Y. Zhang, M. V. Kovalenko, D. Cadavid and A. Cabot, *Chem. Soc. Rev* **2017**, 46, 3510-3528.
5. G. J. Snyder and E. S. Toberer, in *materials for sustainable energy: a collection of peer-reviewed research and review articles from Nature Publishing Group*, World Scientific, 2011, 101-110.
6. J.-F. Li, W.-S. Liu, L.-D. Zhao and M. Zhou, *NPG Asia Mater* **2010**, 2, 152-158.
7. W. Liu, Q. Jie, H. S. Kim and Z. Ren, *Acta Mater.* **2015**, 87, 357-376.
8. Z.-G. Chen, G. Han, L. Yang, L. Cheng and J. Zou, *Prog. Nat. Sci.* **2012**, 22, 535-549.
9. J. P. Heremans, V. Jovovic, E. S. Toberer, A. Saramat, K. Kurosaki, A. Charoenphakdee, S. Yamanaka and G. J. Snyder, *Science*, **2008**, 321, 554-557.
10. M. Ibáñez, A. Genç, R. Hasler, Y. Liu, O. Dobrozhan, O. Nazarenko, M. Mata, J. Arbiol, A. Cabot and M. V. Kovalenko, *ACS nano*, **2019**, 13, 6572-6580.
11. J. Li, Q. Tan, J. F. Li, D. W. Liu, F. Li, Z. Y. Li, M. Zou and K. Wang, *Adv. Funct. Mater.* **2013**, 23, 4317-4323.
12. Y. Cao, X. Zhao, T. Zhu, X. Zhang and J. Tu, *Appl. Phys. Lett.* **2008**, 92, 143106.
13. B. Yu, M. Zebarjadi, H. Wang, K. Lukas, H. Wang, D. Wang, C. Opeil, M. Dresselhaus, G. Chen and Z. Ren, *Nano lett* **2012**, 12, 2077-2082.
14. P. Jood, R. J. Mehta, Y. Zhang, G. Peleckis, X. Wang, R. W. Siegel, T. Borca-Tasciuc, S. X. Dou and G. Ramanath, *Nano lett* **2011**, 11, 4337-4342.
15. A. Banik, B. Vishal, S. Perumal, R. Datta and K. Biswas, *Energy Environ. Sci.* **2016**, 9, 2011-2019.
16. L.-D. Zhao, S.-H. Lo, J. He, H. Li, K. Biswas, J. Androulakis, C.-I. Wu, T. P. Hogan, D.-Y. Chung and V. P. Dravid, M. G. Kanatzidis, *J. Am. Chem. Soc.* **2011**, 133, 20476-20487.

17. J. He, S. N. Girard, J. C. Zheng, L. Zhao, M. G. Kanatzidis and V. P. Dravid, *Adv. Mater.* **2012**, 24, 4440-4444.
18. J. He, J. R. Sootsman, S. N. Girard, J.-C. Zheng, J. Wen, Y. Zhu, M. G. Kanatzidis and V. P. Dravid, *J. Am. Chem. Soc.* **2010**, 132, 8669-8675.
19. H. Choi, K. Jeong, J. Chae, H. Park, J. Baeck, T. H. Kim, J. Y. Song, J. Park, K.-H. Jeong and M.-H. Cho, *Nano Energy*, **2018**, 47, 374-384.
20. G. Pernot, M. Stoffel, I. Savic, F. Pezzoli, P. Chen, G. Savelli, A. Jacquot, J. Schumann, U. Denker, I. Mönch C. Deneke, O. G. Schmidt, J. M. Rampnoux, S. Wang, M. Plissonnier, A. Rastelli, S. Dilhaire and N. Mingo, *Nat. mater.* **2010**, 9, 491-495.
21. M. Ibáñez, R. Hasler, A. Genç, Y. Liu, B. Kuster, M. Schuster, O. Dobrozhan, D. Cadavid, J. Arbiol, A. Cabot and M. Kovalenko, *J. Am. Chem. Soc.* **2019**, 141, 8025-8029.
22. G. Zhang, H. Fang, H. Yang, L. A. Jauregui, Y. P. Chen and Y. Wu, *Nano let.* **2012**, 12, 3627-3633.
23. H. Fang, T. Feng, H. Yang, X. Ruan and Y. Wu, *Nano let.* **2013**, 13, 2058-2063.
24. H. Fang, H. Yang and Y. Wu, *Chem. Mater.* **2014**, 26, 3322-3327.
25. H. Yang, J.-H. Bahk, T. Day, A. M. Mohammed, B. Min, G. J. Snyder, A. Shakouri and Y. Wu, *Nano letters*, 2014, **14**, 5398-5404.
26. M. Ibáñez, Z. Luo, A. Genc, L. Piveteau, S. Ortega, D. Cadavid, O. Dobrozhan, Y. Liu, M. Nachtegaal, M. Zebarjadi, J. Arbiol, M. Kovalenko and A. Cabot, *Nat. Commun.* **2016**, 7, 10766.
27. J. P. Heremans, C. M. Thrush, D. T. Morelli and M.-C. Wu, *Phys. Rev. Lett.*, **2002**, 88, 216801.
28. Q. Yao, L. Chen, W. Zhang, S. Liufu and X. Chen, *ACS Nano*, **2010**, 4, 2445-2451.
29. X. Zhao, X. Ji, Y. Zhang, T. Zhu, J. Tu and X. Zhang, *Appl. Phys. Lett.* **2005**, 86, 062111.
30. W. S. Liu, Q. Zhang, Y. Lan, S. Chen, X. Yan, Q. Zhang, H. Wang, D. Wang, G. Chen and Z. Ren, *Adv. Energy Mater.* **2011**, 1, 577-587.
31. W. Xie, J. He, H. J. Kang, X. Tang, S. Zhu, M. Laver, S. Wang, J. R. Copley, C. M. Brown, Q. Zhang and T. Tritt, *Nano lett.* **2010**, 10, 3283-3289.
32. M. Ibáñez, R. Hasler, Y. Liu, O. Dobrozhan, O. Nazarenko, D. Cadavid, A. Cabot and M. V. Kovalenko, *Chem. Mater.* **2017**, 29, 7093-7097.
33. Y. Liu, D. Cadavid, M. Ibáñez, S. Ortega, S. Martí-Sánchez, O. Dobrozhan, M. V.

- Kovalenko, J. Arbiol and A. Cabot, *APL Mater.* **2016**, 4, 104813.
34. M. Ibáñez, R. Zamani, S. Gorsse, J. Fan, S. Ortega, D. Cadavid, J. R. Morante, J. Arbiol and A. Cabot, *ACS nano*, **2013**, 7, 2573-2586.
35. M. Ibáñez, R. J. Korkosz, Z. Luo, P. Riba, D. Cadavid, S. Ortega, A. Cabot and M. G. Kanatzidis, *Journal of the American Chemical Society*, **2015**, 137, 4046-4049.
36. T. Zhu, L. Hu, X. Zhao and J. He, *Adv. Sci.* **2016**, 3, 1600004.
37. Y. Liu, Y. Zhang, K. H. Lim, M. Ibáñez, S. Ortega, M. Li, J. David, S. Martí-Sánchez, K. M. Ng, J. Arbiol, M. Kovalenko, D. Cadavid and A. Cabot, *ACS nano* **2018**, 12, 7174-7184.
38. Y. Liu, Y. Zhang, S. Ortega, M. Ibáñez, K. H. Lim, A. Grau-Carbonell, S. Martí-Sánchez, K. M. Ng, J. Arbiol and M. V. Kovalenko, *Nano let.* **2018**, 18, 2557-2563.
39. J. M. Song, J. U. Rahman, J. Y. Cho, S. Lee, W. S. Seo, S. Kim, S.-i. Kim, K. H. Lee, D. Roh and W. H. Shin, *Scr. Mater.* **2019**, 165, 78-83.
40. W. Zhu, W. Hu, P. Wei, X. Nie and W. Zhao. *Electron. Mater.* **2020**, 49, 2962-2967.
41. H.-L. Zhuang, Y. Pan, F.-H. Sun, J. Dong, J. Pei, B. Cai, H. Hu, H. Tang and J.-F. Li, *Nano Energy* **2019**, 60, 857-865.
42. H.-J. Wu and W.-T. Yen, *Acta Materialia*, **2018**, 157, 33-41.
43. J. Bludska, I. Jakubec, Č. Drašar, P. Lošťák and J. Horak, *Philosophical Magazine* **2007**, 87, 325-335.
44. M. Sinduja, S. Amirthapandian, A. Masarrat, R. Krishnan, S. Srivastava and A. Kandasami, *Thin Solid Films* **2020**, 697, 137834.
45. K. H. Seo, B. G. Kim, C.-H. Lim, S.-H. Kim, K.-M. Lee, J.-Y. Kim and S.-M. Choi, *CrystEngComm* **2017**, 19, 2750-2757.
46. Q. Lognoné and F. Gascoin, *J. Alloys Compd.* **2014**, 610, 1-5.
47. G. Zhang, B. Kirk, L. A. Jauregui, H. Yang, X. Xu, Y. P. Chen and Y. Wu, *Nano let.* **2012**, 12, 56-60.
48. Y. G. Asadov, L. Rustamova, G. Gasimov, K. Jafarov and A. Babajev, *Phase Transitions: A Multinational Journal*, **1992**, 38, 247-259.
49. A. Pashinkin and V. Fedorov, *Inorg. Mater.* **2003**, 39, 539-554.
50. M. Huang, A. Maljusch, F. Calle-Vallejo, J. B. Henry, M. T. Koper, W. Schuhmann and A. S. Bandarenka, *RSC Adv.* **2013**, 3, 21648-21654.
51. D. Haneman, *J. Phys. Chem. Solids* **1959**, 11, 205-214.

Chapter 5 Influence of copper telluride nanodomains on the transport properties of n-type bismuth telluride



5.1 Abstract

Bi_2Te_3 is the most used TE material, but its high processing cost, poor mechanical properties and moderate performance limit the cost-effectiveness of TE devices. In the present work, I detail a simple, low temperature and solution-based approach to produce Bi_2Te_3 - Cu_{2-x}Te NCs with controlled composition. Our strategy is based on combining proper ratios of colloidal NPs and to consolidate the resulting NP mixture by hot-press. The transport properties of the NCs are then characterized and compared with those of a bare Bi_2Te_3 nanomaterial obtained following the same protocol. On the contrary to most previously reported NCs, the presence of Cu_{2-x}Te nanodomains does not lead to a significant reduction of the lattice thermal conductivity of the reference Bi_2Te_3 , which is already very low here, but it results in a nearly threefold increase of its power factor. Cu_{2-x}Te nanostructures, with a relatively low electron affinity, are able to inject electrons into Bi_2Te_3 , enhancing in this way its electrical conductivity. Additionally, the presence of Cu_{2-x}Te results in a strong increase

of the Seebeck coefficient. This increase is related to the energy filtering of charge carriers at energy barriers within Bi_2Te_3 domains created by the accumulation of electrons in the regions nearby $\text{Cu}_{2-x}\text{Te}/\text{Bi}_2\text{Te}_3$ heterojunctions. Overall, a significant improvement of figure of merit, up to a 250%, is obtained with the incorporation of a proper amount of Cu_{2-x}Te NPs.

5.2 Introduction

TE devices, able to convert temperature gradients into electricity and vice versa, have a plethora of potential applications, especially around ambient temperature. However, their use is currently limited by their moderate cost-effectiveness. The efficiency of TE devices is determined by three interdependent material parameters that are combined in a dimensionless figure of merit $ZT = \sigma S^2 T \kappa^{-1}$.¹⁻⁴ On the other hand, the high cost of current TE devices is related to the large amount of highly crystalline Bi-Sb-Te-Se alloys used in available commercial devices, which are optimized toward cooling applications. The amount of TE material could be strongly reduced when optimizing devices to harvest small temperature gradients. Besides, high crystallinity materials are not only unnecessary but even detrimental to the device performance as they have associated higher thermal conductivities and poorer mechanical properties than their polycrystalline counterparts, especially when relying on layered materials such as Bi_2Te_3 .

Bottom-up strategies based on solution-processed building blocks offer a solution in both directions. Properly designed and engineered NCs allow to partially decouple TE properties, adjusting the charge carrier concentration without major reduction of the mobility by modulation doping, increasing the Seebeck coefficient through energy filtering and quantum confinement, and reducing thermal conductivity through extensive phonon scattering.⁴⁻²⁰ At the same time, because bottom-up approaches do not require the large scale organization of atoms into macroscopic crystal domains, the energy usage, processing time and overall cost can be strongly reduced. As a bonus advantage, beyond providing improved TE properties at a potentially lower cost,

nanomaterials allow improving mechanical performances, especially for layered materials, which are particularly fragile toward fracture along van der Waals planes.

In the last decade, several strategies have been developed to improve the TE properties of Bi_2Te_3 -based alloys.^{12, 21-33} One successful approach to increase the power factor (σS^2) while at the same time reducing thermal conductivity has been the incorporation of doping elements, such as Cu. Besides promoting phonon scattering, the incorporation of Cu has usually associated an increase in the charge carrier concentration that results in a large increase of electrical conductivity and a moderate decrease of the Seebeck coefficient, overall translating into higher power factors and figures of merit.³⁴⁻⁴² Cu ions electronically dope Bi_2Te_3 in different ways, depending on the conductivity type of the Bi_2Te_3 -based alloy and the Cu concentration and location. When Cu^+ ions intercalate at the van der Waals gap between Bi_2Te_3 layers, they act as donors.^{34, 36} Cu^+ ions substituting Bi act as acceptors.^{34, 41} Besides, the presence of Cu may modify the concentration of electroactive defects within Bi_2Te_3 -based alloys, altering the amount of Te vacancies and Bi and Te antisites, for instance.⁴² On the other hand, amounts of Cu above the solubility limit lead to the segregation of Cu_{2-x}Te phases. This segregation reduces the amount of Te within the alloy and consequently increases the amount of Te vacancies and/or reduces the concentration of Te antisites, both acting as electron donors.^{34, 41-42} Additionally, the presence of Cu_{2-x}Te domains within the Bi_2Te_3 matrix can electronic affect the material in ways that remain largely unexplored. Cu_{2-x}Te is generally characterized by a relatively low work function⁴³ and a degenerated p-type conductivity associated to its Cu deficiency.^{11, 44-47} Thus, in $\text{Bi}_2\text{Te}_3/\text{Cu}_{2-x}\text{Te}$ heterostructures Cu_{2-x}Te is most probably able to inject charge carriers to the Bi_2Te_3 while at the same time strongly modifying its electron energy band structure at the interphase.

In this work, I produce $\text{Bi}_2\text{Te}_3\text{-Cu}_{2-x}\text{Te}$ NCs with controlled phase ratio by mixing proper amounts of Bi_2Te_3 and Cu_{2-x}Te colloidal NPs. I characterize their

structural and chemical properties and discuss their TE performance taking into account the heterojunctions formed between the two materials.

5.3 Experimental section

Chemicals and solvents: OAm (technical grade 70%), oleic acid (OAc, technical grade 90%), bismuth(III) chloride (BiCl_3 , $\geq 98\%$), copper(II) acetate monohydrate ($\text{Cu}(\text{AC})_2$, $(\text{CH}_3\text{COO})_2\text{Cu}\cdot\text{H}_2\text{O}$, $\geq 98\%$), tellurium dioxide (TeO_2 , $\geq 99\%$), potassium hydroxide (KOH , $\geq 98\%$), hydrazine monohydrate ($\text{NH}_2\text{NH}_2\cdot\text{H}_2\text{O}$, 64~65%) and polyvinylpyrrolidone (PVP, $(\text{C}_6\text{H}_9\text{NO})_n$, average molecular weight ~55,000) were purchased from Sigma Aldrich. Tri-n-octylphosphine (TOP, 97%) was purchased from Strem. Ethylene glycol (EG, $\text{HOCH}_2\text{CH}_2\text{OH}$, 99%) was purchased from Fisher. Analytical grade ethanol, isopropanol and acetone were obtained from various sources. All chemicals were used as received without further purification. Syntheses were carried out using a standard vacuum/dry argon Schlenk line.

Synthesis of bismuth telluride nanowires: Bi_2Te_3 nanowires were synthesized following a previously reported protocol.⁴⁸ In a typical synthesis, a mixture of 5.6 mmol of TeO_2 , 56 mL of EG, 37 mmol of KOH and 1.5 g of PVP were added into a three neck flask and heated to 140 °C to completely dissolve them. Afterwards, 0.87 mL hydrazine monohydrate was injected to reduce the Te and the solution was maintained at 140 °C for 1 h. Then temperature was raised to 160 °C and a hot solution of BiCl_3/EG was injected into the flask. The hot BiCl_3/EG solution was prepared by adding 3.6 mmol BiCl_3 into 15 mL EG in a glass vial that was heated to 100–120 °C before injection. The BiCl_3 solution was allowed to react with the tellurium nanowires for 1 h at 160 °C. After that, the mixture was cooled down naturally to room temperature. The products were firstly purified by adding acetone and centrifuging. Then ethanol was used as solvent to disperse the particles and acetone was used as antisolvent to precipitate them. In the next step, deionized water was introduced to dissolve remaining impurities and products were precipitated by slow centrifugation. This procedure was repeated twice. In the last step, particles were dispersed in ethanol and

precipitated with acetone. The final products were dried under vacuum and stored in an Ar-filled glovebox until posterior use.

Synthesis of copper telluride NPs: TOPTe was prepared in an argon filled glovebox one week before synthesis: 6.38 g tellurium powder (0.05 mol) was dissolved in 100 mL TOP to form the 0.5 M tellurium precursor solution (TOPTe) which had a clear yellow color. In a typical synthesis of Cu_{2-x}Te colloidal NPs, 0.3 mmol of $\text{Cu}(\text{AC})_2$ was mixed with 6 ml of OAm in a 25 mL three-neck flask. The mixture was kept under vacuum for 20 min at room temperature and then heated to 120 °C for 60 min under vacuum in order to obtain a clear solution and remove low boiling point impurities. Then the temperature was increased to 220 °C under Ar. After ~10 min, the initial bright yellow solution became light clear brown. At this point, 1.5 mL of the 0.5 M TOPTe was injected into this brown solution, which immediately changed color, to deep green. Upon injection, the temperature of the reaction mixture dropped to ~210 °C. Temperature was allowed to recover to 220 °C and maintained at this point for 1 h. Afterward, the colloidal solution was rapidly cooled to room temperature with a water bath at an initial approximate rate of ~80 °C/min. During the cooling down process, when the solution reached ~70 °C, 2 mL of OAc were added to replace the weakly bound OAm molecules. Finally, 5 mL of chloroform were added to the crude solution and the mixture was sonicated for several minutes. The final deep green product was precipitated by centrifugation at 8000 rpm for 5 min. Then it was redispersed in chloroform and precipitated one more time by centrifugation in the presence of isopropanol. Finally, Cu_{2-x}Te NPs were re-dispersed in chloroform and kept in an Ar-filled glovebox until their posterior use.

Nanomaterial consolidation: Dried Bi_2Te_3 and Cu_{2-x}Te NPs were mixed at the proper ratio in solution. The mixture was sonicated for 1 h to obtain a homogeneous dispersion. Then the NPs were dried out from the solvent. The obtained nanopowder was introduced inside a tube furnace and annealed at 450 °C for 1 h under an Ar flow. The annealed material was loaded into a graphite die and uniaxially hot-pressed into cylinders (Ø 10 mm×10 mm) using

a custom-made hot-press. This process was carried out within an argon-filled glove box. The hot press temperature was set at 290 °C and pressure was increased up to 50 MPa for 5 min. Relative densities of the consolidated pellets were measured by the Archimedes' method. From these cylinders, rectangular bars of about $6 \times 6 \times 1 \text{ mm}^3$ were cut in two normal directions, along and normal to the pressure axis.

Structural and chemical characterization: The morphology and size of the NPs were characterized by TEM using a ZEISS LIBRA 120, operating at 120 kV, and field-emission SEM on an Auriga Zeiss operated at 5.0 kV. XRD (2θ angle: 20° to 80° ; scanning rate: $2^\circ/\text{min}$) analyses were carried out on a Bruker AXS D8 ADVANCE X-ray diffractometer with Cu-K α radiation ($\lambda = 1.5406 \text{ \AA}$). Chemical composition and crystallographic structure were analyzed by high-resolution TEM and EELS using a Tecnai F20 field-emission gun microscope at 200 keV embedded with a Gatan QUANTUM image filter. Additionally, the NPs composition was analyzed using an Oxford energy EDX combined with a Zeiss Auriga SEM at 20.0 kV.

TE property measurement: Electrical resistivity data was obtained using a standard four-probe method. Seebeck coefficients were determined using a static DC method. Electrical resistivity and Seebeck coefficients were measured simultaneously in a LSR-3 LINSEIS system under helium atmosphere, in the temperature range between room temperature and 573 K. 3 measurements were taken at each temperature in each temperature cycle. Considering the system accuracy and the measurement precision, an error of *ca.* 5 % in the measurement of the electrical conductivity and Seebeck coefficients was estimated. The thermal conductivity was calculated according to $\kappa = \lambda C_p \rho$. C_p was calculated from empirical formulas by the Dulong–Petit limit (3R law), and the density (ρ) values used here were measured using the Archimedes' method. Room temperature all charge carrier concentrations (n_H) and mobilities (μ_H) at room temperature (300 K) were obtained from the Van der Pauw method using a magnetic field of 1 T (ezHEMS, NanoMagnetics). Values provided correspond

to the average of 7 measurements, from which an error of ca. 10% was estimated.

5.4 Result and discussion

Bi_2Te_3 NPs were prepared using a two-step process following a previously reported protocol (see detail in experimental section).⁴⁸ The obtained NPs displayed a uniform nanowire geometry with a narrow distribution of diameters (30 ± 10 nm) and lengths (600 ± 80 nm) as observed by transmission electron microscopy (Figure 1a, b). X-ray diffraction (XRD) analysis showed the Bi_2Te_3 particles to be highly crystalline with the Bi_2Te_3 rhombohedral phase (JCPDS NO. 01-082-0358, Figure 1d). High-resolution TEM characterization confirmed the Bi_2Te_3 rhombohedral phase (space group = R-3M) with $a=b=4.2999$ Å and $c=30.5975$ Å. EELS elemental composition maps revealed the homogeneous composition of the nanowires (Figure 1c).

Cu_{2-x}Te nanocrystals were prepared by reacting a solution containing $\text{Cu}(\text{Ac})_2$ with TOPTe at 220 °C in OAm (see experimental section). Figure 1e shows representative TEM of the as-synthesized Cu_{2-x}Te NPs which displayed a cubic/rectangular morphology with a relatively narrow size distribution. The NPs displayed a complex XRD pattern that did not perfectly match any identified pure phase of copper telluride, consistently with previous reports.^{29,30} HRTEM characterization allowed to tentatively assign the crystal structure of the NPs to a $\text{Cu}_{1.81}\text{Te}$ trigonal phase (space group = P3M1) with $a=b=8.3700$ Å, $c=21.6000$ Å (Figure 1g). EELS elemental composition maps showed a homogeneous distribution of the two elements within the Cu_{2-x}Te NPs (Figure 1f).

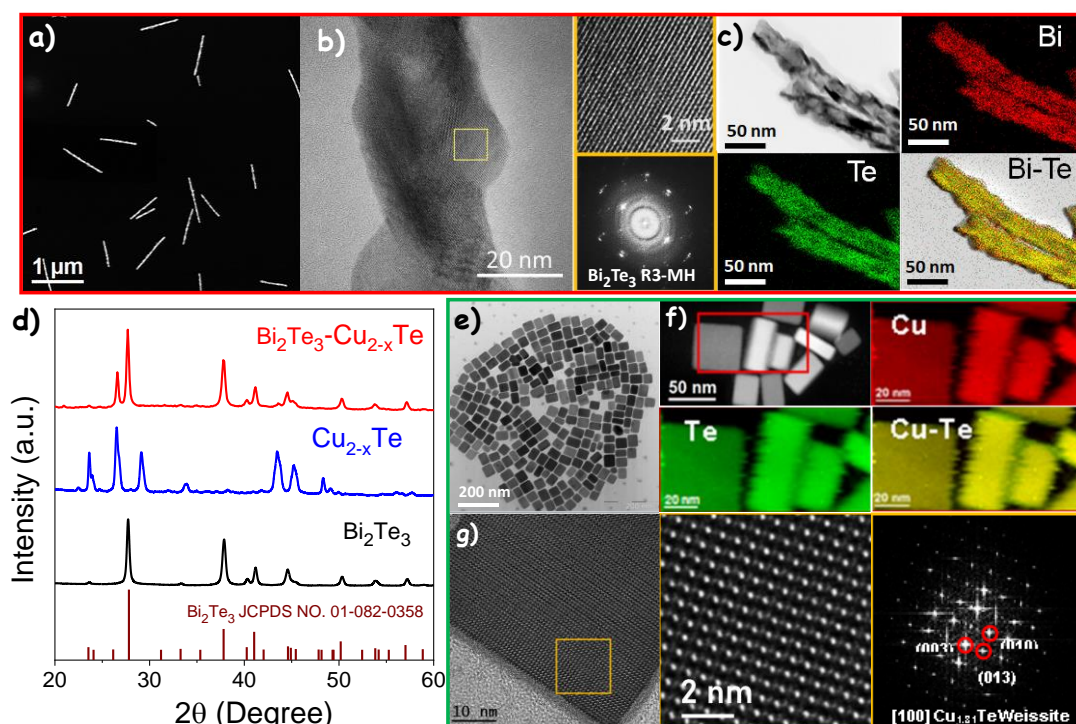


Figure 1. (a) Representative HAADF-STEM and bright field TEM micrographs of Bi_2Te_3 nanowires. (b) HRTEM micrograph, detail of the orange squared region and its corresponding power spectrum. (c) STEM micrograph and EELS chemical composition maps obtained from the red squared area in the STEM micrograph. Bi $\text{N}_{6,7}$ -edge at 157 eV (red), Te $\text{M}_{4,5}$ -edge at 572 eV (green). (d) Powder XRD pattern of as-synthesized Bi_2Te_3 and Cu_{2-x}Te NPs and of a consolidated Bi_2Te_3 - Cu_{2-x}Te NC. (e) Representative TEM images of Cu_{2-x}Te nanocubes. (f) STEM micrograph and EELS chemical composition maps obtained from the red squared area in the STEM micrograph. Cu $\text{L}_{2,3}$ -edges at 931 eV (red), Te $\text{M}_{4,5}$ -edge at 572 eV (green). (g) HRTEM micrograph, detail of the orange squared region and its corresponding power spectrum. Cu_{2-x}Te lattice fringe distances were 0.735 nm, 0.521 nm and 0.733 nm, at 44.21° and 88.65° which was interpreted as the $\text{Cu}_{1.81}\text{Te}$ trigonal phase, visualized along its [100] zone axis.

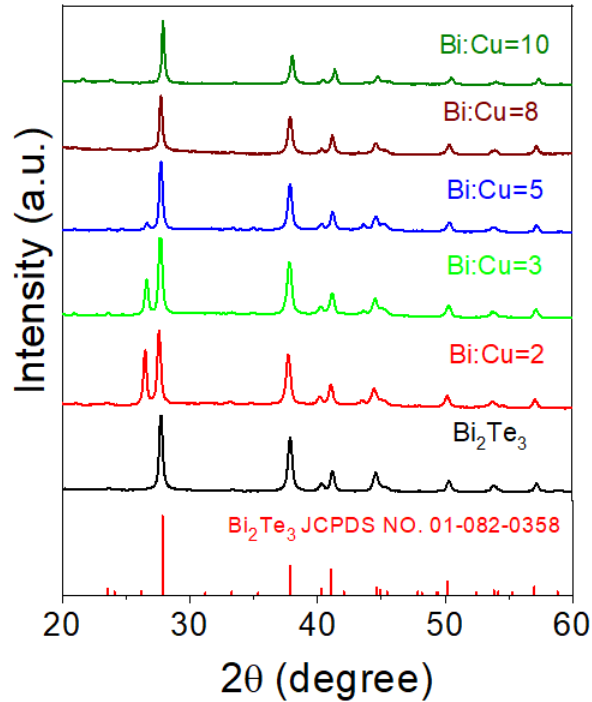


Figure 2. XRD pattern of as-prepared $\text{Bi}_2\text{Te}_3\text{-Cu}_{2-x}\text{Te}$ NCs. Red arrow indicates the position of main peak from Cu_{2-x}Te at $2\theta=26.7^\circ$.

Colloidal Bi_2Te_3 nanowires and Cu_{2-x}Te nanocrystals were mixed at the proper molar ratio ($0 < \text{Bi}/\text{Cu} < 0.5$) in solution (Figure 3a). SEM characterization of the dried mixture revealed a homogeneous dispersion of the two types of particles (Figure 3b). After solvent evaporation, the obtained $\text{Bi}_2\text{Te}_3\text{-Cu}_{2-x}\text{Te}$ nanopowder was annealed at 450°C to remove organic residues. After this process, particles maintained their initial geometry and both phases remained homogeneously dispersed (Figure 3c). Afterwards, the annealed powder was loaded inside a graphite die and hot-pressed into cylindrical pellets with relative densities in the range 85-89 % (Table 1). XRD patterns of the $\text{Bi}_2\text{Te}_3\text{-Cu}_{2-x}\text{Te}$ pellets showed the main peaks of the Bi_2Te_3 phase and a smaller XRD peak at $2\theta = 26.7^\circ$ that was assigned to the same Cu_{2-x}Te phase observed from the Cu_{2-x}Te NPs (Figure 1e, 5). SEM characterization showed the consolidated pellet to conserve the presence of elongated structures resembling the Bi_2Te_3 nanowires, with no obvious grain growth after hot pressing (Figure 6).

EDX analysis of the $\text{Bi}/\text{Cu}=8$ composite showed a $\text{Cu}/\text{Bi}/\text{Te}$ molar ratio around 1/7.6/11.4, and consequently a $\text{Te}/(\text{Bi}+\text{Cu})$ molar ratio close to the

stoichiometric value of 3/2. Similar Te/(Bi+Cu) ratios were obtained for Bi:Cu=5 and Bi:Cu=10 samples (Figure 4). Additionally, EDX compositional maps showed a homogeneous distribution of the three elements at the 100 nm scale.

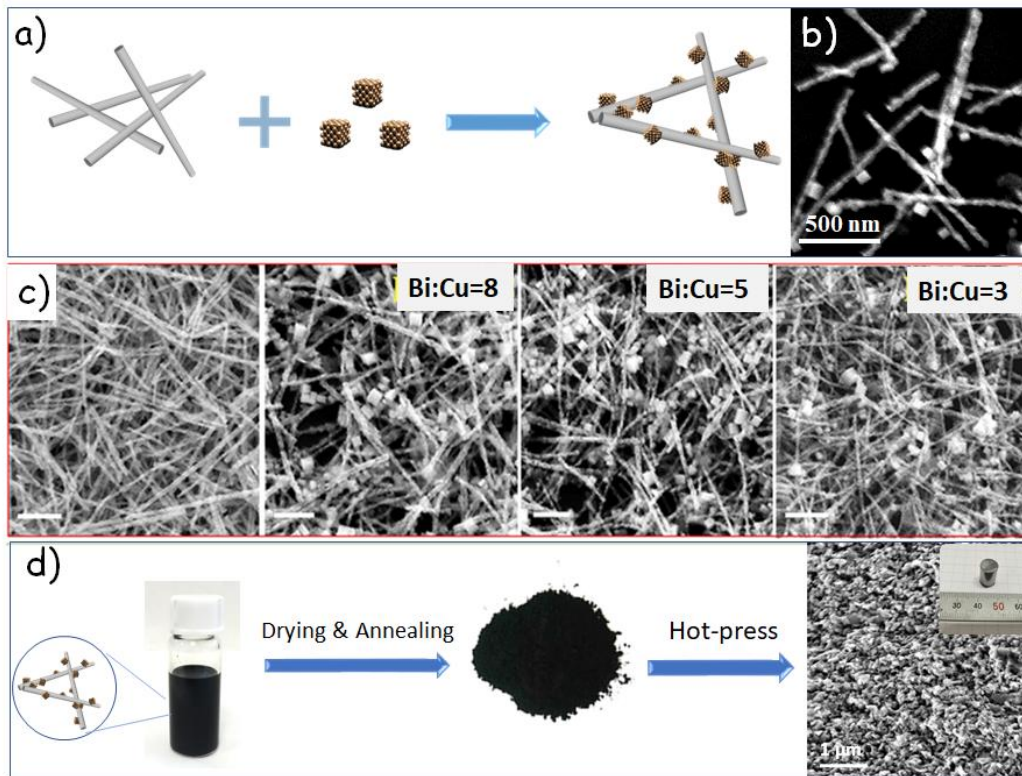


Figure 3. (a) Schematic illustration of the preparation of the of $\text{Bi}_2\text{Te}_3\text{-Cu}_{2-x}\text{Te}$ NCs. (b) Representative SEM images of the dried mixture of Cu_{2-x}Te and Bi_2Te_3 NPs. (c) Representative SEM images of annealed $\text{Bi}_2\text{Te}_3\text{-Cu}_{2-x}\text{Te}$ nanopowders with different phase ratios, scale bar = 200 nm. (d) Schematic illustration of sample drying and cross section SEM image of consolidated pellet.

The TE properties of NCs were measured in two directions, parallel and normal to the pressure axis (Figure 6). In spite of the highly anisotropic structure of Bi_2Te_3 , similar transport properties were obtained in both directions, which I associated to the random orientation of the small crystallites within the NC, i.e. to the lack of crystallographic texture within the nanomaterials. Thus, in the following I discuss in detail only the results obtained in the direction normal to the pressure axis.

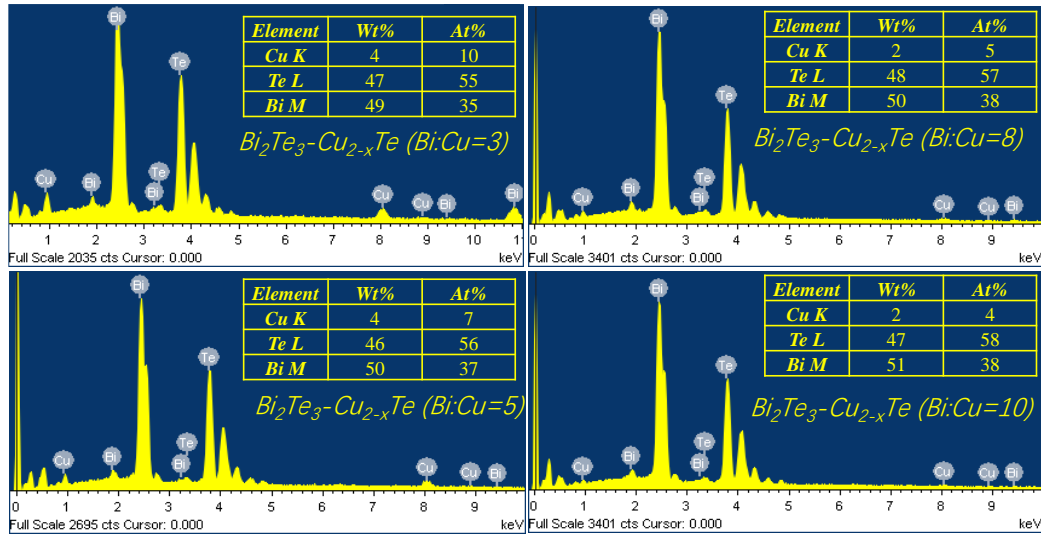


Figure 4. EDX pattern and composition analysis of Bi_2Te_3 and $\text{Bi}_2\text{Te}_3\text{-Cu}_{2-x}\text{Te}$ composites (Bi:Cu=3, 5, 8, 10), respectively.

Figure 7 shows the TE properties of a series $\text{Bi}_2\text{Te}_3\text{-Cu}_{2-x}\text{Te}$ NCs obtained by combining different amounts of Bi_2Te_3 and Cu_{2-x}Te (Bi/Cu=5, 8 and 10). Data for a bare Bi_2Te_3 nanomaterial obtained by annealing and hot pressing just Bi_2Te_3 nanowires was also plotted as a reference.

Bi_2Te_3 showed moderate electrical conductivities, which slightly increased with temperature from 17,800 S/m to 30,300 S/m (Figure 7a). The incorporation of Cu_{2-x}Te resulted in a decrease of both electrical conductivity and Seebeck coefficient at ambient temperature (Figure 7a,b), which translated in lower power factors (Figure 7c). Hall measurements showed the charge carrier concentration at ambient temperature to increase with the presence of Cu_{2-x}Te (Figure 7c), which I associated with the spillover of charges carriers from the Cu_{2-x}Te phase to the Bi_2Te_3 matrix, in line with the much lower electronic affinity of the former.^{31,32} The charge carrier mobility decreased with the presence of Cu_{2-x}Te , consistently with a higher scattering of charge carriers due to the presence of a second phase. Thus the lower electrical conductivity measured at ambient temperature in $\text{Bi}_2\text{Te}_3\text{-Cu}_{2-x}\text{Te}$ NCs compared with bare Bi_2Te_3 was associated to the lower electron mobilities of the former. On the other hand, the lower Seebeck coefficients measured at ambient temperature were consistent with the higher charge carrier concentrations measured in the NCs, as

observed with a Pisarenko plot using a single parabolic band model and an effective mass $m^*=0.30 m_0$ (Figure 8).

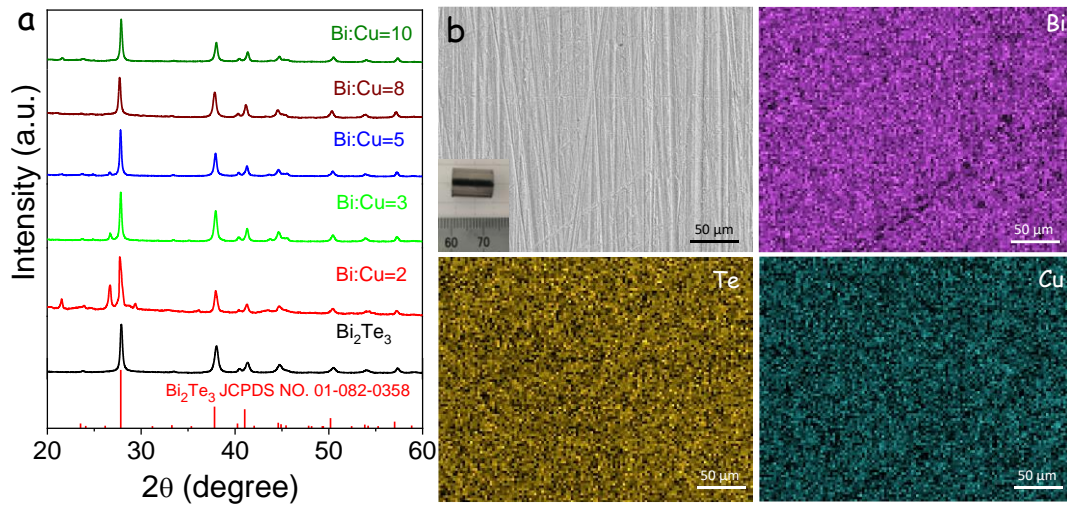


Figure 5. (a) XRD pattern of consolidated Bi₂Te₃-Cu_{2-x}Te pellets with different modulation compositions. (b) SEM micrograph of Bi₂Te₃-Cu_{2-x}Te (Bi:Cu=8) pellet and corresponding EDX mapping analysis of Bi (purple), Te (yellow) and Cu (cyan), respectively.

All NCs were characterized by much stronger dependences of the electrical conductivities and Seebeck coefficients with temperature, when compared with bare Bi₂Te₃. This strong dependence on temperature was ascribed to the important role played by energy barriers on the transport of charge within NCs, i.e. charge carriers strongly relied on an activation energy to move along the NCs. The activation energy was estimated at 130 meV from a linear fitting of $\ln(\sigma T^{1/2})$ with $(kT)^{-1}$. As temperature increased, the electrical conductivity of NCs increased up to values two to threefold higher than those of bare Bi₂Te₃. The Seebeck coefficient showed a parallel evolution but only up to 460 K, because at higher temperatures bipolar effects became dominant. Surprisingly, in spite of the larger charge carrier concentrations measured in NCs and associated to the electron spillover from Cu_{2-x}Te to Bi₂Te₃, much higher Seebeck coefficients were measured for Bi₂Te₃-Cu_{2-x}Te NCs compared with bare Bi₂Te₃ at temperatures above 350 °C. I associate these larger S values to an energy related differential scattering of charge carriers at energy barriers within the NC, i.e. to

an energy filtering effect.

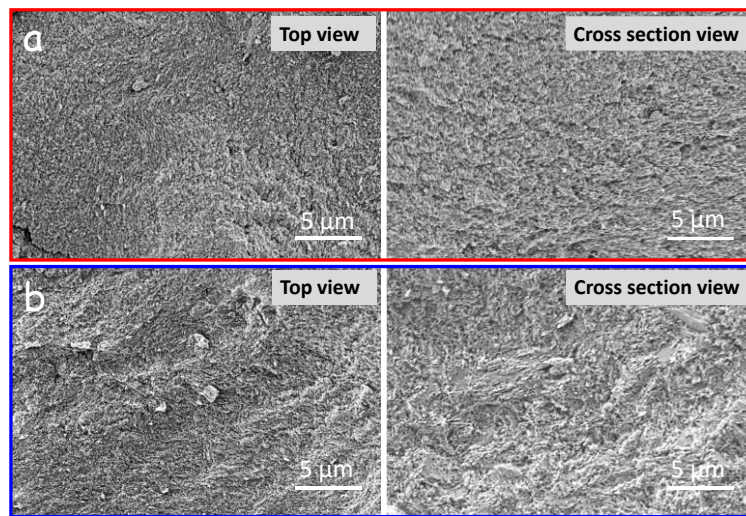


Figure 6. SEM micrographs of (a) Bi_2Te_3 and (b) $\text{Bi}_2\text{T}_3\text{-Cu}_{2-x}\text{Te}$ (Bi:Cu=8) consolidated pellets in two perpendicular directions as marked in with the insert graphs.

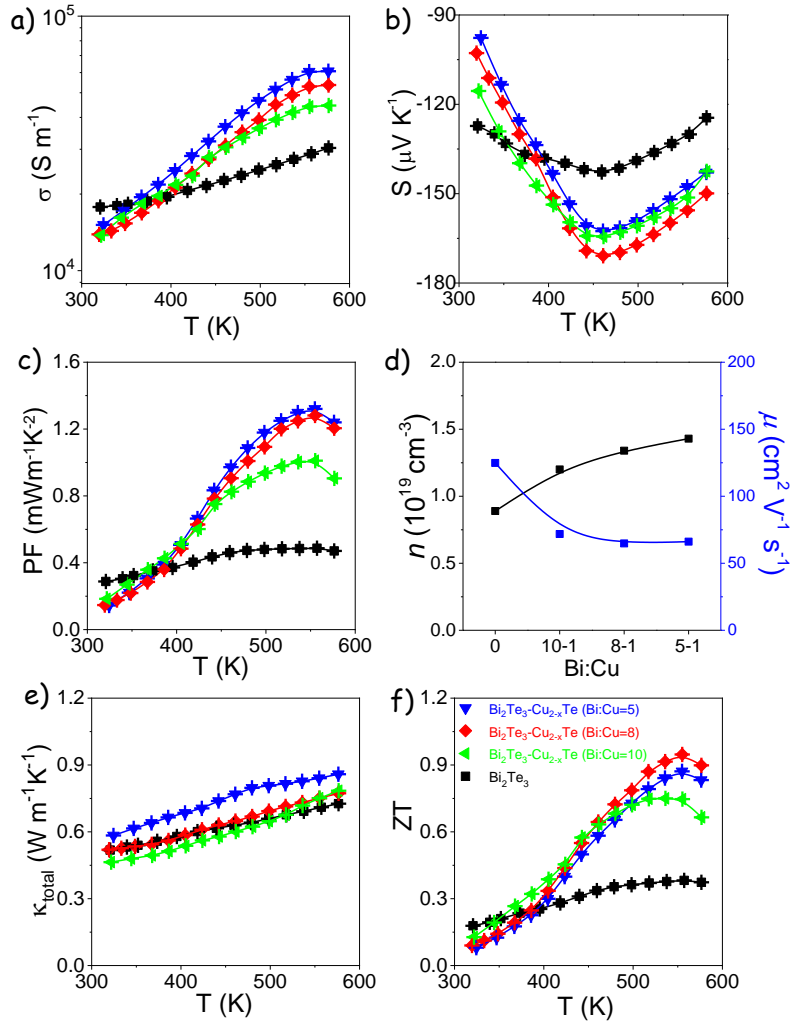


Figure 7. Temperature dependence of TE properties of $\text{Bi}_2\text{Te}_3\text{-Cu}_{2-x}\text{Te}$ pellets: (a) electric conductivity, σ ; (b) Seebeck coefficient, S ; (c) power factor or $S^2\sigma$; (d) room temperature charge carrier concentration and mobility; (e) total thermal conductivity, κ_{total} ; (f) TE figure of merit, ZT .

I believe that owing to the large difference in electron affinity between Cu_{2-x}Te and Bi_2Te_3 , when nanodomains of the two materials are combined, Cu_{2-x}Te injects electrons to Bi_2Te_3 , modifying the electron energy band structure of both materials. The Bi_2Te_3 region nearby the heterojunction becomes flooded with electrons and its electron energy bands suffer an important downward bending (Figure 10). Thus injected electrons need to overcome an energy barrier to freely move around the material. At the same time, free but low energy electrons within Bi_2Te_3 might become trapped in these potential wells (Figure 10). Thus within

$\text{Bi}_2\text{Te}_3\text{-Cu}_{2-x}\text{Te}$, free electrons with higher energies are characterized by higher mobilities than lower energy electrons, which results in higher Seebeck coefficients. This enhancement of the Seebeck coefficient associated with the presence of $\text{Bi}_2\text{Te}_3/\text{Cu}_{2-x}\text{Te}$ heterojunctions competes with the decrease of the Seebeck coefficient due to the higher charge carrier concentration. These two competing effects resulted in a non-monotonous dependence of the maximum Seebeck coefficient with the amount of Cu_{2-x}Te introduced. Seebeck coefficients of $\text{Bi}_2\text{Te}_3\text{-Cu}_{2-x}\text{Te}$ NC reached the highest value for the Bi/Cu=8 sample at 460 K, $-170 \mu\text{V/K}$. In all $\text{Bi}_2\text{Te}_3\text{-Cu}_{2-x}\text{Te}$ NCs, at moderate temperatures, the concomitant increase of electrical conductivity and Seebeck coefficient when compared with bare Bi_2Te_3 resulted in a significant increase of the power factor, up to 1.32 at 554 K.

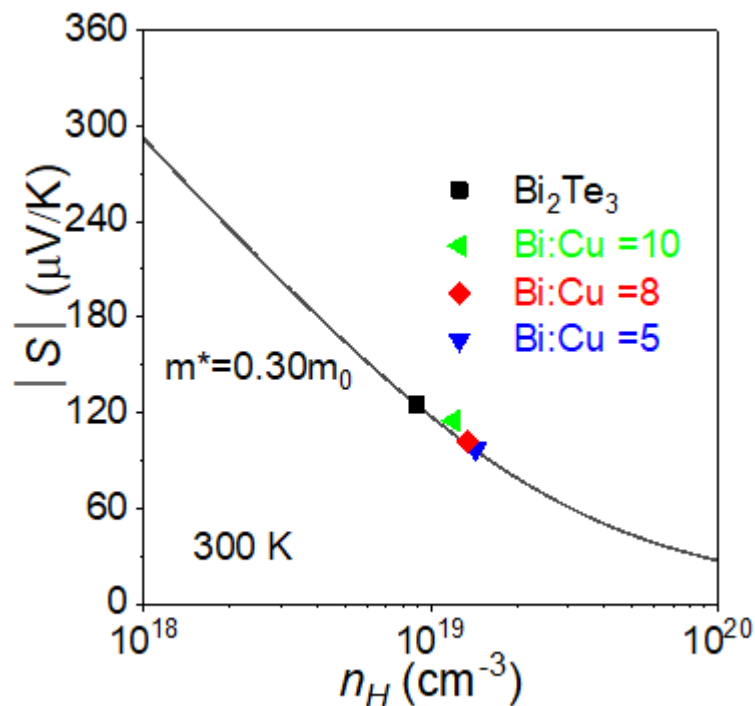


Figure 8. Experimental data and theoretical Seebeck values as a function of carrier concentration calculated by single parabolic band model.

Notice that on the contrary to previous reports,⁴⁰ the temperature of the maximum Seebeck coefficient remained unaltered with the Cu_{2-x}Te introduction.

This experimental result points toward a moderate contribution of the amount of injected charge carriers to the total electron concentration at the temperature at which the free electron concentration is matched by the thermal generated carriers.

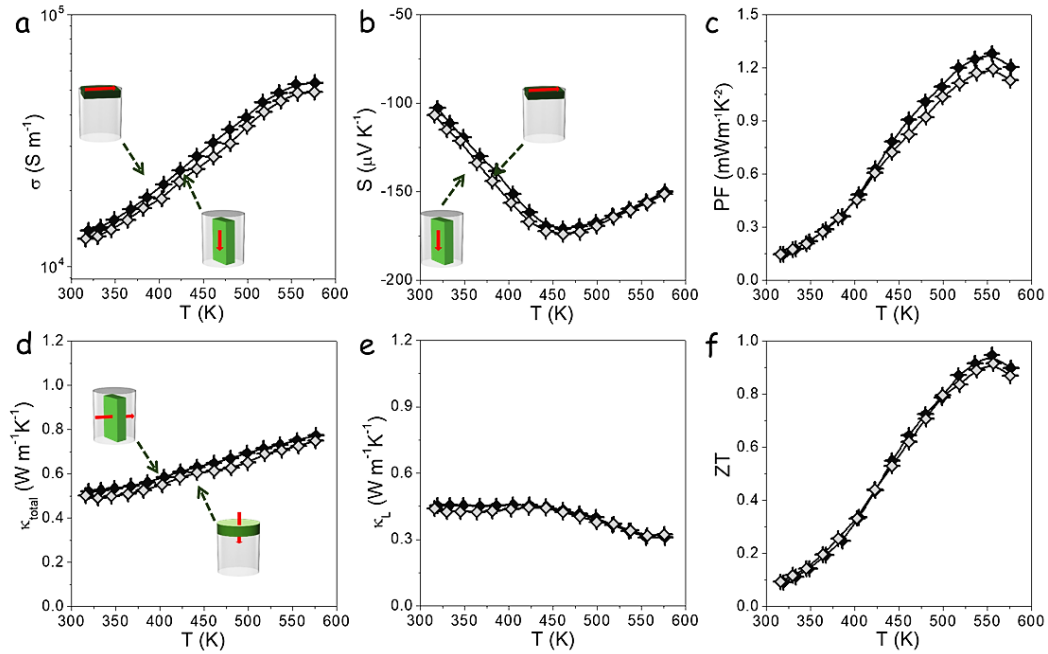


Figure 9. Temperature dependence of TE properties of $\text{Bi}_2\text{Te}_3\text{-Cu}_{2-x}\text{Te}$ (Bi:Cu=8) in both directions: (a) electric conductivity, σ ; (b) Seebeck coefficient, S ; (c) power factor or $S^2\sigma$, PF; (d) total thermal conductivity, κ_{total} ; (e) lattice thermal conductivity, κ_L ; (f) TE figure of merit, ZT.

Table 1. Density of hot pressed $\text{Bi}_2\text{Te}_3\text{-Cu}_{2-x}\text{Te}$ pellet samples.

Samle	Density (g/cm^3)	Relative Density
Bi_2Te_3	6.57	85.3%
$\text{Bi}_2\text{Te}_3\text{-CuTe}$ (Bi:Cu=10)	6.52	85.7%
$\text{Bi}_2\text{Te}_3\text{-CuTe}$ (Bi:Cu=8)	6.64	88.5%
$\text{Bi}_2\text{Te}_3\text{-CuTe}$ (Bi:Cu=5)	6.49	87.7%

On the other hand, the thermal conductivities of all the nanomaterials tested here

were very low when compared with that of highly crystalline Bi_2Te_3 . However, the thermal conductivities of $\text{Bi}_2\text{Te}_3\text{-Cu}_{2-x}\text{Te}$ NCs were not significantly lower than those of the Bi_2Te_3 nanomaterial because the decrease of the lattice thermal conductivity associated with an enhanced phonon scattering in the composite was compensated by an increase of the electronic contribution (Figure 3e).

Figure 3f displays the figure of merit obtained from $\text{Bi}_2\text{Te}_3\text{-Cu}_{2-x}\text{Te}$ NCs and the bare Bi_2Te_3 nanomaterial. For Bi_2Te_3 , a maximum $ZT = 0.38$ was achieved at 560 K, which is a notable value for bare Bi_2Te_3 . As for $\text{Bi}_2\text{Te}_3\text{-Cu}_{2-x}\text{Te}$ NCs, the largest ZT value was obtained from the $\text{Bi}/\text{Cu}=8$ sample, reaching a $ZT = 0.94$ at 576 K. The highly improved figures of merit ZT from $\text{Bi}_2\text{Te}_3\text{-Cu}_{2-x}\text{Te}$ NCs was associated to two factors: (1) An effective electron spillover from Cu_{2-x}Te nanoinclusions to Bi_2Te_3 matrix to improve electrical conductivity; and (2) the energy filtering of charge carriers at energy wells introduced within Bi_2Te_3 by the nearby presence of a Cu_{2-x}Te domain, and which significantly enhanced the Seebeck coefficient.

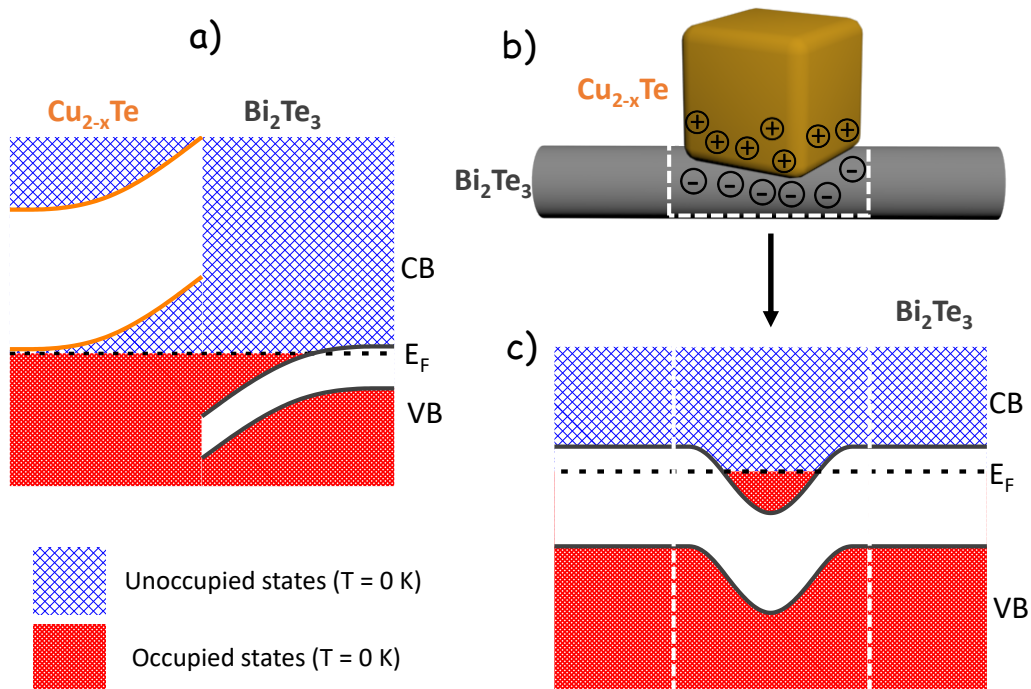


Figure 10. (a) Electron energy band diagram at a heterojunction between Cu_{2-x}Te and Bi_2Te_3 . (b) Charge distribution within a Bi_2Te_3 nanowire in contact with a Cu_{2-x}Te cubic NP. (c) Electron energy band diagram of the same Bi_2Te_3

nanowire having a Cu_{2-x}Te NP on its surface.

5.5 Conclusions

In summary, I detailed a simple bottom-up procedure to produce $\text{Bi}_2\text{Te}_3\text{-Cu}_{2-x}\text{Te}$ NCs with adjusted composition from combining proper ratios of solution processed Bi_2Te_3 and Cu_{2-x}Te building blocks. With the introduction of Cu_{2-x}Te , the electrical conductivity of Bi_2Te_3 was greatly improved by charge carrier spillover from the lower work function Cu_{2-x}Te domains to the Bi_2Te_3 matrix. This electron spillover from the Cu_{2-x}Te valence band to the Bi_2Te_3 conduction band, resulted in regions of accumulated electrons within the Bi_2Te_3 domains. In these composites, the Seebeck coefficient was also significantly increased by filtering the low energy carriers at potential wells created at $\text{Bi}_2\text{Te}_3\text{-Cu}_{2-x}\text{Te}$ interfaces. The enhanced Seebeck coefficient, together with improved electrical conductivity resulted in a 3-fold increase in power factor. While NCs did not provide lower thermal conductivities than bare Bi_2Te_3 , the thermal conductivity of all the tested nanomaterials was already very low. As a consequence, a significant improvement of figure of merit was observed, from 0.35 to 0.95 at 560 K.

5.6 References

1. Sootsman, J. R.; Chung, D. Y.; Kanatzidis, M. G., *Angew Chem. Int. Ed.* **2009**, *48* (46), 8616-8639.
2. Wood, C., *Rep. Prog.* **1988**, *51* (4), 459.
3. Snyder, G. J.; Toberer, E. S., World Scientific: 2011; pp 101-110.
4. Ortega, S.; Ibáñez, M.; Liu, Y.; Zhang, Y.; Kovalenko, M. V.; Cadavid, D.; Cabot, A., *Chem. Soc. Rev.* **2017**, *46* (12), 3510-3528.
5. Min, Y.; Roh, J. W.; Yang, H.; Park, M.; Kim, S. I.; Hwang, S.; Lee, S. M.; Lee, K. H.; Jeong, U., *Adv. Mater.* **2013**, *25* (10), 1425-1429.
6. Yu, B.; Zebarjadi, M.; Wang, H.; Lukas, K.; Wang, H.; Wang, D.; Opeil, C.; Dresselhaus, M.; Chen, G.; Ren, Z., *Nano Lett.* **2012**, *12* (4), 2077-2082.
7. Zhao, X.; Ji, X.; Zhang, Y.; Zhu, T.; Tu, J.; Zhang, X., *Appl. Phys. Lett.* **2005**, *86*

(6), 062111.

8. Wang, Y.; Liu, W.-D.; Shi, X.-L.; Hong, M.; Wang, L.-J.; Li, M.; Wang, H.; Zou, J.; Chen, Z.-G., *Chem. Eng.* **2019**, 123513.
9. Shi, X. L.; Tao, X.; Zou, J.; Chen, Z. G., *Adv. Sci.* **2020**, 7, 1902923.
10. Roychowdhury, S.; Biswas, R. K.; Dutta, M.; Pati, S. K.; Biswas, K., *ACS Energy Lett.* **2019**, 4 (7), 1658-1662.
11. Chandra, S.; Biswas, K., *J. Am. Chem. Soc.* **2019**, 141 (15), 6141-6145.
12. Liu, Y.; Zhang, Y.; Lim, K. H.; Ibáñez, M.; Ortega, S.; Li, M.; David, J.; Martí-Sánchez, S.; Ng, K. M.; Arbiol, J.; Kovalenko, M. V.; Cadavid, D.; Cabot, A., *ACS nano* **2018**, 12 (7), 7174-7184.
13. Liu, Y.; Zhang, Y.; Ortega, S.; Ibáñez, M.; Lim, K. H.; Grau-Carbonell, A.; Martí-Sánchez, S.; Ng, K. M.; Arbiol, J.; Kovalenko, M. V.; Cadavid, D.; Cabot, A., *Nano lett.* **2018**, 18 (4), 2557-2563.
14. Zhang, Y.; Liu, Y.; Lim, K. H.; Xing, C.; Li, M.; Zhang, T.; Tang, P.; Arbiol, J.; Llorca, J.; Ng, K. M.; M, Ibáñez.; Guardia, P.; Prato, M.; Cadavid, D.; Cabot, A., *Angew. Chem.* **2018**, 130 (52), 17309-17314.
15. Ibáñez, M.; Hasler, R.; Genç, A.; Liu, Y.; Kuster, B.; Schuster, M.; Dobrozhan, O.; Cadavid, D.; Arbiol, J.; Cabot, A. *J. Am. Chem. Soc.* **2019**, 141 (20), 8025-8029.
16. Ibáñez, M.; Hasler, R.; Liu, Y.; Dobrozhan, O.; Nazarenko, O.; Cadavid, D.; Cabot, A.; Kovalenko, M. V., *Chem. Mater.* **2017**, 29 (17), 7093-7097.
17. Ibáñez, M.; Genç, A.; Hasler, R.; Liu, Y.; Dobrozhan, O.; Nazarenko, O.; Mata, M. a. d. l.; Arbiol, J.; Cabot, A.; Kovalenko, M. V., *ACS nano* **2019**, 13 (6), 6572-6580.
18. Liu, Y.; Cadavid, D.; Ibáñez, M.; Ortega, S.; Martí-Sánchez, S.; Dobrozhan, O.; Kovalenko, M. V.; Arbiol, J.; Cabot, A., *Apl Mater.* **2016**, 4 (10), 104813.
19. Ibáñez, M.; Korkosz, R. J.; Luo, Z.; Riba, P.; Cadavid, D.; Ortega, S.; Cabot, A.; Kanatzidis, M. G., *J. Am. Chem. Soc.* **2015**, 137 (12), 4046-4049.
20. Cadavid, D.; Ortega, S.; Illera, S.; Liu, Y.; Ibáñez, M.; Shavel, A.; Zhang, Y.; Li, M.; López, A. M.; Noriega, G.; O, Dura.; M, Torre.; J, Prades.; Cabot, A., *ACS Appl. Energy Mater.* **2020**, 3 (3), 2120-2129.
21. Ibáñez, M.; Luo, Z.; Genc, A.; Piveteau, L.; Ortega, S.; Cadavid, D.; Dobrozhan, O.; Liu, Y.; Nachttegaal, M.; Zebarjadi, M.; Arbiol, J.; Kovalenko, M. V.; Cabot, A., *Nature comm.* **2016**, 7, 10766.
22. Poudel, B.; Hao, Q.; Ma, Y.; Lan, Y.; Minnich, A.; Yu, B.; Yan, X.; Wang, D.; Muto, A.; Vashaee, D.; Chen, X.; Liu, J.; Dresselhaus, M.; Chen, G.; Ren, Z., *Science* **2008**, 320 (5876), 634-638.

23. Hu, L.; Zhu, T.; Liu, X.; Zhao, X., *Adv. Funct. Mater.* **2014**, *24* (33), 5211-5218.
24. Liu, Y.; Zhou, M.; He, J., *Scr. Mater.* **2016**, *111*, 39-43.
25. Hong, M.; Chasapis, T. C.; Chen, Z.-G.; Yang, L.; Kanatzidis, M. G.; Snyder, G. J.; Zou, J., *ACS nano* **2016**, *10* (4), 4719-4727.
26. Zhao, L.; Zhang, B.-P.; Liu, W.; Zhang, H.; Li, J.-F., *J. Alloys Compd.* **2009**, *467* (1-2), 91-97.
27. Zhao, L.; Zhang, B.-P.; Li, J.-F.; Zhang, H.; Liu, W., *Solid State Sci.* **2008**, *10* (5), 651-658.
28. Zhao, L.-D.; Zhang, B.-P.; Liu, W.-S.; Li, J.-F., *J. Appl. Phys.* **2009**, *105* (2), 023704.
29. Zhao, L.-D.; Zhang, B.-P.; Li, J.-F.; Zhou, M.; Liu, W.-S.; Liu, J., *J. Alloys Compd.* **2008**, *455* (1-2), 259-264.
30. Bao, D.; Chen, J.; Yu, Y.; Liu, W.; Huang, L.; Han, G.; Tang, J.; Zhou, D.; Yang, L.; Chen, Z.-G., Texture-dependent TE properties of nano-structured Bi₂Te₃. *Chem. Eng.* **2020**, *388*, 124295.
31. Yan, X.; Poudel, B.; Ma, Y.; Liu, W.; Joshi, G.; Wang, H.; Lan, Y.; Wang, D.; Chen, G.; Ren, Z., *Nano lett.* **2010**, *10* (9), 3373-3378.
32. Hong, M.; Chen, Z. G.; Yang, L.; Zou, J., *Nano Energy* **2016**, *20*, 144-155.
33. Cha, J.; Zhou, C.; Cho, S.-P.; Park, S. H.; Chung, I., *ACS Appl. Mater. Interfaces.* **2019**, *11* (34), 30999-31008.
34. Seo, K. H.; Kim, B. G.; Lim, C.-H.; Kim, S.-H.; Lee, K.-M.; Kim, J.-Y.; Choi, S.-M., *CrystEngComm* **2017**, *19* (20), 2750-2757.
35. Sinduja, M.; Amirthapandian, S.; Masarrat, A.; Krishnan, R.; Srivastava, S.; Kandasami, A., *Thin Solid Films* **2020**, *697*, 137834.
36. Bludska, J.; Jakubec, I.; Drašar, Č.; Lošřák, P.; Horak, J., *Philos. Mag.* **2007**, *87* (2), 325-335.
37. Wu, H.-J.; Yen, W.-T., *Acta Materialia* **2018**, *157*, 33-41.
38. Zhuang, H.-L.; Pan, Y.; Sun, F.-H.; Dong, J.; Pei, J.; Cai, B.; Hu, H.; Tang, H.; Li, J.-F., *Nano Energy* **2019**, *60*, 857-865.
39. Zhu, W.; Hu, W.; Wei, P.; Nie, X.; Zhao, W., *Journal of Electronic Materials* **2020**, *49*, 2962-2967.
40. Song, J. M.; Rahman, J. U.; Cho, J. Y.; Lee, S.; Seo, W. S.; Kim, S.; Kim, S.-i.; Lee, K. H.; Roh, D.; Shin, W. H., *Scr. Mater.* **2019**, *165*, 78-83.

41. Liu, W. S.; Zhang, Q.; Lan, Y.; Chen, S.; Yan, X.; Zhang, Q.; Wang, H.; Wang, D.; Chen, G.; Ren, Z., *Adv. Energy Mater.* **2011**, *1* (4), 577-587.
42. Lognoné, Q.; Gascoin, F., *Journal of alloys and compounds* **2014**, *610*, 1-5.
43. Huang, M.; Maljusch, A.; Calle-Vallejo, F.; Henry, J. B.; Koper, M. T.; Schuhmann, W.; Bandarenka, A. S., *RSC Adv.s* **2013**, *3* (44), 21648-21654.
44. Ballikaya, S.; Chi, H.; Salvador, J. R.; Uher, C., *Journal of Materials Chemistry A* **2013**, *1* (40), 12478-12484.
45. Qiu, Y.; Liu, Y.; Ye, J.; Li, J.; Lian, L., *J. Mater. Chem. A* **2018**, *6* (39), 18928-18937.
46. Mallick, M. M.; Vitta, S., *J. Appl. Phys.* **2017**, *122* (2), 024903.
47. Zhao, K.; Liu, K.; Yue, Z.; Wang, Y.; Song, Q.; Li, J.; Guan, M.; Xu, Q.; Qiu, P.; Zhu, H., *Adv. Mater.* **2019**, *31* (49), 1903480.
48. Zhang, G.; Kirk, B.; Jauregui, L. A.; Yang, H.; Xu, X.; Chen, Y. P.; Wu, Y., *Nano lett.* **2012**, *12* (1), 56-60.

Result and Discussions

The TE nanomaterials included in this thesis are produced by solution processing technologies, directly from atomic or molecular precursors in a controlled manner. The synthesis of nanocrystals in solution enables the cost effective production of large amounts of nanostructured material even with higher levels of control over nanodomain parameters than other technologies as allow control of material parameters in the three dimensions. In this regards, SnSe₂ hexagonal NPLs were firstly synthesized by a fast solution-based methodology that makes use of molecular inks taht decompose directly at moderate temperature. The molecular precursor was simply prepared by mixing tin and selenium powder in an organic amine-dithiol mixture to form a liquid ink. The synthetic procedure can be easily scaled up and applied to printed patterns, paving the way for commercial application. Then we applied this effective methodology in our second work to do large scale synthesis of nanocrystalline SnSe. At the same time, we improve the ink component to get a thiol-free SnSe molecular ink to minimize its toxicity, which can be directly printed into SnSe layers. The shape evolution of SnSe NPLs was also systematically investigated by introducing small amount of surfactant (oleic acid) into SnSe ink, which allows to form dendritic structures from a square shape in a controlled way. Meanwhile, both SnSe₂ and SnSe are 2D materials, which are formed by atomically thin layers that display strong covalent in plane bonding and weak layer-to-layer bonding. Since properly designed NCs allow improving TE performance by several mechanisms, including phonon scattering, modulation doping and energy filtering, we subsequently focus on producing nanomaterials with more complicated phase and structure. A two-step solution-based process to produce the Bi₂Te₃-Cu_{2-x}Te nanoheterostructures was investigated, based on the growth of Cu_{2-x}Te nanocrystals on the surface of Bi₂Te₃ nanowires. Bi₂Te₃-Cu_{2-x}Te heterostructures with tuned molar ratio (Bi:Cu= 10; 8; 5) were synthesized by adjusting the concentration of precursor ratio of Bi:Cu. This synthesis protocol was carried out at a sufficient scale to produce 4 g of material per batch. On the

other hand, colloidal synthesis routes also allow producing multi-material nanostructures with organized phase distribution. $\text{Bi}_2\text{Te}_3\text{-Cu}_{2-x}\text{Te}$ NCs were produced by mixing proper amounts of individual Bi_2Te_3 and Cu_{2-x}Te colloidal NPs, as a comparison of forming heterostructures. This strategy allows to precisely turning on various parameters e.g. size and shape, on each NP building blocks through solution-based bottom-up synthetic method, which makes it available to produce $\text{Bi}_2\text{Te}_3\text{-Cu}_{2-x}\text{Te}$ NCs with adjusted composition from combining proper ratios of Bi_2Te_3 nanowires and cubic Cu_{2-x}Te nano building blocks.

As-synthesized SnSe_2 , SnSe , Bi_2Te_3 and Cu_{2-x}Te NPs are stabilized by a layer of organic surfactants attached to their surface, for example OAm, ethylene glycol and TOP, which have been used to control their growth. The presence of such organic ligands at the surface of NPs strongly limits the material performance in any application where charge transport or transfer from/to/between NPs is involved. The strategy to remove surface organic ligands in this thesis is to apply an annealing process at relative high temperature (higher than organic ligands' boiling point) under Ar gas atmosphere for 1 hour. The annealed SnSe_2 particles still displayed plate-like geometries but with larger lateral dimensions. The size and shape of SnSe , Bi_2Te_3 and Cu_{2-x}Te NPs keep relative stable after annealing process. The initial particle geometry would influence the texture of the final polycrystalline material after consolidation process (hot press). The hot pressed SnSe_2 and SnSe material displayed a clear crystallographic texture, with a certain crystal direction oriented along the pressure axis, which is mainly origin from their initial 2D NPL structure.

The TE performance has been studied by testing electric and thermal transport properties of consolidated nanomaterials in a wide temperature range. The overall TE (TE) figures of merit of layered structure n-type SnSe_2 and p-type SnSe nanomaterials is limited by their relatively low electrical conductivity. Two different strategies were applied to improve electrical conductivity. An atomic substitution doping strategy was applied for p-type semiconductor SnSe . Small

amounts of Te were added to the ink in replacement of equivalent amounts of Se, which result in a slightly reduced band gap in obtained $\text{SnSe}_{1-x}\text{Te}_x$. The presence of this small amount of Te resulted in an important increase of electrical conductivity cross plane associated to an increase of charge carrier concentration and especially mobility with a minor variation of the Seebeck coefficient. Being SnSe_2 an n-type semiconductor, we selected Ag NPs as a dopant phase with a large charge carrier concentration and a relatively low work function that allowed injection of electrons to the SnSe_2 matrix. A large increase of electric conductivity and a moderate decrease of the Seebeck coefficient were observed with the Cu NPs introduction in both directions. This translated into significantly larger power factors in the SnSe_2 -Cu NC when compared with pure SnSe_2 . The thermal conductivity of SnSe_2 -Cu was significantly reduced in plane with respect to SnSe_2 , due to the additional scattering at Cu nanoinclusions. Since NCs are particularly appealing in the TE field, we produced Bi_2Te_3 - Cu_{2-x}Te NCs by two approaches: i) Bi_2Te_3 - Cu_{2-x}Te heterostructured NPs and ii) mixing proper ratios of Bi_2Te_3 nanowires and cubic Cu_{2-x}Te NPs, and compared their difference in TE properties. We observed the presence of Cu_{2-x}Te in both cases result in higher ZT values measured in Bi_2Te_3 - Cu_{2-x}Te NCs compared with bare Bi_2Te_3 , which were attributed to a combination of several features: i) the large electrical conductivities measured in the NCs at high temperature, mainly associated to the spillover of charge carrier from Cu_{2-x}Te domains to the Bi_2Te_3 matrix; ii) the enhanced Seebeck coefficients without sacrificing electrical conductivity in the high temperature range associated with the energy-filtering of charge carriers at potential barriers introduced with the formation of the $\text{Bi}_2\text{Te}_3/\text{Cu}_{2-x}\text{Te}$ heterojunctions. The significant difference in these two composites is the mixed NCs did not provide lower thermal conductivities than bare Bi_2Te_3 , while an enhanced phonon scattering at the interphase of $\text{Bi}_2\text{Te}_3/\text{Cu}_{2-x}\text{Te}$ heterojunctions notably reduced the thermal conductivity. This inspires us to rationally design TE NCs in future work.

Conclusions

In this thesis, I detailed the production and characterization of TE nanomaterials by two main solution processed strategies, with remarkably improved TE performance by means of controllable nanoengineering and particularly NCs. The characterization of nanomaterials has been detailed investigated in each project, including: nanocrystal phase, morphology, optical property, surface chemistry, etc. The TE performance has been studied by testing electric and thermal transport properties of consolidated nanomaterials in a wide temperature range. Two main optimization methodologies to achieve higher TE performance were specifically explored in this thesis: atomic doping and modulation doping approach. The related mechanism to improved TE performance was further analyzed to explain how to achieve desired TE properties.

In the first part, I have investigated a SnSe₂ molecular precursor decomposition approach to produce hexagonal SnSe₂ NPL by screw dislocation-driven mechanism which contribute to crystallographically textured structure after consolidation. From this work I concluded that the electrical conductivities could be improved by blending SnSe₂ NPL with Cu NPs which lead to a three-fold increase in the TE figure of merit compared with bare SnSe₂. Afterwards, I demonstrated that crystallographic textured SnSe bulk nanomaterials and layers could be obtained after hot-pressing the SnSe nanomaterials produced from molecular ink. I concluded the SnSe TE performance could be significantly improved by introducing small amounts of Te during ink formulation, which enhanced electrical conductivity cross plane associated to an increase of charge carrier concentration and especially mobility with a minor variation of the Seebeck coefficient. In the third part, I produced heterostructured Bi₂Te₃-Cu_{2-x}Te composites by means of bottom-up approach. From this work, I concluded that a significantly low thermal conductivity was achieved by efficiently phonon scattering at grain boundaries, together with enhanced Seebeck coefficient through filtering of charge carriers at energy barriers. These effects result in an improvement of over 50% of the TE figure of merit of Bi₂Te₃. As a comparison,

I detailed another strategy to produce $\text{Bi}_2\text{Te}_3\text{-Cu}_{2-x}\text{Te}$ NCs in the last part, by mixing proper ratios of building blocks of Bi_2Te_3 nanowires and Cu_{2-x}Te nanocubes. From this work, I concluded that 3-fold increase in ZT could be obtained from the enhanced Seebeck coefficient and improved electrical conductivity compared with bare Bi_2Te_3 nanomaterials. As a consequence, a significant improvement of figure of merit was observed, from 0.35 to 0.95 at 560 K, which is significantly higher than ZT obtained in heterostructure-based NCs.

In summary, this thesis has detailed different strategies to improve TE performance of bulk nanomaterials produced from solution processed methods with well controlled parameters. In addition, it has been demonstrated that solution processed synthesis appears to be a high-throughput, high yield, low cost, feasible at ambient pressure and low temperature chemical routes, which allows production of TE materials with composition, size, shape and phases control to optimize their TE properties.

Future work

The concept of using nanocrystals as building blocks to create NCs is extremely appealing, but slow movement is being achieved in terms of industrialization and TE devices development.

The industrialization of solution-processed nanomaterials will require major engineering innovations. The scale-up of the procedures used to produce high-quality nanocrystals is not fully addressed, especially for applications with big potential markets that demands for low costs and large batches of functional nanomaterials, as thermoelectricity. Scale-up will inevitably means achieve near to 100% yields, very high NP concentrations in solution, cost effective and safe solvents, precursors, surfactant and reductants and the recycling of chemicals and possibly side products. Future work should focus on improving our atomistic understanding of the pathways of precursor-to-NP reaction through mechanistic experimental investigation and fundamental theoretical chemistry simulations, to be able to adjust the process not only in terms of NP parameters but also the cost and repeatability.

Another future work is to fabricate prototype TE devices and test their efficiency. This would help to accelerate the selection and development of new TE materials. For thin film TE devices, apart from common difficulties such as crack formation and layer adhesion, a major challenge is to produce densified layers with sufficient thickness and contact them at two different planes needed to be overcome. Some emerging manufacturing technologies based on material jetting such as 3D printing may offer significant help to this area.

CURRICULUM VITAE

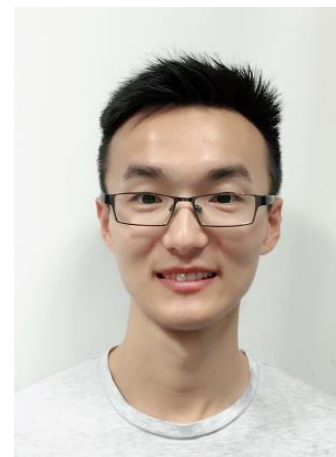
Name: Yu Zhang

Address: Jardins de les Dones de Negre, 1, Barcelona

Tel: +34 652407338

Email: peterzhang@irec.cat

Date of Birth: September 2, 1990



Education

10/2016- 09/2020 PhD, Nanoscience, Catalonia Institute for Energy Research-
IREC, University of Barcelona, Spain

- ✧ Dissertation: Solution processed chalcogenide nanomaterials for TE application
- ✧ Supervisor: Andreu Cabot.

09/2014 – 09/2016 Master, Erasmus Mundus: Chemical Innovation and
Regulation

- ✧ 09/2014-07/2015, University of Barcelona, Barcelona, Spain
- ✧ 09/2015-07/2016, Heriot-Watt University, Edinburgh, UK
- ✧ Supervisor: Helinor Johnston

09/2012-07/2014 Master, Chemical Engineering, Central South University,
China

09/2008-07/2012 Bachelor, Chemical Engineering, Anqing Normal
University, China

Research Experience

My PhD research is focused on optimizing TE performance of metal chalcogenide (CuX, SnX, BiX) by using precisely designed nanocrystals as building blocks. My research experience mainly covers:

- ✧ Colloidal syntheses of nanocrystals.
- ✧ Unravelling of nanocrystal surface chemistry.
- ✧ Nanocrystals assembly and consolidation.
- ✧ Transport properties of nanocrystal-based solids.
- ✧ Bottom-up processed TE nanomaterials.

Research Interests

Unravelling of structure-property relationships of nanomaterials and their use in developing efficient TE materials.

Awards

- ✧ Erasmus Mundus Scholarship in Chemical Innovation and Regulation (2014-2016)
- ✧ Chinese Scholarship Council (2016)
- ✧ EIT InnoEnergy PhD scholarship (2016-2020)

Conferences/Presentations

Oral presentation: “Bottom-up engineering of TE nanomaterials and devices from solution-processed NPs” in the 1st Iberian TE Conference in Porto (September 2017)

Oral presentation: “Solution processed copper chalcogenides NPs for TE application” in the Heraeus "Exciting nanostructures" Conference in Bad Honnef (July 2017)

Publications

1. **Y Zhang**, Y Liu, K Lim, C Xing, M Ibañez, P Guardia, A Cabot. *Tin Diselenide*

- Molecular Precursor for Solution-Processable thermoelectric Materials. Angewandte Chemie*, 2018, 130 (52), 17309-17314. (IF:12.257)
2. **Y Zhang**, Y Liu, J Arbiol, J Llorca, D Cadavid, M Ibáñez, A Cabot. *Tin Selenide Molecular Precursor for the Solution Processing of thermoelectric Materials and Devices. ACS Appl. Mater. Interfaces*, 2020, 12, 24, 27104–27111. (IF:8.758)
 3. Y. Liu, **Y. Zhang**, S. Ortega, M. Ibáñez, K. H. Lim, A. Grau Carbonell, S. Martí-Sánchez, K. M. Ng, J. Arbiol and M. V. Kovalenko, D. Cadavid, A. Cabot, “*Crystallographically Textured Nanomaterials Produced from the Liquid Phase Sintering of $Bi_xSb_{2-x}Te_3$ Nanocrystal Building Blocks.*” *Nano Letters* 2018, 18, 2557-2563. (IF=12.08)
 4. Y. Liu, **Y. Zhang**, K. H. Lim, M. Ibáñez, S. Ortega M. Li, K. M. Ng, M. V. Kovalenko, D. Cadavid, A. Cabot, “*High thermoelectric Performance in Crystallographically Textured n-type $Bi_2Te_{3-x}Se_x$ Produced from Asymmetric Colloidal Nanocrystals*” *ACS Nano* 2018, 12 (7) : 7174-7184. (IF=13.71)
 5. C. Xing, Y. Liu, **Y. Zhang**, J Liu, T. Zhang, A. Cabot and J. Llorca. *Porous NiTiO₃/TiO₂ nanostructures for photocatalytic hydrogen evolution. Journal of materials chemistry A*, 2019, 7(28): 17053-17059. (IF=11.301)
 6. S. Ortega, M. Ibáñez, Y. Liu, **Y. Zhang**, M. V Kovalenko, D. Cadavid, A. Cabot, “*Bottom-up engineering of thermoelectric nanomaterials and devices from solution-processed NP building blocks.*” *Chemical Society Reviews* 2017, 46, 3510-3528. (IF=40.18)
 7. O. Moghaddam, A. Shokuhfar, **Y. Zhang**, T. Zhang, J. Arbiol and A. Cabot. *Ge-Doped ZnSb/ β -Zn₄Sb₃ nanocomposite with High thermoelectric Performance. Advanced Materials Interfaces*, 2019, 6(18): 1900467. (IF=4.948)
 8. M. Li, Y. Liu, **Y. Zhang**, Y. Zuo, J. Li, K. Lim and A. Cabot. *Crystallographically textured SnSe nanomaterials produced from the liquid phase sintering of nanocrystals. Dalton Transactions*, 2019, 48(11): 3641-3647. (IF=4.174)
 9. K. H. Lim, Y. Liu, **Y. Zhang**, D. Cadavid, K. Wong, A. Cabot, K. M. Ng, “*Bulk Semiconducting/Insulating Polymer with Hetero-Substructure and Enhanced thermoelectric Performance*” *Composites Part B: Engineering* 164, 54-60. (IF=4.92)

10. K. H. Lim, Y. Liu, **Y. Zhang**, D. Cadavid, K. Wong, A. Cabot, K. M. Ng, "Critical role of nanoinclusions in silver selenide nanocomposites as a promising room temperature thermoelectric material." *Journal of Materials Chemistry C*, 7(9), 2646-2652. (IF=7.059)
11. A. Moghaddam, A. Shokuhfar, P. Guardia, **Y. Zhang** and A. Cabot. Substantial role of doping in the thermoelectric and hardness properties of nanostructured bornite, Cu₅FeS₄. *Journal of Alloys and Compounds*, 2019, 773: 1064-1074. (IF=4.65)

Annex



Tin Diselenide Molecular Precursor for Solution-Processable Thermoelectric Materials

Yu Zhang, Yu Liu, Khak Ho Lim, Congcong Xing, Mengyao Li, Ting Zhang, Pengyi Tang, Jordi Arbiol, Jordi Llorca, Ka Ming Ng, Maria Ibáñez, Pablo Guardia, Mirko Prato, Doris Cadavid,* and Andreu Cabot*

Abstract: In the present work, we detail a fast and simple solution-based method to synthesize hexagonal SnSe₂ nanoplates (NPLs) and their use to produce crystallographically textured SnSe₂ nanomaterials. We also demonstrate that the same strategy can be used to produce orthorhombic SnSe nanostructures and nanomaterials. NPLs are grown through a screw dislocation-driven mechanism. This mechanism typically results in pyramidal structures, but we demonstrate here that the growth from multiple dislocations results in flower-like structures. Crystallographically textured SnSe₂ bulk nanomaterials obtained from the hot pressing of these SnSe₂ structures display highly anisotropic charge and heat transport properties and thermoelectric (TE) figures of merit limited by relatively low electrical conductivities. To improve this parameter, SnSe₂ NPLs are blended here with metal nanoparticles. The electrical conductivities of the blends are significantly improved with respect to bare SnSe₂ NPLs, what translates into a three-fold increase of the TE Figure of merit, reaching unprecedented ZT values up to 0.65.

The use of molecular precursors to produce inorganic nanomaterials in the form of nanoparticles, thin films, supported nanostructures or self-standing porous or dense nanomaterials is potentially advantageous in terms of reducing fabrication costs and improving performances. In this direction, the amine-dithiol system has been reported as a versatile solvent to prepare molecular precursors from the dissolution at ambient conditions of metal chalcogenides, pure metals and metal oxides, among others.^[1]

Two dimensional (2D) materials have attracted increasing attention in the past decade. The structure of these materials is formed by atomically thin layers that display strong


covalent in-plane bonding and weak layer-to-layer bonding. This type of structure results in extraordinary and at the same time highly anisotropic physical, electronic and optical properties. In particular, charge and heat transport properties are especially affected by the strong lattice asymmetry, and much higher thermal and electrical conductivities are measured in-plane than cross-plane. Owing to these highly anisotropic properties, to produce bulk 2D nanomaterials with a proper crystallographic texture is necessary to optimize their performance in most applications. However, to control the crystallographic texture of materials produced by bottom-up procedures and/or solution-based approaches is not straightforward.

A particularly interesting 2D material family is that of metal chalcogenides, owing to their good chemical stability and semiconducting characteristics. 2D metal chalcogenides are used in numerous applications in a variety of fields, including energy conversion and storage,^[2] flexible electronics^[3] and medical diagnosis.^[4] Among them, tin chalcogenides are especially interesting materials for energy conversion.^[5] In particular, p-type SnSe single crystals have shown unprecedentedly high thermoelectric (TE) figures of merit: ZT = 2.6 at 923 K.^[6] On the other hand, n-type SnSe₂ could be an ideal compound to complement an all Sn-Se based device, but the measurement of its TE properties and their optimization has been rarely targeted.^[7]

In contrast to previous synthetic methods,^[8] here we report on a fast solution-based methodology that makes use of molecular precursors to produce SnSe₂ nanoplates (NPLs) and SnSe₂ nanomaterials. Our synthetic procedure can be easily scaled up, paving the way for commercial application. These NPLs are hot pressed to produce crystallographically

[*] Y. Zhang, Dr. Y. Liu, C. C. Xing, M. Y. Li, Dr. P. Guardia, Prof. A. Cabot
 Catalonia Energy Research Institute—IREC
 Sant Adria de Besòs, 08930 Barcelona (Spain)
 E-mail: acabot@irec.cat
 K. H. Lim, Prof. K. M. Ng
 Department of Chemical and Biological Engineering, Hong Kong
 University of Science and Technology
 Hong Kong (China)
 C. C. Xing, Prof. J. Llorca
 Institute of Energy Technologies, department of Chemical Engineer-
 ing and Barcelona Research Center in Multiscale Science and
 Engineering, Universitat Politècnica de Catalunya
 08019 Barcelona (Spain)
 T. Zhang, P. Y. Tang, Prof. J. Arbiol
 Catalan Institute of Nanoscience and Nanotechnology (ICN2)
 Campus UAB, Bellaterra, 08193 Barcelona (Spain)

Prof. J. Arbiol, Prof. A. Cabot
 ICREA
 Pg. Lluís Companys, 08010 Barcelona, Catalonia (Spain)
 Prof. M. Ibáñez
 Institute of Science and Technology Austria
 Am Campus 1, 3400 Klosterneuburg (Austria)
 Dr. M. Prato
 Materials Characterization Facility, Istituto Italiano di Tecnologia
 Via Morego 30, 16163 Genova (Italy)
 Dr. D. Cadavid
 Departamento de Física, Universidad Nacional de Colombia
 111321, Ciudad Universitaria, Bogotá (Colombia)
 E-mail: dycadavidr@unal.edu.co

 Supporting information and the ORCID identification number(s) for the author(s) of this article can be found under:
<https://doi.org/10.1002/anie.201809847>.

textured nanomaterials, which TE properties are characterized. The final TE performance of SnSe₂ is further optimized through modulation doping by combining SnSe₂ NPLs with metal nanoparticles (NPs).

Tin diselenide NPs were produced through the thermal decomposition of an ink prepared by the dissolution of elemental Sn and Se powders with a Sn/Se = 0.5 molar ratio in an amine-dithiol mixture (Figure S2, see experimental section for details). Upon heating of the ink to 380 °C, the solvent was evaporated and a very rapid crystallization of tin diselenide NPs took place. This simple process could be carried out at virtually any scale and in a continuous manner, using a flow system, to produce very large amounts of material in a short period of time. The ink could be also directly deposited on the proper substrate to simultaneously produce the material and fabricate the device.

This procedure resulted in hexagonal plate-like NPs with average thickness of ca. 70 nm, which were found assembled into flower-like clusters with average size of ca. 4 μm (Figure 1). X-ray powder diffraction (XRD) patterns of the

obtained materials (Figure 1c) were consistent with a SnSe₂ crystal structure (*P*3̄m1 space group, JCPDS NO. 01-089-2939). Along the *z*-axis of this structure, three-atom-thick and covalently bond Se–Sn–Se slabs are piled up together through weak van der Waals interaction (Figure 1d). The relatively strong intensity of the (001) XRD peak pointed at the [001] direction as the normal to the nanoplate plane. No additional phases were identified by XRD. High-resolution transmission electron microscopy (HRTEM) analysis (Figure 1e) confirmed the SnSe₂ trigonal phase (space group = *P*3̄m1) with *a* = *b* = 3.8110 Å, *c* = 6.1360 Å and the growth of the NPLs with preferentially exposed (001) facets. UV/Vis spectra showed the SnSe₂ NPLs to have an indirect band gap at 1.27 eV (Figure S9 in Supporting Information).

Energy dispersive X-ray spectroscopy (EDX) analysis showed the SnSe₂ NPLs to be slightly Sn-rich, with a composition Se/Sn = 1.9 (Figure S3). X-ray photoelectron spectroscopy (XPS) analysis showed the surface of SnSe₂ NPLs to be slightly more Sn rich: Se/Sn = 1.7. The Se 3d and Sn 3d regions of the XPS spectra (Figure S4) could be fitted with a unique doublet each one, further proving the phase purity of the sample.^[9] Electron energy loss spectroscopy (EELS) chemical composition maps displayed a homogeneous distribution of both Sn and Se elements in all SnSe₂ NPLs (Figure 1f), although slightly Sn-rich edges could be detected, in agreement with XPS analysis.

Extensive scanning electron microscopy (SEM) characterization displayed SnSe₂ particles to grow through a screw dislocation mechanism.^[10] Figure 2b shows the top view and side view of a SnSe₂ multi-layer nanostructure displaying a helical surface on the top layer with clockwise spiral direction (Figure 2a, S5a). Bright field TEM images of some of the particles also displayed multiple contours with different contrast (Figure S6c) also indicating screw dislocation phenomenon. Through the screw dislocation growth mechanism, self-perpetuating steps along a screw dislocation axis cause an oriented growth.^[11] The smallest SnSe₂ structures produced following our procedure were found to originate from a single or few dislocations, resulting in approximately planar circular pyramids due to the overall faster vertical growth of the center of the structure compared to the edges (Figure 2b). However, in contrast with previous nanostructures obtained by screw dislocation,^[12] larger SnSe₂ structures were produced from the screw growth of multiple dislocations generated at the edge of the growing structure. These multiple growth centres resulted in a faster overall growth at the nanostructure edges than the centre and thus led to the formation of flower-like structures (Figure 2c and d). At the edge, SnSe₂ layers became detached due to the stress generated during growth from multiple dislocations and the weak layer-to-layer bonding in the 2D SnSe₂ crystal structure.

The decomposition temperature and nominal molecular ratio of Sn and Se precursors were key parameters to produce phase pure SnSe₂ NPLs (Figure 3a). Sn/Se molar ratios above 0.5 in the initial ink resulted in the additional formation of a secondary SnSe phase. However, at a nominal Sn/Se = 1 the ink decomposition at 380 °C did not result in pure orthorhombic SnSe, but a combination of SnSe, SnSe₂ and SnS₂ due to the reaction of part of the Sn with EDT. Pure-phase SnSe

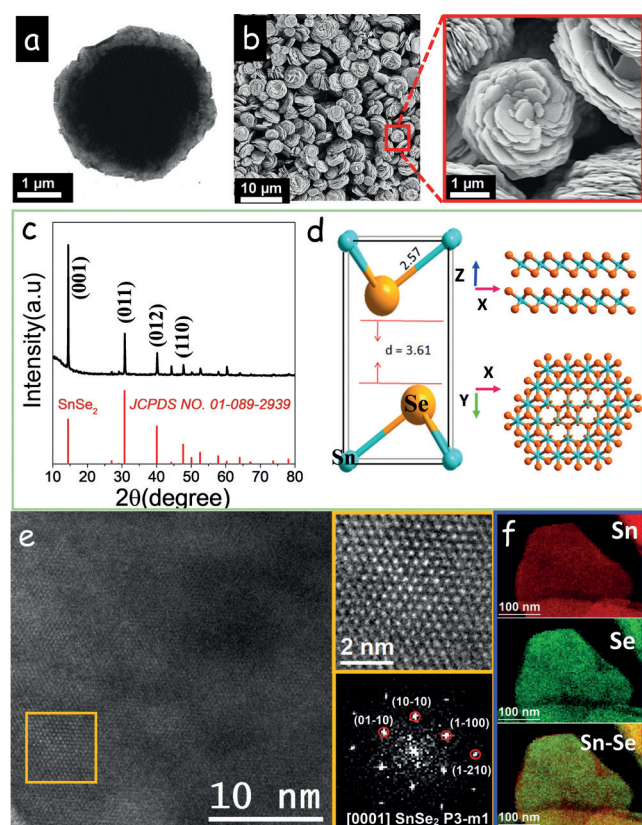


Figure 1. a) TEM image of a SnSe₂ nanostructure. b) Representative SEM image of flower-like SnSe₂ nanostructures, including micrograph of an individual particle. c) XRD pattern of SnSe₂ NPLs. d) Atomic model of the SnSe₂ crystal structure (*P*3̄m1 space group) along Y and Z axis: Se = orange; Sn = light blue. e) HRTEM micrograph of a SnSe₂ nanostructure, magnified detail of the orange squared region and its corresponding power spectrum. The SnSe₂ lattice fringe distances were measured to be 0.332 nm, 0.327 nm and 0.326 nm, with crystal plane angles of 61.23 and 121.25°, which can be assigned to the trigonal SnSe₂ phase, visualized along its [0001] zone axis. f) EELS chemical composition maps of SnSe₂ NPLs.

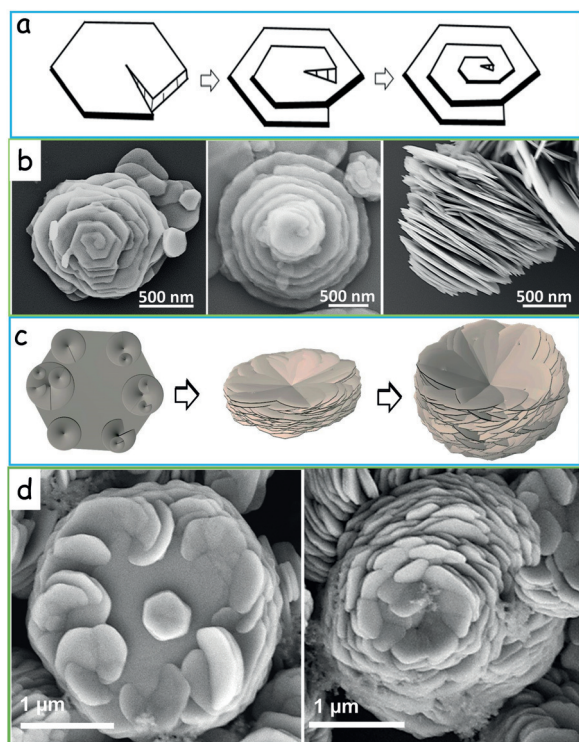


Figure 2. a) Schematic illustration of the screw dislocation-driven growth mechanism. b) Representative SEM images of SnSe₂ NPL-based structures revealing the screw dislocation growth from top and side views. c) Scheme of the formation of a flower-like nanostructure from multiple growing centres. d) Representative SEM images of SnSe₂ nanostructures with multiple dislocation centres and the final flower-like structure.

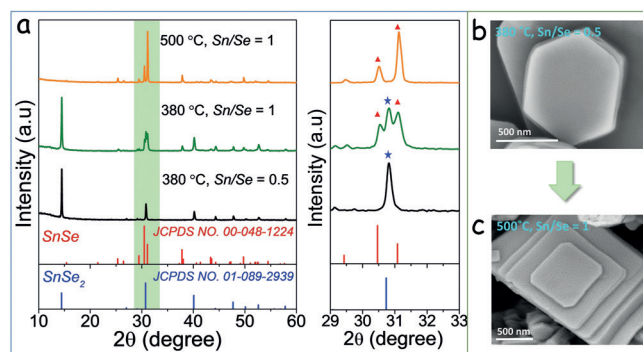


Figure 3. a) XRD pattern of the material obtained from the decomposition of the precursor ink with different Sn/Se ratios and at different temperatures as specified in each pattern. A magnification of the relevant area around $2\theta = 31^\circ$ is also shown for clarity. b) SEM images of SnSe₂ NPLs with hexagonal structure and c) SnSe NPLs with orthorhombic nanostructure obtained in the specified conditions.

was obtained only at higher ink decomposition temperatures of ca. 500 °C, and only when using equal concentrations of the two elements (Figure 3c).

SnSe₂ NPLs were purified by multiple precipitation and redispersion steps using chloroform as solvent and ethanol as antisolvent. The purified and dried NPLs were annealed at 450 °C for 60 mins inside a tube furnace under argon flow. The

annealed particles maintained plate-like geometries although with larger lateral dimensions and without displaying the flower-like shape (Figure 4a). We hypothesize the multiple layers of the initial NPL-based nanoflowers combined within a unique plate, resulting in planar but larger nanostructures.

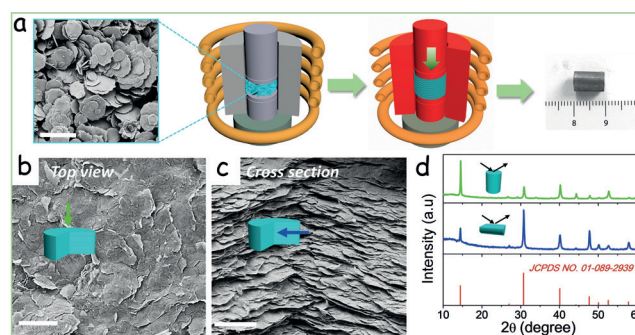


Figure 4. a) Schematic illustration of the consolidation of the annealed nanopowder into a cylindrical pellet. A representative SEM image of the annealed nanopowder and an optical image of the final pellet are included in the Scheme. b) Top-view SEM image of a SnSe₂ pellet. c) Cross-section SEM image of the same pellet. d) XRD pattern of the SnSe₂ pellet laid along the cross-plane direction (blue) and the in-plane direction (green). Scale bar = 10 μm .

Subsequently, the annealed NPLs were loaded into a graphite die and were hot-pressed within an Ar-filled glovebox at 460 °C for 5 min under 80 MPa of uniaxial pressure. This methodology allowed obtaining 10 × 10 (length × diameter) mm² cylinders with relative densities of ca. 90 % as measured by Archimedes' method.

Such pellets, obtained from the uniaxial press of SnSe₂ NPLs, displayed a clear crystallographic texture, with the SnSe₂ [001] crystallographic direction oriented along the pressure axis, as observed from XRD characterization (Figure 4d). Top view and cross-section SEM images displayed a clear laminar structure of the pellets (Figure 4b,c), with layers extending tens of microns in the disk plane and having a thickness of ca. 80 nm.

Such layered structure anticipated anisotropic transport properties. Thus, the TE properties of the material were measured in two normal directions: cross-plane, which corresponds to the pressure axis and the preferential [001] crystallographic direction, and in-plane, which is the normal to the pressure axis and mainly corresponds to the *ab* plane of the SnSe₂ structure (Figure S10).

As expected, the electrical conductivities measured cross-plane (σ_{\perp}), were lower than those measured in-plane (σ_{\parallel}): $\sigma_{\parallel}/\sigma_{\perp} = 2.7$ at 750 K. However, SnSe₂ nanomaterials exhibited relatively low electric conductivities in both measured directions (Figure 5a).

Negative Seebeck coefficients were obtained in all the temperature range (Figure 5b). The Seebeck coefficients displayed similar values in the two directions: $S_{\parallel}/S_{\perp} = 0.91$ at 750 K. These similar values are explained by the relatively low dependence of this parameter on scattering. Nevertheless, as generally observed in similar crystallographically textured layered nanomaterials, slightly higher values were obtained

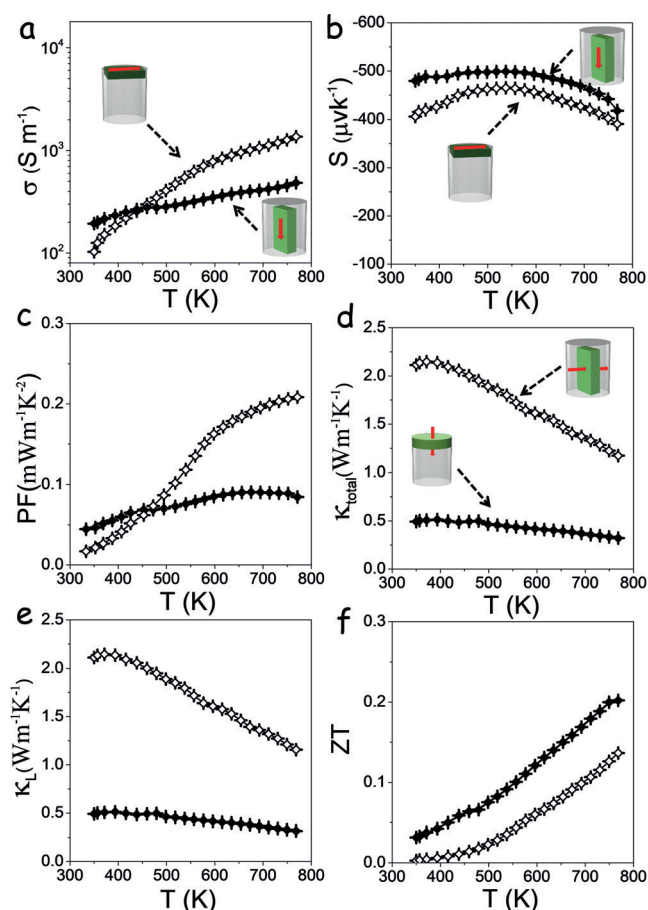


Figure 5. Temperature dependence of a) electrical conductivity, σ ; b) Seebeck coefficient, S ; c) power factor ($S^2 \sigma$), PF; d) total thermal conductivity, κ_{total} ; e) lattice thermal conductivity, κ_{L} ; and f) TE Figure of merit, ZT of a SnSe_2 pellet measured in the two directions, in-plane (\parallel , open symbols ☆) and cross-plane (\perp , solid symbols ★).

cross-plane, which can be related to a slight preferential scattering of minoritarian and/or low energy carriers, that is, a filtering mechanism.^[13]

Much lower thermal conductivities were obtained cross-plane than in-plane: $\kappa_{\parallel}/\kappa_{\perp} = 3.64$ at 750 K (Figure 5d). This anisotropy was associated to the more efficient phonon scattering at the higher density of grain boundaries in the cross-plane direction and the anharmonicity of the SnSe_2 crystal structure. In this regard, already in SnSe_2 single crystals highly anisotropic transport properties were generally measured, with electrical conductivity and thermal conductivity ratios up to 6.^[14]

Overall, higher TE figures of merit were obtained cross-plane, with values up to $ZT_{\perp} = 0.2$ at 770 K (Figure 5f). These values were comparable to those previously measured for this material obtained by other methods.^[7] Overall, while SnSe_2 nanomaterials displayed relatively high Seebeck coefficients and very low thermal conductivities, their main limitation was a moderate electrical conductivity. This low electrical conductivity was in part related to a moderate charge carrier concentration due to the lack of extrinsic dopants.

To increase electrical conductivity, instead of a conventional doping strategy, we used a modulation doping approach. While ionic doping generally relies on the introduction within a semiconductor matrix of small amounts of substituting impurities with different valence than the replaced element, thus freeing or trapping additional electrons, modulation doping relies on the introduction within a semiconductor matrix of nanodomains of a different material having an electron energy band structure suitable for injection of majority carriers to the matrix semiconductor.^[15] The modulation doping approach allows separating the ionized donor/acceptor from the charge carrier path, thus strongly reducing charge carrier scattering and improving mobilities. Additionally, in NP-based bottom-up assembly approaches, the modulation doping strategy provides a very simple and versatile strategy to optimize electrical properties of semiconductor materials,^[16] since proper amounts of the charge injection nanodomains can be easily introduced during the assembly or consolidation steps.

Being SnSe_2 an n-type semiconductor, we selected a dopant phase with a large charge carrier concentration and a relatively low work function that allowed injection of electrons to the SnSe_2 matrix. Thus, we blended SnSe_2 NPLs with Cu, Sn, and Ag NPs (Figure 6a). While Sn had moderate effect on the transport properties of the material, upon incorporation of Cu or Ag NPs a dramatic increase in electric conductivity was measured (Figure S13a). As expected, a parallel decrease of the Seebeck coefficient was also obtained. This Seebeck coefficient decrease was more abrupt with the introduction of Ag NPs than with Cu. Overall, among the different metals tested, the highest power factors were obtained from SnSe_2 -Cu nanocomposites (Figure S13c), reaching values three-fold higher than in pure SnSe_2 .

We further studied the effect of the concentration of Cu NPs (Figure S14). We observed the electrical conductivity to increase with the amount of Cu introduced up to a certain loading. However, with the introduction of a too high amount of Cu (1.9 at %), a decrease in electrical conductivity was observed, which we associated to the formation of significant amounts of Cu_2Se , as observed by XRD (Figure S7). An optimal concentration of 1.4 at % Cu was finally established to maximize TE properties of the material. Hall measurements showed the charge carrier concentration to increase with the amount of Cu introduced (Figure S15), from 8×10^{17} for SnSe_2 to 7.5×10^{18} for SnSe_2 -Cu (1.9%).

Figure 6 displays the TE properties measured in the two normal directions of the SnSe_2 -Cu nanocomposite containing 1.4 at % of Cu. In both directions, a large increase of electric conductivity and a moderate decrease of the Seebeck coefficient were observed with the Cu introduction. This translated into significantly larger power factors in the SnSe_2 -Cu nanocomposite when compared with pure SnSe_2 . The thermal conductivity of SnSe_2 -Cu was significantly reduced in-plane with respect to SnSe_2 , due to the additional scattering at Cu nanoinclusions, but maintained cross-plane at the already very low values measured from the SnSe_2 nanomaterial. Overall, a three-fold increase of the TE Figure of

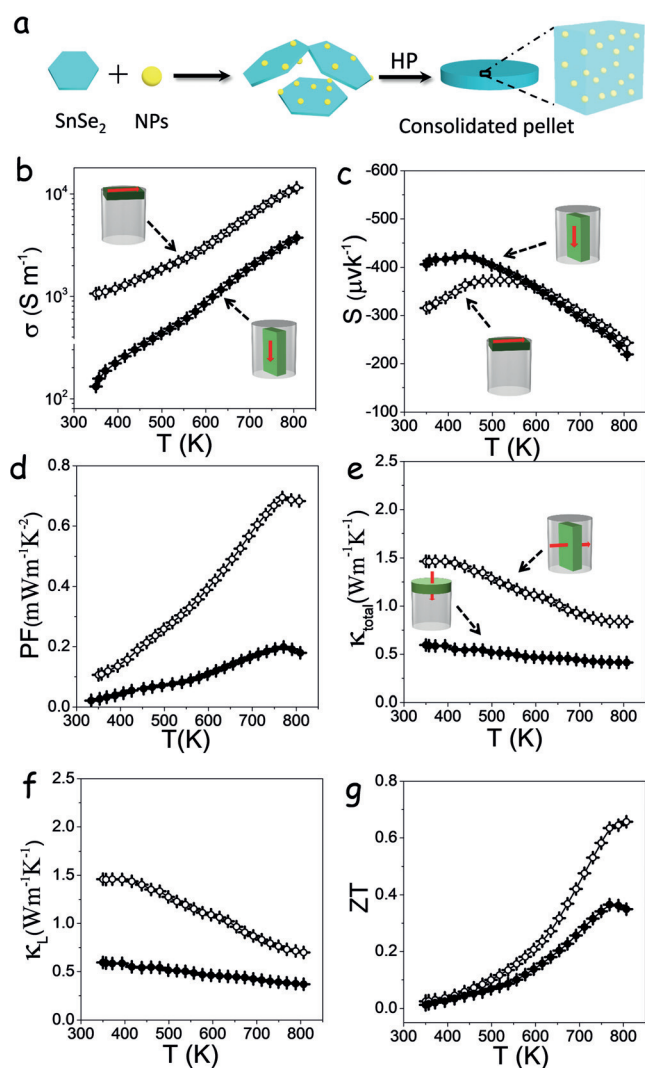


Figure 6. a) Scheme of the process to produce SnSe₂-NPs nanocomposites. Thermoelectric characterization of SnSe₂-Cu (1.4 at%) nanocomposites. Temperature dependence of b) electric conductivity, σ ; c) Seebeck coefficient, S ; d) power factor, PF; e) total thermal conductivity, κ_{total} ; f) lattice thermal conductivity, κ_{L} ; and g) TE Figure of merit, ZT. In-plane (open symbols ☆); cross-plane (solid symbols ★).

merit was obtained with the incorporation of Cu, reaching ZT values up to ZT = 0.65 at 810 K along the in-plane directions.

In conclusion, we presented a solution-based approach to produce SnSe₂ NPLs and crystallographically textured SnSe₂ bulk nanomaterials and nanocomposites. The precursor solution was prepared by directly dissolving Sn and Se powders in an amine-thiol co-solvent solution. Uniform and pure phase SnSe₂ NPLs could be readily obtained by the crystallization of the ink at 380 °C. The growth of these SnSe₂ nanostructures took place through a screw dislocation mechanism from single or multiple dislocations, resulting in the detachment of the newly forming layers. The TE properties of crystallographically textured SnSe₂ bulk nanomaterials and SnSe₂-Cu nanocomposites obtained from the hot-press of SnSe₂ particles and blends of SnSe₂ and Cu particles, respectively, were measured in two perpendicular directions, along the press axis (cross-plane) and normal to it (in-plane).

While bare SnSe₂ nanomaterials displayed notable TE figures of merit, especially cross-plane, their relatively low electrical conductivity limited their performance. A modulation doping strategy was used to improve this parameter, reaching TE figures of merit up to ZT = 0.65 at 810 K in in-plane SnSe₂-Cu nanocomposites.

Acknowledgements

This work was supported by the European Regional Development Funds. Y.L., T.Z. and Y.Z. thank the China Scholarship Council for scholarship support. T.Z., P.Y. T. and J.A. acknowledge funding from Generalitat de Catalunya 2017 SGR 327 and the Spanish MINECO coordinated project VALPEC (ENE2017-85087-C3). ICN2 acknowledges support from the Severo Ochoa Programme (MINECO, Grant no. SEV-2013-0295) and is funded by the CERCA Programme/Generalitat de Catalunya. J.L. is a Serra Hünter Fellow and is grateful to ICREA Academia program and GC 2017 SGR 128.

Conflict of interest

The authors declare no conflict of interest.

Keywords: modulation doping · nanomaterial · reactive ink · SnSe₂ · thermoelectricity

How to cite: *Angew. Chem. Int. Ed.* **2018**, *57*, 17063–17068
Angew. Chem. **2018**, *130*, 17309–17314

- [1] a) D. H. Webber, R. L. Brutchey, *J. Am. Chem. Soc.* **2013**, *135*, 15722–15725; b) P. D. Antunez, D. A. Torelli, F. Yang, F. A. Rabuffetti, N. S. Lewis, R. L. Brutchey, *Chem. Mater.* **2014**, *26*, 5444–5446; c) C. L. McCarthy, D. H. Webber, E. C. Schueller, R. L. Brutchey, *Angew. Chem. Int. Ed.* **2015**, *54*, 8378–8381; *Angew. Chem.* **2015**, *127*, 8498–8501; d) D. H. Webber, J. J. Buckley, P. D. Antunez, R. L. Brutchey, *Chem. Sci.* **2014**, *5*, 2498–2502; e) R. Zhang, S. Cho, D. G. Lim, X. Hu, E. A. Stach, C. A. Handwerker, R. Agrawal, *Chem. Commun.* **2016**, *52*, 5007–5010; f) Z. Lin, C. Hollar, J. S. Kang, A. Yin, Y. Wang, H. Y. Shiu, Y. Huang, Y. Hu, Y. Zhang, X. Duan, *Adv. Mater.* **2017**, *29*, 1606662.
- [2] D. Voiry, M. Salehi, R. Silva, T. Fujita, M. Chen, T. Asefa, V. B. Shenoy, G. Eda, M. Chhowalla, *Nano Lett.* **2013**, *13*, 6222–6227.
- [3] a) G. Fiori, F. Bonaccorso, G. Iannaccone, T. Palacios, D. Neumaier, A. Seabaugh, S. K. Banerjee, L. Colombo, *Nat. Nanotechnol.* **2014**, *9*, 768–779; b) D. Akinwande, N. Petrone, J. Hone, *Nat. Commun.* **2014**, *5*, 5678.
- [4] C. Lu, Y. Liu, Y. Ying, J. Liu, *Langmuir* **2017**, *33*, 630–637.
- [5] a) A. Banik, U. S. Shenoy, S. Saha, U. V. Waghmare, K. Biswas, *J. Am. Chem. Soc.* **2016**, *138*, 13068–13075; b) A. Banik, F. Biswas, *J. Mater. Chem. A* **2014**, *2*, 9620–9625; c) A. Banik, U. S. Shenoy, S. Anand, U. V. Waghmare, K. Biswas, *Chem. Mater.* **2015**, *27*, 581–587; d) A. Banik, S. Roychowdhury, K. Biswas, *Chem. Commun.* **2018**, *54*, 6573–6590; e) A. Banik, B. Vishal, S. Perumal, R. Datta, K. Biswas, *Energy Environ. Sci.* **2016**, *9*, 2011–2019; f) S. Chandra, A. Banik, K. Biswas, *ACS Energy Lett.* **2018**, *3*, 1153–1158.

- [6] L.-D. Zhao, S.-H. Lo, Y. Zhang, H. Sun, G. Tan, C. Uher, C. Wolverton, V. P. Dravid, M. G. Kanatzidis, *Nature* **2014**, *508*, 373–377.
- [7] a) S. Saha, A. Banik, K. Biswas, *Chem. Eur. J.* **2016**, *22*, 15634–15638; b) P. Xu, T. Fu, J. Xin, Y. Liu, P. Ying, X. Zhao, H. Pan, T. Zhu, *Sci. Bull.* **2017**, *62*, 1663–1668; c) Y. Luo, Y. Zheng, Z. Luo, S. Hao, C. Du, Q. Liang, Z. Li, K. A. Khor, K. Hippalgaonkar, J. Xu, Q. Yan, C. Wolverton, M. G. Kanatzidis, *Adv. Energy Mater.* **2018**, *8*, 1702167.
- [8] a) L. A. Burton, D. Colombara, R. D. Abellon, F. C. Grozema, L. M. Peter, T. J. Savenije, G. Dennler, A. Walsh, *Chem. Mater.* **2013**, *25*, 4908–4916; b) Y. Lei, S. Song, W. Fan, Y. Xing, H. Zhang, *J. Phys. Chem. C* **2009**, *113*, 1280–1285; c) P. Ramasamy, P. Manivasakan, J. Kim, *CrystEngComm* **2015**, *17*, 807–813; d) K. Liu, H. Liu, J. Wang, L. Feng, *Mater. Lett.* **2009**, *63*, 512–514; e) X. Zhou, L. Gan, W. Tian, Q. Zhang, S. Jin, H. Li, Y. Bando, D. Golberg, T. Zhai, *Adv. Mater.* **2015**, *27*, 8035–8041; f) C. Zhai, N. Du, H. Z. D. Yang, *Chem. Commun.* **2011**, *47*, 1270–1272; g) Y. Du, Z. Yin, X. Rui, Z. Zeng, X.-J. Wu, J. Liu, Y. Zhu, J. Zhu, X. Huang, Q. Yan, *Nanoscale* **2013**, *5*, 1456–1459; h) P. Zheng, Z. Dai, Y. Zhang, K. N. Dinh, Y. Zheng, H. Fan, J. Yang, R. Dangol, B. Li, Y. Zong, *Nanoscale* **2017**, *9*, 14820–14825.
- [9] a) S. J. Patil, V. C. Lokhande, D.-W. Lee, C. D. Lokhande, *Opt. Mater.* **2016**, *58*, 418–425; b) N. D. Boscher, C. J. Carmalt, R. G. Palgrave, I. P. Parkin, *Thin Solid Films* **2008**, *516*, 4750–4757; c) E. P. Mukhokosi, S. B. Krupanidhi, K. K. Nanda, *Sci. Rep.* **2017**, *7*, 15215.
- [10] a) W.-K. Burton, N. Cabrera, F. Frank, *Philos. Trans. R. Soc. London Ser. A* **1951**, *243*, 299–358; b) F. Wang, X. Wang, *Nanoscale* **2014**, *6*, 6398–6414.
- [11] a) L. Chen, B. Liu, A. N. Abbas, Y. Ma, X. Fang, Y. Liu, C. Zhou, *ACS Nano* **2014**, *8*, 11543–11551; b) F. Meng, S. A. Morin, A. Forticaux, S. Jin, *Acc. Chem. Res.* **2013**, *46*, 1616–1626; c) A. Forticaux, L. Dang, H. Liang, S. Jin, *Nano Lett.* **2015**, *15*, 3403–3409; d) S. A. Morin, M. J. Bierman, J. Tong, S. Jin, *Science* **2010**, *328*, 476–480; e) A. Zhuang, J. J. Li, Y. C. Wang, X. Wen, Y. Lin, B. Xiang, X. Wang, J. Zeng, *Angew. Chem. Int. Ed.* **2014**, *53*, 6425–6429; *Angew. Chem.* **2014**, *126*, 6543–6547.
- [12] S. A. Morin, A. Forticaux, M. J. Bierman, S. Jin, *Nano Lett.* **2011**, *11*, 4449–4455.
- [13] a) Y. Liu, Y. Zhang, K. H. Lim, M. Ibáñez, S. Ortega, M. Li, J. David, S. Martí-Sánchez, K. M. Ng, J. Arbiol, *ACS Nano* **2018**, *12*, 7174–7184; b) Y. Liu, Y. Zhang, S. Ortega, M. Ibáñez, K. H. Lim, A. Grau-Carbonell, S. Martí-Sánchez, K. M. Ng, J. Arbiol, M. V. Kovalenko, *Nano Lett.* **2018**, *18*, 2557–2563.
- [14] B.-Z. Sun, Z. Ma, C. He, K. Wu, *Phys. Chem. Chem. Phys.* **2015**, *17*, 29844–29853.
- [15] a) M. Zebarjadi, G. Joshi, G. Zhu, B. Yu, A. Minnich, Y. Lan, X. Wang, M. Dresselhaus, Z. Ren, G. Chen, *Nano Lett.* **2011**, *11*, 2225–2230; b) B. Yu, M. Zebarjadi, H. Wang, K. Lukas, H. Wang, D. Wang, C. Opeil, M. Dresselhaus, G. Chen, Z. Ren, *Nano Lett.* **2012**, *12*, 2077–2082.
- [16] a) M. Ibáñez, Z. Luo, A. Genc, L. Piveteau, S. Ortega, D. Cadavid, O. Dobrozhan, Y. Liu, M. Nachtegaal, M. Zebarjadi, J. Arbiol, M. V. Kovalenko, A. Cabot, *Nat. Commun.* **2016**, *7*, 10766; b) S. Ortega, M. Ibáñez, Y. Liu, Y. Zhang, M. V. Kovalenko, D. Cadavid, A. Cabot, *Chem. Soc. Rev.* **2017**, *46*, 3510–3528; c) Y. Liu, D. Cadavid, M. Ibáñez, S. Ortega, S. M. Sánchez, O. Dobrozhan, M. V. Kovalenko, J. Arbiol, A. Cabot, *APL Mater.* **2016**, *4*, 104813.

Manuscript received: August 27, 2018

Revised manuscript received: October 23, 2018

Accepted manuscript online: November 6, 2018

Version of record online: November 25, 2018

Tin Selenide Molecular Precursor for the Solution Processing of Thermoelectric Materials and Devices

Yu Zhang,[§] Yu Liu,[§] Congcong Xing, Ting Zhang, Mengyao Li, Mercè Pacios, Xiaoting Yu, Jordi Arbiol, Jordi Llorca, Doris Cadavid, Maria Ibáñez,* and Andreu Cabot*



Cite This: *ACS Appl. Mater. Interfaces* 2020, 12, 27104–27111



Read Online

ACCESS |



Metrics & More



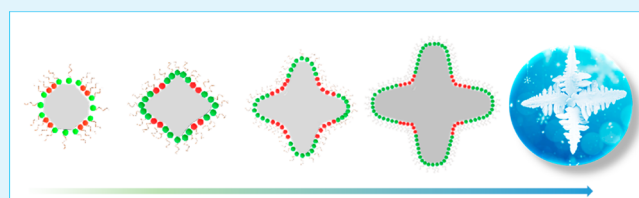
Article Recommendations



Supporting Information

ABSTRACT: In the present work, we report a solution-based strategy to produce crystallographically textured SnSe bulk nanomaterials and printed layers with optimized thermoelectric performance in the direction normal to the substrate. Our strategy is based on the formulation of a molecular precursor that can be continuously decomposed to produce a SnSe powder or printed into predefined patterns. The precursor formulation and decomposition conditions are optimized to produce pure phase 2D SnSe nanoplates. The printed layer and the bulk material obtained after hot press displays a clear preferential orientation of the crystallographic domains, resulting in an ultralow thermal conductivity of $0.55 \text{ W m}^{-1} \text{ K}^{-1}$ in the direction normal to the substrate. Such textured nanomaterials present highly anisotropic properties with the best thermoelectric performance in plane, i.e., in the directions parallel to the substrate, which coincide with the crystallographic *bc* plane of SnSe. This is an unfortunate characteristic because thermoelectric devices are designed to create/harvest temperature gradients in the direction normal to the substrate. We further demonstrate that this limitation can be overcome with the introduction of small amounts of tellurium in the precursor. The presence of tellurium allows one to reduce the band gap and increase both the charge carrier concentration and the mobility, especially the cross plane, with a minimal decrease of the Seebeck coefficient. These effects translate into record out of plane ZT values at 800 K.

KEYWORDS: molecular ink, SnSe, thermoelectricity, printing, nanomaterial



INTRODUCTION

Solid state thermoelectric (TE) devices offer a direct and solid state means of conversion between thermal and electrical energy, which makes them extremely appealing for a wide range of applications.^{1–8} However, the relatively low-energy conversion efficiency and high manufacturing cost of current TE devices, which are in most cases designed for cooling applications, makes them cost efficient only in a few niche markets.^{1,9} Toward improving the cost efficiency of TE devices, it is imperative to (i) implement lower cost fabrication processes, (ii) optimize device parameters for each particular application to maximize efficiency and minimize the amount of used material, and (iii) develop high-performance and lower cost TE materials.

Thermoelectric performance is generally quantified using an adimensional figure of merit, $ZT = \sigma S^2 T / \kappa$, where σ , S , T , and κ are the electrical conductivity, Seebeck coefficient, absolute temperature, and thermal conductivity, respectively.^{3,7,10} Among the different families of TE materials proposed,^{2,4} some two-dimensional chalcogenides exhibit the best TE performance.^{11–17} Bi₂Te₃-based alloys provide the highest ZT values at temperatures around ambient, up to 1.96 at 420 K,¹⁶ and dominate the TE market.^{18–21} On the other hand, SnSe single crystals have recently achieved unprecedented record

ZT values in the medium–high temperature range, 2.6 at 923 K.^{13,22} SnSe has a layered crystal structure with weak van der Waals bonds along the *a* axis and tight covalent bonds along the *bc* plane, which results in highly anisotropic transport properties and an impressively low lattice thermal conductivity. Nonetheless, the high production cost and poor mechanical properties of SnSe single crystals limit their use in real applications. All of these have sparked much interest in producing polycrystalline SnSe with TE performance approaching that of SnSe single crystals. Owing to the anisotropic properties of the material, optimization of polycrystalline SnSe generally requires producing crystallographic textured samples.^{23–35} In this direction, while severe plastic deformation techniques are conventionally used to produce textured polycrystalline materials,^{36,37} spark plasma sintering and hot press approaches, more commonly used to consolidate TE polycrystalline materials, are also able to produce textured

Received: March 6, 2020

Accepted: May 21, 2020

Published: May 21, 2020



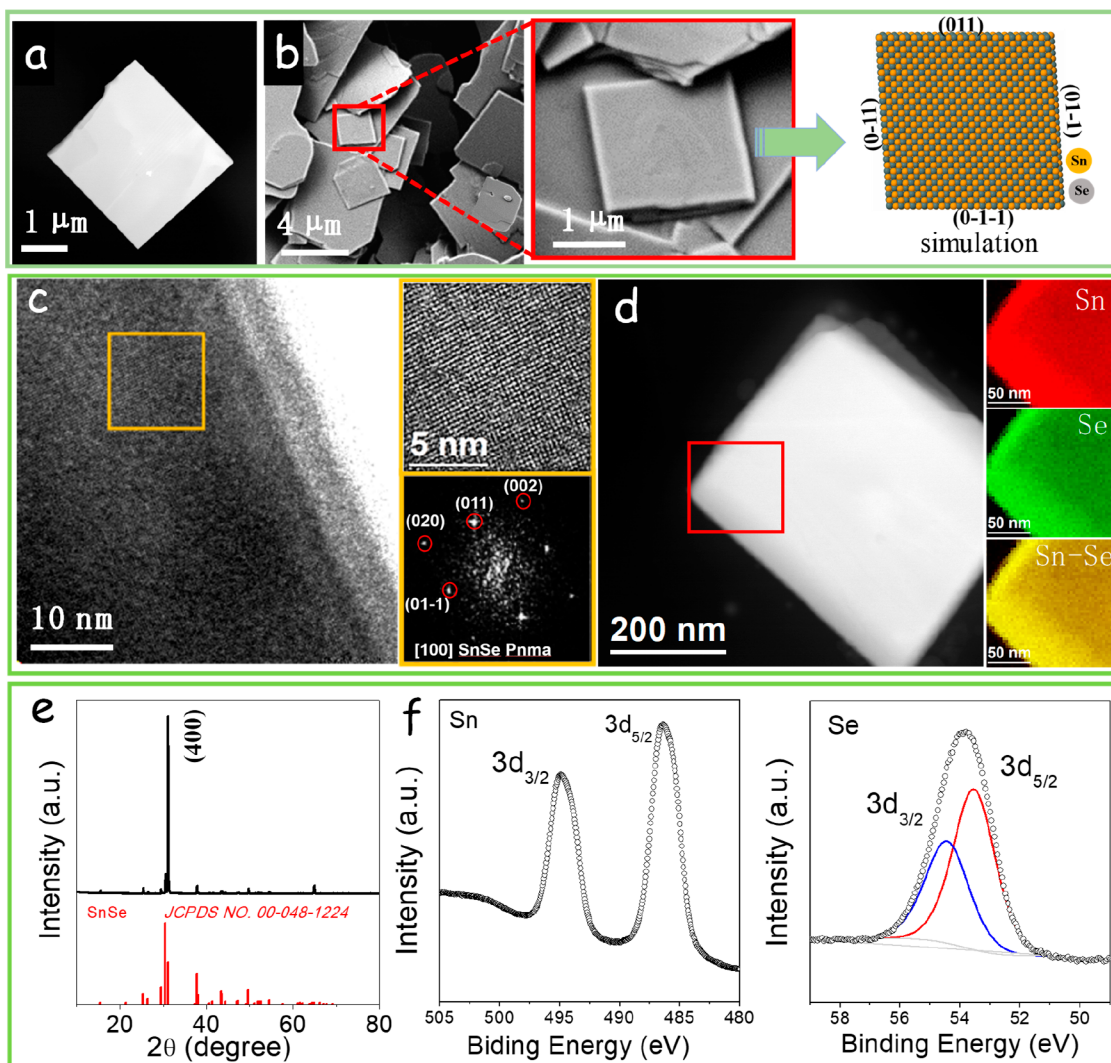


Figure 1. (a) Representative TEM and (b) SEM micrographs of square-like SnSe nanostructures, and structure model of an individual nanoplate. (c) HRTEM micrograph of a SnSe nanoplate, magnified detail of the orange squared region, and its corresponding power spectrum. SnSe lattice fringe distances were measured to be 0.304, 0.207, and 0.302 nm at 43.53° and 87.51°, which was interpreted as the orthorhombic SnSe phase, visualized along its [100] zone axis. (d) EELS chemical composition maps obtained from the red squared area of the STEM micrograph. Individual Sn $M_{4,5}$ -edges at 485 eV (red) and Se $L_{2,3}$ -edges at 1436 eV (green) as well as its composite. (e) XRD pattern of SnSe. (f) Sn 3d and Se 3d regions of the XPS spectrum of SnSe.

materials when using an open dye to induce extrusion or when incorporating a liquid phase in the process.^{15,16,38–42}

Beyond engineering TE materials with improved performance and lower cost, novel strategies to fabricate TE devices that are less labor intensive and which allow a more rational use of the TE material need to be developed. One potential alternative strategy is inkjet printing. The main advantages of printing techniques are low cost, potential to produce shape-adaptable or flexible devices, control over the thickness of the TE material, and high material use efficiency. While printing strategies are currently well developed and used in a large number of applications, their implementation in new technologies strongly relies on the formulation of proper functional inks. SnSe inks could be formulated from colloidal nanoparticles produced from the decomposition/reaction of a tin precursor with selenium oxide or trioctylphosphine selenium at moderate temperatures as previously reported.^{43–47} However, it is more convenient, in terms of cost and quality

of the produced layers, to formulate ionic or molecular precursors.

We report here a thiol-free SnSe molecular precursor, which can be used to produce bulk nanocrystalline SnSe or can be directly printed into SnSe layers. We study the decomposition conditions and demonstrate the possibility to produce pure phase SnSe at moderate temperatures. We further analyze here the processing conditions necessary to obtain crystallographically textured SnSe bulk nanomaterials and layers and characterize their anisotropic TE properties. Finally, the TE performance of the material in the direction normal to the layer substrate is optimized by including small amounts of tellurium within the precursor.

RESULTS AND DISCUSSION

To prepare a SnSe molecular ink, the tin and selenium precursors and the solvent were selected taking into account four main parameters: (i) minimize cost, (ii) direct the crystal morphology toward obtaining planar structures that facilitate

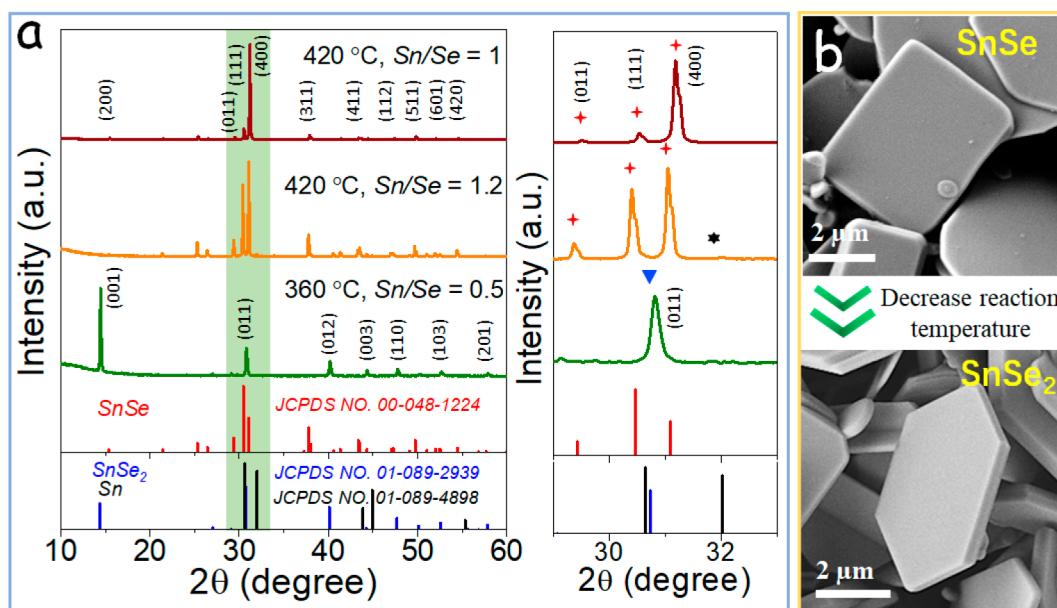


Figure 2. (a) XRD pattern of the powder produced from the decomposition at different temperatures of a precursor containing different ratios of Sn/Se. Detail of the XRD pattern around $2\theta = 31^\circ$ is displayed for clarity. (b) SEM micrographs of SnSe plates with orthorhombic structure and SnSe₂ plates with hexagonal phase obtained when decomposing a precursor containing Sn/Se = 1 at 420 °C and a precursor containing Sn/Se = 0.5 at 360 °C.

posterior assembly into textured nanomaterials, (iii) reach a compromise between solvent volatility, which has implications in toxicity and precursor stability, and decomposition temperature, which is a key parameters determining production costs, and (iv) reduce toxicity, avoiding the use of thiols and hydrazine. Taking into account these points, a SnSe precursor was prepared by dissolving SnCl₂ and SeO₂ in a combination of OAm and TOP. OAm played a double role, it reduced Se⁴⁺ to Se⁰, and it coordinated to Sn²⁺ to form a Sn–OAm complex, Sn(R-NH)₂.^{48–50} TOP coordinated with Se⁰ to yield TOPSe⁵¹ (see Figure S1 in the Supporting Information, SI).

To analyze the product of its decomposition, the precursor was dropped onto a substrate heated at 420 °C. Upon reaching the heated substrate, the precursor was rapidly decomposed and a black powder was produced. Large amounts of powder could be obtained by continuously injecting/spraying the molecular ink toward a heated receptacle/support (Figure S1). TEM and SEM characterization of the powder obtained from the decomposition of the precursor showed the presence of square-like plates with a lateral size of $4 \pm 1 \mu\text{m}$ and a thickness of $90 \pm 20 \text{ nm}$ (Figure 1a, b). HRTEM and XRD analyses demonstrated the powder to be highly crystalline and to display a unique crystallographic phase that matched that of orthorhombic SnSe (JCPDS No. 00-048-1224, *Pnma* space group, Figure 1c and 1e). From the XRD pattern, the relatively strong intensity of the $2\theta = 31.0^\circ$ diffraction peak indexed as (400) indicated a preferential growth in the *bc* plane, i.e., the plane perpendicular to the [100] crystallographic direction. The UV–vis spectrum showed the SnSe powder to have an indirect band gap at 0.96 eV (Figure S2). XPS analysis of SnSe displayed two Sn 3d peaks at 494.9 (Sn 3d_{3/2}) and 486.4 eV (Sn 3d_{5/2}), which matched well with a Sn²⁺ environment (Figure 1f). Besides, Se 3d_{3/2} and Se 3d_{5/2} peaks located at 54.4 and 53.5 eV evidenced the presence of a Se²⁻ oxidation state. EDX chemical analysis showed the SnSe powder to be slightly Sn rich, with a composition ratio Se/Sn = 0.95 (Figure S3). EELS chemical composition maps displayed a homoge-

neous distribution of both Sn and Se within each particle and from particle to particle (Figure 1d).

To obtain single-phase SnSe, proper adjustment of the nominal element ratio, Sn/Se, and decomposition temperature was fundamental. When increasing the nominal amount of Sn in the precursor formulation, a combination of Sn and SnSe phases was obtained upon decomposition at 420 °C (Figures 2a). On the other hand, when using a nominal ratio Sn/Se < 1, a combination of SnSe and SnSe₂ was produced. Using a nominal Sn/Se = 0.5 and decreasing the decomposition temperature to 360 °C, pure-phase SnSe₂ could be produced (Figure 2a). Figure S4 shows XRD patterns of the materials obtained at different temperatures using a nominal element ratio Sn/Se = 1.

TOP coordinated with Se to yield TOPSe. Without TOP in the precursor solution, SnSe nanostructures could be also obtained, but the decomposition required reaction temperatures above 500 °C.⁵² In addition, the aspect ratio of the SnSe nanostructures produced in the absence of TOP was strongly reduced (Figure S5). When adding small amounts of TOP to the solution, the precursor decomposition temperature could be reduced down to 420 °C for $V_{\text{TOP}}/V_{\text{OAm}} > 0.13$, which we associated with the relatively high reactivity of the formed TOPSe.⁵⁰ On the other hand, when replacing OAm by octadecene, SnSe was not formed, probing the important role of OAm in reducing SeO₂ and complexing with Sn²⁺. In addition, we tested the influence of the OAm purity on the final product, finding no obvious difference in crystal phase and morphology when using two different OAm qualities (80–90% vs 98%, Figure S6).

When adding OAc to the precursor ink, a significant change of the geometry of the produced SnSe particles was observed. Figure 3 shows the evolution of the particle shape with the OAc/OAm ratio. We believe the carboxylic group in OAc to have a selective interaction with particular SnSe facets during crystal growth;^{53,54} thus, the morphology of SnSe transformed gradually from square shaped to dendritic with increasing ratio

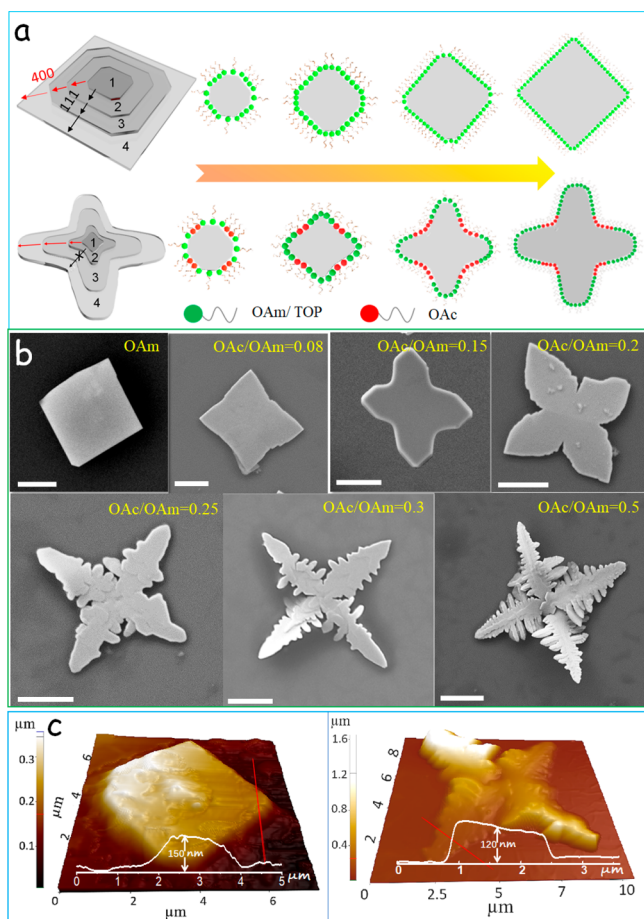


Figure 3. (a) Schematic illustration of the shape evolution for square-like and dendritic crystals. (b) SEM micrographs of the morphology evolution with increasing OAc/OAm ratios. Dendritic nanostructures were obtained when OAc/OAm > 0.2. Scale bars = 2 μm . (c) AFM topography images of a square-like and a dendritic nanostructure, and height profiles taken from the displayed red line.

of OAc/OAm. At relatively high OAc concentrations, OAc/OAm > 0.2, dendritic structures were produced. Through AFM analysis, the thickness of plates and dendritic structures supported on a substrate was measured to be in the range of 100–150 nm, which is slightly larger than values obtained from SEM statistics (Figure 3c).

The SnSe powder obtained from precursor decomposition was thermally annealed at 500 $^{\circ}\text{C}$ for 60 min inside a tube furnace with argon flow to remove residual organic ligands. The annealed crystals maintained the original plate geometry and showed no appreciable growth. The annealed powder was subsequently loaded into a graphite die and hot pressed at 500 $^{\circ}\text{C}$ for 5 min under a uniaxial pressure of 80 MPa. A cylindrical pellet with a relative density of ca. 95% was finally obtained (Figure 4a, Table S2). The material cost to produce one cylindrical pellet is estimated in Table S3.

The hot-pressed material displayed a clear crystallographic texture, with the SnSe [100] crystal direction oriented along the pressure axis, as shown by XRD analysis of the pellet held with the diffraction plane coincident and normal to the pressure axis (Figure 4b). This crystallographic orientation is consistent with the [100] being the *softer* crystallographic direction in SnSe. SEM micrographs showed the pellet to have a layered structure, with layers of material assembling normal

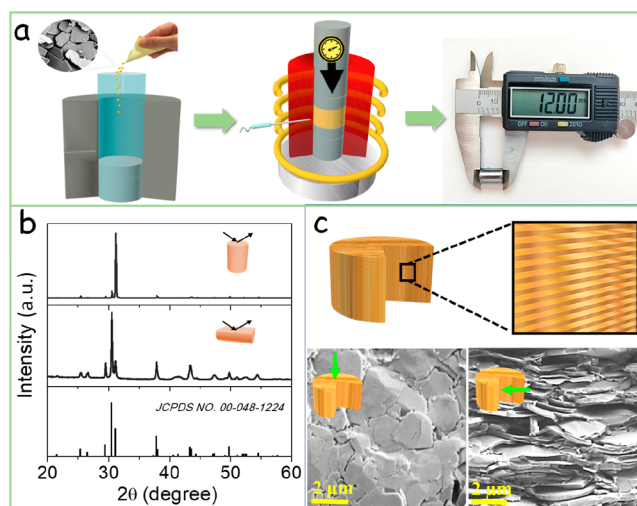


Figure 4. (a) Schematic illustration of the process of consolidation of the SnSe powder into a cylindrical pellet. SEM micrograph of the annealed SnSe nanopowder and actual image of a consolidated pellet are included in the scheme. (b) XRD pattern of the SnSe pellet laid along the in-plane and cross-plane directions. (c) Representative top-view and cross-section SEM micrographs of a SnSe pellet.

to the pressure axis, consistent with XRD results (Figure 4c). The grain size became slightly larger after the hot-press process as noted by SEM characterization.

To determine the influence of the shape of the SnSe particles on the crystallographic texture of the consolidated material, we hot pressed SnSe particles with 100 nm average size and 50 nm thickness produced by a reported method (Figure S9a).³¹ The hot press of these less asymmetric particles in the same conditions as the SnSe plates resulted in polycrystalline materials with no significant texture (Figure S9b,c), proving the influence of the initial particle geometry in the texture of the final polycrystalline material.^{15,16}

To demonstrate the potential of the SnSe molecular precursor to produce printed SnSe layers/patterns, the precursor was printed on a flexible graphite foil using an ink jet nozzle. The graphite foil was then annealed on a hot plate at 420 $^{\circ}\text{C}$ for 5 min and additionally hot pressed at 500 $^{\circ}\text{C}$ for 3 min under 80 MPa pressure. SEM and XRD analyses of the printed layer demonstrated it to contain SnSe plates oriented parallel to the substrate (Figure S10).

The TE properties of the polycrystalline SnSe obtained from the precursor decomposition were characterized in two directions (Figure S12): cross plane (\parallel), i.e., parallel to the pressure axis, and in plane (\perp), i.e., normal to the pressure axis. Electrical conductivities measured in plane (σ_{\perp}) were higher than those measured in the cross plane (σ_{\parallel}) with $\sigma_{\perp}/\sigma_{\parallel} = 3.30$. This result is consistent with the much higher charge carrier mobilities in the *bc* crystal plane of SnSe when compared with its *a* direction.

Positive Seebeck coefficients were measured in all of the temperature range, consistent with the p-type semiconductor character of undoped SnSe. As expected from the minor dependence of this parameter on scattering, similar values of the Seebeck coefficient were measured in both directions, $S_{\perp} \approx S_{\parallel}$. The slightly higher values systematically obtained in the cross plane could be ascribed to an energy filtering mechanism at the grain boundaries, i.e., a preferential scattering of low-

energy carriers at the plate interfaces, as previously reported for layered materials.^{15,16}

SnSe nanomaterials displayed very low thermal conductivities in both directions but slightly higher than those obtained from single crystals, most probably due to a certain degree of oxidation.⁵⁵ Significantly lower thermal conductivities were obtained in the cross plane when compared with the in plane, $\kappa_{\perp}/\kappa_{\parallel} = 1.75$ at 750 K, which was again consistent with the preferential orientation of the plates lying normal to the pressure axis.

Overall, the highest ZT values, up to $ZT = 0.5$ at 770 K, were obtained in plane. This result is consistent with measurements on single crystals and previous reports,^{13,23,25,56,57} but it is unfortunate toward the development of printed SnSe-based modules that target the generation/harvesting of the cross plane temperature gradient.

To further promote the TE performance of polycrystalline SnSe layers, small amounts of Te were added to the precursor in replacement of equivalents amounts of Se. The polycrystalline material obtained from decomposition of the Te-containing precursor, $\text{SnSe}_{1-x}\text{Te}_x$, was characterized by a slightly reduced band gap (Figure S2), a slightly larger charge carrier concentration, n_{H} , and most important a significantly increased charge carrier mobility, particularly in the cross plane (Figure S13). The best TE performance was obtained from the material containing a 2 atom % of Te, $\text{SnSe}_{0.98}\text{Te}_{0.02}$ (Figure 5). This material displayed significantly higher electric conductivities than SnSe without a major reduction of the Seebeck coefficient and a minor increase of the total thermal conductivity, associated with the increase of its electronic component. Overall, TE figures of merit up to 3-fold larger than those measured for SnSe were obtained. Most important, the highest TE figures of merit were obtained in the cross plane, reaching $ZT = 1.05$ at 805 K, which is the highest value reported at this temperature and in this direction for polycrystalline SnSe. This excellent performance was related to the presence of Te, facilitating charge transport, especially in the cross plane, which translated into a significant increase of the charge carrier mobility.

CONCLUSION

We detailed a fast solution-based approach to produce crystallographic textured SnSe bulk nanomaterials and printed layers. The molecular precursor solution was prepared directly by dissolving ionic Sn and Se species in a thiol-free and nontoxic solvent. Pure-phase SnSe powder was obtained by decomposing the molecular precursor at 420 °C. The composition, crystal phase, and shape of the produced SnSe nanostructures could be tuned by modifying the nominal elemental ratio, the decomposition temperature, and the use of additional surfactants. Crystallographic textured SnSe bulk nanomaterials and layers were obtained after hot pressing the precursor decomposition products. These materials showed moderate TE performance in the cross plane, which was unfortunate for design of TE devices that generate/harvest temperature gradients in the direction normal to the substrate. The SnSe TE performance was significantly improved, up to 3-fold, by introducing small amounts of Te during precursor formulation. The presence of this small amount of Te resulted in an important increase of the electrical conductivity cross plane associated with an increase of the charge carrier concentration and especially mobility with a minor variation of the Seebeck coefficient. The presence of 2 atom % of Te in

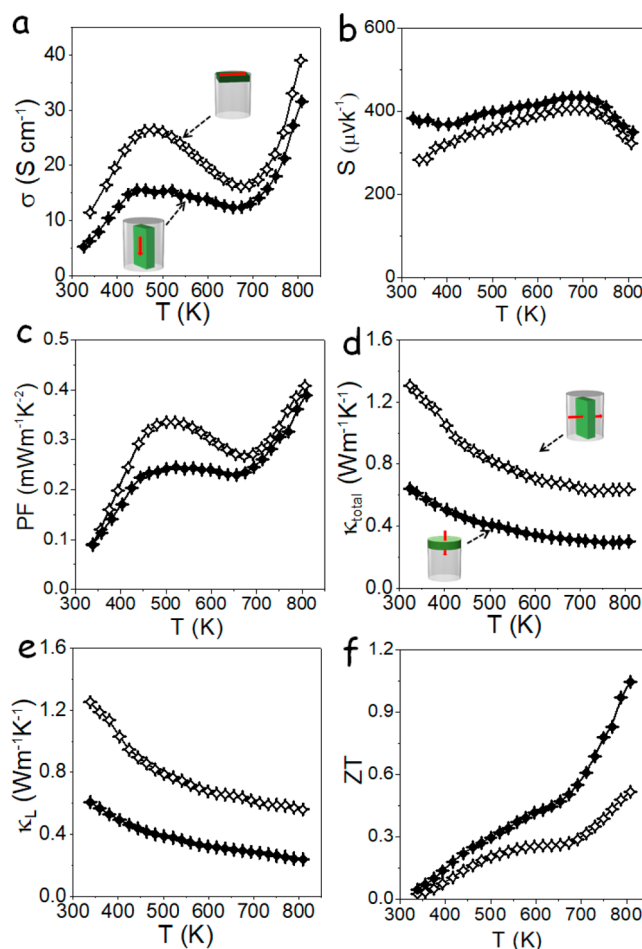


Figure 5. Temperature dependence of (a) electrical conductivity, σ , (b) Seebeck coefficient, S , (c) power factor, $S^2\sigma$, PF, (d) total thermal conductivity, κ_{total} , (e) lattice thermal conductivity, κ_L , and (f) TE figure of merit, ZT of a $\text{SnSe}_{0.98}\text{Te}_{0.02}$ pellet measured in two directions: in-plane (\perp , open symbols) and cross-plane (\parallel , solid symbols).

$\text{SnSe}_{0.98}\text{Te}_{0.02}$ finally translated into record cross plane ZT values at 800 K for polycrystalline SnSe.

EXPERIMENTAL SECTION

Chemicals. Tin chloride (SnCl_2 , 98%) and selenium dioxide (SeO_2 , 99.8%) were purchased from Acros Organics. Tri-*n*-octylphosphine (TOP, $\text{C}_{24}\text{H}_{51}\text{P}$, 97%), oleic acid (OAc, $\text{C}_{18}\text{H}_{34}\text{O}_2$, 90%), and oleylamine (OAm, $\text{C}_{18}\text{H}_{37}\text{N}$, $\geq 98\%$) were purchased from Sigma-Aldrich. Sodium tellurite (Na_2TeO_3 , 99.5%) was purchased from Fisher. Analytical-grade chloroform and ethanol were ordered from various sources. All chemicals were used as received unless specifically noted.

SnSe Precursor. Within an argon-filled glovebox, 5.76 g of SnCl_2 (30 mmol) and 3.33 g of SeO_2 (30 mmol) were weighted and placed inside a glass bottle. Then 150 mL of OAm and 20 mL of TOP were added inside the bottle. The mixture was subsequently sonicated for 20 min until precursors dissolved completely. Small amounts of OAc were included within the precursor to produce dendritic SnSe nanostructures.

$\text{SnSe}_{1-x}\text{Te}_x$ Precursor. To produce $\text{SnSe}_{1-x}\text{Te}_x$ ($x = 0.01, 0.02, 0.03$) precursor precursors, 5.76 g of SnCl_2 (30 mmol), 3.33 g of SeO_2 (30 mmol), and 6.65 g of Na_2TeO_3 were weighted and placed in a glass bottle, where 150 mL of OAm and 20 mL of TOP were subsequently added. The mixture was sonicated for 20 min until all precursors dissolved completely.

SnSe Precursor Decomposition. The SnSe precursor was continuously injected into a preheated glass flask (420 °C), where it immediately decomposed. The flask was naturally cooled down to room temperature (RT), and the crystalline product was collected by dispersion in chloroform and precipitation with ethanol. Dispersion/precipitation steps were repeated three times using chloroform and ethanol aided by centrifugation at 7200 rpm for 5 min. The produced SnSe material was kept inside the glovebox for further use.

Bulk Material Consolidation. SnSe particles were thermally annealed at 500 °C (heating rate = 10 °C/min) for 60 min inside a tube furnace with argon flow to remove organic residues. After cooling to RT, the annealed material was grounded in a mortar and subsequently loaded into a graphite die. The die was then transferred to a custom-made hot-press system inside the glovebox, where it was heated to 500 °C using an induction coil. The die was held at this temperature for 5 min under 80 MPa pressure. Afterward, the pressure was released and the die was naturally cooled down to RT. The obtained cylindrical pellets (8 mm × 12 mm) were cut in rectangular bars in two directions: along the pressure axis (cross-plane direction) and normal to this axis (in-plane direction). The consolidated pellets were subsequently kept inside the glovebox. Before performing measurement, the pellets were polished slightly to remove a possible surface oxide layer.

Printed Layers. The SnSe molecular precursor was printed on a graphite foil using an ink jet nozzle. The graphite foil was then annealed on a hot plate at 420 °C for 5 min within an argon-filled glovebox. Afterward, the foil was hot pressed at 500 °C for 3 min under 80 MPa pressure.

Structural and Chemical Characterization. The particle size and morphology were characterized by transmission electron microscopy (TEM, ZEISS LIBRA 120), working at 120 kV, and field-emission scanning electron microscopy (SEM, Zeiss Auriga), operating at 5.0 kV. High-resolution TEM (HRTEM) images and scanning TEM (STEM) studies were conducted on a FEI Tecnai F20 field emission gun microscope operated at 200 kV with a point-to-point resolution of 0.19 nm, which was equipped with high-angle annular dark field (HAADF) and Gatan Quantum electron energy loss spectroscopy (EELS) detectors. Elemental analysis was performed using an Oxford energy-dispersive X-ray spectrometer (EDX) combined with the Zeiss Auriga SEM working at 20.0 kV. X-ray diffraction analyses (XRD, 2 θ : 5°–80°, scanning rate was set at 5°/min) were carried out on a Bruker AXS D8 Advance X-ray diffractometer with Ni-filtered Cu K α radiation (λ = 1.5406 Å), operating at 40 mA and 40 kV. X-ray photoelectron spectroscopy (XPS) was performed on a SPECS system equipped with a Phoibos 150 MCD-9 detector, working at 150 W with an Al anode XR50 source. Fourier transform infrared spectroscopy (FTIR, Alpha Bruker) was carried out with a platinum attenuated total reflectance single-reflection module. The surface topology was measured by atomic force microscopy (AFM, XE 100 Park System Corp.) Scans were conducted in noncontact mode with a silicon Tap300Al-G cantilever (Budget Sensors, spring constant of ~40 N/m and resonant frequency of ~300 kHz). AFM images were analyzed in the XEI software (Park System Corp). Ultraviolet–visible spectrophotometry (UV–vis) optical absorption spectra were recorded on a LAMBDA 950 UV–vis spectrophotometer from PerkinElmer.

Thermoelectric Characterization. Seebeck coefficients were measured with a static DC method. Electric resistivity data was obtained using a standard four probe method. Electric resistivity and Seebeck coefficients were measured simultaneously in a LSR-3 LINSEIS system in the temperature range from 323 to 803 K under a helium atmosphere. Bearing in mind the measurement precision and system accuracy, an error of ca. 5% in the measurement of Seebeck coefficient and electrical conductivity was estimated. A xenon flash apparatus was used to measure the thermal diffusivities (D) of all samples with accuracies better than 6%. Thermal conductivities were then calculated by the relation $\kappa = C_p D \rho$, where C_p is the heat capacity that was estimated from the Dulong–Petit law, D is the measured thermal diffusivity, and ρ is the mass density that was measured using Archimedes' method. Hall charge carrier concentrations (n_H) and

mobilities (μ_H) at room temperature (300 K) were measured with a Van der Pauw and Hall Bar measurements (ezHEMS 1000, NanoMagnetics) using a magnetic field of 1 T. Values provided correspond to the average of 10 consecutive measurements, from which an error of ca. 10% was estimated.

■ ASSOCIATED CONTENT

Supporting Information

The Supporting Information is available free of charge at <https://pubs.acs.org/doi/10.1021/acsami.0c04331>.

Precursor formation mechanism, UV–vis spectra, SEM–EDX, electrical transport properties, stability and reproducibility test (PDF)

■ AUTHOR INFORMATION

Corresponding Authors

Maria Ibáñez – IST Austria, Klosterneuburg 3400, Austria;

✉ orcid.org/0000-0001-5013-2843; Email: mibanez@ist.ac.at

Andreu Cabot – Catalonia Energy Research Institute-IREC,

Barcelona, Catalonia 08930, Spain; ICREA, Barcelona, Catalonia 08010, Spain; ✉ orcid.org/0000-0002-7533-3251; Email: acabot@irec.cat

Authors

Yu Zhang – Catalonia Energy Research Institute-IREC,

Barcelona, Catalonia 08930, Spain; ✉ orcid.org/0000-0002-0332-0013

Yu Liu – IST Austria, Klosterneuburg 3400, Austria;

✉ orcid.org/0000-0001-7313-6740

Congcong Xing – Catalonia Energy Research Institute-IREC,

Barcelona, Catalonia 08930, Spain; Institute of Energy Technologies, Department of Chemical Engineering and Barcelona Research Center in Multiscale Science and Engineering, Universitat Politècnica de Catalunya, EEBE, Barcelona, Catalonia 08019, Spain; ✉ orcid.org/0000-0001-7674-6720

Ting Zhang – Catalan Institute of Nanoscience and

Nanotechnology (ICN2), CSIC, and BIST, Barcelona, Catalonia 08193, Spain

Mengyao Li – Catalonia Energy Research Institute-IREC, Barcelona, Catalonia 08930, Spain

Mercè Pacios – Catalonia Energy Research Institute-IREC, Barcelona, Catalonia 08930, Spain

Xiaoting Yu – Catalonia Energy Research Institute-IREC, Barcelona, Catalonia 08930, Spain

Jordi Arbiol – Catalan Institute of Nanoscience and Nanotechnology (ICN2), CSIC, and BIST, Barcelona, Catalonia 08193, Spain; ICREA, Barcelona, Catalonia 08010, Spain; ✉ orcid.org/0000-0002-0695-1726

Jordi Llorca – Institute of Energy Technologies, Department of Chemical Engineering and Barcelona Research Center in Multiscale Science and Engineering, Universitat Politècnica de Catalunya, EEBE, Barcelona, Catalonia 08019, Spain; ✉ orcid.org/0000-0002-7447-9582

Doris Cadavid – Departamento de Física, Universidad Nacional de Colombia 111321, Ciudad Universitaria, Bogotá, Colombia; ✉ orcid.org/0000-0002-1376-6078

Complete contact information is available at:

<https://pubs.acs.org/doi/10.1021/acsami.0c04331>

Author Contributions

[§]Y.Z. and Y.L. contributed equally to this work.

Author Contributions

The manuscript was written through contributions of all authors. All authors have given approval to the final version of the manuscript.

Notes

The authors declare no competing financial interest.

ACKNOWLEDGMENTS

M.I. acknowledges financial support from IST Austria. Y.L. acknowledges funding from the European Union's Horizon 2020 Research and Innovation Programme under the Marie Skłodowska-Curie grant agreement no. 754411. J.L. is a Serra Hünter Fellow and is grateful to ICREA Academia program and projects MICINN/FEDER RTI2018-093996-B-C31 and GC 2017 SGR 128. This work was supported by the European Regional Development Funds and by the Spanish Ministerio de Economía y Competitividad through the project SEHTOP (ENE2016-77798-C4-3-R). Y.Z., C.X., M.L., X.Y., and T.Z. thank the China Scholarship Council for scholarship support. ICN2 acknowledges funding from Generalitat de Catalunya 2017 SGR 327 and the Spanish MINECO project ENE2017-85087-C3. ICN2 is supported by the Severo Ochoa program from the Spanish MINECO (grant no. SEV-2017-0706) and is funded by the CERCA Programme/Generalitat de Catalunya. Part of the present work has been performed in the framework of Universitat Autònoma de Barcelona Materials Science PhD program.

REFERENCES

- (1) Bell, L. E. Cooling, Heating, Generating Power, and Recovering Waste Heat with Thermoelectric Systems. *Science* **2008**, *321* (5895), 1457–1461.
- (2) Sootsman, J. R.; Chung, D. Y.; Kanatzidis, M. G. New and Old Concepts in Thermoelectric Materials. *Angew. Chem., Int. Ed.* **2009**, *48* (46), 8616–8639.
- (3) Snyder, G.; Toberer, E. Complex Thermoelectric Materials. *Nat. Mater.* **2008**, *7*, 105–114.
- (4) Minnich, A.; Dresselhaus, M.; Ren, Z.; Chen, G. Bulk Nanostructured Thermoelectric Materials: Current Research and Future Prospects. *Energy Environ. Sci.* **2009**, *2* (5), 466–479.
- (5) Leonov, V.; Torfs, T.; Fiorini, P.; Van Hoof, C. Thermoelectric Converters of Human Warmth for Self-powered Wireless Sensor Nodes. *IEEE Sens. J.* **2007**, *7* (5), 650–657.
- (6) Kraemer, D.; Poudel, B.; Feng, H.-P.; Caylor, J. C.; Yu, B.; Yan, X.; Ma, Y.; Wang, X.; Wang, D.; Muto, A.; McEnaney, K.; Chiesa, M.; Ren, Z.; Chen, G. High-performance Flat-Panel Solar Thermoelectric Generators with High Thermal Concentration. *Nat. Mater.* **2011**, *10* (7), 532–538.
- (7) Ortega, S.; Ibáñez, M.; Liu, Y.; Zhang, Y.; Kovalenko, M. V.; Cadavid, D.; Cabot, A. Bottom-Up Engineering of Thermoelectric Nanomaterials and Devices From Solution-processed Nanoparticle Building Blocks. *Chem. Soc. Rev.* **2017**, *46* (12), 3510–3528.
- (8) Ibáñez, M.; Luo, Z.; Genc, A.; Piveteau, L.; Ortega, S.; Cadavid, D.; Dobrozhan, O.; Liu, Y.; Nachttegaal, M.; Zebarjadi, M.; Arbiol, J.; Kovalenko, M. V.; Cabot, A. High-performance Thermoelectric Nanocomposites from Nanocrystal Building Blocks. *Nat. Commun.* **2016**, *7*, 10766.
- (9) Snyder, G. J.; Ursell, T. S. Thermoelectric Efficiency and Compatibility. *Phys. Rev. Lett.* **2003**, *91* (14), 148301.
- (10) Ibáñez, M.; Hasler, R.; Genç, A.; Liu, Y.; Kuster, B.; Schuster, M.; Dobrozhan, O.; Cadavid, D.; Arbiol, J.; Cabot, A.; Kovalenko, M. Ligand-Mediated Band Engineering in Bottom-Up Assembled SnTe Nanocomposites for Thermoelectric Energy Conversion. *J. Am. Chem. Soc.* **2019**, *141* (20), 8025–8029.
- (11) Zhou, Y.; Zhao, L. D. Promising Thermoelectric Bulk Materials with 2D Structures. *Adv. Mater.* **2017**, *29* (45), 1702676.
- (12) Dresselhaus, M.; Dresselhaus, G.; Sun, X.; Zhang, Z.; Cronin, S.; Koga, T. Low-dimensional Thermoelectric Materials. *Phys. Solid State* **1999**, *41* (5), 679–682.
- (13) Zhao, L.-D.; Lo, S.-H.; Zhang, Y.; Sun, H.; Tan, G.; Uher, C.; Wolverton, C.; Dravid, V. P.; Kanatzidis, M. G. Ultralow Thermal Conductivity and High Thermoelectric Figure of Merit in SnSe Crystals. *Nature* **2014**, *508* (7496), 373–377.
- (14) Rhyee, J. S.; Ahn, K.; Lee, K. H.; Ji, H. S.; Shim, J. H. Enhancement of the Thermoelectric Figure-of-Merit in a Wide Temperature Range in In₄Se_{3-x}Cl_{0.03} Bulk Crystals. *Adv. Mater.* **2011**, *23* (19), 2191–2194.
- (15) Liu, Y.; Zhang, Y.; Lim, K. H.; Ibanez, M.; Ortega, S.; Li, M.; David, J.; Martí-Sánchez, S.; Ng, K. M.; Arbiol, J.; Kovalenko, M. V.; Cadavid, D.; Cabot, A. High Thermoelectric Performance in Crystallographically Textured n-Type Bi₂Te_{3-x}Se_x Produced from Asymmetric Colloidal Nanocrystals. *ACS Nano* **2018**, *12* (7), 7174–7184.
- (16) Liu, Y.; Zhang, Y.; Ortega, S.; Ibáñez, M.; Lim, K. H.; Grau-Carbonell, A.; Martí-Sánchez, S.; Ng, K. M.; Arbiol, J.; Kovalenko, M. V.; Cadavid, D.; Cabot, A. Crystallographically Textured Nanomaterials Produced from the Liquid Phase Sintering of Bi_xSb_{2-x}Te₃ Nanocrystal Building Blocks. *Nano Lett.* **2018**, *18* (4), 2557–2563.
- (17) Dun, C.; Liu, Y.; Al-Qawasmeh, A.; Hewitt, C. A.; Guo, Y.; Xu, J.; Jiang, Q.; Wang, J.; Marcus, G.; Cadavid, D.; Montgomery, D.; Wang, H.; Kovnir, K.; Cabot, A.; Carroll, D. L. Topological Doping Effects in 2D Chalcogenide Thermoelectrics. *2D Mater.* **2018**, *5* (4), 045008.
- (18) Poudel, B.; Hao, Q.; Ma, Y.; Lan, Y.; Minnich, A.; Yu, B.; Yan, X.; Wang, D.; Muto, A.; Vashaee, D.; Chen, X.; Liu, J.; Dresselhaus, M. S.; Chen, G.; Ren, Z. High-Thermoelectric Performance of Nanostructured Bismuth Antimony Telluride Bulk Alloys. *Science* **2008**, *320* (5876), 634–638.
- (19) Zhao, X. B.; Ji, X. H.; Zhang, Y. H.; Zhu, T. J.; Tu, J. P.; Zhang, X. B. Bismuth Telluride Nanotubes and the Effects on the Thermoelectric Properties of Nanotube-Containing Nanocomposites. *Appl. Phys. Lett.* **2005**, *86* (6), 062111.
- (20) Yamashita, O.; Tomiyoshi, S.; Makita, K. Bismuth Telluride Compounds with High Thermoelectric Figures of Merit. *J. Appl. Phys.* **2003**, *93* (1), 368–374.
- (21) Goldsmid, H. J. Bismuth Telluride and Its Alloys as Materials for Thermoelectric Generation. *Materials* **2014**, *7* (4), 2577–2592.
- (22) Chang, C.; Wu, M.; He, D.; Pei, Y.; Wu, C.-F.; Wu, X.; Yu, H.; Zhu, F.; Wang, K.; Chen, Y.; Huang, L.; Li, J.-F.; He, J.; Zhao, L.-D. 3D Charge and 2D Phonon Transports Leading to High Out-of-plane ZT in n-type SnSe Crystals. *Science* **2018**, *360* (6390), 778–783.
- (23) Chen, C.-L.; Wang, H.; Chen, Y.-Y.; Day, T.; Snyder, G. J. Thermoelectric Properties of P-type Polycrystalline SnSe Doped with Ag. *J. Mater. Chem. A* **2014**, *2* (29), 11171–11176.
- (24) Sassi, S.; Candolfi, C.; Vaney, J.-B.; Ohorodniichuk, V.; Masschelein, P.; Dauscher, A.; Lenoir, B. Assessment of the Thermoelectric Performance of Polycrystalline p-type SnSe. *Appl. Phys. Lett.* **2014**, *104* (21), 212105.
- (25) Wei, T.-R.; Tan, G.; Zhang, X.; Wu, C.-F.; Li, J.-F.; Dravid, V. P.; Snyder, G. J.; Kanatzidis, M. G. Distinct Impact of Alkali-ion Doping on Electrical Transport Properties of Thermoelectric p-type Polycrystalline SnSe. *J. Am. Chem. Soc.* **2016**, *138* (28), 8875–8882.
- (26) Chere, E. K.; Zhang, Q.; Dahal, K.; Cao, F.; Mao, J.; Ren, Z. Studies on Thermoelectric Figure of Merit of Na-doped p-type Polycrystalline SnSe. *J. Mater. Chem. A* **2016**, *4* (5), 1848–1854.
- (27) Shi, X.; Wu, A.; Liu, W.; Moshwan, R.; Wang, Y.; Chen, Z.-G.; Zou, J. Polycrystalline SnSe with Extraordinary Thermoelectric Property via Nanoporous Design. *ACS Nano* **2018**, *12* (11), 11417–11425.
- (28) Chandra, S.; Banik, A.; Biswas, K. N-Type Ultrathin Few-Layer Nanosheets of Bi-doped SnSe: Synthesis and Thermoelectric Properties. *ACS Energy Lett.* **2018**, *3* (5), 1153–1158.
- (29) Banik, A.; Biswas, K. A game-changing strategy in SnSe thermoelectrics. *Joule* **2019**, *3* (3), 636–638.

- (30) Chandra, S.; Biswas, K. Realization of high thermoelectric figure of merit in solution synthesized 2D SnSe nanoplates via Ge alloying. *J. Am. Chem. Soc.* **2019**, *141* (15), 6141–6145.
- (31) Han, G.; Popuri, S. R.; Greer, H. F.; Bos, J. W. G.; Zhou, W.; Knox, A. R.; Montecucco, A.; Siviter, J.; Man, E. A.; Macauley, M.; Paul, D. J.; Li, W.-G.; Paul, M. C.; Gao, M.; Sweet, T.; Freer, R.; Azough, F.; Baig, H.; Sellami, N.; Mallick, T. K.; Gregory, D. H. Facile Surfactant-Free Synthesis of p-Type SnSe Nanoplates with Exceptional Thermoelectric Power Factors. *Angew. Chem., Int. Ed.* **2016**, *55* (22), 6433–6437.
- (32) Ge, Z. H.; Qiu, Y.; Chen, Y. X.; Chong, X.; Feng, J.; Liu, Z. K.; He, J. Multipoint Defect Synergy Realizing the Excellent Thermoelectric Performance of n-Type Polycrystalline SnSe via Re Doping. *Adv. Funct. Mater.* **2019**, *29*, 1902893.
- (33) Luo, Y.; Cai, S.; Hua, X.; Chen, H.; Liang, Q.; Du, C.; Zheng, Y.; Shen, J.; Xu, J.; Wolverton, C.; Dravid, V.; Yan, Q.; Kanatzidis, M. G. High Thermoelectric Performance in Polycrystalline SnSe Via Dual-Doping with Ag/Na and Nanostructuring with Ag₆SnSe₆. *Adv. Energy Mater.* **2019**, *9* (2), 1803072.
- (34) Shi, X.; Wu, A.; Feng, T.; Zheng, K.; Liu, W.; Sun, Q.; Hong, M.; Pantelides, S. T.; Chen, Z. G.; Zou, J. High Thermoelectric Performance in p-type Polycrystalline Cd-doped SnSe Achieved by a Combination of Cation Vacancies and Localized Lattice Engineering. *Adv. Energy Mater.* **2019**, *9* (11), 1803242.
- (35) Heo, S. H.; Jo, S.; Kim, H. S.; Choi, G.; Song, J. Y.; Kang, J.-Y.; Park, N.-J.; Ban, H. W.; Kim, F.; Jeong, H.; Jung, J.; Jang, J.; Lee, W. B.; Shin, H.; Son, J. S. Composition change-driven texturing and doping in solution-processed SnSe thermoelectric thin films. *Nat. Commun.* **2019**, *10* (1), 1–10.
- (36) Ashida, M.; Hamachiyo, T.; Hasezaki, K.; Matsunoshita, H.; Kai, M.; Horita, Z. Texture of Bismuth Telluride-based Thermoelectric Semiconductors Processed by High-pressure Torsion. *J. Phys. Chem. Solids* **2009**, *70* (7), 1089–1092.
- (37) Rogl, G.; Setman, D.; Schafner, E.; Horky, J.; Kerber, M.; Zehetbauer, M.; Falmbigl, M.; Rogl, P.; Royanian, E.; Bauer, E. High-pressure Torsion, A New Processing Route for Thermoelectrics of High ZTs by Means of Severe Plastic Deformation. *Acta Mater.* **2012**, *60* (5), 2146–2157.
- (38) Angerer, P.; Neubauer, E.; Yu, L.; Khor, K. A. Texture and Structure Evolution of Tantalum Powder Samples During Spark-Plasma-Sintering (SPS) and Conventional Hot-pressing. *Int. J. Refract. Hard Met.* **2007**, *25* (4), 280–285.
- (39) Jiang, J.; Chen, L.; Bai, S.; Yao, Q.; Wang, Q. Fabrication and Thermoelectric Performance of Textured n-type Bi₂(Te, Se)₃ by Spark Plasma Sintering. *Mater. Sci. Eng., B* **2005**, *117* (3), 334–338.
- (40) Jiang, J.; Chen, L.; Bai, S.; Yao, Q.; Wang, Q. Thermoelectric Properties of Textured P-type (Bi, Sb)₂Te₃ Fabricated by Spark Plasma Sintering. *Scr. Mater.* **2005**, *52* (5), 347–351.
- (41) Li, M.; Liu, Y.; Zhang, Y.; Zuo, Y.; Li, J.; Lim, K. H.; Cadavid, D.; Ng, K. M.; Cabot, A. Crystallographically Textured SnSe Nanomaterials Produced from the Liquid Phase Sintering of Nanocrystals. *Dalton Trans.* **2019**, *48* (11), 3641–3647.
- (42) Zhang, J.; Xu, J.; Tan, X.; Wang, H.; Liu, G.-Q.; Shao, H.; Yu, B.; Yue, S.; Jiang, J. Optimized Orientation and Enhanced Thermoelectric Performance in Sn_{0.97}Na_{0.03}Se with Te Addition. *J. Mater. Chem. C* **2019**, *7* (9), 2653–2658.
- (43) Liu, X.; Li, Y.; Zhou, B.; Wang, X.; Cartwright, A. N.; Swihart, M. T. Shape-controlled synthesis of SnE (E = S, Se) semiconductor nanocrystals for optoelectronics. *Chem. Mater.* **2014**, *26* (11), 3515–3521.
- (44) Li, L.; Chen, Z.; Hu, Y.; Wang, X.; Zhang, T.; Chen, W.; Wang, Q. Single-layer single-crystalline SnSe nanosheets. *J. Am. Chem. Soc.* **2013**, *135* (4), 1213–1216.
- (45) Liu, S.; Guo, X.; Li, M.; Zhang, W. H.; Liu, X.; Li, C. Solution-phase synthesis and characterization of single-crystalline SnSe nanowires. *Angew. Chem., Int. Ed.* **2011**, *50* (50), 12050–12053.
- (46) Baumgardner, W. J.; Choi, J. J.; Lim, Y.-F.; Hanrath, T. SnSe nanocrystals: synthesis, structure, optical properties, and surface chemistry. *J. Am. Chem. Soc.* **2010**, *132* (28), 9519–9521.
- (47) Ning, J.; Xiao, G.; Jiang, T.; Wang, L.; Dai, Q.; Zou, B.; Liu, B.; Wei, Y.; Chen, G.; Zou, G. Shape and size controlled synthesis and properties of colloidal IV–VI SnSe nanocrystals. *CrystEngComm* **2011**, *13* (12), 4161–4166.
- (48) Yarema, M.; Caputo, R.; Kovalenko, M. V. Precision Synthesis of Colloidal Inorganic Nanocrystals Using Metal and Metalloid Amides. *Nanoscale* **2013**, *5* (18), 8398–8410.
- (49) Kravchyk, K.; Protesescu, L.; Bodnarchuk, M. I.; Krumeich, F.; Yarema, M.; Walter, M.; Guntlin, C.; Kovalenko, M. V. Monodisperse and Inorganically Capped Sn and Sn/SnO₂ Nanocrystals for High-performance Li-ion Battery Anodes. *J. Am. Chem. Soc.* **2013**, *135* (11), 4199–4202.
- (50) Mourdikoudis, S.; Liz-Marzan, L. M. Oleylamine in Nanoparticle Synthesis. *Chem. Mater.* **2013**, *25* (9), 1465–1476.
- (51) Evans, C. M.; Evans, M. E.; Krauss, T. D. Mysteries of TOPSe Revealed: Insights into Quantum Dot Nucleation. *J. Am. Chem. Soc.* **2010**, *132* (32), 10973–10975.
- (52) Zhang, Y.; Liu, Y.; Lim, K. H.; Xing, C.; Li, M.; Zhang, T.; Tang, P.; Arbiol, J.; Llorca, J.; Ng, K. M.; Ibáñez, M.; Guardia, P.; Prato, M.; Cadavid, D.; Cabot, A. Tin Diselenide Molecular Precursor for Solution-Processable Thermoelectric Materials. *Angew. Chem.* **2018**, *130* (52), 17309–17314.
- (53) Berestok, T.; Guardia, P.; Blanco, J.; Nafria, R.; Torruella, P.; Lopez-Conesa, L.; Estrade, S.; Ibáñez, M.; De Roo, J.; Luo, Z.; Cadavid, D.; Martins, J. C.; Kovalenko, M. V.; Peiró, F.; Cabot, A. Tuning Branching in Ceria Nanocrystals. *Chem. Mater.* **2017**, *29* (10), 4418–4424.
- (54) Watt, J.; Cheong, S.; Toney, M. F.; Ingham, B.; Cookson, J.; Bishop, P. T.; Tilley, R. D. Ultrafast Growth of Highly Branched Palladium Nanostructures for Catalysis. *ACS Nano* **2010**, *4* (1), 396–402.
- (55) Lee, Y. K.; Luo, Z.; Cho, S. P.; Kanatzidis, M. G.; Chung, I. Surface Oxide Removal for Polycrystalline SnSe Reveals Near-Single-Crystal Thermoelectric Performance. *Joule* **2019**, *3* (3), 719–731.
- (56) Shi, X.; Zheng, K.; Hong, M.; Liu, W.; Moshwan, R.; Wang, Y.; Qu, X.; Chen, Z.-G.; Zou, J. Boosting the Thermoelectric Performance of P-type heavily Cu-doped Polycrystalline SnSe via Inducing Intensive Crystal Imperfections and Defect Phonon Scattering. *Chem. Sci.* **2018**, *9* (37), 7376–7389.
- (57) Ge, Z.-H.; Song, D.; Chong, X.; Zheng, F.; Jin, L.; Qian, X.; Zheng, L.; Dunin-Borkowski, R. E.; Qin, P.; Feng, J.; Zhao, L.-D. Boosting the Thermoelectric Performance of (Na, K)-Codoped Polycrystalline SnSe by Synergistic Tailoring of the Band Structure and Atomic-Scale Defect Phonon Scattering. *J. Am. Chem. Soc.* **2017**, *139* (28), 9714–9720.



Cite this: DOI: 10.1039/d0tc02182b

Bismuth telluride–copper telluride nanocomposites from heterostructured building blocks†

Yu Zhang,^a Yu Liu,^{*ab} Mariano Calcabrini,^b Congcong Xing,^a Xu Han,^c Jordi Arbiol,^{cd} Doris Cadavid,^e Maria Ibáñez^b and Andreu Cabot^{*ad}

Appropriately designed nanocomposites allow improving the thermoelectric performance by several mechanisms, including phonon scattering, modulation doping and energy filtering, while additionally promoting better mechanical properties than those of crystalline materials. Here, a strategy for producing Bi₂Te₃–Cu_{2–x}Te nanocomposites based on the consolidation of heterostructured nanoparticles is described and the thermoelectric properties of the obtained materials are investigated. We first detail a two-step solution-based process to produce Bi₂Te₃–Cu_{2–x}Te heteronanostructures, based on the growth of Cu_{2–x}Te nanocrystals on the surface of Bi₂Te₃ nanowires. We characterize the structural and chemical properties of the synthesized nanostructures and of the nanocomposites produced by hot-pressing the particles at moderate temperatures. Besides, the transport properties of the nanocomposites are investigated as a function of the amount of Cu introduced. Overall, the presence of Cu decreases the material thermal conductivity through promotion of phonon scattering, modulates the charge carrier concentration through electron spillover, and increases the Seebeck coefficient through filtering of charge carriers at energy barriers. These effects result in an improvement of over 50% of the thermoelectric figure of merit of Bi₂Te₃.

Received 4th May 2020,
Accepted 3rd September 2020

DOI: 10.1039/d0tc02182b

rsc.li/materials-c

Introduction

Solid state thermoelectric (TE) devices, allowing the direct and reversible conversion between heat and electricity, provide numerous advantages over competing technologies for thermal energy harvesting and precise temperature control. Advantages include silent operation, high durability, low weight, no fluid or moving parts and flexible design with great adaptability. Because of their versatility, TE devices can be used in a multitude of applications in waste heat recovery, refrigeration, energy harvesting for autonomous remote sensing, air conditioning and so on. However, their moderate efficiency and high cost currently limits the spread of this technology in its many potential markets.^{1,2}

The conversion efficiency of TE devices is in large part determined by a material dimensionless figure of merit: $ZT = \sigma S^2 T / \kappa$, where σ is the electrical conductivity, S the Seebeck coefficient, T the absolute temperature, and κ the thermal conductivity.^{3–5} To produce an efficient TE material one needs to maximize the power factor ($PF = \sigma S^2$) by optimizing the charge carrier concentration and introducing mechanisms to increase the Seebeck coefficient. Simultaneously, the thermal conductivity needs to be minimized through phonon scattering at different scales. Since all these material parameters are strongly interrelated, it is extremely challenging to maximize the energy conversion efficiency of TE materials.^{6–9}

The combination of multiple phases offers additional degrees of freedom to design materials with optimized functional properties.¹⁰ Nanocomposites are particularly appealing in the TE field^{11–14} as they provide not only effective phonon scattering at interphases that dramatically reduce thermal conductivity,^{15–21} but also potential quantum effects and selective charge carrier scattering to increase the Seebeck coefficient.^{22–26} Additionally, appropriately designed composites allow activating the required large amounts of charge carriers without dramatically decreasing their mobility by means of modulation doping.^{26–33}

The properties of composite materials not only depend on the type and amount of each of the different phases, but also on

^a Catalonia Energy Research Institute – IREC, Sant Adria de Besòs, Barcelona 08930, Spain. E-mail: acabot@irec.cat

^b IST Austria, Am Campus 1, Klosterneuburg 3400, Austria. E-mail: yu.liu@ist.ac.at

^c Catalan Institute of Nanoscience and Nanotechnology (ICN2), CSIC and BIST, Campus UAB, Bellaterra, Barcelona 08193, Catalonia, Spain

^d ICREA, Pg. Lluís Companys 23, Barcelona 08010, Catalonia, Spain

^e Departamento de Física, Universidad Nacional de Colombia, Ciudad Universitaria, Bogota 111321, Colombia

† Electronic supplementary information (ESI) available. See DOI: 10.1039/d0tc02182b

their distribution, which is extremely difficult to control. Beyond the use of thin film vacuum-based techniques that are limited in terms of cost, production volume, three dimensional control of the phase distribution and material thickness, the most effective strategy for the large and cost-effective production of nanocomposites with accurate phase control is the assembly of heterostructured building blocks.^{10,34,35}

Bi_2Te_3 -based alloys provide the highest TE performance at around ambient temperatures and thus most TE commercial devices are produced from highly crystalline ingots of these materials. However, the current performance of Bi_2Te_3 -based alloys is still far from optimum. Besides, owing to their layered structure, these materials are mechanically fragile, which calls for alternative processing strategies that are able to deliver polycrystalline materials.

When synthesized in an excess of Te, Bi_2Te_3 is generally a degenerated n-type semiconductor because it retains abundant Te_{Bi} antisites due to the similar electronegativities and ionic radii of Bi and Te.³⁶ The excessive charge carrier concentration of Bi_2Te_3 deteriorates the Seebeck coefficient and results in low power factors. To adjust this parameter, and at the same time decrease the lattice thermal conductivity, part of the Te within Bi_2Te_3 is generally replaced by Se to produce n-type $\text{Bi}_2\text{Te}_{3-x}\text{Se}_x$.³⁷

To further increase the power factor and decrease thermal conductivity, different elements have been incorporated into Bi_2Te_3 -based alloys.³⁸ Among them, Cu has provided some of the best results.^{30,33–40} The presence of Cu has usually been associated with an enhanced phonon scattering yielding lower thermal conductivities. Besides, the electronic properties of Bi_2Te_3 are influenced by the presence of Cu in a rather complex way, depending on the Cu amount, location and chemical environment and on the Bi_2Te_3 conductivity type.^{30,39–46} The incorporation of very low amounts of Cu has been reported to reduce the charge carrier concentration presumably due to the reduction of tellurium vacancies.⁴⁶ On the other hand, low concentration Cu^+ ions intercalated at the van der Waals gap between Bi_2Te_3 layers act as a donor.^{43,45} Besides, Cu^+ ions substituting Bi, $\text{Cu}_{\text{Bi}}^{2-}$, act as acceptors.^{30,45} The presence of Cu during material sintering also affects the size of the Bi_2Te_3 crystal domains. Additionally, amounts of Cu above the solubility limit may result in the segregation of Cu_{2-x}Te , thus removing Te_{Bi} antisites and/or introducing Te vacancies, $\text{V}_{\text{Te}}^{2+}$, both acting as donors.^{30,45,46} The Cu presence has been also associated with an enhancement of reproducibility from batch to batch, related to a reduction of the fluctuation of charge concentration owing to the hindered formation of tellurium vacancies.^{30,46}

Here we report on a strategy to produce $\text{Bi}_2\text{Te}_3\text{-Cu}_{2-x}\text{Te}$ nanocomposites based on the consolidation of $\text{Bi}_2\text{Te}_3\text{-Cu}_{2-x}\text{Te}$ heterostructured nanoparticles. This strategy allows us to separate the contribution of Cu ions within the Bi_2Te_3 lattice from that of Cu_{2-x}Te phases. We analyze the TE properties of the produced composites and discuss them in terms of the heterojunctions formed between Cu_{2-x}Te and Bi_2Te_3 nanodomains.

Experimental section

Chemicals

Bismuth(III) chloride (BiCl_3 , $\geq 98\%$), potassium hydroxide (KOH , $\geq 98\%$), polyvinylpyrrolidone (PVP, $(\text{C}_6\text{H}_9\text{NO})_n$, average molar weight $\sim 55\,000$), tellurium dioxide (TeO_2 , $\geq 99\%$), copper(I) chloride (CuCl , $\geq 99.995\%$) and hydrazine monohydrate ($\text{NH}_2\text{NH}_2\cdot\text{H}_2\text{O}$, 64–65%) were purchased from Sigma Aldrich. Ethylene glycol (EG, $\text{HOCH}_2\text{CH}_2\text{OH}$, 99%) was purchased from Fisher. Analytical grade acetone, isopropanol and ethanol were obtained from various sources. All chemicals were used as received without further purification.

Bi_2Te_3 nanowire synthesis

Bi_2Te_3 nanowires were prepared following a previously reported approach based on the reaction of the Bi precursor with pre-synthesized Te nanowires.⁴⁷ In a typical synthesis, 5.6 mmol of TeO_2 , 37 mmol of KOH , 1.5 g of PVP, and 56 mL of EG were added into a 250 mL three-neck flask. The mixture was stirred and heated to 140 °C. At this temperature, after all the chemicals were dissolved, 0.87 mL of a 64–65% $\text{N}_2\text{H}_4\cdot\text{H}_2\text{O}$ solution was injected into the solution. The reaction mixture was maintained at 140 °C for 1 h to allow all Te to be reduced. Then, the temperature of the solution was raised to 160 °C. At this point, a hot BiCl_3/EG solution was injected into the flask. This BiCl_3/EG solution was produced by adding 3.6 mmol of BiCl_3 into 15 mL of EG in a glass vial that was heated to 100–120 °C. The BiCl_3/EG solution was allowed to react with the Te nanowires for 1 h at 160 °C. Afterward, the mixture was naturally cooled to room temperature. The product was purified firstly by adding acetone to the solution and centrifuging it. In a second step, ethanol was used to redisperse the particles and acetone ($V_{\text{ethanol}}/V_{\text{acetone}} = 1:2$) to precipitate them again. In a third step, deionized water was added to solubilize the remaining impurities and nanoparticles were precipitated by slow centrifugation. This procedure was repeated twice. In a last step, particles were redispersed once more with ethanol, precipitated with acetone, and dried under vacuum at room temperature.

$\text{Bi}_2\text{Te}_3\text{-Cu}_{2-x}\text{Te}$ heterostructures

Bismuth telluride–copper telluride heterostructures were produced by adding copper precursor to a solution containing Bi_2Te_3 nanowires. Briefly, to produce $\text{Bi}_2\text{Te}_3\text{-Cu}_{2-x}\text{Te}$ with a ratio of Bi:Cu = 8, after 1 h of reaction at 160 °C to form the Bi_2Te_3 nanowires, 0.4 mmol CuCl was added into 5 mL of EG in a glass vial to form a clear solution which was kept at 100–120 °C. After 1 h, 1.86 mL of 50–60% $\text{N}_2\text{H}_4\cdot\text{H}_2\text{O}$ was first added into the reaction and then the CuCl/EG solution was injected into the reaction, which continued for another 1 h before naturally cooling down to room temperature. Bi:Cu = 5 and 10 samples were produced following the above procedure, but using appropriate amounts of the copper precursor. Finally, the obtained material was purified following the same procedure as for Bi_2Te_3 nanowires.

Nanomaterial consolidation

Dried Bi_2Te_3 and $\text{Bi}_2\text{Te}_3\text{-Cu}_{2-x}\text{Te}$ particles were annealed at 330 °C for 60 min under Ar flow inside a tube furnace.

Annealing at 450 °C was also tested as noted below. The annealed powders were loaded into a graphite die and compacted into cylinders (\varnothing 8 mm \times 10 mm) using a custom-made hot press held at 270 °C and 60 MPa for 5 min. This process was carried out inside an Ar-filled glove box. The relative densities of the compacted pellets were measured using the Archimedes method. From these cylinders, rectangular bars of about 8 \times 6 \times 1 mm³ were cut in two normal directions, along the pressing direction and within the cylinder plane.

Structural and chemical characterization

X-Ray diffraction (XRD, 2θ angle: 20° to 80°; scanning rate: 5° min⁻¹) analyses were carried out on a Bruker AXS D8 ADVANCE X-ray diffractometer with Cu-K α radiation (λ = 1.5406 Å). The size and morphology of the initial materials were examined *via* transmission electron microscopy (TEM) using a ZEISS LIBRA 120 operated at 120 kV, and field-emission scanning electron microscopy (SEM) on an Auriga Zeiss operated at 5.0 kV. The crystallographic structure and chemical composition were analyzed by high resolution TEM (HRTEM) and electron energy loss spectroscopy (EELS), respectively, using a Tecnai F20 field-emission gun microscope at 200 kV with an embedded Gatan QUANTUM image filter. The material composition was analyzed using an Oxford energy dispersive X-ray spectrometer (EDX) attached to a Zeiss Auriga SEM at 20.0 kV.

TE property measurements

Seebeck coefficients were measured using a static DC method. Electrical resistivity data were obtained using a standard four-probe method. Both the Seebeck coefficient and the electrical resistivity were measured simultaneously in a LSR-3 LINSEIS system in the temperature range between room temperature and 573 K, in a helium atmosphere. Taking into account system accuracy and measurement precision, an error of *ca.* 4% in the measurement of the electrical conductivity and Seebeck coefficient was estimated. The thermal conductivity was calculated by $\kappa = \lambda C_p \rho$, where λ is the thermal diffusivity, C_p is the heat capacity, and ρ is the mass density of the specimen. A XFA 600 Xenon Flash Apparatus was used to determine the thermal diffusivities (λ) of the samples with an estimated error of *ca.* 5%. The constant pressure heat capacity (C_p) was estimated from empirical formulae using the Dulong–Petit limit (3R law), and the density (ρ) values used here were calculated using the Archimedes method. To avoid cluttering the plots, error bars were not included in the figures. Hall charge carrier concentrations (n_H) and mobilities (μ_H) at room temperature (300 K) were obtained using the van der Pauw method using a magnetic field of 1 T (ezHEMS, NanoMagnetics). Values provided correspond to the average of 5 measurements, from which an error of *ca.* 10% was estimated.

Results and discussion

Polycrystalline Bi₂Te₃ nanowires were synthesized in a two-step approach using Te nanowires as the reactive template.²²

Te nanowires were produced by reducing TeO₂ in EG at 140 °C. Afterwards, a BiCl₃/EG solution was injected to react with Te (see the Experimental section). The as-synthesized Bi₂Te₃ retained the Te nanowire geometry, with a relatively narrow distribution of diameters (30 \pm 10 nm) and lengths (600 \pm 80 nm). XRD characterization showed the samples to be highly crystalline and to present a single phase: Bi₂Te₃ (JCPDS 01-082-0358, Fig. 1b). No elemental Te was detected in the final product. HRTEM micrographs confirmed the Bi₂Te₃ nanowires to display a rhombohedral Bi₂Te₃ phase (space group = *R3 \bar{M} H*) with $a = b = 4.2999$ Å and $c = 30.5975$ Å (Fig. 1f). EELS elemental composition maps revealed the nanowires to be uniformly composed of Bi and Te (Fig. 1e).

Bi₂Te₃-Cu_{2-x}Te heterostructures with a tuned molar ratio (Bi:Cu = 10:8:5) were synthesized by injecting a CuCl/EG solution into the flask containing Bi₂Te₃ nanowires at 160 °C (see the Experimental section, Fig. S1, ESI†). This synthesis protocol was carried out on a sufficient scale to produce 4 g of material per batch. Fig. 1b displays the XRD pattern of the material produced with a nominal composition Bi:Cu = 8. Only the XRD peaks of the Bi₂Te₃ phase were detected. After Cu incorporation, the particles preserved the nanowire geometry (Fig. 1g).

HRTEM and power spectrum analysis revealed the presence of small Cu_{2.86}Te₂ crystallites (space group = *F43M*; $a = b = c = 6.0320$ Å) on the surface of Bi₂Te₃ nanowires (Fig. 1i). EELS analysis also showed the presence of Cu and Te on such crystallites, further confirming the formation of Bi₂Te₃-Cu_{2-x}Te heterostructures (Fig. 1h).

Bi₂Te₃-Cu_{2-x}Te nanowires were purified, dried, annealed and finally used as building blocks to produce cylindrical pellets with 10 mm thickness and 8 mm diameter. The consolidated nanomaterials had relative densities of around 86–87% (Fig. 2a and Table S1, ESI†). XRD patterns of Bi₂Te₃-Cu_{2-x}Te pellets showed the Bi₂Te₃ phase to be predominant, but the small peak at $2\theta = 26.7^\circ$ indicated the presence of a small fraction of a Cu_{2-x}Te phase that we tentatively associated with tetragonal Cu_{2.8}Te₂ (JCPDS 01-085-0606, Fig. 2b). The crystallographic transition from the cubic to the tetragonal Cu_{2-x}Te phase during annealing and hot press is consistent with previous reports and with the complex Cu–Te phase diagram.^{48,49} SEM characterization of the pellets showed them to maintain a filamentous structure denoting a minor sintering of the nanowires (Fig. 2c). EDX elemental maps of the pellets displayed a homogeneous distribution of the three elements at the 100 μ m scale (Fig. S3, ESI†). Quantitatively, the Cu/Bi/Te atomic ratio of the Bi:Cu = 8 sample was 1/7.9/11.9, and the Te/(Bi + Cu) ratio was 1.34, very close to the nominal value (3/2.25 = 1.33). Te/(Bi + Cu) compositions close to the nominal were also obtained for the other samples (Fig. S2, ESI†).

Taking into account the highly anisotropic transport properties of Bi₂Te₃ and the very asymmetric particles used as building blocks to produce the Bi₂Te₃-Cu_{2-x}Te composites, one could expect the pellet to present anisotropic transport properties. Thus, we measured the TE properties of the composites along two directions: parallel and normal to the pressure axis (Fig. S4, ESI†).

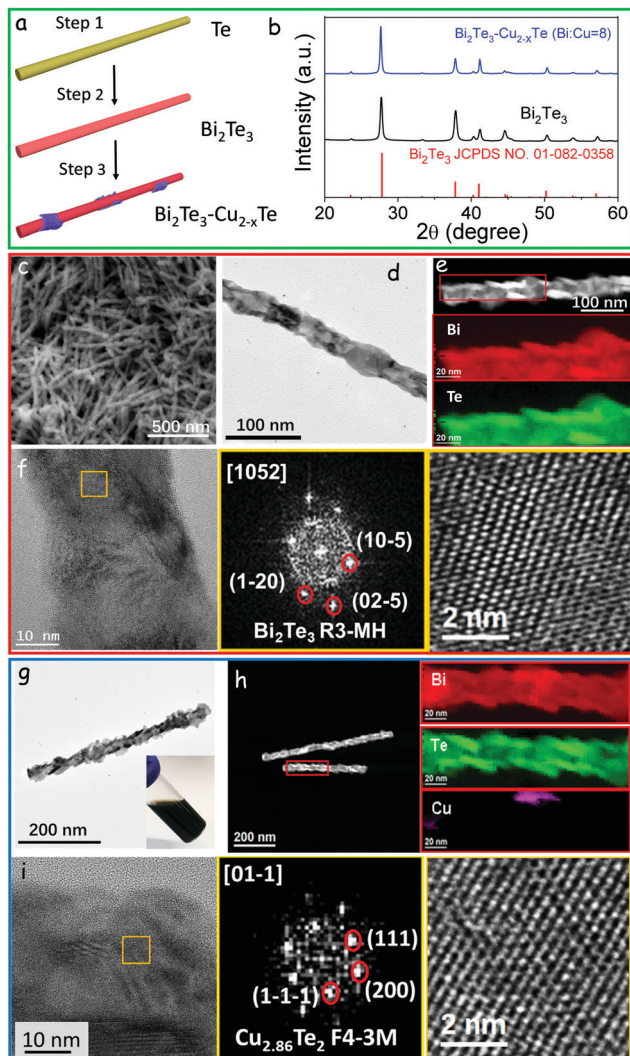


Fig. 1 (a) Schematic illustration of the formation of $\text{Bi}_2\text{Te}_3\text{-Cu}_{2-x}\text{Te}$ heterostructures. (b) Powder XRD pattern of as-synthesized Bi_2Te_3 and $\text{Bi}_2\text{Te}_3\text{-Cu}_{2-x}\text{Te}$ nanomaterials. (c) SEM micrograph of Bi_2Te_3 nanowires. (d) Representative TEM micrograph of a Bi_2Te_3 nanowire. (e) STEM micrograph and EELS chemical composition maps obtained from the red squared area. Individual Bi $N_{6,7}$ -edge at 157 eV (red), Te $M_{4,5}$ -edge at 572 eV (green). (f) HRTEM micrograph of a Bi_2Te_3 nanowire, details of the orange square region and its corresponding power spectrum. Lattice fringe distances were 0.314 nm, 0.177 nm and 0.216 nm, at 56.18° and 90.07° which was interpreted as the rhombohedral Bi_2Te_3 phase, visualized along its [1052] zone axis. (g) Representative TEM micrograph of a $\text{Bi}_2\text{Te}_3\text{-Cu}_{2-x}\text{Te}$ heterostructure. The inset shows a vial containing a $\text{Bi}_2\text{Te}_3\text{-Cu}_{2-x}\text{Te}$ solution. (h) EELS chemical composition maps obtained from the red square area in the STEM micrograph. Individual Bi $N_{6,7}$ -edge at 157 eV (red), Te $M_{4,5}$ -edge at 572 eV (green), Cu $L_{2,3}$ -edges at 931 eV (pink). (i) HRTEM micrograph of a $\text{Bi}_2\text{Te}_3\text{-Cu}_{2-x}\text{Te}$ heterostructure, details of the orange square region and its corresponding power spectrum. Lattice fringe distances were 0.341 nm, 0.305 nm and 0.340 nm, at 51.65° and 106.01° which was interpreted as the cubic $\text{Cu}_{2.86}\text{Te}_2$ phase visualized along its [01-1] zone axis.

Similar results were obtained in both directions, which was ascribed to the lack of crystallographic texture in the produced nanomaterials. Indeed, SEM characterization of the consolidated material showed a random distribution of short-range order

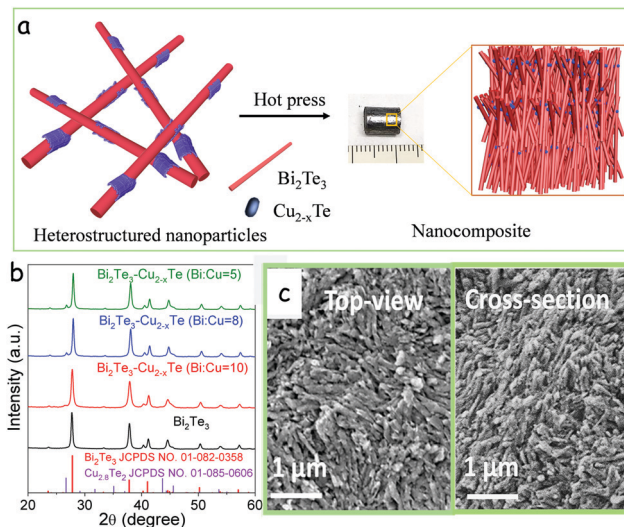


Fig. 2 (a) Scheme of the process used to produce a $\text{Bi}_2\text{Te}_3\text{-Cu}_x\text{Te}$ pellet from $\text{Bi}_2\text{Te}_3\text{-Cu}_x\text{Te}$ nanowires. (b) XRD patterns of consolidated $\text{Bi}_2\text{Te}_3\text{-Cu}_x\text{Te}$ pellets with different compositions. (c) Top-view and cross-section SEM micrographs of a consolidated $\text{Bi}_2\text{Te}_3\text{-Cu}_{2-x}\text{Te}$ pellet.

domains of quasi-aligned nanowires (Fig. 2c). The presence of randomly oriented domains was further confirmed by XRD, which displayed similar relative peak intensities when analysing the samples in two normal directions (Fig. S5, ESI[†]). Owing to this lack of anisotropy in the material transport properties, in the following discussion we focus only on results obtained in the direction normal to the pressure axis.

We initially studied the influence of the annealing temperature on the TE properties of $\text{Bi}_2\text{Te}_3\text{-Cu}_{2-x}\text{Te}$ composites by analysing samples annealed at 330°C and 450°C . The materials annealed at a higher temperature, 450°C , displayed lower ZT values than those annealed at 330°C . We associated this lower performance with the higher crystallinity of the samples annealed at the higher temperature, which translated into lower S and higher κ values (Fig. S6, ESI[†]). Therefore, the following discussion is focused on the properties of materials annealed at 330°C .

Fig. 3 displays the TE properties in the plane normal to the pressure axis of pellets produced from Bi_2Te_3 and $\text{Bi}_2\text{Te}_3\text{-Cu}_{2-x}\text{Te}$ nanowires annealed at 330°C . Bare Bi_2Te_3 displayed electrical conductivities on the order of 10^4 S m^{-1} . This material presented a relatively high charge carrier concentration, close to 10^{19} cm^{-3} (Fig. 4), which was related to a high density of Te_{Bi} antisite donors.³⁶ Its relatively low electrical conductivity compared with highly crystalline materials is associated with the porosity and large density of grain boundaries, which resulted in a relatively low mobility, $20\text{ cm}^2\text{ V}^{-1}\text{ s}^{-1}$.

With the introduction of moderate amounts of Cu, a decrease in σ at room temperature was observed, consistent with a lower Hall charge carrier concentration and a slight decrease of mobility (Fig. 4). This decrease of the carrier concentration was related to the removal of Te from the Bi_2Te_3 nanowires to form Cu_{2-x}Te domains, reducing the concentration of n-type electroactive Te_{Bi} defects. At higher Cu content, Bi:Cu = 5, the electrical

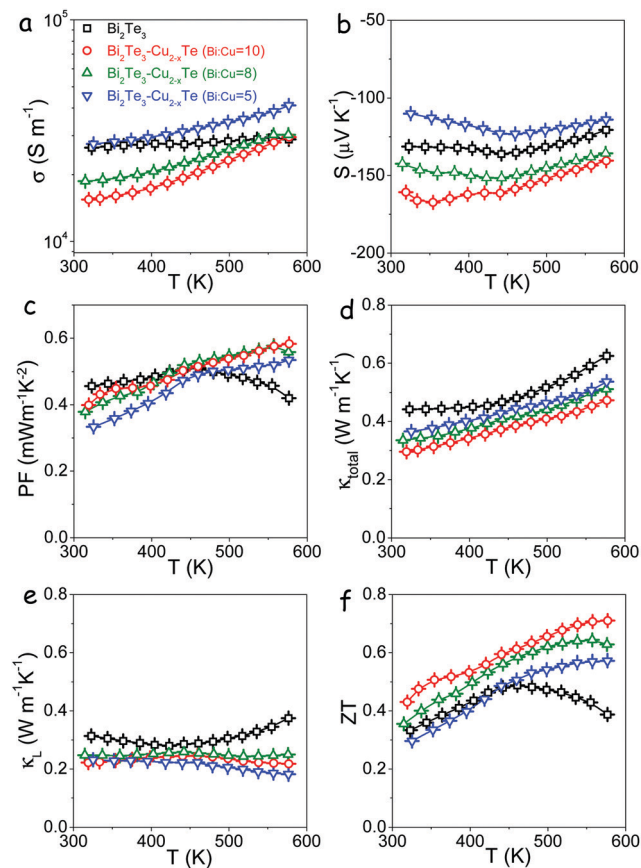


Fig. 3 Thermoelectric properties of Bi_2Te_3 and $\text{Bi}_2\text{Te}_3\text{-Cu}_{2-x}\text{Te}$ pellets: (a) electrical conductivity, σ ; (b) Seebeck coefficient, S ; (c) power factor or $S^2\sigma$, PF; (d) total thermal conductivity, κ_{total} ; (e) lattice thermal conductivity, κ_L ; and (f) TE figure of merit, ZT .

conductivity and charge carrier concentration increased with respect to that of bare Bi_2Te_3 . We related this increase to a further depletion of Te from Bi_2Te_3 , creating donor Te vacancies V_{Te} . Additionally, Cu_{2-x}Te domains could contribute to increased charge carrier concentration through spillover of electrons to Bi_2Te_3 , according to the lower work function of $\text{Cu}_{2.8}\text{Te}_2$ (4.7 eV) compared with the Bi_2Te_3 one (5.3 eV).^{50,51} This injection of charge carriers compensate for the decrease in mobility with the introduction of large amounts of Cu (Fig. 4).

The Seebeck coefficient of Bi_2Te_3 nanomaterials and $\text{Bi}_2\text{Te}_3\text{-Cu}_{2-x}\text{Te}$ nanocomposites was negative in all the temperature range explored. Compared with Bi_2Te_3 , nanocomposites containing relatively small amounts of Cu_{2-x}Te displayed higher Seebeck coefficients, which was consistent with their lower charge carrier concentration. On the other hand, samples containing larger amounts of Cu, Bi:Cu = 5, exhibited lower S values, also consistently with their higher carrier concentration.

For most of the samples, the Seebeck coefficient increased with temperature up to ca. 450 K and then decreased at higher temperatures. In contrast to previous studies,³⁹ the introduction of Cu barely influenced the temperature of the maximum Seebeck coefficient, which depends on the concentration of extrinsic carriers and the source of thermally generated charge

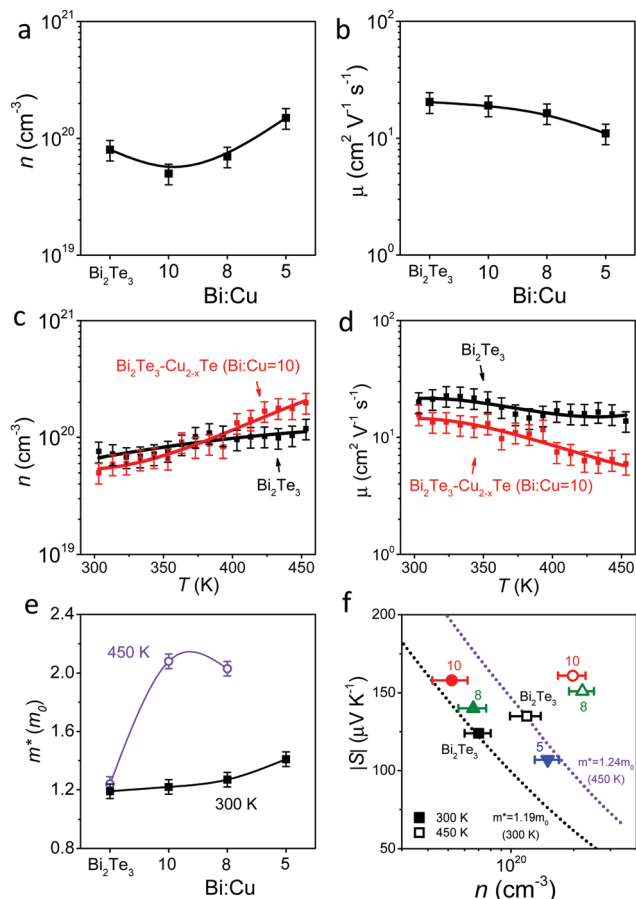


Fig. 4 (a) Ambient temperature Hall charge carrier concentration and (b) carrier mobility as the function of the pellet composition. (c) Temperature dependence of the Hall charge carrier concentration and (d) carrier mobility of Bi_2Te_3 and $\text{Bi}_2\text{Te}_3\text{-Cu}_{2-x}\text{Te}$ (Bi:Cu = 10). (e) Effective mass calculated using a SPB model at room temperature and 450 K as a function of the pellet composition. (f) $|S|$ vs. n for the different samples at 300 K (solid symbols) and 450 K (open symbols). The composition corresponding to each point (Bi_2Te_3 or the Bi:Cu ratio in $\text{Bi}_2\text{Te}_3\text{-Cu}_{2-x}\text{Te}$) is specified for each point. Short dot lines show the theoretical $|S|$ vs. n dependence considering an SPB model obtained using the m^* of bare Bi_2Te_3 at 300 K (black line) and 450 K (purple line).

carriers that are responsible for the bipolar effect. We associated this experimental evidence with a moderate relative change of the concentration of free electrons with the introduction of Cu.

Compared with bare Bi_2Te_3 , all $\text{Bi}_2\text{Te}_3\text{-Cu}_{2-x}\text{Te}$ nanocomposites displayed a stronger increase of electrical conductivity with temperature. In the high temperature range tested, the electrical conductivity of all nanocomposites was similar to or higher than that of bare Bi_2Te_3 , in spite of the higher density of scattering centres of the former. This stronger dependence of electrical conductivity with temperature was associated with a larger influence of electron energy barriers on the charge transport within nanocomposites.

Taking into account the higher charge carrier scattering in composites compared with bare Bi_2Te_3 , to explain their high electrical conductivities in the high temperature range, one needs to assume an increase of the concentration of electrons

participating in the charge transport. Besides thermal generation in Bi_2Te_3 , which should be similar for all materials, this higher concentration of free carriers need to be provided by spillover from Cu_{2-x}Te domains. This strong enhancement of the electrical conductivity with temperature did not come with the expected decrease of the Seebeck coefficient. Thus, in the high temperature range, the power factors of all nanocomposites were significantly larger than those of bare Bi_2Te_3 (Fig. 3c). We hypothesise that these higher power factors are associated with an energy filtering of charge carrier at the energy barriers introduced by the $\text{Bi}_2\text{Te}_3/\text{Cu}_{2-x}\text{Te}$ heterojunctions.

In order to better understand the transport property dependence with temperature, charge carrier concentrations and mobilities were measured as a function of temperature for samples Bi_2Te_3 and $\text{Bi}_2\text{Te}_3\text{-Cu}_{2-x}\text{Te}$ (Bi:Cu = 10). As shown in Fig. 4c, the charge carrier concentration of the Bi_2Te_3 sample monotonously increased with temperature in all the range tested. On the other hand, the $\text{Bi}_2\text{Te}_3\text{-Cu}_{2-x}\text{Te}$ (Bi:Cu = 10) displayed a higher rate of activation of charge carriers, particularly at temperatures above 350 K. We associate this activation with the injection of electrons from Cu_{2-x}Te to Bi_2Te_3 . This different rate of activation of charge carriers resulted in the $\text{Bi}_2\text{Te}_3\text{-Cu}_{2-x}\text{Te}$ composites having higher charge carrier concentrations in the high temperature range than bare Bi_2Te_3 . Surprisingly, this large increase of the charge carrier concentration in the nanocomposites was not correlated with a similar decrease of the absolute value of the Seebeck coefficient. Besides, the charge carrier mobility monotonously decreased for both materials with temperature, the mobility of the composite being lower than that of bare $\text{Bi}_2\text{Te}_3\text{-Cu}_{2-x}\text{Te}$ at all temperatures.

When calculating the effective mass of Bi_2Te_3 and $\text{Bi}_2\text{Te}_3\text{-Cu}_{2-x}\text{Te}$ composites using a single parabolic band (SPB) model (Fig. 4e), we observe all composites to have slightly higher apparent effective masses at 300 K. This apparent effective mass strongly increases at 450 K, becoming close to twofold higher than that of Bi_2Te_3 . Fig. 4f displays a plot of the absolute value of the Seebeck coefficient as a function of the charge carrier concentration. Lines displaying the theoretical dependence (SPB model) of $|S|$ as a function of n for the calculated effective masses of Bi_2Te_3 at 300 K and 450 K are also plotted as a reference. Notice how at 450 K, the presence of Cu_{2-x}Te results in Seebeck coefficients up to 50% larger than those predicted for bare Bi_2Te_3 with the same charge carrier concentration.

The large differential electron affinity of Cu_{2-x}Te and Bi_2Te_3 , and the small size of the Cu_{2-x}Te crystal domains inevitably lead to a spillover of electrons from the valence band of Cu_{2-x}Te to the conduction band of Bi_2Te_3 and the consequent pinning of the Cu_{2-x}Te Fermi level within its valence band (Fig. 5a). Simultaneously, within the Bi_2Te_3 nanowires, a downward bending of the electron energy bands around the Cu_{2-x}Te domains is expected (Fig. 5b and c). Thus, electrons injected from Cu_{2-x}Te accumulate in potential wells within the Bi_2Te_3 nanowire. Upon increasing temperature, higher amounts of electrons are injected from Cu_{2-x}Te to Bi_2Te_3 , and electrons in

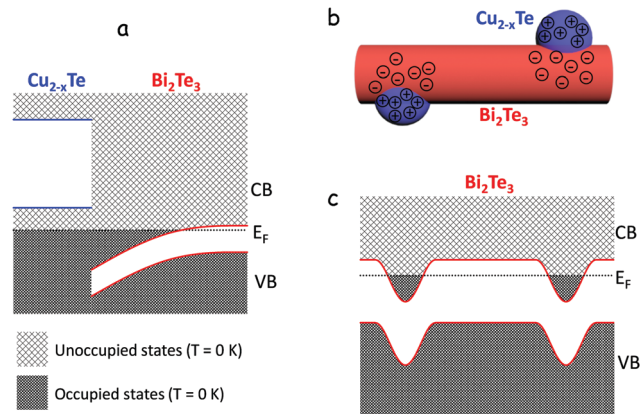


Fig. 5 (a) Electron energy band alignment in a heterojunction between a small Cu_{2-x}Te crystal and a larger Bi_2Te_3 domain. (b) Cartoon of the charge distribution within a Bi_2Te_3 nanowire having two Cu_{2-x}Te domains on its surface. (c) Qualitative electron energy band diagram of the same Bi_2Te_3 nanowire having two Cu_{2-x}Te domains on its surface.

the Bi_2Te_3 potential wells have more energy to overcome the barriers and move freely through the Bi_2Te_3 domains. These two phenomena explain the strong increase of the electrical conductivity with temperature in nanocomposites. Besides, electrons travelling through the Bi_2Te_3 crystal domains encounter abundant energy wells able to trap low energy charge carriers. This mechanism of filtering of charge carriers as a function of their energy may be responsible for the significantly higher Seebeck coefficients measured in nanocomposites compared with bare Bi_2Te_3 .

As expected, all $\text{Bi}_2\text{Te}_3\text{-Cu}_{2-x}\text{Te}$ nanocomposites exhibited significantly lower thermal conductivities than pure Bi_2Te_3 due to enhanced phonon scattering at extensive interphases (Fig. 3d and e). The lowest thermal conductivities were obtained from the sample containing the smallest amount of Cu, Bi:Cu = 10, because the electronic contribution to the thermal conductivity increased with the Cu_{2-x}Te content (Fig. S7, ESI†). Fig. S9 (ESI†) displays the lattice thermal conductivity obtained with the phonon relaxation time based on the Debye–Callaway model considering the effect of grain boundaries and the presence of Cu_{2-x}Te nanodomains (see the ESI† for details). Compared to the calculations, experimental data showed a slightly lower effect of the incorporation of Cu_{2-x}Te nanodomains on the lattice thermal conductivity, especially at low temperature. This discrepancy could be in part explained by the overestimation of this parameter in nanomaterials when calculated by extracting the electronic contribution, as recently reported by Snyder *et al.*⁵² This overestimation of the lattice thermal conductivity, especially in the lower temperature range, also hides the bipolar contribution to the thermal conductivity, which is only evident for the Bi_2Te_3 sample in the form of an increase of the calculated lattice thermal conductivity at temperature above 450 K. Notice finally that the low thermal conductivities obtained for Bi_2Te_3 and $\text{Bi}_2\text{Te}_3\text{-Cu}_{2-x}\text{Te}$ are in part related to the relatively high porosity of the produced materials, with densities of around 86–87%

(see the ESI† for an estimation of the porosity contribution to the lattice thermal conductivity and a comparison with the Cahill limit, Fig. S8, ESI†).

Fig. 3f displays the TE figure of merit obtained from Bi₂Te₃ and Bi₂Te₃-Cu_{2-x}Te samples. For pure Bi₂Te₃, a maximum *ZT* value of 0.48 was achieved at 460 K, which is notable for pure Bi₃Te₃. At higher temperatures, *ZT* decreased severely due to the bipolar contribution. On the other hand, Bi₂Te₃-Cu_{2-x}Te composites displayed significantly larger *ZT* values, up to 0.74 at 576 K for Bi:Cu = 10.

Conclusions

In conclusion, we have reported a solution-based protocol to synthesize Bi₂Te₃-Cu_{2-x}Te heterostructured nanowires that were used to produce Bi₂Te₃-Cu_{2-x}Te nanocomposites with relative densities close to 90%. We observed that the presence of Cu_{2-x}Te to result in an increase of the TE figure of merit of up to 50%. The higher *ZT* values measured in Bi₂Te₃-Cu_{2-x}Te nanocomposites compared with bare Bi₂Te₃ were attributed to a combination of several features: (i) the large electrical conductivities measured in the nanocomposites at high temperature, mainly associated with the spillover of charge carriers from Cu_{2-x}Te domains to the Bi₂Te₃ matrix; (ii) the enhanced Seebeck coefficients without sacrificing electrical conductivity in the high temperature range associated with the energy-filtering of charge carriers at potential barriers introduced with the formation of the Bi₂Te₃/Cu_{2-x}Te heterojunctions; and (iii) the enhanced phonon scattering at the interphase of two different materials, which notably reduced the thermal conductivity.

Conflicts of interest

There are no conflicts to declare.

Acknowledgements

This work was supported by the European Regional Development Funds and by the Spanish Ministerio de Economía y Competitividad through the project SEHTOP (ENE2016-77798-C4-3-R). Y. Z. and X. H., thank the China Scholarship Council for scholarship support. M. C. has received funding from the European Union's Horizon 2020 Research and Innovation programme under the Marie Skłodowska-Curie Grant Agreement No. 665385. M. I. acknowledges financial support from IST Austria. Y. L. acknowledges funding from the European Union's Horizon 2020 Research and Innovation Programme under the Marie Skłodowska-Curie grant agreement no. 754411. ICN2 acknowledges funding from Generalitat de Catalunya 2017 SGR 327 and the Spanish MINECO project ENE2017-85087-C3. ICN2 is supported by the Severo Ochoa program from the Spanish MINECO (grant no. SEV-2017-0706) and is funded by the CERCA Programme/Generalitat de Catalunya. Part of the present work

has been performed in the framework of Universitat Autònoma de Barcelona Materials Science PhD program.

References

- 1 Q. H. Zhang, X. Y. Huang, S. Q. Bai, X. Shi, C. Uher and L. D. Chen, *Adv. Eng. Mater.*, 2016, **18**, 194–213.
- 2 G. J. Snyder and T. S. Ursell, *Phys. Rev. Lett.*, 2003, **91**, 148301.
- 3 T. Humphrey and H. Linke, *Phys. Rev. Lett.*, 2005, **94**, 096601.
- 4 S. Ortega, M. Ibáñez, Y. Liu, Y. Zhang, M. V. Kovalenko, D. Cadavid and A. Cabot, *Chem. Soc. Rev.*, 2017, **46**, 3510–3528.
- 5 G. J. Snyder and E. S. Toberer, *Materials for sustainable energy: a collection of peer-reviewed research and review articles from Nature Publishing Group*, World Sci., 2011, pp. 101–110.
- 6 J.-F. Li, W.-S. Liu, L.-D. Zhao and M. Zhou, *NPG Asia Mater.*, 2010, **2**, 152–158.
- 7 W. Liu, Q. Jie, H. S. Kim and Z. Ren, *Acta Mater.*, 2015, **87**, 357–376.
- 8 Z.-G. Chen, G. Han, L. Yang, L. Cheng and J. Zou, *Prog. Nat. Sci.: Mater. Int.*, 2012, **22**, 535–549.
- 9 J. P. Heremans, V. Jovovic, E. S. Toberer, A. Saramat, K. Kurosaki, A. Charoenphakdee, S. Yamanaka and G. J. Snyder, *Science*, 2008, **321**, 554–557.
- 10 M. Ibáñez, A. Genc, R. Hasler, Y. Liu, O. Dobrozhan, O. Nazarenko, M. Mata, J. Arbiol, A. Cabot and M. V. Kovalenko, *ACS Nano*, 2019, **13**, 6572–6580.
- 11 J. Li, Q. Tan, J. F. Li, D. W. Liu, F. Li, Z. Y. Li, M. Zou and K. Wang, *Adv. Funct. Mater.*, 2013, **23**, 4317–4323.
- 12 Y. Cao, X. Zhao, T. Zhu, X. Zhang and J. Tu, *Appl. Phys. Lett.*, 2008, **92**, 143106.
- 13 B. Yu, M. Zebarjadi, H. Wang, K. Lukas, H. Wang, D. Wang, C. Opeil, M. Dresselhaus, G. Chen and Z. Ren, *Nano Lett.*, 2012, **12**, 2077–2082.
- 14 P. Jood, R. J. Mehta, Y. Zhang, G. Peleckis, X. Wang, R. W. Siegel, T. Borca-Tasciuc, S. X. Dou and G. Ramanath, *Nano Lett.*, 2011, **11**, 4337–4342.
- 15 A. Banik, B. Vishal, S. Perumal, R. Datta and K. Biswas, *Energy Environ. Sci.*, 2016, **9**, 2011–2019.
- 16 L.-D. Zhao, S.-H. Lo, J. He, H. Li, K. Biswas, J. Androulakis, C.-I. Wu, T. P. Hogan, D.-Y. Chung, V. P. Dravid and M. G. Kanatzidis, *J. Am. Chem. Soc.*, 2011, **133**, 20476–20487.
- 17 J. He, S. N. Girard, J. C. Zheng, L. Zhao, M. G. Kanatzidis and V. P. Dravid, *Adv. Mater.*, 2012, **24**, 4440–4444.
- 18 J. He, J. R. Sootsman, S. N. Girard, J.-C. Zheng, J. Wen, Y. Zhu, M. G. Kanatzidis and V. P. Dravid, *J. Am. Chem. Soc.*, 2010, **132**, 8669–8675.
- 19 H. Choi, K. Jeong, J. Chae, H. Park, J. Baeck, T. H. Kim, J. Y. Song, J. Park, K.-H. Jeong and M.-H. Cho, *Nano Energy*, 2018, **47**, 374–384.
- 20 G. Pernot, M. Stoffel, I. Savic, F. Pezzoli, P. Chen, G. Savelli, A. Jacquot, J. Schumann, U. Denker, I. Mönch, C. Deneke,

- O. G. Schmidt, J. M. Rampnoux, S. Wang, M. Plissonnier, A. Rastelli, S. Dilhaire and N. Mingo, *Nat. Mater.*, 2010, **9**, 491–495.
- 21 M. Ibáñez, R. Hasler, A. Genc, Y. Liu, B. Kuster, M. Schuster, O. Dobrozhan, D. Cadavid, J. Arbiol, A. Cabot and M. Kovalenko, *J. Am. Chem. Soc.*, 2019, **141**, 8025–8029.
- 22 G. Zhang, H. Fang, H. Yang, L. A. Jauregui, Y. P. Chen and Y. Wu, *Nano Lett.*, 2012, **12**, 3627–3633.
- 23 H. Fang, T. Feng, H. Yang, X. Ruan and Y. Wu, *Nano Lett.*, 2013, **13**, 2058–2063.
- 24 H. Fang, H. Yang and Y. Wu, *Chem. Mater.*, 2014, **26**, 3322–3327.
- 25 H. Yang, J.-H. Bahk, T. Day, A. M. Mohammed, B. Min, G. J. Snyder, A. Shakouri and Y. Wu, *Nano Lett.*, 2014, **14**, 5398–5404.
- 26 M. Ibáñez, Z. Luo, A. Genc, L. Piveteau, S. Ortega, D. Cadavid, O. Dobrozhan, Y. Liu, M. Nachtegaal, M. Zebarjadi, J. Arbiol, M. Kovalenko and A. Cabot, *Nat. Commun.*, 2016, **7**, 10766.
- 27 J. P. Heremans, C. M. Thrush, D. T. Morelli and M.-C. Wu, *Phys. Rev. Lett.*, 2002, **88**, 216801.
- 28 Q. Yao, L. Chen, W. Zhang, S. Liufu and X. Chen, *ACS Nano*, 2010, **4**, 2445–2451.
- 29 X. Zhao, X. Ji, Y. Zhang, T. Zhu, J. Tu and X. Zhang, *Appl. Phys. Lett.*, 2005, **86**, 062111.
- 30 W. S. Liu, Q. Zhang, Y. Lan, S. Chen, X. Yan, Q. Zhang, H. Wang, D. Wang, G. Chen and Z. Ren, *Adv. Energy Mater.*, 2011, **1**, 577–587.
- 31 W. Xie, J. He, H. J. Kang, X. Tang, S. Zhu, M. Laver, S. Wang, J. R. Copley, C. M. Brown, Q. Zhang and T. Tritt, *Nano Lett.*, 2010, **10**, 3283–3289.
- 32 M. Ibáñez, R. Hasler, Y. Liu, O. Dobrozhan, O. Nazarenko, D. Cadavid, A. Cabot and M. V. Kovalenko, *Chem. Mater.*, 2017, **29**, 7093–7097.
- 33 Y. Liu, D. Cadavid, M. Ibáñez, S. Ortega, S. Martí-Sánchez, O. Dobrozhan, M. V. Kovalenko, J. Arbiol and A. Cabot, *APL Mater.*, 2016, **4**, 104813.
- 34 M. Ibáñez, R. Zamani, S. Gorsse, J. Fan, S. Ortega, D. Cadavid, J. R. Morante, J. Arbiol and A. Cabot, *ACS Nano*, 2013, **7**, 2573–2586.
- 35 M. Ibáñez, R. J. Korkosz, Z. Luo, P. Riba, D. Cadavid, S. Ortega, A. Cabot and M. G. Kanatzidis, *J. Am. Chem. Soc.*, 2015, **137**, 4046–4049.
- 36 T. Zhu, L. Hu, X. Zhao and J. He, *Adv. Sci.*, 2016, **3**, 1600004.
- 37 Y. Liu, Y. Zhang, K. H. Lim, M. Ibáñez, S. Ortega, M. Li, J. David, S. Martí-Sánchez, K. M. Ng, J. Arbiol, M. Kovalenko, D. Cadavid and A. Cabot, *ACS Nano*, 2018, **12**, 7174–7184.
- 38 Y. Liu, Y. Zhang, S. Ortega, M. Ibáñez, K. H. Lim, A. Grau-Carbonell, S. Martí-Sánchez, K. M. Ng, J. Arbiol, M. V. Kovalenko, D. Cadavid and A. Cabot, *Nano Lett.*, 2018, **18**, 2557–2563.
- 39 J. M. Song, J. U. Rahman, J. Y. Cho, S. Lee, W. S. Seo, S. Kim, S.-i. Kim, K. H. Lee, D. Roh and W. H. Shin, *Scr. Mater.*, 2019, **165**, 78–83.
- 40 W. Zhu, W. Hu, P. Wei, X. Nie and W. Zhao, *J. Electron. Mater.*, 2020, **49**, 2962–2967.
- 41 H.-L. Zhuang, Y. Pan, F.-H. Sun, J. Dong, J. Pei, B. Cai, H. Hu, H. Tang and J.-F. Li, *Nano Energy*, 2019, **60**, 857–865.
- 42 H.-J. Wu and W.-T. Yen, *Acta Mater.*, 2018, **157**, 33–41.
- 43 J. Bludská, I. Jakubec, Č. Drašar, P. Lošťák and J. Horak, *Philos. Mag.*, 2007, **87**, 325–335.
- 44 M. Sinduja, S. Amirthapandian, A. Masarrat, R. Krishnan, S. Srivastava and A. Kandasami, *Thin Solid Films*, 2020, **697**, 137834.
- 45 K. H. Seo, B. G. Kim, C.-H. Lim, S.-H. Kim, K.-M. Lee, J.-Y. Kim and S.-M. Choi, *CrystEngComm*, 2017, **19**, 2750–2757.
- 46 Q. Lognonné and F. Gascoin, *J. Alloys Compd.*, 2014, **610**, 1–5.
- 47 G. Zhang, B. Kirk, L. A. Jauregui, H. Yang, X. Xu, Y. P. Chen and Y. Wu, *Nano Lett.*, 2012, **12**, 56–60.
- 48 Y. G. Asadov, L. Rustamova, G. Gasimov, K. Jafarov and A. Babajev, *Phase Transitions*, 1992, **38**, 247–259.
- 49 A. Pashinkin and V. Fedorov, *Inorg. Mater.*, 2003, **39**, 539–554.
- 50 M. Huang, A. Maljusch, F. Calle-Vallejo, J. B. Henry, M. T. Koper, W. Schuhmann and A. S. Bandarenka, *RSC Adv.*, 2013, **3**, 21648–21654.
- 51 D. Haneman, *J. Phys. Chem. Solids*, 1959, **11**, 205–214.
- 52 J. Kuo, W. Max, S. Tyler, M. Kanatzidis and J. Snyder, *Energy Environ. Sci.*, 2020, **13**, 1250–1258.